State-to-State Chemistry
with Ultracold Neutral Rb Atoms

Dissertation

zur Erlangung des akademischen Grades
Doktor der Naturwissenschaften (Dr. rer. nat.)

eingereicht an der
Fakultät für Naturwissenschaften
der
Universität Ulm

von
Joschka Wolf
aus

Ulm

Betreuer der Dissertation: Johannes Hecker Denschlag

2019

Amtierender Dekan: Prof. Dr. Peter Dürre

Erstgutachter: Prof. Dr. Johannes Hecker Denschlag

Zweitgutachter: Prof. i.R. Dr. Peter Reineker

Tag der mündlichen Prüfung:

Die in dieser Dissertation beschriebenen Arbeiten wurden durchgeführt an der

Universität Ulm

Institut für Quantenmaterie

Albert-Einstein-Allee 45

D-89069 Ulm

Abstract

In this thesis, I report on experiments on the detection and the production of molecules in an ultracold atomic gas. These experiments can be divided into two main parts. The first part is about state-to-state experiments where chemical reaction products are detected in a quantum state resolved way. The second part is about Rydberg molecules.

In the first part, I investigate three-body recombination of neutral Rb, which is a chemical reaction leading to the formation of Rb_2 dimers. The quantum states of the three-body recombination product molecules are investigated for different initial atomic samples. This includes different atomic hyperfine states and different atomic magnetic sub states that are prepared. The molecular reaction product is state-selectively ionized and detected afterwards. The detection scheme resolves total electron spin, the vibrational, the rotational, the hyperfine and even the magnetic sub state of the product molecules. We determine the population distribution of the product molecules covering the majority of all produced molecules. The insights gained enable us to formulate various propensity rules for the three-body recombination of ^{87}Rb.

The second part is furthermore divided into two parts: the investigations of charged and uncharged Rydberg molecules. The investigations of charged Rydberg molecules are the first step towards one of our goals, the photoassociation of $BaRb^+$ or Rb_2^+ Rydberg molecules. For this work, we have developed a novel method to measure Stark spectra within an ion trap.

In experiments with neutral Rb_2 Rydberg molecules we observe a complex spin structure of the molecular states. The substructure emerges partially due to a novel, recently predicted spin-orbit interaction of the Rydberg electron and the perturber atom, which we prove for the first time.

Zusammenfassung

In dieser Dissertation berichte ich von Experimenten, die sich mit der Detektion und der Produktion von Molekülen in einem ultrakalten Atomgas befassen. Die durchgeführten Experimente können in zwei Teile aufgeteilt werden. Der erste Teil behandelt Experimente in denen chemische Reaktionsprodukte quantenzustandsaufgelöst detektiert werden. Der zweite Teil behandelt Rydbergmoleküle.

Im ersten Teil untersuche ich die Dreikörperrekombination von neutralem Rb. Diese chemische Reaktion führt zur Bildung eines Rb_2 Dimers. Die Quantenzustände der Produktmoleküle der Dreikörperrekombination werden für Atomgase mit unterschiedlichen initialen Zuständen untersucht. Dies beinhaltet die Präparation von verschiedenen atomaren Hyperfeinzuständen sowie von verschiedenen atomaren magnetischen Subzuständen. Das molekulare Reaktionsprodukt wird zustandsselektiv ionisiert und danach detektiert. Das Detektionsschema löst den totalen Elektronenspin, den Vibrations-, den Rotations-, den Hyperfein- und sogar den magnetischen Subzustand der Produktmoleküle auf. Mithilfe der beschriebenen Methode bestimmen wir die Zustandsverteilung für den größten Teil der erzeugten Produktmoleküle. Die dabei gewonnen Erkenntnisse erlauben es uns Neigungsregeln für die Dreikörperrekombination von ^{87}Rb aufzustellen.

Der zweite Teil, untergliedert sich weiterhin in zwei Teile: Untersuchungen von geladene und ungeladene Rydbergmolekülen. Die Untersuchungen bezüglich der geladenen Rydbergmoleküle sind der erste Schritt für eines unserer Ziele, der erstmaligen Photoassoziation von BaRb$^+$ oder Rb_2^+ Rydbergmolekülen. Im Zuge dessen haben wir eine neuartige Methode entwickelt, um Starkspektren in einer Ionenfalle zu messen.

In Experimenten mit neutralen Rb_2 Rydbergmolekülen haben wir eine komplexe Spinstruktur der molekularen Rydbergzustände beobachtet. Diese Substruktur wird teilweise durch eine neuartige Spin-Bahn Wechselwirkung zwischen dem Rydbergelektron und dem Grundzustandsatom erzeugt, welche wir zum ersten Mal nachweisen.

Contents

Contents

1 Introduction

According to Immanuel Kant, it is necessary to assign our environment a causal order to be able to comprehend it and live in it. Physics is the science of nature's causality, as it tries to model the interaction of entities around us. Therefore physicist have always been driven to model the causal processes around us on a more fundamental level.

In the beginning of the 20$^{\text{th}}$ century the fundamentally new theory of quantum mechanics was introduced. It describes many of the most fundamental processes on the smallest scale of energy and size. This new theory did not only massively change the understanding of physics, but connected to this also chemistry.

General chemistry is the scientific discipline of chemical reactions. A chemical reaction is a process were an initial substance (educt) changes its properties and becomes a final substance (product). Quantum mechanics governs the underlying reaction dynamics. These dynamics are not always understood in all details, especially for more complicated reaction systems. A full understanding of the reaction dynamics includes knowing which quantum state of the educts leads to which quantum state of the products. This research field is called state-to-state chemistry. For a state-to-state chemistry measurement, the initial quantum states of the educts need to be prepared and the quantum states of the products need to be measured. An important goal after understanding the reaction process is to be able to control chemical reactions on the quantum level.

We investigated mainly the chemical reaction of three-body recombination. In a three-body recombination, three atoms collide and two of the atoms form a diatomic molecule. Since in our experiments initial quantum states of the atoms are known, we can extract information of the reaction dynamics by measuring the quantum states of the product molecules.

In the following a historical overview of how quantum mechanics entered the realm of chemistry will be given. Quickly after the discovery of the Schrödinger equation (1926), Walter Heitler and Fritz London applied it to the diatomic hydrogen molecule (1927) [1]. Their calculations can be seen as the first milestone of connecting quantum mechanics

and chemistry, as the chemical bonding of two atoms was described with the Schrödinger equation. Afterwards, it was believed that the field of chemistry can be reduced simply to physics and will vanish soon. Within a few years it became clear that the complexity of chemical systems was highly underestimated and a general pessimism was entering the field [2].

By simplifications of the quantum mechanical models, a deep understanding of the bonding mechanics of molecules was gained. The first Nobel Prize in Chemistry in the field of quantum chemistry was awarded to Linus Pauling in 1954 "*for his research into the nature of the chemical bond and its application to the elucidation of the structure of complex substances*". He investigated chemical bonds and his work lead to the concept of orbital hybridization. This concept is important to understand the quantum mechanical effects leading to the binding of a molecule. The next Nobel Prize in Chemistry in the field was awarded to Robert S. Mulliken in 1966 "*for his fundamental work concerning chemical bonds and the electronic structure of molecules by the molecular orbital method*". R. Mulliken together with F. Hund, developed the molecular orbital method. This method is crucial for the calculation of the electronic structure of molecules.

The main topic of these Nobel Prizes and many other publications during that time was to understand molecules with their quantum mechanical properties. With the understanding of the structure of molecules, experiments started to verify and use the models to investigate quantum chemistry. A very important tool to investigate chemical processes on the quantum level experimentally are atomic and molecular beams. Louis Dunoyer de Segonzac developed the molecular beam method already in 1911. In a beam experiment, a reservoir of particles is connected with a thin nozzle to a vacuum chamber. The particles from the reservoir that can pass the nozzle have a certain velocity distribution. Therefore, they form a beam of particles in the vacuum. By applying an external state selective force to the particles, this method can be used to separate the components in the beam state selective. This state selectivity was used by Otto Stern to measure the magnetic moment of the proton. He was awarded the Nobel Prize in Physics in 1943 "*for his contribution to the development of the molecular ray method and his discovery of the magnetic moment of the proton*".

To investigate collisions of particles i.e. investigating reaction dynamics, often crossed molecular beam experiments are used. At the intersection of the beams, two particles of the two beams can collide. These experiments allow for the tuning of the relative velocity of the two beams and for setting the collision energy in a certain range. The scattered

particles typically fly in different directions as the original beams and can be detected. As described before, by applying external fields, the beams can be detected state selectively, but also spectroscopic methods are possible to investigate the reaction products. These techniques have been used by Dudley R. Herschbach, Yuan T. Lee, and John C. Polanyi, which were awarded in 1986 with the Nobel Prize in Chemistry "*for their contributions concerning the dynamics of chemical elementary processes*". Crossed molecular beam experiments have been and are still very important to understand how quantum mechanics governs chemical reactions. There is a huge amount of publications in the field of molecular beam experiments. We only give here a few reviews for further reading [3, 4, 5].

Another approach to investigate state-to-state chemistry is to use ultracold atomic gases. Ultracold atom gas experiments are comparatively young, but two Nobel Prizes have been awarded in the wake of their development. In 1997 Steven Chu, Claude Cohen-Tannoudji, and William D. Phillips were awarded with the Nobel Prize in Physics "*for development of methods to cool and trap atoms with laser light*". Quickly after the Nobel Prize for the cooling and trapping of atomic gases, the Nobel Prize was awarded for creating a Bose-Einstein condensate, the coldest substance made. In 2001, Eric A. Cornell, Wolfgang Ketterle, and Carl E. Wieman were awarded with the Nobel Prize in Physics "*for the achievement of Bose-Einstein condensation in dilute gases of alkali atoms, and for early fundamental studies of the properties of the condensates.*"

These works are the foundation to investigate chemical reaction dynamics in ultracold atomic gases. By being able to use ultracold atomic gases, it is possible to perform state-to-state chemistry experiments in a regime that is generally not accessible for beam experiments. An ultracold atomic gas can be very cold ($< 1\,\mu$K). Therefore, very low collision energies of the particles in it can be achieved. The comparatively high densities ($\approx 10^{14}\,$cm^{-3}) allow to investigate collisions of more than two particles.

First theoretical and experimental investigations of chemical reactions in ultracold atomic gases were performed for reactions with a limited number of product channels e.g. [6, 7, 8, 9] or for resonant interparticle interactions e.g. [10, 11]. Arne Härter et al. [12] recently investigated the population distribution of product molecules after three-body recombination for non-resonant interactions of neutral ^{87}Rb atoms. During my dissertation I extended this scheme, which among other things enabled us to measure the population distribution quantitatively.

Besides studying three-body recombination of neutral atoms, our group in Ulm has also investigated three-body recombination of two neutral atoms with an ion [13, 14, 15]. The

interaction between an atom and an ion is generally of longer range ($1/r^4$) than the interaction between two neutral atoms, which is governed by the $1/r^6$ van der Waals potential. In our atom-ion experiments we are typically working with a single Ba^+ immersed in an ultracold ^{87}Rb atom gas. This allows to investigate chemical reactions of a single ion in a bath of atoms. Recently, ideas were developed in our group to control the collision, using a shielding scheme that utilizes Rydberg levels [16]. I will present our results of first Rydberg spectroscopy measurements.

In the following an outline of the thesis is given. In the next Chapter 2, I will present an overview of the experimental setup. In Chapter 4 I show state-to-state measurements of ultracold three-body recombination in an $f = 1$ $m_f = -1$ atomic sample measured via an excited singlet potential. In these measurements, we probe the electron spin singlet part of the product molecules in the mixed singlet - triplet ground state potential.

In Chapter 5 I discuss the state-to-state measurements resolving the magnetic quantum number of the three-body recombination product molecules.

In Chapter 5.6 I present preliminary results of state-to-state measurements where we use a detection path via spin triplet states, which therefore probes the triplet content of the product molecules in the mixed singlet - triplet ground state potential.

In Chapter 6 I will present Stark map measurements. In Chapter 7 I will discuss photoassociation of Rb_2 Rydberg molecules. I will end this thesis with an outlook given in Chapter 8.

2 The experimental setup

2.1   The hybrid atom-ion machine

In this section, I will only give a short overview of the experimental setup, as it has been already discussed in various other sources [17, 18, 19, 20]. The **Ba**rium **Ru**bidium **I**on **E**xperiment (BaRbIE) in Ulm can combine ultracold ^{87}Rb atoms with ionic atoms and molecules i.e. Rb$^+$, Rb$_2^+$, BaRb$^+$ and Ba$^+$.

The vacuum apparatus consists of three chambers (see Fig. 2.1), which are separated to grant maximum optical access of the Paul trap. The preparation of the atom cloud starts in the **MOT chamber**, where we load the ^{87}Rb Magneto-Optical-Trap (MOT) within approximately $4\,s$ out of the background gas. During the following optical molasses phase the atom cloud is cooled, before we optically pump the atom cloud into the $f = 1$, $m_f = -1$ state, where f is the total angular momentum quantum number and m_f the spin projection quantum number. By adding one $\lambda/4$ waveplate into the beam path of the spin polarization lasers the polarization of the used lasers can easily be changed to polarize into the $f = 2$, $m_f = 2$ atomic state. Only the magnetically trappable spin states can be transported with the **magnetic transport**. This ensures a spin-polarized ensemble of atoms. After the magnetic transport, the atom cloud is in the **BEC chamber**. Here the cloud is held in a magnetic trap and optical dipole trap combination, where the temperature of the cloud is reduced via radio frequency (RF) evaporation. In the final step of this RF evaporation the cloud is evaporated i.e. cooled into the dipole trap and the magnetic trap is turned off. From the dipole trap in the BEC chamber, the atom cloud is loaded into a 1-D optical lattice, which is used for a vertical **optical transport**. After the lower dipole trap beam has passed the BEC chamber, we couple it into an optical fiber and use the light for the dipole trap in the **science chamber**. After the optical transport of about $30\,cm$, the
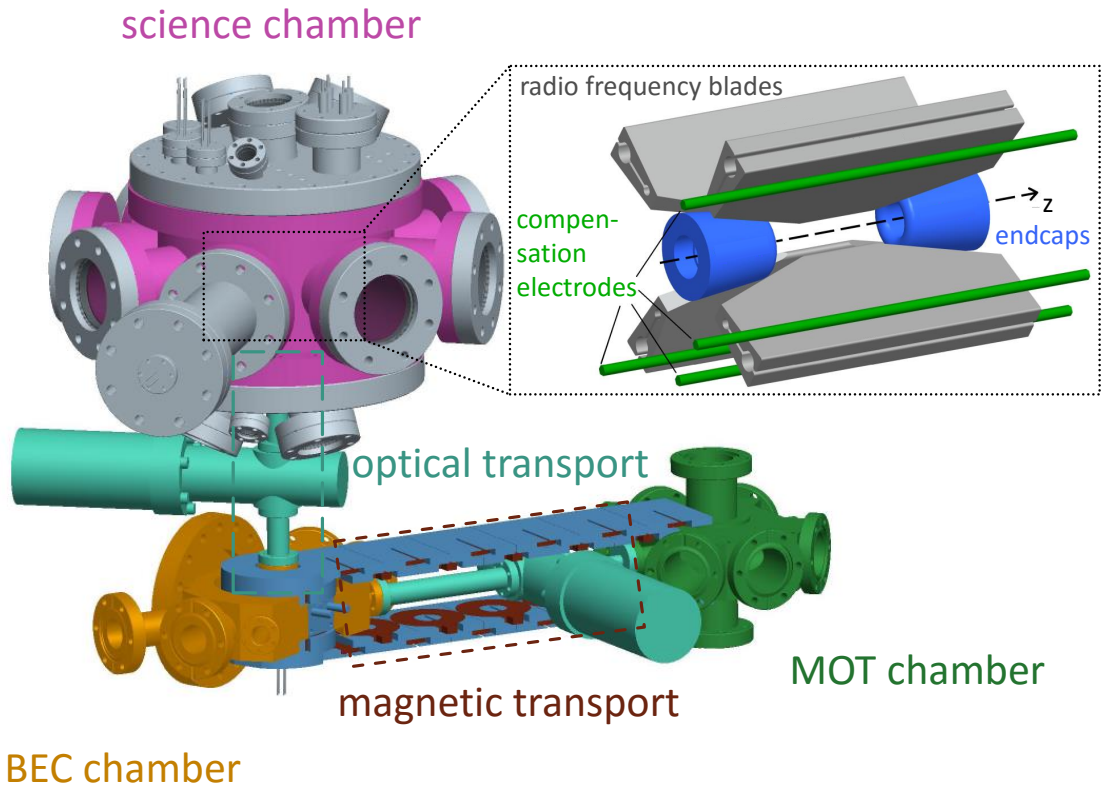
Figure 2.1: The BaRbIE setup. A drawing of the three-chamber vacuum system of the Ulm experiment with a zoomed in picture of the linear Paul trap, which is located in the science chamber. In the center of the Paul trap, a crossed optical dipole trap is used to confine the Rb atom cloud (not displayed).

cloud is loaded into the optical dipole trap in the science chamber. The upper lattice beam stays turned on and therefore forms a crossed optical dipole trap. The atom cloud is held in the linear Paul trap center during the interaction time. After the experiment, a time of flight absorption image of the atom cloud is made. The **Paul trap** is sketched in Figure 2.1. It is a linear Paul trap, which consists of four RF blades producing the oscillating quadrupole field. The endcaps are responsible for the DC field along the axial direction i.e. z-axis. During the transport phase of the atom cloud, the ion can be displaced along the axial direction of the trap to prevent unwanted atom-ion interaction. With the four compensation electrodes, we can apply DC fields along the radial trap directions. These fields are used to compensate for stray electric fields that increase the ions collision energy or to increase the collision energy of the ion on purpose by shifting the ion out of the trap center. Our Barium ions $^{138}Ba^+$ are photoionized from a Barium oven which is

located below the Paul trap.

2.1.1 Introduction into the measurement scheme

In this section, I will introduce the basics of our measurement scheme. In all of our state-to-state chemistry experiments a molecule is formed, state selectively ionized and afterwards detected. Here, I will focus on the molecule formation and the state selective ionization. The ion detection scheme is explained in Section 4.2.5. The experimental details of our measurement scheme will be given in the corresponding chapters.

Three-body recombination product molecules
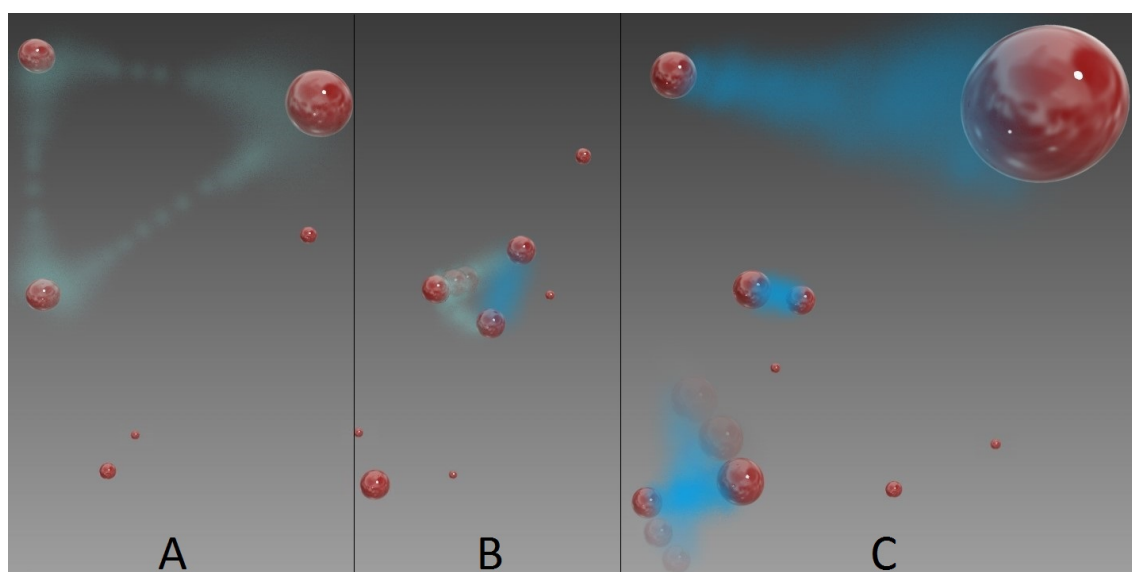
Figure 2.2: An artistic presentation of three-body recombination. The red spheres are representing atoms. The light blue shading between the atoms depicts an interaction. The blue shading is used for a molecular binding of two atoms. **A**, three atoms approach each other closely enough to interact with each other. **B**, this can lead to the formation of a molecule. The released binding energy is distributed between the atom and the product molecule. **C**, the resulting product molecules can have different properties. For example, from top to bottom in the figure, they can be weakly bound or more deeply bound, and have rotational excitation.

In our state-to-state chemistry experiments, we are mainly interested in the product molecules of three-body recombination. A three-body recombination is a chemical process where

three colliding atoms are recombining into an atom and a molecule, see Figure 2.2. The product molecule can be formed in different states. We are investigating the product distribution of these states. In our case, the three-body recombination follows the reaction equation

$$A + A + A => A + A_2 + E$$
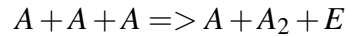
with A being an atom and E the binding energy of the molecule.

The three-body recombination is typically an exothermic reaction. With respect to the relative mass, the released binding energy is distributed on the atom and the product molecule as kinetic energy. Due to momentum conservation, the atom and the product molecule will fly apart. The kinetic energy is in our case sufficient to eject the atom and the molecule out of the optical dipole trap of the atom gas. By state selectively ionizing the molecule before it has left, it can be detected.

To ionize the product molecules we are using a two-color ($n = 1$, $m = 2$) REMPI (resonance enhanced multi photon ionization). The number of photons used to excite the product molecule to the first excited state i.e. intermediate state is denoted with n. From this intermediate state m photons are used to ionize the molecule. Since, we use two different lasers with different frequencies for the steps, it is called two-color (1,2) REMPI. The excitation into the intermediate state is done with the so-called probe laser. As we are exciting the product molecule with one photon into the intermediate state, it is a simple bound-to-bound transition. Fig. 2.3A shows a scheme of the excitation from the ground state (red interaction potential) to the intermediate state (green interaction potential). The subsequent ionization via a virtual state is performed with two photons of the so called ionization laser.

Photoassociation

An excitation i.e. association of two free atoms into an excited molecular bound state with the help of a photon is called photoassociation. It is a free-to-bound transition. In our case, the photoassociation follows the reaction equation

$$A + A + \nu => A_2^*$$
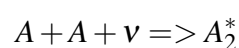
with A being an atom, ν being a photon with sufficient energy, and * denotes an excited state. Figure 2.3B shows a sketch of a photoassociation process. Two free atoms are
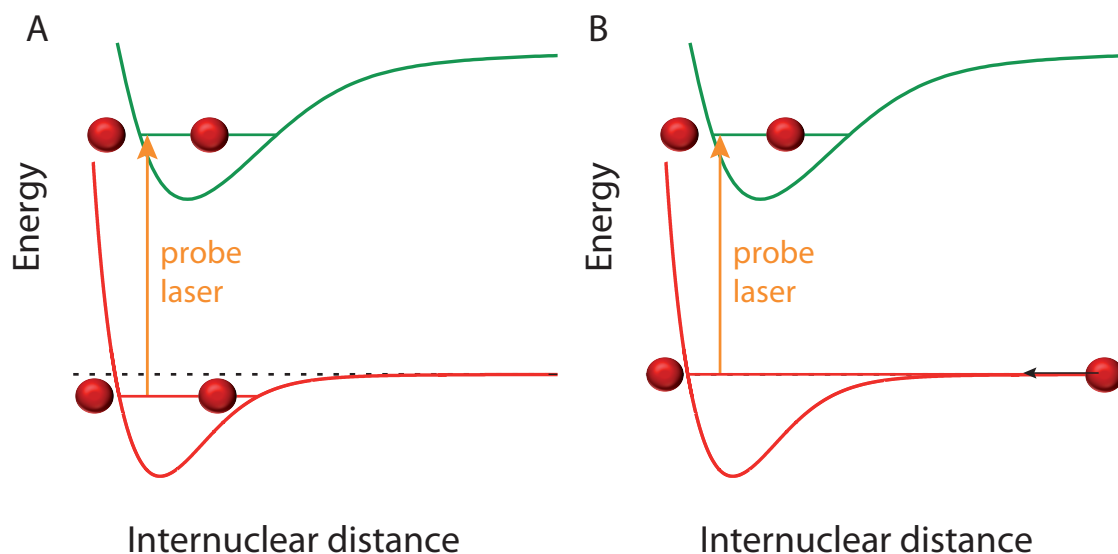
Figure 2.3: Bound-to-bound and free-to-bound transition of the first resonant two-color (1,2) REMPI step. The red spheres are atoms. The red curves are the ground state interaction potentials and the green ones are the excited state interaction potentials. From the excited bound state (intermediate state), the molecules are ionized with two photons of the ionization laser (not shown). **A**, a sketch of a resonant excitation of a molecule into the intermediate state. **B**, a sketch of two free colliding atoms that are excited into the intermediate state (photoassociation).

colliding in the asymptote of their interaction potential (red interaction potential). In this collision, the atoms can be excited into the molecular intermediate state (green interaction potential) by a resonant photon. The produced molecules are electronically excited, but motionally cold. A detailed review article about photoassociation can be found in [21]. For our experiments, the important part about the photoassociation is that the three-body recombination product molecules occupy a bound state below the ground state asymptote, as visible in Figure 2.3. The necessary transition frequency of the three-body recombination product molecules will be always larger as for the photoassociation (into the same intermediate state). Therefore, the photoassociation transition to the intermediate state is a frequency reference. This reference can be used to calculate the expected transition frequencies of the by three-body recombination produced molecules (see Ch. 4). Furthermore, the photoassociation is also useful because we can produce a controlled number of molecules in the intermediate state by photoassociation and afterwards measure the resulting number of ions (see Chs. 4 and 5.6). This enables us to determine the ionization efficiency of the two-color (1,2) REMPI.

2.2 The Rydberg laser setup

A recent topic of our BaRbI experiment is studying Rydberg physics. A review about Rydberg physics in general can be found in [22]. We drive the Rydberg transition in a single step, with a frequency doubled dye laser[1]. This laser can produce up to 500 mW of 300 nm light out of 3.5 W at 600 nm. The 600 nm dye laser is frequency locked to a high-finesse cavity. The length of the cavity is stabilized utilizing our wavemeter lock system. This enables us to tune the laser frequency with the already existing control software. After the frequency doubling the 300 nm beam is controlled with an acousto-optical-modulator[2] and a standard camera shutter used in our system.

The laser is placed in a room adjacent to our lab. We use a 15 m long optical fiber[3] to transport the laser between the rooms. We have used a multi-mode optical fiber since there are no single-mode fibers for 300 nm light available, because of photodarkening (solarization). A silica fiber is in principle transparent for UV-light. However, impurities exposed to the high energy UV-light produce color center, which absorb light. The production rate of the color centers depends on the laser intensity. Since a single-mode fiber has a higher light intensity in the fiber as a multi-mode fiber the photodarkening is stronger. To be able to use the multi-mode fiber, we therefore also reduced the laser power. We worked with ≈ 5 mW of 300 nm light in the experiment and had about 15% transmission efficiency.

To reduce the photodarkening effect H_2 loaded photonic crystal fibers can be used. Hydrogen reacts with the color centers and converts them into either being optically inactive or to be active for another wavelength (for more information see [23]). We are planning to get such a fiber manufactured for us. This fiber type is still in the experimental phase and it needs to be shown how well it is able to handle the used high-power UV laser light.

---

[1] Sirah Matisse 2 DX with WaveTrain2
[2] Gooch & Housego I-M110-3C10BB-3-GH27 AOM
[3] UM22-100-Custom-Muc with 15 m length

3 Publications

The following articles were prepared during the course of this thesis:

- Joschka Wolf, Markus Deiß, Artjom Krükow, Eberhard Tiemann, Brandon P. Ruzic, Yujun Wang, José P. D'Incao, Paul S. Julienne, and Johannes Hecker Denschlag, "State-to-state chemistry for three-body recombination in an ultracold rubidium gas", *Science* **358**, 921 (2017). (congruent with Chapter 4, additional content marked with *)

- Joschka Wolf, Markus Deiß, and Johannes Hecker Denschlag, "Magnetic quantum number resolved state-to-state chemistry", *arXiv* **1909.00777** (2019). (congruent with Chapter 5)

- Shinsuke Haze, Joschka Wolf, Markus Deiß, Limei Wang, Georg Raithel, and Johannes Hecker Denschlag, "Stark spectroscopy of Rydberg atoms in an atom-ion hybrid trap", *arXiv* **1901.11069** (2019). (congruent with Chapter 6, additional content marked with *)

- Markus Deiß, Shinsuke Haze, Joschka Wolf, Limei Wang, Florian Meinert, Christian Fey, Frederic Hummel, Peter Schmelcher and Johannes Hecker Denschlag, "Observation of spin-structure of ultralong-range Rydberg molecules", *arXiv* **1901.08792** (2019). (preliminary revised version in Chapter 7, additional content marked with *)

- Björn Drews, Markus Deiß, Joschka Wolf, Eberhard Tiemann, and Johannes Hecker Denschlag, "Level structure of deeply bound levels of the $c\,^3\Sigma_g^+$ state of ^{87}Rb$_2$", *Physical Review A* **95**, 062507 (2017).

- Amir Mohammadi, Joschka Wolf, Artjom Krükow, Markus Deiß, and Johannes Hecker Denschlag, "Minimizing rf-induced excess micromotion of a trapped ion with the help of ultracold atoms", *Applied Physics B* **125**, 122 (2019).

- Joschka Wolf, Markus Deiß, and Johannes Hecker Denschlag, "Molekülbildung unter der Lupe", *G.I.T. Labor-Fachzeitschrift 4/2018*, page **50** (2018), and "Watching Chemical Reactions on the Quantum Level", *G.I.T. Laboratory Journal 6/2018*, page **24** (2018), (popular science, non-peer-reviewed).

4 State-to-state chemistry for three-body recombination in an ultracold rubidium gas

Additional data to the original publication (marked with *) can be found in Section 4.2.5.

4.1   Article

4.1.1   Abstract

Experimental investigation of chemical reactions with full quantum state resolution for all reactants and products has been a long term challenge. Here, we prepare an ultracold few-body quantum state of reactants and demonstrate state-to-state chemistry for the recombination of three spin-polarized ultracold Rb atoms to form a weakly bound Rb_2 molecule. The measured product distribution covers about 90% of the final products and we are able to discriminate between product states with a level splitting as small as $20\,\text{MHz} \times h$. Furthermore, we formulate propensity rules for the distribution of products and we develop a theoretical model which predicts many of our experimental observations. The scheme can readily be adapted to other species and opens a door to detailed investigations of inelastic or reactive processes.

4.1.2   Introduction

Although the quantum mechanical principles underlying chemical reactivity are known, calculating the full state-to-state dynamics is only possible when the number of product exit channels is very limited [6, 7, 8]. In a typical chemical reaction, however, where hundreds of molecular states are involved, a direct solution is currently beyond reach. Experimental investigations of state-to-state processes are challenging as both the preparation of the reactants and the detection of the products have to take place in a quantum state resolved manner. Until now state-to-state experiments have been typically carried out with atomic and molecular beams (for reviews see e.g. [3, 4, 5]). These studies are restricted to collisions between only two particles due to low densities, the collision energies are such that many partial waves are involved, and hyperfine states are generally not resolved. Three-body recombination is an exothermic reaction, whereby three atoms collide to form a diatomic molecule and a free atom, each of which carries away a portion of the released kinetic energy [24, 25, 26]. These reactions strongly depend on the collision energy, the initial quantum state of the reactants and the details of their interactions. Ultracold atomic gases are amenable to extraordinary control of these parameters [27, 28, 29], enabling studies that determine the scaling properties of the total three-body recombination, see e.g. [14, 30, 31, 32, 33, 34, 35, 36, 37]. In principle, there is a wide range of molecular states that can be formed, ranging from weakly to deeply bound. In order to form a molecule with a given bond-length, the three atoms need to approach each other within roughly one bond-length. Because for dilute gases three-body collisions happen more frequently at long distances than at short ones, the formation of weakly bound molecules with long bonds is favored [33]. At ultracold temperatures the scattering length sets a typical length scale for the minimal distance between the reactants as they pass each other in a collision. Indeed, early investigations of three-body recombination showed that for resonant interactions (large scattering lengths) molecules formed almost exclusively in the most-weakly bound state, which has a typical size given by the scattering length [10, 11]. For non-resonant interactions (small scattering lengths), population of more deeply bound molecular states is also expected, and it is an open question how sensitive the product distribution is to the details of the interaction potential [38, 39].

Here, we demonstrate state-to-state chemistry for three-body recombination at ultra-low temperatures. The experiments were carried out with a gas of ultracold ^{87}Rb atoms with non-resonant interactions confined in a crossed optical dipole trap (Sec. 4.2.1). Each

atom was in the electronic ground state with total angular momentum and magnetic quantum numbers $f = 1$ and $m_f = -1$, respectively. Three-body recombination produced Rb_2 molecules in the mixed $X^1\Sigma_g^+$ and $a^3\Sigma_u^+$ electronic state manifolds. In a recent precursor experiment [12] we had observed first signals of such Rb_2 product states and could tentatively assign some of them. In order to reach the realm of state-to-state chemistry we have now overcome the limitations of this first experiment by extending the detection scheme as well as the analysis. The assignment of the observed lines is now unambiguous and we have developed a method to calibrate the flux into each final product state. Furthermore, instead of only probing isolated vibrational levels, we can now investigate the population distribution over a sequence of vibrational levels, covering about 90% of all produced molecules. On the basis of this technical progress we gained a number of new scientific results and were able to formulate several propensity rules. Furthermore we have carried out a state-of-the-art parameter-free model calculation that can be directly compared to our data and is a key tool for their interpretation.

4.1.3   Spectroscopic method

To detect the molecular product quantum states, we ionized the newly formed molecules in a state-selective fashion using a two-color (1,2) REMPI technique (resonance-enhanced multi-photon ionization). Subsequently, the ions were captured in a Paul trap. After a given delay, during which several ions accumulate, we counted them. Figure 4.1A shows the two-color REMPI scheme. By tuning the frequency of the probe laser (Sec. 4.2.4), we state-selectively excited weakly bound molecules to the $v' = 66$ vibrational level of the $A^1\Sigma_u^+$ potential (for selection rules see Sec. 4.2.2). This level exhibits a simple rotational substructure [40, 41] (see inset) with predicted hyperfine splittings of less than 3 MHz. From there, two photons from an ionization laser ionized the molecule (Sec. 4.2.4). In Figure 4.1B we plot the term energies of the most relevant weakly bound molecular levels with $F = 2$ for the atom pair $f_a = 1, f_b = 1$, where the indices represent atom a and b, and F denotes the total angular momentum of the molecule excluding its rotational angular momentum R. The term energies were obtained from coupled-channel calculations (Sec. 4.2.3). As preparation for the assignment of the product states we first calibrated the probe laser frequency with respect to the term energies of the probed weakly bound levels by carrying out a photoassociation measurement [21] that sets a marker for zero binding energy. The ion trap was turned off and the probe laser frequency ν scanned in small steps of 5 MHz while the dipole trap laser was kept at a fixed frequency. For
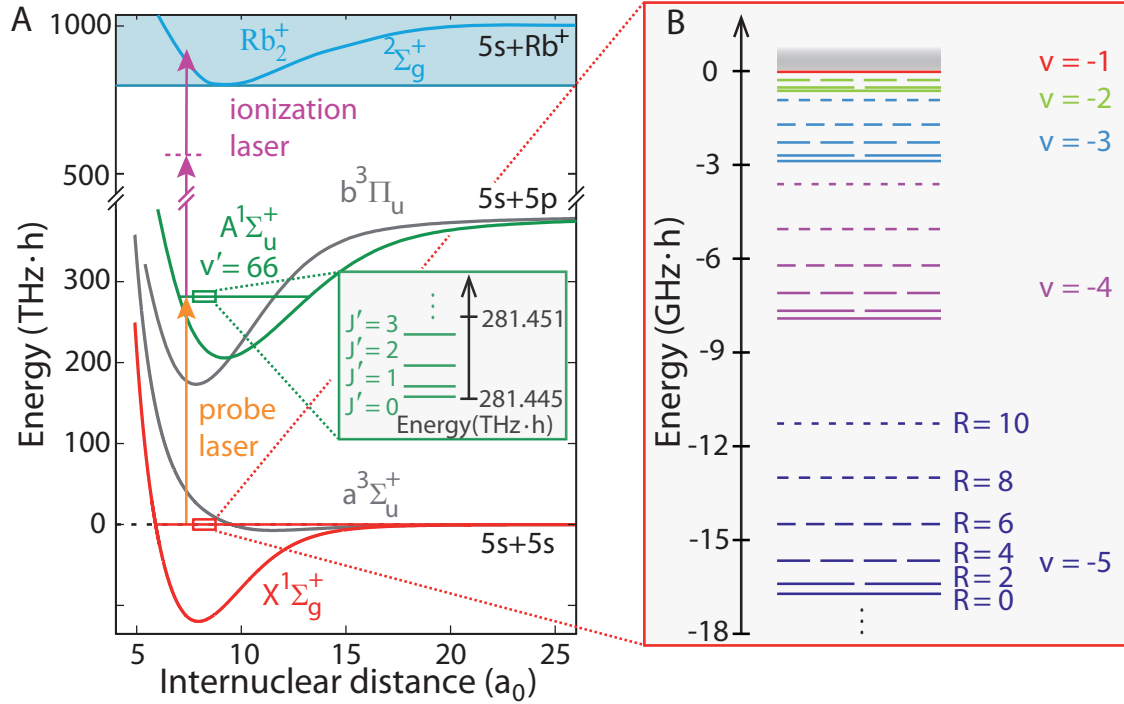
Figure 4.1: REMPI scheme and overview of relevant molecular states. (A) A two-color (1,2) REMPI scheme detects weakly bound molecules close to the $5s + 5s$ dissociation threshold. The probe laser drives a resonant transition towards the $A^1\Sigma_u^+$, $v' = 66$ vibrational level which exhibits a simple rotational substructure (see inset). J' is the total angular momentum quantum number excluding nuclear spins. Afterwards, two photons from the ionization laser ionize the molecule. a_0 is the Bohr radius. (B) Calculated energy levels of selected, weakly bound molecular states with the quantum numbers v, R for vibration and mechanical rotation, respectively. Only levels with total positive parity and angular momentum $F = 2$ that correlate to the $f_a = f_b = 1$ atomic asymptote are shown. This asymptote marks the zero energy reference level. The vibrational quantum number v is counted downwards starting at v$= -1$ for the most-weakly bound vibrational state.

every step we exposed a freshly prepared atom cloud to the probe laser for a duration of 2 s and afterwards measured the remaining number of atoms N via absorption imaging. On resonance the probe laser couples two ultracold Rb atoms colliding in a s-wave (i.e. $R = 0$) to the bound level $A^1\Sigma_u^+$, $v' = 66$, $J' = 1$ and atom loss occurs. Here, J' is the total angular momentum quantum number excluding nuclear spins. As shown in Figure 4.2 (orange data), we observed a single photoassociation line at a frequency of $v_0 = 281,445.045(60)$ GHz where the error is the nominal uncertainty of the wavemeter. The linewidth of the photoassociation dip is 15 MHz, close to the natural linewidth of about 10 MHz. The next photoassociation line is expected 570 GHz away [41].

4.1.4 Spectroscopic data
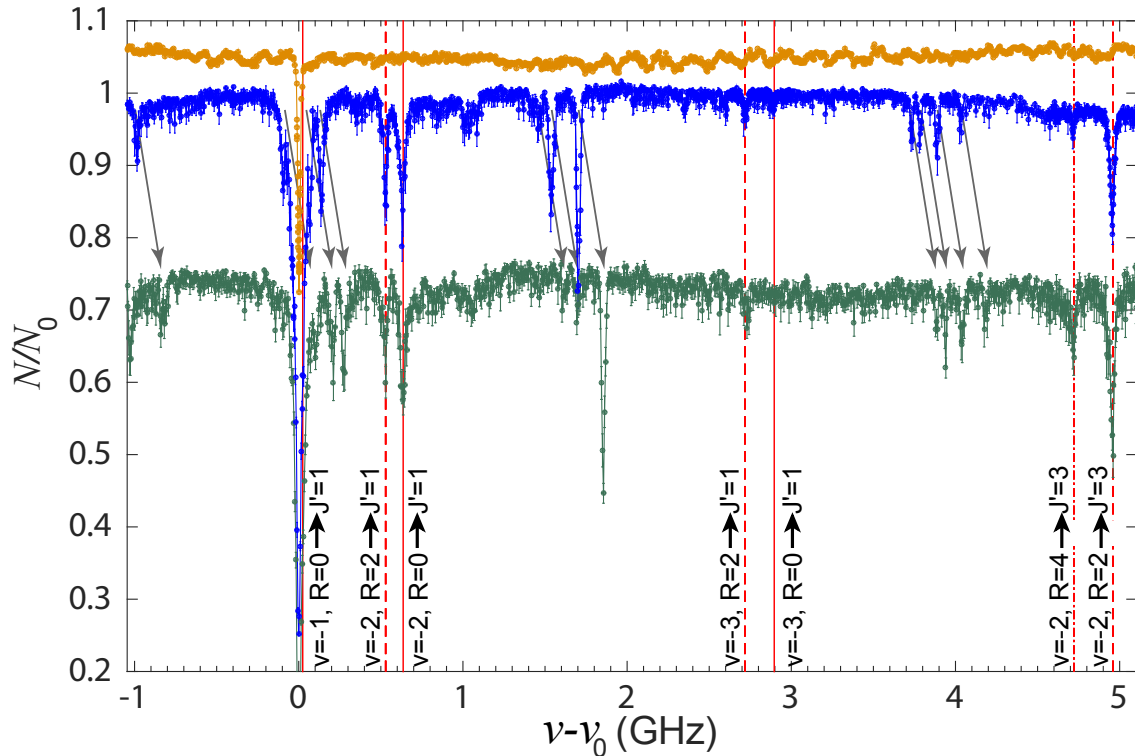
Figure 4.2: Photoassociation and REMPI spectra. Shown is the remaining atom fraction N/N_0 as a function of the probe laser frequency ν, where N_0 is the number of remaining atoms for a far off-resonant probe laser. Orange data correspond to the photoassociation spectrum, with a single line at $\nu = \nu_0 \equiv 281{,}445.045\,\text{GHz}$. For better visibility the record is shifted up by 0.05 units. The blue and green data are REMPI spectra. For the blue data the ionization laser frequency is $281{,}629.15\,\text{GHz}$, whereas for the green data the laser was red-shifted by $150\,\text{MHz}$. Each REMPI data point is the average of 10 repetitions with the error bars representing the statistical standard deviation. For better visibility the green spectrum is vertically shifted by -0.25 units, which cuts off part of its photoassociation line. The vertical lines mark assigned resonant transitions of the first REMPI step. For grey arrows see text.

We then turned on the ion trap and repeated the experiment with an exposure time of $0.5\,\text{s}$ (blue data). In addition to the strong photoassociation dip at $\nu = \nu_0$ a number of other loss dips were observed. As our analysis will show, these resonances belong to product molecules from three-body recombination which are state-selectively ionized as the probe laser is scanned. The ionized molecules were immediately trapped in the Paul trap, which was arranged to immerse them in the cold atom cloud. The ions undergo collisions with the atoms and induce atomic losses that can be substantial during exposure time. A larger number of ions leads to a larger loss of atoms. Resonance dips in Figure 4.2 with a depth

of about 0.2^1 are typically induced by an average of about five ions. This measurement of atomic loss constitutes a semi-quantitative ion detection method which we refer to as ion detection scheme I (see Sec. 4.2.5). We first consider REMPI transitions towards $A^1\Sigma_u^+$, $v' = 66, J' = 1$ and turn to $J' > 1$ afterwards. As the probe laser frequency increases, starting from ν_0, it probes increasingly deeply bound molecular levels. In the given frequency range of Figure 4.2 we observed signals from the most weakly bound vibrational states $v = -1, -2, -3$. The five vertical lines at $\nu - \nu_0 < 3\,\mathrm{GHz}$ show the predicted resonance positions for the transitions as labeled next to the lines, probing weakly bound states characterized by $f_a = f_b = 1, F = 2, R = 0$ and 2 (see also Fig. 4.1B). These predicted lines match our measured resonances within a few MHz. We note that in the given spectrum the signal corresponding to $v = -1$ is buried under the strong photoassociation line. As shown in Figure 4.10, however, it was clearly resolved in a refined scan. Some of the observed molecular states have non-vanishing rotational angular momentum R (see e.g. $R = 4$ in Fig. 4.2). This is noteworthy, as at ultracold temperatures the atoms originally collide in s-waves where $R = 0$. The rotational excitation is due to an anisotropic interaction between the formed molecule and the remaining atom in the three-body collision complex. As a consistency check of our assignment, we can make use of the fact that for molecules with $R > 0$ each level can give rise to two transition lines, $R \to J' = R \pm 1$. Indeed, we verified that e.g. the level $v = -2, R = 2$ not only produces a transition line at $\approx 0.5\,\mathrm{GHz}$ ($J' = 1$) but also one at $\approx 5\,\mathrm{GHz}$ ($J' = 3$) (see Fig. 4.2). Both transition lines are of similar strength, as expected. After determining that the observed resonance lines belong to weakly bound molecules in well defined quantum states, one might still question whether the origin of the molecules is three-body recombination. We have performed test measurements on the density dependence of the ion signal for transition lines (see Fig. 4.9). The ion signals normalized to the total atom numbers show a clear quadratic scaling behavior which points to the three-body nature of the molecule formation. Besides the weakly bound molecular states with the quantum numbers $f_a = f_b = 1$, there exist other states near threshold with the quantum numbers $f_a = f_b = 2$ or $f_{a/b} = 1, f_{b/a} = 2$ (see data S1-2 in [42]). However, we only observed clear signals from $f_a = f_b = 1$ molecules in our measurements. Furthermore, we only observed molecules with an even rotational quantum number, i.e. $R = 0, 2, 4, ...$, which corresponds to positive total parity. The spin quantum numbers f_a and f_b as well as the total parity of the product molecules are the same as for the two-body atomic scattering state initially prepared in our experiment. The

---

[1] Corrected value

total parity of the scattering state must be even because the colliding atoms are identical bosons and hence their partial wave must be even. Thus our present experiments indicate that the internal spin states of the colliding atoms do not change when a weakly bound molecule is formed in three-body recombination. This is in contrast to our previous measurements where we investigated more deeply bound Rb_2 molecules and observed a broad range of spin states, including even and odd R [12]. This apparent change in the propensity rule with increasing binding energy might be linked to the accidental near degeneracy of the weakly bound singlet and triplet levels of Rb_2, as explained in the Section 4.2.14. In addition to the assigned transition lines several other unidentified resonance dips are visible in Figure 4.2 (blue data). In order to investigate their origin, we measured the spectrum again, but with the ionization laser frequency shifted by $-150\,\mathrm{MHz}$ (green data in Fig. 4.2). Both scans exhibit the already assigned transition lines at the same probe laser frequencies. The positions of several unidentified resonance dips, however, shifted by $+150\,\mathrm{MHz}$. Thus, for these dips, the sum of the ionization and probe laser frequencies remains constant. This indicates a two-photon process, where the combination of a probe and an ionization photon resonantly populates an intermediate molecular level. A third photon finally ionizes the molecule. Therefore, these transition lines correspond to a (2,1) REMPI process. Currently, we have not yet assigned these lines to specific molecular transitions. We note that further unidentified resonance dips can be found in the spectrum, which, however, belong to more deeply bound states with other REMPI paths and need to be further analyzed.

4.1.5   Hyperfine resolved signals

Our spectroscopic method reveals fine details of hyperfine and exchange interaction in the molecular level structure. Figure 4.3 shows the transitions $v = -3, R = 0, 2 \rightarrow J' = 1$, observed with ion detection scheme II (see Sec. 4.2.5), where the ions are first accumulated in a displaced ion trap and counted afterwards via the loss they inflict on a newly prepared atom cloud. Each of the $R = 0, 2$ levels consists of two ($F = 0$ and $F = 2$) hyperfine sublevels with a small splitting of about $20\,\mathrm{MHz}$. (An additional substructure of these levels due to coupling of F to R is negligible Sec. 4.2.2.). The small splitting is linked to the fact that the singlet $X^1\Sigma_g^+$ and triplet $a^3\Sigma_u^+$ potentials have slightly different scattering lengths. The calculated transition frequencies are indicated as vertical lines in Figure 4.3. In the spectrum we only observe hyperfine levels with $F = 2$. From the peak-heights and the noise we estimate that residual $F = 0$ signals must be at least a factor of four smaller as
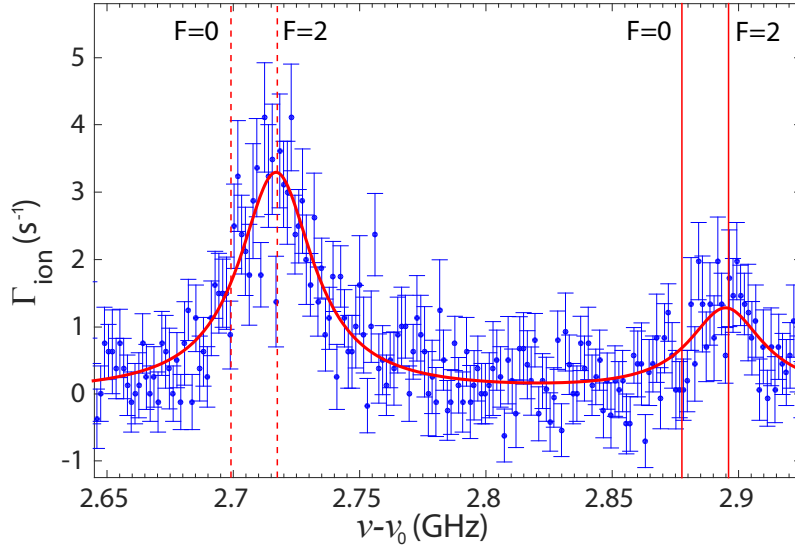
Figure 4.3: Discrimination of hyperfine levels. This REMPI spectrum shows two transition lines to $J' = 1$ starting from $v = -3, R = 0$ (peak on the right) and $v = -3, R = 2$ (peak on the left), respectively (see also Fig. 4.2). Γ_{ion} is the ion production rate. The vertical lines show calculated positions of possible product signals with hyperfine quantum numbers $F = 0$ and 2. The data reveal that only $F = 2$ states are significantly populated. Each data point is the average of 43 repetitions, and error bars indicate the statistical standard deviation. The red solid line is a Lorentzian fit of the two transition lines. The fit was not weighted to the error bars and has reduced chi-squared value of $\chi^2 = 0.96$. As before, $\nu_0 = 281,445.045$ GHz.

compared to $F = 2$. In all other measurements for weakly bound molecules we also found signatures only for levels with total internal spin $F = 2$. Interestingly, F is the same as for two-body scattering state. Thus, this finding supports our hypothesis that the molecular product has the same internal spin state as the two-body atomic scattering state.

4.1.6   Population distribution

We calibrated the ion signals in order to determine the three-body recombination induced loss rate constants $L_3(v, R)$ for the flux into individual rovibrational levels in absolute terms. For this, we determined the probability that a molecule is ionized by the REMPI scheme once it has been formed (Sec. 4.2.10). Figure 4.4 (circles) shows the individual loss rate constants $L_3(v, R)$ as inferred from our experimental data (Sec. 4.2). This corresponds to the population distribution of molecular products. We investigated weakly bound molecular levels up to a binding energy of 17 GHz $\times h$ as marked by vibrational and rotational quantum numbers in the plot. The observed lines can unambiguously be assigned to molecular product states as measurements and calculated resonance frequen-
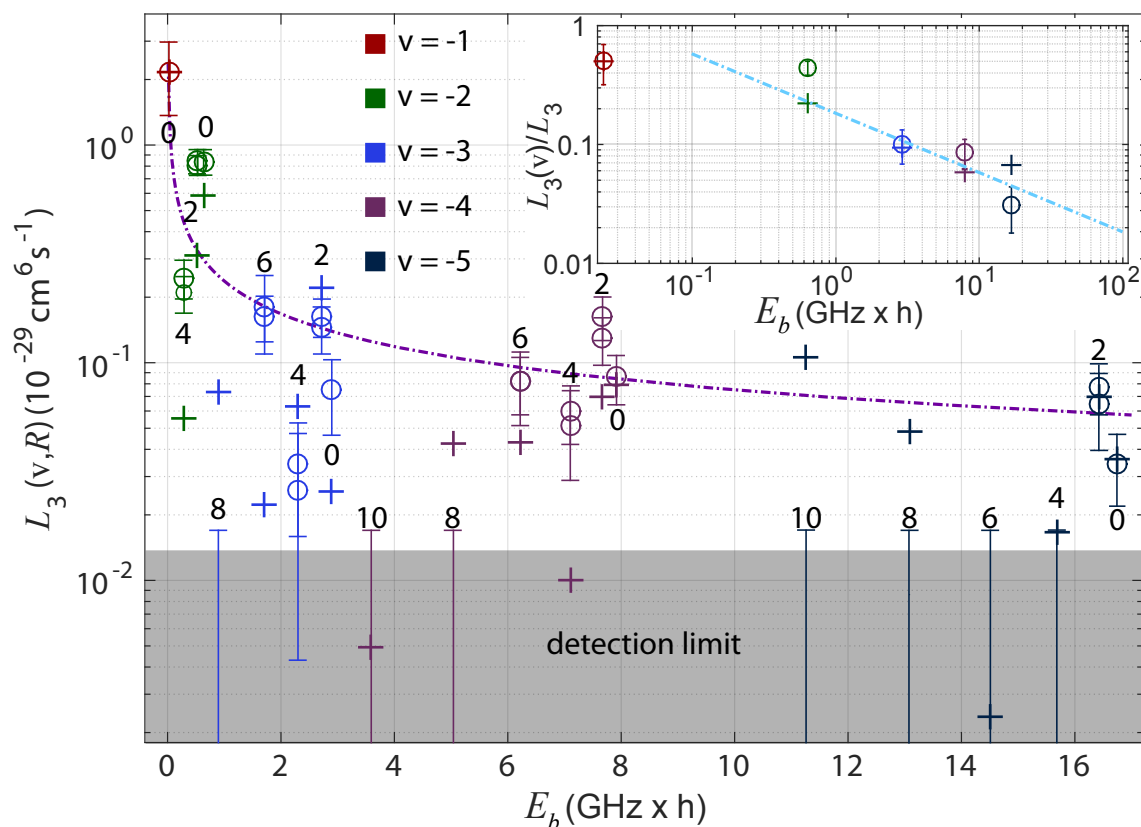
Figure 4.4: Population distribution of molecular product states following three-body recombination. The plot shows the loss rate constants $L_3(v,R)$ due to three-body recombination into various molecular product channels, as specified by the quantum numbers v, R and the respective binding energy E_b. R is indicated next to the data points. All product channels belong to the $f_a = 1, f_b = 1$ atomic asymptote and have $F = 2$. Circles are measurements. Crosses are calculations, rescaled as described in Sec 4.2.13. Error bars in the grey region indicate upper limits derived from the experimental noise level. Two circles for the same product channel correspond to REMPI transitions to two different excited levels, $J' = R \pm 1$. The inset presents the branching ratio into the five vibrational levels, calculated by summing over all respective rotational contributions and by normalizing with the total loss rate constant L_3. The dashed dotted lines (figure and inset) are proportional to $1/\sqrt{E_b}$ where E_b is the binding energy. The error bars correspond to the statistical standard deviation.

cies accurately match within the experimental resolution of a few megahertz. Generally, the error bars shown in Figure 4.4 represent the statistical uncertainties of the ion signals. We note, however, that additional large uncertainties arise, dominated by a global normalization error of up to 60% due to imperfect atom number calibration (Sec. 4.2.15). Our data show an overall tendency for the loss rate constants $L_3(\mathrm{v}, R)$ to drop for increasing binding energies as anticipated for a dilute ultracold gas, but with fluctuations with R as discussed below. The decrease is not abrupt and roughly agrees with a $1/\sqrt{E_b}$ dependence, where E_b is the binding energy. The $1/\sqrt{E_b}$) dependence is a simple propensity rule that can be tested further in future research. To better understand the measured population distribution, we have also carried out state-of-the-art numerical three-body calculations (crosses in Fig. 4.4) based on a simplified model of long-range potentials (Sec. 4.2.13). In agreement with the data, we find a again the $1/\sqrt{E_b}$) dependence for $L_3(\mathrm{v}, R)$. For a fixed v, both theory and experiment show large variations of $L_3(\mathrm{v}, R)$ with R. In particular, the $R = 4$ signals are generally suppressed with respect to the $R = 2$ signals for a given vibrational level. This is also supported by our calculations which suggest that the variation of population with R is oscillatory. In general, variations as a function of R are expected because the state-to-state S-matrix elements will be influenced by multiple paths and Stückelberg oscillations associated with one or more curve crossings in the adiabatic potential curves, as indicated in [7, 30, 31] (see also Fig. 4.14). While in the experiment we observe rotational angular momenta up to $R = 6$, theory predicts population of even higher rotational quantum numbers. In our calculations the variations for the v$= -2$ and -3 levels seem to have converged with respect to increasing the number N_s of $R = 0$ bound states in the model (see Sec. 4.2.13). However, the v$= -4$ and -5 rotational distributions have not yet fully converged with respect to adding bound states. Thus, the rotational distribution for these more-deeply bound levels is sensitive to shorter-range details that our model is not treating fully. Despite these limitations the theoretical model suggests that the rotational distributions for given v might have non-negligible sensitivity to three-body corrections that are not pairwise additive (Sec. 4.2.13). In general, the sum $L_3(\mathrm{v}) = \sum_R L_3(\mathrm{v}, R)$ over all rotational contributions for a given v might be less subject to variation. The inset in Figure 4.4 presents the measured and calculated values of $L_3(\mathrm{v})$ for the individual vibrational levels, normalized to the total loss rate of $L_3 = (4.3 \pm 1.8) \times 10^{-29}\,\mathrm{cm}^6\,\mathrm{s}^{-1}$ determined by Burt et al. [28]. Indeed, the results show a similar qualitative drop off tracking near a line that varies as $1/\sqrt{E_b}$. According to the given normalization the measurements reveal that roughly 50% of all molecules produced

via three-body recombination are formed in level v$= -1$. We can estimate that about 10% of the molecules are more deeply bound than v$= -5$, using the $1/\sqrt{E_b}$ scaling law for the vibrational population. The total population of levels v < -5 is then approximately given by $\sum_{i<-5} E_b(v)^{-1/2}/\sum_{v} E_b(v)^{-1/2}$. Here, $E_b(v)$ is the calculated $R=0$ bound state energy for the vibrational level v of the mixed $a^3\Sigma_u^+$ state. Indeed, some of the more deeply bound levels were observed in [12].

4.1.7   Conclusion

Our experimental scheme can readily be adapted to other bosonic or fermionic elements or isotopes. In general, the product measurement technique introduced here can be used to investigate a wide range of inelastic processes at ultra-low temperatures well beyond three-body recombination such as molecular relaxation and rearrangement reactions. Therefore, the present work sets the stage for experiments where chemical reactions and inelastic collisions can be explored in a state-to-state fashion with full resolution on the quantum level.

4.2   Supplementary materials and methods

4.2.1   Preparation of the atomic sample and setting the total three-body loss rate

The atomic cloud is prepared in a crossed optical dipole trap at a wavelength of $1,064.5\,\text{nm}$ with trapping frequencies of $\omega_{x,y,z} = 2\pi \times (23, 180, 178)\,\text{Hz}$, where z denotes the vertical direction. The magnetic field[2] is about $4.5\,\text{G}$. Typically, we work with a thermal sample at an initial temperature of about $750\,\text{nK}$ that consists of $N_{at} \approx 5 \times 10^6$ atoms. It is a Gaussian-shaped cloud and has a cloud size of $\sigma_{x,y,z} \approx (58.6, 7.5, 7.5)\,\mu\text{m}$. The initial peak particle density is $n_0 \approx 0.9 \times 10^{14}\,\text{cm}^{-3}$. The atomic density distribution n sets the total three-body loss rate $\dot{N}_{at} = \int \dot{n}\,d^3r = -L_3 \int n^3 d^3r$, where L_3 is the total loss rate constant. L_3 has been measured, e.g., by Burt *et al.* [28] to be $L_3 = (4.3 \pm 1.8) \times 10^{-29}\,\text{cm}^6\,\text{s}^{-1}$. Using this loss rate constant, $N_{at} \approx 150,000$ atoms are typically lost due to three-body recombination in the first $500\,\text{ms}$.

4.2.2   Properties of molecular states and selection rules

In order to label the molecular quantum states of the weakly bound a/X-state molecules we use the atomic pair basis (similar to Hund's case e), $|f_a, f_b, F, R, F_{tot}, m_{Ftot}\rangle$. The angular momenta $\vec{F}$ and $\vec{R}$ couple to each other to form the total angular momentum $\vec{F}_{tot}$, giving rise to level splittings for different F_{tot} that are smaller than 1 MHz. In the present experiments we do not resolve this F_{tot}, m_{Ftot} substructure. According to the selection rules for optical dipole transitions, only molecules containing a $X^1\Sigma_g^+$ component can be excited towards $A^1\Sigma_u^+$. Fortunately, a majority of the weakly bound molecular states exhibit a sizeable singlet admixture of at least 10%, due to the hyperfine interaction (see Supplementary Data [42]). For Rb_2 these states are characterized by $F = 2, 0$ ($F = 1, 3$) for positive (negative) total parity, respectively.

The excited state $A^1\Sigma_u^+$, $v' = 66$ has hyperfine splittings off less than $3\,\text{MHz}$, despite the fact that spin-orbit coupling mixes in 16% of the $b^3\Pi_u$ state (see [40, 41]). Therefore $A^1\Sigma_u^+$, $v' = 66$ exhibits an essentially pure rotational substructure $\propto B'_v J'(J'+1)$ with a rotational constant of $B'_v = 443\,\text{MHz}$. For exciting a molecule towards the state $A^1\Sigma_u^+$, optical dipole selection rules demand $R \to J' = R + 1$ for $R = 0$, and $R \to J' = R \pm 1$,

---

2 Corrected value

otherwise.

4.2.3   Coupled-channel calculations

The Rb_2 energy levels are calculated with a coupled-channel model which uses the Hamiltonian for atom pairs of $s+s$ or $s+p$ states (see e.g. [43, 44]) and potentials derived from former spectroscopic work of several groups. We have reevaluated the analysis of the singlet and triplet ground states [44] correcting the assignment of some high rotational levels as remarked in [45] and derived improved potentials for $X^1\Sigma_g^+$ and $a^3\Sigma_u^+$. Because the analysis includes a number of Feshbach resonances we obtain reliable predictions for the asymptotic level structure. The potential system for the atom pair $s+p$ was derived from spectroscopic work collected in [40] and work from our own group [43, 41]. The coupled-channel calculation describes in full detail the singlet-triplet mixing needed for deriving reliable Franck-Condon factors. It predicts the hyperfine structure in the state $A^1\Sigma_u^+$ to be small, such that it is negligible for the present analysis.

4.2.4   REMPI lasers

The first excitation step for the REMPI is driven by a cw external-cavity diode laser (the 'probe laser'). It has a Gaussian beam waist ($1/e^2$-radius) of $\approx 280\,\mu m$ at the position of the atomic sample, so that the intensity[3] is $\approx 6\,W\,cm^{-2}$. The second REMPI step is driven by the dipole trap laser (the 'ionization laser'). Since we work with a crossed dipole trap, the ionization laser consists of two beams. The beam in the horizontal (vertical) direction is focused to a beam waist of $\approx 90\,\mu m$ ($\approx 230\,\mu m$) with an intensity[4] of $\approx 19\,kW\,cm^{-2}$ ($\approx 2\,kW\,cm^{-2}$), and their relative detuning is always 160 MHz. The wavelength of the ionization laser is fine tuned for producing a minimal background ionization signal of $\approx 1\,s^{-1}$ when the probe laser is turned off. The probe and ionization lasers have a short-term frequency stability on the order of 100 kHz and 1 kHz, respectively. Both are stabilized to a wavelength meter achieving a shot-to-shot and long-term stability of a few megahertz. The polarization of the lasers can equally drive σ- and π-transitions.

---

[3] Corrected value
[4] Corrected values

4.2.5 Ion detection (*)

The Rb_2^+ ions produced via the REMPI process are first captured in a $1\,eV$ deep Paul trap before they are detected with near unit efficiency. During the process each Rb_2^+ molecule typically dissociates into $Rb^+ + Rb$. However, the number of trapped ions is conserved. Since fluorescence detection is neither available for Rb^+ nor for Rb_2^+, we use the following two detection methods.

Ion detection scheme I: The trapped ion cloud is centered on the cold atom cloud. Thus, from the moment that the ions are produced, they can elastically collide with the neutral atoms and expel them from the shallow dipole trap. Typically, after $500\,ms$ we end the experimental run, and measure the number of remaining atoms. The larger the atom loss, the larger the number of trapped ions. Detection scheme I is fast, allowing for a high repetition rate. However, it is not very precise in measuring the absolute number of trapped ions. For ion detection scheme I we operate the Paul trap with a micromotion energy of about $1\,K \times k_B$, where k_B is Boltzmann's constant. At these energies, three-body recombination of two Rb atoms with an ion is strongly suppressed [14], and two-body collisions of an atom and an ion dominate.

Ion detection scheme II: Here, the centers of the optical dipole trap and of the Paul trap are separated by about $300\,\mu m$ from each other, similar to the configuration given in Härter *et al.* [12]. Consequently, a produced Rb_2^+-ion is quickly pulled outside of the atom cloud into the ion trap such that further atom-ion collisions are suppressed. In order to trap one to three ions we typically set an appropriate accumulation time in the range between 2 to $500\,ms$. We count the trapped ions by immersing them into a new atom cloud with a comparably low density of $4 \times 10^{12}\,cm^{-3}$ for an interaction time of $1.5\,s$. As in detection scheme I, the ions inflict atom losses which increase stepwise with the number of ions, see [13, 46]. The scheme can count up to five ions. The micromotion energy is set to about $0.1\,K \times k_B$.

Additional content: Ion detection*

In the following, the microscopic mechanisms behind the detection schemata are explained in more detail. We will start with discussing the dynamics of an ion in a Paul trap. After this, we are discussing the behavior of the atom loss for measurements per-

formed with ion detection scheme I. Finally, we compare both detection schemata. These discussions are not part of the original publication and are marked with *.

Atom-ion collisions*
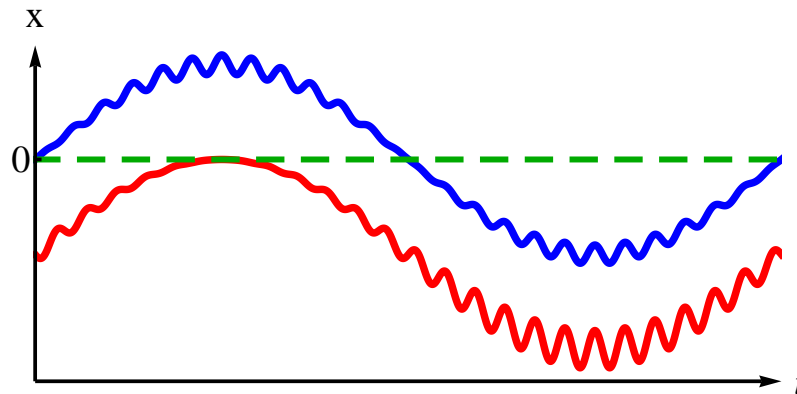
Figure 4.5: Two one-dimensional ion trajectories in a Paul trap. Two different trajectories of an ion in a Paul trap. The blue (upper) curve shows a well-centered ion trajectory. The red (lower) curve shows an ion trajectory, where the ion is pushed out of the radio frequency field node in negative direction of the x-axis e.g. possibly due to an offset electrical field. Both curves have the same secular amplitude (slow oscillation), but different micromotion amplitudes (fast oscillation). On average, the micromotion is increased for the off-centered curve. This additional micromotion is called excess micromotion. The figure is adapted from [20].

In a linear Paul trap, an ion is confined by a radio frequency electric field in two dimensions (radial direction) and in one dimension by a constant electrical field (axial direction). In Figure 4.5 two different trajectories of an ion in one radial axis of a Paul trap are shown. The upper curve (blue) shows an ion, which is moving with a slow harmonic oscillation (secular oscillation) around the node of the radio frequency field. Its frequency is the trap frequency of the ion in the quasi-harmonic potential of the Paul trap. The fast oscillation that is overlaid is the so-called micromotion. Its origin is the oscillating quadrupole field of the Paul trap. Therefore, it has the frequency of the radio frequency trap drive. The micromotion is a driven oscillation. The micromotion amplitude increases the further the ion is away from the radio frequency field node (for more detail see [20]).
The lower curve (red, Fig. 4.5) shows a trajectory, where the trap center is shifted out of the radio frequency field node by a constant force e.g. a DC electric field. The ion trajectory is therefore in regions of higher restoring force of the Paul trap i.e. regions of larger micromotion amplitude. For a single ion in a Paul trap the secular oscillation and

the micromotion are decoupled i.e. they cannot exchange energy.

In our system, this situation changes drastically if the ion collides with an atom. In an elastic atom-ion collision, the relatively hot ion with a kinetic energy of typically an mK, can transfer kinetic energy to the atomic collision partner. The initially cold atomic collision partner (1μk) is typically ejected out of its shallow optical dipole trap, which is only about $10\,\mu$K deep. In such a collision, the secular oscillation and the micromotion are coupled and can exchange energy. Depending on the phase of the micromotion during the collision, the ions secular oscillation amplitude can become larger than before the collision. Hence, the ion will have an equilibrium kinetic energy that is determined by collisional cooling and the possible micromotion heating. The micromotion is a driven motion and therefore a quasi-unlimited energy source. Since, the ion is in general hotter as the atoms and is not lost out of the trap, it can eject many atoms out of the atomic dipole trap during the interaction time. The atom loss induced by two-body atom-ion collisions of an ion roughly follows an exponential decay.

The atom losses that are produced by two-body atom-ion collisions are also depending on the collision energy [13, 46]. As it turns out, it can be beneficial to apply a DC electric field to increase the excess micromotion (as it increases the collision energy) and with it the observable atom loss of the ion detection scheme. Another advantage of the higher collision energies is that three-body recombination of two atoms with an ion is suppressed (see [14]). This suppression is important because the atom-atom-ion three-body recombination can lead to a high-energy ion trajectory that is mostly outside of the atom cloud. This would reduce the atomic loss and therefore reduce the ionic signal of the ion detection scheme.

Atom loss for ion detection scheme I*

In the following, the atom loss behavior for multiple ions will be explained in more detail as it is crucial for most of the measurements presented in this thesis. The amount of atom loss increases for higher micromotion energies, as well as for multiple ions since more atomic collision partners are addressed.

Many competing processes are involved if multiple ions cause collisional atom loss in our experiments. Consequently, this atom loss is not linear concerning the ion number. The atom losses that are produced by two-body atom-ion collisions are depending on the

collision energy, on the number of ions in the atom cloud, the density of atoms around the respective ion and the interaction time [13, 46].

To simplify the situation we are starting the discussion considering only cold ions that
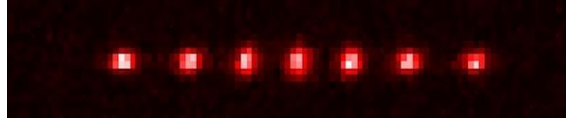
Figure 4.6: A laser cooled string of seven Ba$^+$ ions with an axial extension of $z \approx 150 \, \mu$m. Every white spot is the fluorescence of a single ion.

are localized at a certain trap position i.e. they are crystallized. The ions interact with each other via Coulomb interaction. This interaction between the ions leads to a repulsion between the ions. In our linear Paul trap, the axial direction is the weakest trap axis. Therefore, if the ion number is increased (starting from one ion) the ions will first form a string of ions (Fig. 4.6). This string has different overlap with the atom cloud for different ion numbers, as the distance between the ions is comparable to the atom cloud size. The overlap changes not linearly, but in general higher ion numbers will compress the string more into the centered atom cloud. The ions motions are coupled by the Coulomb interaction. Therefore, if one ion changes its position, for example during a collision with an atom all other ions interact with this ion's motion. Hence, this collision can increase the kinetic energy of the complete string. The micromotion couples differently to different positions in the trap[5]. Since all ions are coupled motionally with each other, this can lead to an increase of the mean total kinetic energy.

If more ions are added, this eventually leads to a reorganization of the string and it will extend into the radial direction. For cold ions in high numbers, this results in a cigar shaped crystal (Fig. 4.7). This has two consequences for atom-ion collisions. First, by being pushed into higher micromotion regions of the trap, the available micromotion energy of the ions becomes much larger. Due to the Coulomb interaction, this energy can be transferred to all other ions of the crystal. Second, the spatial overlap between the ions and the atom cloud changes, since the ion crystal is much larger (up to the millimeter range), than the atom cloud with an extension of about a few tens of micrometer. The number of ions having overlap with the atom cloud will rise for more ions, as the force in the crystal pushing the centered ions together is larger. The ions overlapping with the

---

[5] In a non-ideal linear Paul trap even the axial direction can have a RF-potential, which induces micromotion.
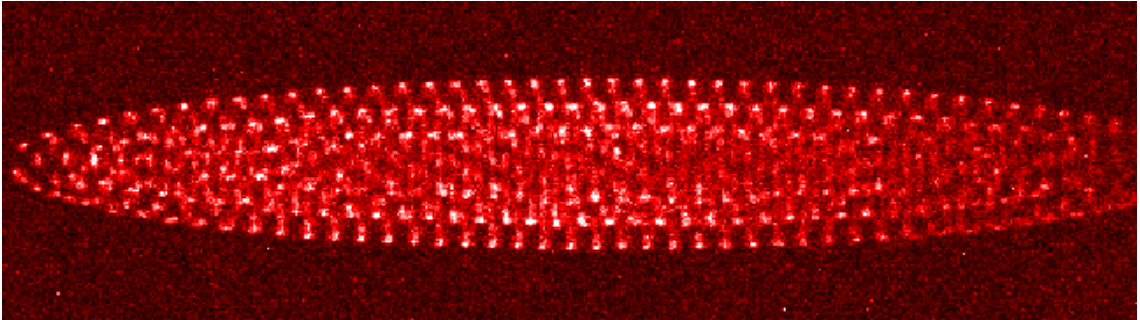
Figure 4.7: A laser cooled Ba$^+$ ion crystal with a radial extension of $d \approx 0.2$ mm and an axial extension of $z \approx 1$ mm (about 1000 ions). Every white spot is the fluorescence of a single ion. Not laser-cooled isotopes are located in the darker region on the right side of the crystal.

atom cloud, will then have a higher collision energy for larger ion numbers. By applying a DC electric field (excess micromotion), the collision energy and therefore the induced atom loss can be increased as described before.

In the course of this thesis measurements are performed with Rb$^+$ (Rb$_2^+$) ions, which cannot be laser cooled. They are produced directly out of the atom cloud by three-body recombination, an exothermic process. It is therefore save to assume that in most of our measurements we are not working with initially cold ions (ion crystal). Initially hot ions form an ion cloud in the Paul trap, as the kinetic energy of the ions is too large to allow them to crystallize. The hot ion cloud has a time dependent ion density at the position of the atom cloud. This density in connection with the ion kinetic energy is determining the observable atom loss. In the regime of low ion numbers ($\approx$1-10) the atom cloud can sympathetically cool the ions relatively quickly. In this regime the atom loss can be increased by applying additional micromotion energy (excess micromotion).

In the case of large ion numbers (tens to hundreds) sympathetically cooled ions are quickly heated up again by passing ions with high kinetic energy. In this case, the applied micromotion energy (excess micromotion) is irrelevant compared to the already high kinetic energy of the ion cloud. For very hot and large ion clouds, the overlap with the atom cloud can be very low. Because of the low overlap, most of the time the ions cannot collide with the atoms and are therefore not cooled well. These ion clouds need more than one atom cloud cycle[6] to cool the ions sympathetically and to observe a reasonable atom

---

[6] By dropping the atom cloud, it falls through high energy trapping regions of the Paul trap where atom-ion collisions can happen. The colder ion cloud then has better overlap with a new atom cloud in the Paul trap center.

loss signal.

The discussion until now assumed a fixed ion number. This is not the case for ion detection scheme I. This measurement scheme starts initially without an ion and the ions are produced out of the atom cloud. Therefore, the ion number and the ion production rate is time dependent.

For an initially large ion production rate, the atom number is quickly reduced by atom-ion collisions. The reduced atom number leads to a lower ion production rate. This effect reduces the measured atom loss. In case of an initially small ion production rate, the atom cloud has a high density for a longer time increasing the chance to produce an ion. If the ion is produced, the ion has a high overlap with the atomic cloud, but it has a shorter time to induce atomic loss. Therefore, it is important to have applied enough excess micromotion for the ion detection to produce still a reasonable atom loss signal. This leads to a relative amplification of small ion production rates.

All of the described processes lead to a strong non-linearity of the observed atom loss. The non-linearity enables us to measure sub-Hertz to Kilohertz ion production rates with one experimental parameter set. In Figure 4.8, an exemplary measurement of a photoassociation signal measured with ion detection scheme I is shown. Note that in the case of a photoassociation signal, atoms are also lost by the photoassociation itself (a small contribution compared to the atom-ion collision induced atom loss). The second y-axis on the right hand side shows the estimated ion number for a respective atom number i.e. atom loss. The exact scaling of this second y-axis is very much depending on the exact used experimental parameters. The shown axis is only supposed to demonstrate the idea of the non-linear atom loss for a respective ion number.

Comparison of the ion detection schemata*

We are using two different ion detection schemata, as described before. The main difference between the two is, that ion detection scheme I utilizes only one high-density atom cloud for the production and the detection of the ions. Ion detection scheme II utilizes two successive and different atom clouds. In the first atom cloud, the ions are produced and pulled out by a displaced Paul trap center. Compared to scheme I this has the advantage that the production cloud is less heated and the density is less changed by atom-ion collisions. The second cloud is used to count the number of up to about five ions. The parameters are chosen such that every ion number has its own characteristic atom loss.
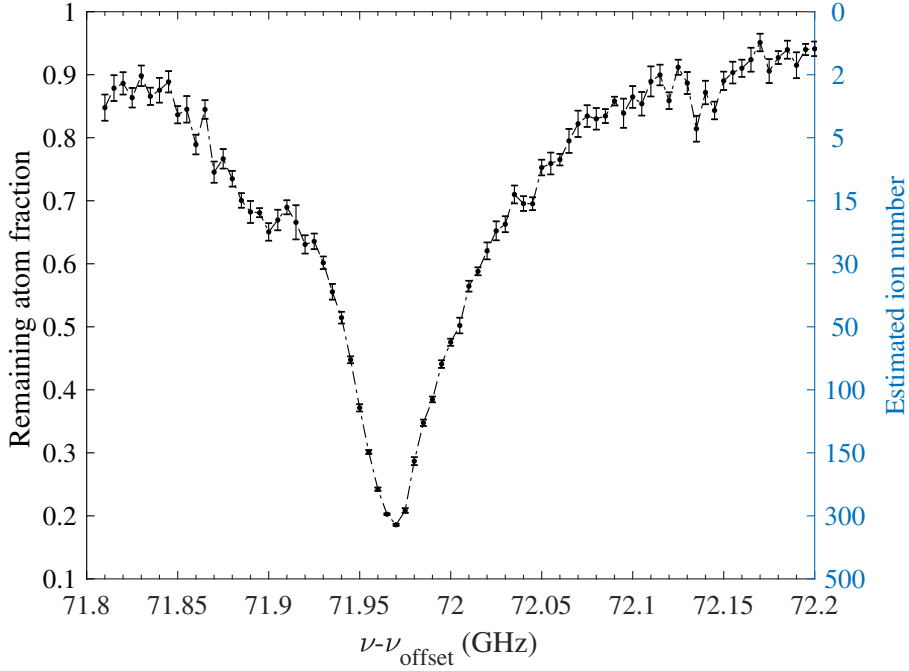
Figure 4.8: An exemplary measurement of ion detection scheme I. The remaining atom fraction is plotted over the probe laser frequency where $\nu_{offset} = 281\,\text{THz}$. The second y-axis on the right hand side gives a rough estimate of the ion number to give a feeling of the effect of the non-linear scaling of the atom loss. The interaction time used is 500 ms. Each data point is the mean of 10 repetitions of the experiment.

For this, the excess micromotion needs to be reduced compared to scheme I, as described above. A too large excess micromotion compresses the atom loss signals for respective ion numbers to a too small range and they cannot be distinguished anymore. To suppress atom-atom-ion three-body recombination sufficiently, the density of the atom cloud needs to be reduced. By choosing the right parameter set the number of ions can be counted, see [46].

We generally preferred ion detection scheme I in our experiments, as it is much faster considering the measurement time. To get good results, only one atomic cloud with about ten repetitions of the experiment for each data point is necessary. Compared to this, Ion detection scheme II needs two atom clouds with about 50 repetitions of the experiment for each data point. Scheme II needs the larger number of repetitions as more averaging is necessary to count the ions. In addition to being faster, scheme I has a very large dynamic range of the measurable ion number as discussed before. This allows to measure very large and small ion numbers with the same set of parameters. As the number of ions can only be estimated it is used for measurements where the exact number of ions is not the

first priority. We use scheme I to find the first signals of states we want to investigate, to determine frequency shifts, and to estimate the parameter set to count the number of ions with ion detection scheme II. Because of the described applications and properties, ion detection scheme I is a qualitative or semi-quantitative measurement method and ion detection scheme I is a quantitative measurement method.

4.2.6 Density dependence of ion production rate
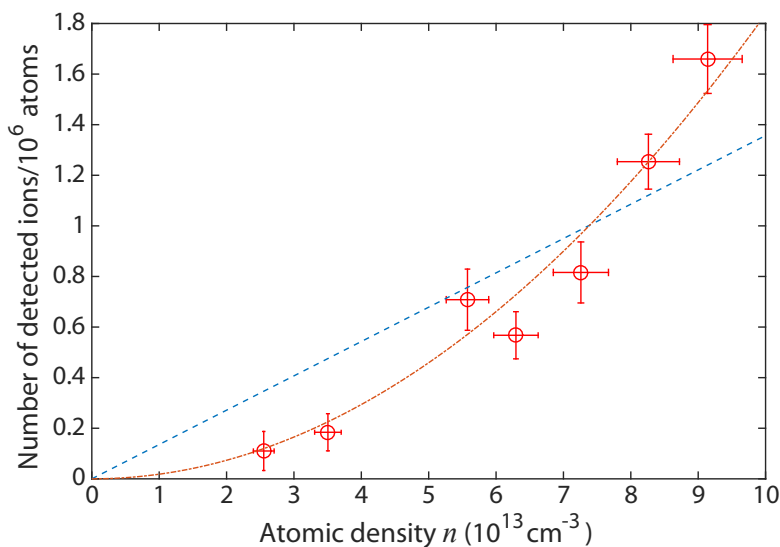
Figure 4.9: Dependence of the ion production rate on atomic density. The ion signal has been normalized by the atom number to represent the ion signal per million atoms in the cloud. Each data point is the average of 55 repetitions with the vertical error bars representing the statistical standard deviation. The horizontal error bars indicate the uncertainty in the determination of the atomic density of $\pm 5\%$. The blue dashed line corresponds to a linear fit with $\chi^2 = 6.8$ and the orange dash-dotted line is obtained from a quadratic fit with $\chi^2 = 1.0$. Both fits were not weighted to the error bars.

In order to check whether resonance lines of our REMPI spectra are the result of three-body recombination we measure how the ion production rate depends on the atomic density. Figure 4.9 shows the ion signal for the level $v = -2, R = 0$ after an accumulation time of 100 ms. The measured signal has been normalized to represent the ion signal per million atoms in the cloud. The scaling in terms of the atomic density n is clearly quadratic, as expected for a three-body process. A two-body process such as photoassociation would be characterized by a linear dependence.

4.2.7   Most weakly bound state
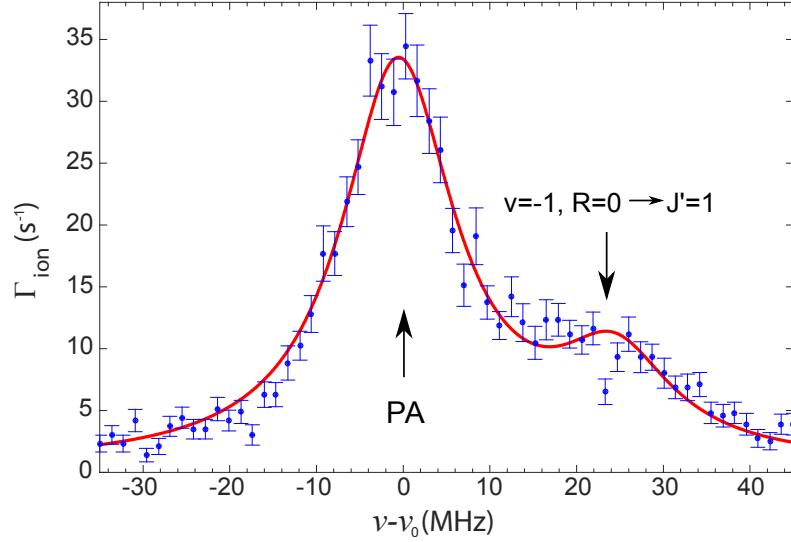
Figure 4.10: Detection of the most weakly bound molecular state. Shown is a measured REMPI spectrum as a function of the probe laser frequency ν. Next to the photoassociation line (PA) at $\nu = \nu_0 \equiv 281,445.045\,\mathrm{GHz}$, there is a second peak at $\nu - \nu_0 = 24\,\mathrm{MHz}$ which is the molecular product signal of the most weakly bound state with even parity ($v = -1, R = 0$). Each data point corresponds to 60 repetitions, and the error bars represent the statistical standard deviations. The red solid line is a fit of two Lorentzians to the data with $\chi^2 = 2.0$. This fit was not weighted to the error bars.

The most weakly bound molecular level with positive parity ($v = -1, R = 0$) is expected to be predominantly populated in ultracold three-body recombination. It has a binding energy of $24\,\mathrm{MHz} \times h$. In Figure 4.2, the REMPI signal of this molecular level is buried under the strong photoassociation line. Therefore, we carried out another scan (see Fig. 4.10) where we enhanced the photoexcitation signal relative to the photoassociation line by reducing the probe laser intensity by a factor of 20 to $\approx 0.3\,\mathrm{W\,cm^{-2}}$[7]. This diminished saturation effects of the photoexcitation peak and resulted in a narrow linewidth of about $16\,\mathrm{MHz}$ (FWHM), close to the natural linewidth of $\approx 10\,\mathrm{MHz}$ for the $A^1\Sigma_u^+$ state. Figure 4.10 shows the ion signal of the photoassociation and photoexcitation lines measured with ion detection scheme II. The photoexcitation line is located at $\nu = \nu_0 + 24\,\mathrm{MHz}$, on the shoulder of the large photoassociation peak. From a fit of two Lorentzians to the lineshape we extract the signal strength of the photoexcitation peak. For the fit both peaks were

---

[7] Corrected value

constrained to have the same width. Our analysis shows that about 50% of all molecules that are formed in three-body recombination are produced in the most weakly bound level at 24 MHz.

4.2.8 Detection efficiency as a function of probe laser intensity
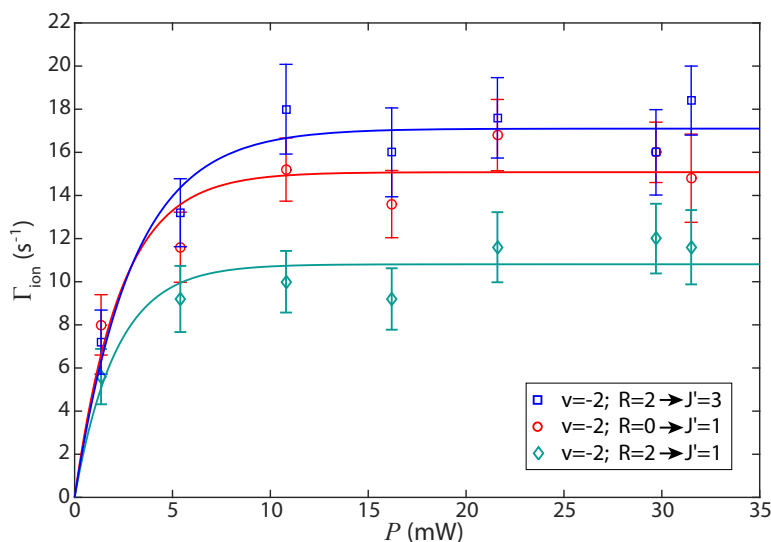
Figure 4.11: Detection signals of two rotational levels of v = −2 molecules as a function of the probe laser power. We investigate REMPI signals for three different $X^1\Sigma_g^+ \to A^1\Sigma_u^+$ transitions as indicated by the legend. Each data point is the average of 50 repetitions with the error bars representing the statistical standard deviation. The continuous lines are fits of the model function $S(P) = S_{\max}(1 - \exp(-C \cdot P))$ to the data with χ^2 values of 0.53 (blue line), 0.98 (red line), and 0.59 (turquois line). None of the fits was weighted to the error bars. The fit constant is roughly the same $C \approx 2.5\,(\text{mW})^{-1}$ for all three curves. P is the total power of the probe laser.

We experimentally investigate the ionization signal of v = −2 molecules as a function of the probe laser power, see Figure 4.11. For powers of more than 15 mW, the signal is strongly saturated for all rotational states. The continuous lines are fits of the model function $S(P) = S_{\max}(1 - \exp(-C \cdot P))$ to the data, where P is the power of the probe laser and C is a fit constant. We have verified that this model function describes well the results of our Monte-Carlo calculations for the expected ionization signal (see Sec. 4.2.9). In our experiments for v = −2 and more-deeply bound states we typically work with a power of 30 mW of the probe laser beam. Using simple scaling laws and taking into account the respective Franck-Condon and Hönl-London factors, the singlet content of the total electronic spin state and the Doppler shifts of the molecules, we have checked that also the signals of the more-deeply bound levels should be strongly saturated. Furthermore,

we observe that the ion signals for the transitions $R \to J' = R \pm 1$ are of similar strength, see, e.g. Figure 4.2 in the main text. (The disparity of the $R = 2 \to J' = 1, 3$ curves in Figure 4.11 is probably a result of measuring the $R = 2 \to J' = 1$ transition slightly off-resonance.) In general, our measurements suggest that the signal saturation is maintained for rotational states up to $J' = 7$.

4.2.9   Monte-Carlo model calculations
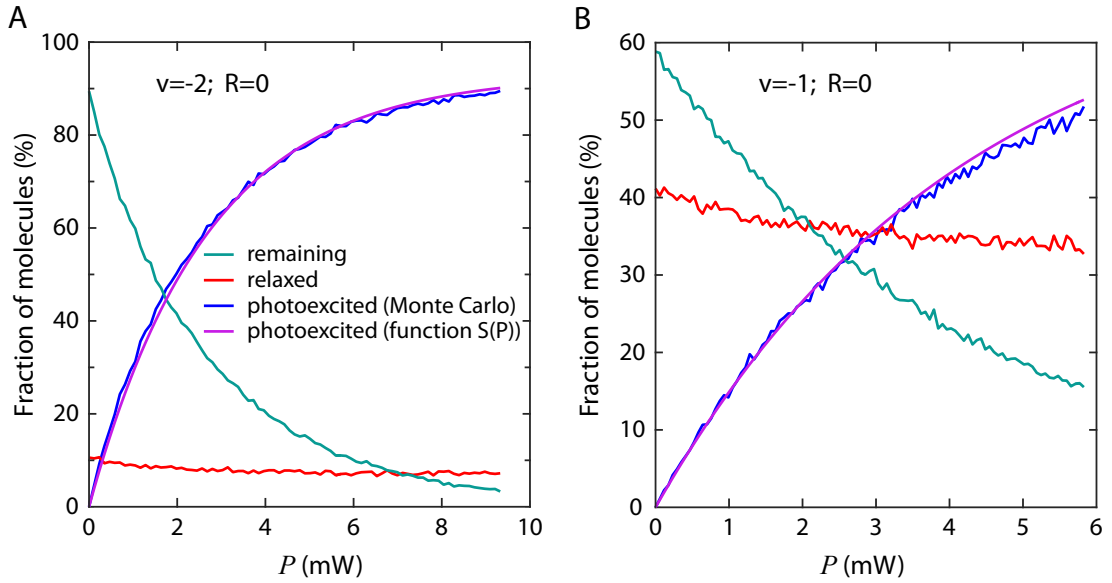
Figure 4.12: Monte-Carlo model calculations. The fractions of molecules that remain unscathed (turquoise), that relax to more-deeply bound states due to collisions with atoms (red), or that are photoexcited (blue), are plotted as a function of the probe laser power. (**A**) and (**B**) show the results for $v = -2, -1$ molecules, respectively. The smooth continuous lines (purple) have the form $\tilde{S}(P) = \tilde{S}_{max}(1 - \exp(-C \cdot P))$, where P is the total probe laser power and $\tilde{S}_{max}$ as well as C can be adapted to achieve a reasonable fit.

Once a weakly bound Rb_2 molecule is formed via three-body recombination it will fly out of the atomic cloud with a velocity $v_{Rb2} = \sqrt{E_b/(3m_{Rb})}$ which is determined by the released binding energy E_b and the mass of the rubidium atom m_{Rb}. On the way out, the molecule can collide with cold atoms and relax to a more-deeply bound state. The rate for this process is $\Gamma_{rel} = K_{rel} n(r)$, where $n(r)$ is the local atomic density and K_{rel} is the relaxation constant. We assume $K_{rel} = 10^{-10} \, \mathrm{cm^3 \, s^{-1}}$, see [47, 48, 49, 50]). At the same time, the probe laser can photoexcite the molecule with a rate $\Gamma_{phot} = \tilde{c} \, I(r) \, f_{FC} \, f_{HL} \, /((\gamma/2)^2 + \delta^2)$, where $I(r)$ is the local intensity of the Gaussian laser beam, f_{FC} is the Franck-Condon factor for the singlet parts of the multicomponent molec-

ular wave functions, f_{HL} is the Hönl-London factor, $\gamma \approx 10\,\mathrm{MHz}$ is the linewidth of the excited molecular level, δ is the laser detuning from resonance, and $\tilde{c}$ is a constant that includes, e.g., the transition electric dipole matrix element. We calculate Monte-Carlo trajectories of produced molecules and determine the probability that the molecules undergo relaxation or photoexcitation within the transient time. The molecules are created according to the spatial probability distribution $n^3(r)/\int n^3(r)d^3r$ with the direction of their respective velocity being random. On average, the molecular velocities will lead to Doppler-broadening and to a reduction of the on-resonance photoexcitation rate by a factor given by $(2v_{Rb2}/(\lambda\gamma))^{-1}\arctan(2v_{Rb2}/(\lambda\gamma))$, where λ is the transition wavelength. However, this reduction can be neglected for our purposes.

Figure 4.12A shows the Monte-Carlo calculations for the $v = -2$ level for the experimental parameters of our setup. The presented curves are the probabilities that for a given power a created molecule is photoexcited, undergoes relaxation, or remains unscathed. For example, at a resonant probe laser power of $9\,\mathrm{mW}$ about 89% of the produced $v = -2$ molecules will be photoexcited. About 8% will be lost due to relaxation collisions and about 3% will leave the cloud and probe laser beam without having relaxed or being photoexcited. We find that the photoexcited fraction can be well described by the model function $\tilde{S}(P) = \tilde{S}_{max}(1 - \exp(-C \cdot P))$. In order to reproduce the power dependence of the $v = -2$ data in Figure 4.11 we have adjusted $\tilde{c}$, which effectively calibrates the total power P in our calculations. Keeping the same $\tilde{c}$, the Monte-Carlo model can now also be used for any other vibrational level, if the respective values for f_{FC}, f_{HL}, and v_{Rb2} are employed. In Figure 4.12B we show calculations for $v = -1$. Compared to $v = -2, R = 0$ the fraction of relaxed molecules is larger and the photoexcitation is smaller. This is because of two reasons. Due to its lower velocity the $v = -1$ molecule spends more time in the atomic cloud which increases the relaxation probability. Secondly, the Franck-Condon factor for the $v = -1$ molecules is smaller by a factor of about 8, which reduces photoexcitation.

4.2.10   Calibration of REMPI efficiency

The overall efficiency of REMPI is the product of the efficiency η_1 to excite the molecule (within its lifetime in the REMPI laser beams) to the $A^1\Sigma_u^+, v' = 66$ level and the efficiency η_2 to ionize this excited molecule.

In order to determine η_1, we use both our measurements and calculations presented in the Sections 4.2.8 and 4.2.9. With the exception of level $v = -1$, we generally work with probe laser powers of about 30 mW for which the ion signal is strongly saturated (see e.g. Fig. 4.11) and the observed linewidths of REMPI signals exceed the natural linewidth of the $A^1\Sigma_u^+$ level (≈ 10 MHz) by roughly a factor of two (see e.g. Fig. 4.3). Despite an apparent saturation of the ion signal it is still possible that a fraction of molecules escape or relax in a collision before they are optically excited. Using our Monte-Carlo model we have calculated this fraction (see Fig. 4.12A). We find that for all the vibrational levels in our measurements with $v < -1$, the excitation efficiency is $\eta_1 > 0.9$, for a probe laser power of ≈ 30 mW. In contrast, for the $v = -1$ level we work in a low power regime where the ion signals are not saturated. If, e.g., we work with a probe laser power of 1.5 mW, Figure 4.12B shows that only 21% of the initially created $v = -1$ molecules are excited in the first step of our REMPI detection scheme, thus we derive $\eta_1 = 0.21$.

We determine the efficiency η_2 with the help of photoassociation. From a cold Rb atom cloud we photoassociate several percent of the atoms to the intermediate level $A^1\Sigma_u^+, v' = 66, J' = 1$ within 1 s. We deduce the number of photoassociated molecules by measuring the corresponding atomic losses from the atomic cloud via absorption imaging. We find that a small fraction η_2 of these molecules is ionized by the ionization laser. Measuring the number of produced ions with detection scheme II, we determine the ionization efficiency to be $\eta_2 = (6.6 \pm 0.7 \pm 2.2) \times 10^{-4}$. Here, the first uncertainty value is of statistical nature, while the second one mainly reflects systematic errors in the atom number measurements by absorption imaging. We note that photoassociated molecules that are not ionized, relax quickly to the molecular ground state $X^1\Sigma_g^+$ by emitting a photon. At this point they are cold and trapped in the atomic cloud, but in general vibrationally excited. Within a few tens of ms, these molecules will then inelastically collide with another atom and relax to more deeply-bound vibrational states. The released binding energy will kick both the molecule and the atom out of the trap. Therefore each photoassociated molecule typically leads to a loss of three atoms from the cloud, a fact that needs to be taken into account when determining the number of photoassociated molecules from the measured atom loss.

4.2.11 Determination of molecule production rates

Once the REMPI efficiency $\eta_1 \eta_2$ is determined, it is used to directly convert a measured ion number into a number of molecules $M(v,R)$ formed in a particular state. The corresponding loss rate constant $L_3(v,R)$ is calculated as

$$L_3(v,R) = \frac{3\,M(v,R)}{\int_0^\tau \int n(\boldsymbol{r},t)^3 d^3r\, dt},$$
(4.1)

where τ is the accumulation time during which molecules are produced via three-body recombination. We determine the time dependent density $n(\boldsymbol{r},t)$ by measuring the total atom number and temperature of the atom cloud at various times during its decay (see Fig. 4.13).

We note, that it is in general not a-priori clear whether all the molecules in a particular level originate directly from three-body recombination, as relaxation of more weakly bound molecules due to a collision with an atom might also contribute to the population of the level. Clearly, the level $v = -1$ is most relevant for this process, and according to the Monte-Carlo calculations (see Sec. 4.2.9), about 40% of the $v = -1$ molecules are expected to relax for our given experimental parameters. Therefore, as an example we tested whether the $v = -2$ level is strongly populated through relaxation of $v = -1$ molecules by repeating the recombination rate measurements for clouds with a factor of five smaller atom number and density. Possible relaxation contributions to the flux into level $v = -2$ level should then be strongly suppressed. Our measurements, however, do not indicate such a suppression, as we obtain a similar loss rate constant $L_3(v,R)$ as before. Therefore, this is evidence that the measured molecular fluxes are mainly originating from a direct three-body recombination into each v,R product channel. Nevertheless, the determined population of the $v = -2, -3, -4, -5$ levels has to be considered as an upper limit for three-body recombination flux.

4.2.12 Decay of atomic cloud

We measure the decay of the number of Rb atoms trapped in our optical dipole trap while the probe laser is switched off (see Fig. 4.13). For times $t > 5\,$s, the decay is exponential, mainly due to collisions with thermal background gas. For short times, additional losses, e.g., due to three-body recombination, photoassociation, and evaporation are present.
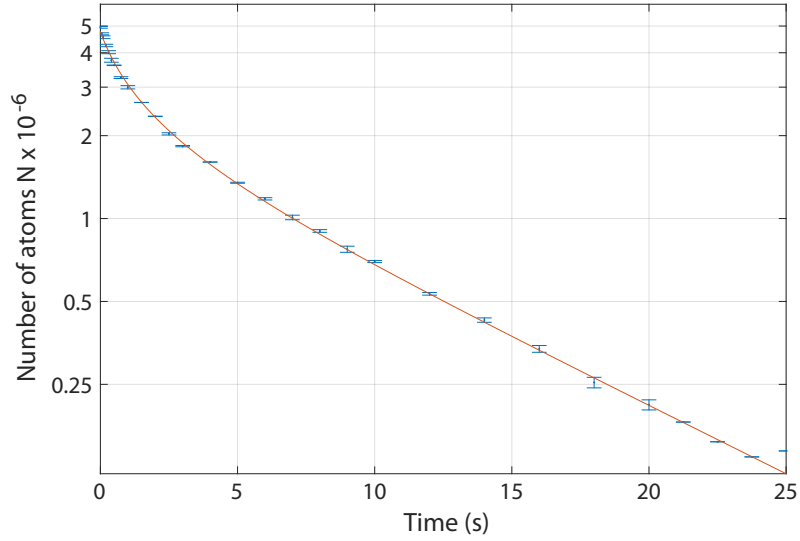
Figure 4.13: Decay of the atomic cloud in the optical dipole trap. The number of remaining atoms of the atom cloud is plotted as a function of time. Each data point corresponds to two repetitions, and the error bars represent the statistical standard deviations. The continuous line is a guide to the eye.

4.2.13   Three-body model and calculations

Besides the experimental determination we calculate the set of loss rate constants $L_3(v, R)$ numerically. Our computational method uses the adiabatic hyperspherical representation to solve the 3-body Schrödinger equation [7, 51]. From the solution of the coupled equations, the elements of the unitary scattering S-matrix are obtained that connect the entrance channel state to the various product channel states v, R. Consistent with the experimental observations, we ignore nuclear spin degrees of freedom so that we assume entrance three-body continuum states of total angular momentum $\vec{J} = 0$ and positive parity. Consequently the product channels also have $\vec{J} = 0$, resulting from the sum of the angular momenta for diatomic molecular rotation $\vec{R}$ and the relative angular momentum of the atom-diatom pair. The total three-body decay rate of an atomic gas of density n is $\dot{n} = -L_3 n^3$, where $L_3 = \sum_{v, R} L_3(v, R)$.
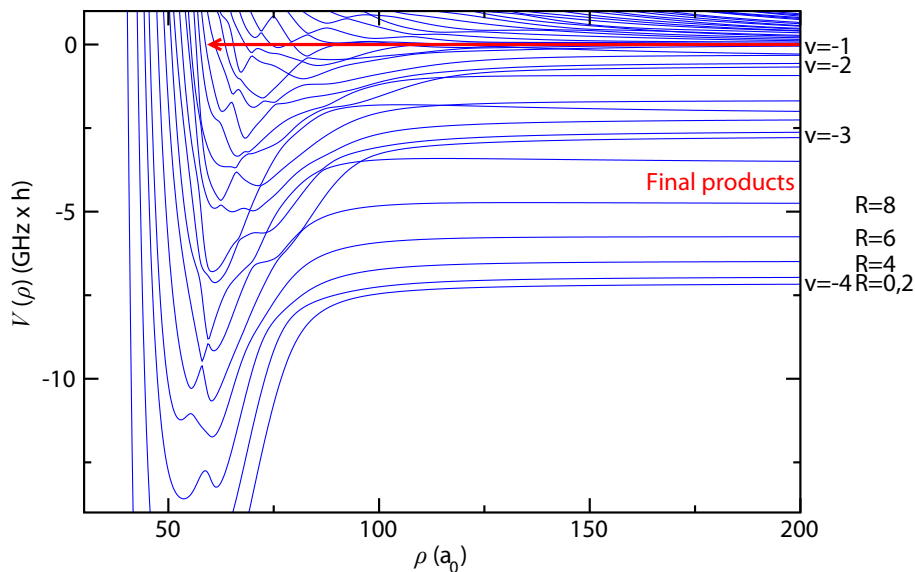
Figure 4.14: Adiabatic hyperspherical potential energy curves $V(\rho)$ versus hyperspherical radius ρ for three ^{87}Rb atoms. The number of s-wave bound states is $N_s = 4$; the vibrational and the rotational quantum number is shown for dimer product vibrational levels $v = -1, -2, -3$, and -4. The arrow indicates the three-body entrance channel threshold at energy $E_{col} = 0$. The potential energy curve asymptotes at negative energy correspond to dimer molecular levels. All states in the diagram have total angular momentum $J = 0$. a_0 is the Bohr radius.

We follow Refs. [34, 52] in assuming that the three-body potential is a pairwise additive sum of two-body Lennard-Jones potentials $V(r) = -(C_6/r_s^6)(1 - (\tilde{\lambda}/r_s)^6)$, where r_s is the pair separation and $C_6 = 4710.22$ a.u. is the known long-range van der Waals coefficient for two Rb atoms in their ground electronic state [44]. The short-range parameter $\tilde{\lambda}$ is adjusted for a selected number N_s of $R = 0$ bound states to give the known scattering length $100.36\,a_0$ for two ^{87}Rb atoms in their $f = 1$, $m_f = -1$ hyperfine state [44]. Here we let N_s range from 1 to 6. For a similar example of calculations with Cs atoms see [52].

Figure 4.14 shows the three-body adiabatic potentials as functions of hyperspherical radius ρ calculated for the case of $N_s = 4$ s-wave bound states. Three atoms come together from large ρ with collision energy $E_{col} > 0$ close to the $E_{col} = 0$ threshold and encounter one another in the shorter range region of the potential, where they may recombine and separate to the product states of a dimer and a free atom. The shared energy release in the separating products is $E_{col} - E_b(v, R) \approx -E_b(v, R)$.

Figure 4.15 shows the calculated $L_3(v, R)$ values for the case of $N_s = 6$. It is evident

that the overall pattern exhibits two clear features: (1) a quite slow overall drop off with increasing binding energy, and (2) strong fluctuations with rotational quantum number R. The slow drop off has the form of $1/\sqrt{E_b}$ and may be related to the classical time for the atom-diatom products to separate from the shorter range "collision complex." The strong fluctuations show an oscillatory pattern and an overall decrease in L_3 with increasing R. This behavior is likely related to the multi-path interference in the shorter range region where the entrance and exit channels can be interconnected, reflected by the presence of multiple avoided crossings of the potentials in Figure 4.14. As a result, there are many pathways on which phase interference might be operative, thereby leading to the fluctuations in the product distributions.
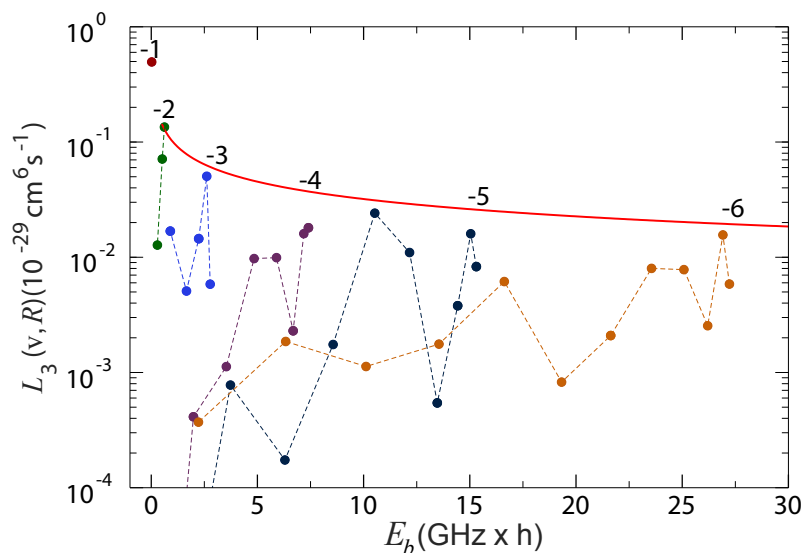
Figure 4.15: Calculated loss rate constants $L_3(\mathbf{v},R)$ versus calculated binding energy $E_b(\mathbf{v},R)$ for our model with $N_s = 6$ *s*-wave bound states. The dashed lines are to guide the eye between the different rotational levels of vibrational states v $= -2, -3, -4, -5$ and -6; the rotational quantum numbers increase in steps of 2 from the lowest energy $R = 0$ level for each v. The solid red line shows a line varying proportional to $1/\sqrt{E_b}$.

Our calculations verify that $L_3(\mathbf{v},R)$ varies by less than 2% as a function of collision energy E_{col} in the range of 0 to $1\,\mu\mathrm{K} \times k_B$. Our total L_3 value is converged with respect to N_s. We obtain $L_3 = 1.5 \times 10^{-29}\,\mathrm{cm}^6\,\mathrm{s}^{-1}$ for $N_s = 1$ and $L_3 = 1.0 \times 10^{-29}\,\mathrm{cm}^6\,\mathrm{s}^{-1}$ for $N_s = 2, 3, 4, 5$, and 6. Our calculated value of $L_3 = 1.0 \times 10^{-29}\,\mathrm{cm}^6\,\mathrm{s}^{-1}$ is a factor of 4 less than the one measured by Burt *et al.* [28] and a factor of 2 less than their lower error range. Clearly more work in experiment and theory is required to establish an accurate magnitude of L_3 with less uncertainty. Therefore, in order to eliminate the differences in magnitude

and compare the relative population distributions between theory and experiment, the calculated values have been scaled by a factor of 4.3 in Figure 4.4 to normalize them to the magnitude reported by [28].

We have also tested the possible effect of pairwise non-additive long-range Axilrod-Teller corrections [53] to the 3-body potential. Assuming a plausible form and magnitude for such corrections shows that they change the total recombination rate less than a few percent. We have observed that a larger effect on product distributions occurs for molecular states with larger binding energies. While these effects can be larger than the few percent level for the most deeply bound molecular states considered in the calculations, we have seen no significant qualitative change in the product distributions of the most weakly bound molecular states.

4.2.14 Suppression of population of odd-R molecular states near threshold

In the current experiment we did not observe population of near-threshold odd-R molecular states, which is in contrast to the observation of the more deeply bound odd-R states in our previous experiment [12]. We give here a simple estimate for the suppression in the formation of near-threshold odd-R molecular states. It is based on the probability of hyperfine-spin-change transitions, which must accompany odd-R states formation due to the identical particle symmetry of the ultracold ^{87}Rb atoms. We approximate the atomic interactions as pair-wise interactions and treat the short-range interactions from the third, initially free atom perturbatively. The third atom gives the colliding two atoms a mechanical nudge such that they can form a bound state, but the hyperfine-spin state is not directly affected by the interaction. According to Fermi's golden rule, the transition amplitude will then be proportional to the overlap of the initial and final hyperfine states of the scattering state and molecular level, respectively.

Weakly bound ^{87}Rb$_2$ states effectively experience very little exchange interaction, i.e. in the absence of hyperfine interaction their corresponding triplet and singlet vibrational levels would be almost energetically degenerate. As a consequence, the weakly bound ^{87}Rb$_2$ states exhibit essentially the same hyperfine structure as the scattering state. Accordingly, a change of the hyperfine state is suppressed in three-body collisions. For more deeply bound molecular states, however, exchange interaction effectively increases, as the near-degeneracy of the singlet and triplet levels progressively vanishes. This leads to a

change of the singlet/ triplet character of the hyperfine levels and as a consequence the recombination can populate a broader range of hyperfine spin states.

We can estimate the effect with a simple two-level toy model. We consider a scattering state of two atoms with only two "hyperfine states" having an hyperfine energy splitting of Δ_{HF}. When bound in a molecular level the atoms additionally experience an "exchange interaction" Δ_{Ex} which mixes the two hyperfine levels. In the absence of hyperfine interaction, the exchange interaction would cause complete mixing and a level splitting of $2\Delta_{Ex}$. In the presence of hyperfine interaction, the admixture amplitude is given by Δ_{Ex}/Δ_{HF} according to perturbation theory, and the transition probability to the formerly "forbidden" product state scales $\propto (\Delta_{Ex}/\Delta_{HF})^2$. For ^{87}Rb $\Delta_{HF} \approx 6.8$ GHz$\times\hbar$, and for the v = -5 vibrational level $2\Delta_{Ex} \approx 0.63$ GHz$\times\hbar$. This suggests that the maximum population in the odd-R states, relative to that in even-R states, should be on the order of 2×10^{-3} for the investigated range of molecular binding energies in the present work.

4.2.15   Error estimation for population distribution

In Figure 4.4 the error bars represent the statistical uncertainties of the ion signals. However, there are also other sources of error. Due to an imperfect atom number calibration in our setup of up to 30% there is an uncertainty of 60% in the global normalization of the flux into the molecular quantum states. Furthermore, for the determination of η_1 we assume the relaxation rate constant of the product molecule to be $K_{\text{rel}} = 10^{-10}$ cm^3 s^{-1} (see [47, 48, 49, 50]), a value which could easily be off by a factor of two. While for the levels with v $= -2, \ldots, -5$ this would entail only a small correction of up to a few percent, for the level v $= -1$ this correction could reach 35%.

5 Magnetic quantum number resolved state-to-state chemistry

This chapter corresponds to the publication:

Joschka Wolf, Markus Deiß, and Johannes Hecker Denschlag,
"Magnetic quantum number resolved state-to-state chemistry ",
arXiv **1909.00777** (2019).

5.1   Abstract

We extend state-to-state chemistry to a realm where besides vibrational, rotational and hyperfine quantum states magnetic quantum numbers are also resolved. For this, we make use of the Zeeman effect which energetically splits levels of different magnetic quantum numbers. The chemical reaction which we choose to study is three-body recombination in an ultracold quantum gas of ^{87}Rb atoms forming weakly-bound Rb$_2$ molecules. Here, we find the propensity rule that the total m_F quantum number of the two atoms forming the molecule is conserved. Our method can be employed for many other reactions and inelastic collisions and will allow for novel insights into few-body processes.

5.2   Introduction

A primary goal of state-to-state chemistry is to gain an understanding about chemical re-actions on a fundamental level (see, e.g. [39]). This includes investigating what the final product states are for a given quantum state of reactants. A proven experimental method for carrying out state-to-state chemistry is based on atomic and molecular beams (for re-cent reviews, see e.g. [3, 4, 5]).

In recent years, a complementary approach has been established, investigating chemical reactions in traps in the ultracold regime (for reviews, see [29, 54, 55, 56, 57, 58]). Within the last decades, it has become standard for state-to-state chemistry experiments to resolve the electronic, vibrational and rotational quantum states of the molecular products. Very recently our group demonstrated that even hyperfine substates of the products can be re-solved, see [12] and Chapter 4. Magnetic substates, however, have in general not yet been identified, apart from the special case where the reaction is essentially only taking place in a single quantum channel. Typical examples for such single-channel dominated reactions occur in the vicinity of Feshbach resonances, e.g. [9, 27, 59, 60, 61], or are photo-induced reactions, e.g. [21, 62]. Clearly, state-to-state aspects become especially of interest when more than one reaction channel is involved. Here, we extend state-to-state chemistry to finally resolve magnetic substates for systems where many reaction channels are present. This is achieved by measuring how the molecular product states are Zeeman shifted as a function of an applied external magnetic field. The chemical reaction which we choose to study is three-body recombination of ^{87}Rb where two atoms combine to form a Rb_2 dimer and the third Rb atom (spectator) carries away part of the released binding energy, see Figure 5.1(a). We work at low magnetic fields of a few G where atomic interactions are non-resonant, see [12] and Chapter 4. We probe molecular quantum states in a range of small binding energies and find the following "no-spin flip" propensity rule. The m_F quantum number of the molecule equals the sum of the initially prepared m_f quantum numbers of the two atoms which form the molecule. Here, m_F is the magnetic quantum number of the total angular momentum F of the molecule excluding mechanical rota-tion and m_f is the magnetic quantum number of the total angular momentum f of the atom. The "no-spin flip" propensity rule indicates that the spectator atom participates in the reaction merely via mechanical forces, so that it induces no spin-flips on the forming molecule.
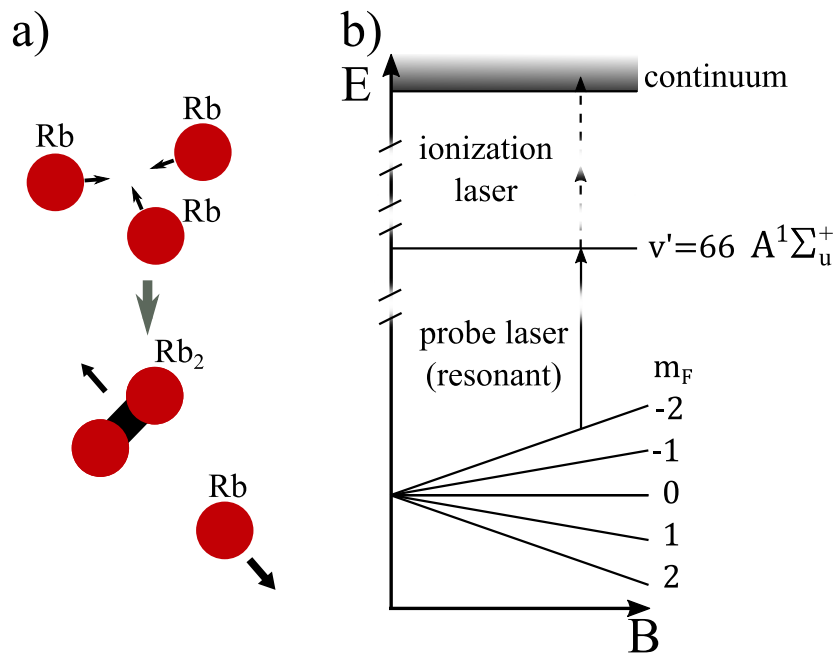
Figure 5.1: Outline of the investigated system. (a) Three-body recombination of three neutral Rb atoms forming a Rb_2 dimer. (b) Schematic of the REMPI detection scheme, resolving the m_F quantum number of the molecule. As an example we consider here a molecular level manifold with $F = 2$. The linear Zeeman effect due to a B-field splits the $F = 2$ levels into magnetic components $m_F = -2, -1, 0, 1, 2$. The splitting is large enough so that each level can be resolved via resonant excitation towards the intermediate level $v' = 66$, $A^1\Sigma_u^+$ with the probe laser. From there, two photons of the ionization laser ionize the molecule.

5.3 Experimental parameters

We carry out our experiments with an ultracold, thermal cloud of ^{87}Rb with a temperature of about 750 nK. The cloud consists of $N_{at} \approx 5 \times 10^6$ atoms which are trapped in a far-detuned, crossed optical dipole trap with a wavelength of about 1064 nm. The trapping frequencies are $\omega_{x,y,z} = 2\pi \times (23, 180, 178)$ Hz, where z represents the vertical direction. The atoms are in the electronic ground state and initially spin-polarized in the hyperfine state $f = 1, m_f = -1$. From this state also other m_f spin polarizations can be prepared. Within the atomic gas, three-body recombination produces weakly-bound Rb_2 molecules in the coupled $X^1\Sigma_g^+ - a^3\Sigma_u^+$ potentials. Given the initial peak particle density $n_0 \approx 0.9 \times 10^{14}$ cm^{-3} and a three-body recombination loss rate constant of $L_3 = (4.3 \pm 1.8) \times 10^{-29}$ cm^{6}s^{-1} [28], about 1.5×10^5 atoms are lost due to three-body recombination in the first 500 ms. The molecular products are distributed over a range of different states, char-

acterized by sets of vibrational, rotational, various spin and magnetic quantum numbers. We state-selectively probe the molecular products via resonance-enhanced multi-photon ionization (REMPI), followed by ion detection, similarly as in Chapter 4. Figure 5.1(b) shows our REMPI scheme. The probe laser resonantly drives a transition to an intermediate level, which is located in the electronic state $A^1\Sigma_u^+$, has vibrational quantum number $v' = 66$ and a total angular momentum (excluding nuclear spin) J'. Hyperfine splittings of this excited level are negligibly small ($< 3\,\mathrm{MHz}$), such that the J'-states form a simple rotational ladder with rotational constant $b_v = 443\,\mathrm{MHz}$ [40, 41]. From the intermediate level, another two photons of the ionization laser ionize the molecule. We use the dipole trap laser as ionization laser. Its optical frequency is about $281.62915(6)\,\mathrm{THz}$. The probe laser and the dipole trap laser are wavemeter locked with a precision of a few MHz. The probe laser intensity is $\approx 3\,\mathrm{W\,cm^{-2}}$ at the location of the atoms. This is sufficient to excite the probed molecules with high probability to the intermediate $A^1\Sigma_u^+$ level.

The ion detection works as follows. Directly after its ionization the molecule is trapped in a Paul trap [1] which is centered on the atomic cloud. Subsequently, the micromotion-driven ion elastically collides with ultracold atoms, see [46] and Chapter 4. This leads to loss of atoms from the shallow dipole trap, which is measured by absorption imaging. The losses increase with the number of trapped ions.

In order to spectrally resolve different m_F quantum numbers we apply a magnetic B-field of several G to induce linear Zeeman splitting. As an example, Figure 5.1(b) shows the splitting of a $F = 2$ molecular bound state. In principle, $\vec{F}$ and the molecular rotation $\vec{R}$ couple to form the total angular momentum $\vec{F}_\mathrm{tot}$. However, for the bound states considered here, this coupling is quite weak, corresponding to splittings between different F_tot levels smaller than 1 MHz (see Ch. 4). Therefore, already the B-field of several G efficiently decouples $\vec{F}$ and $\vec{R}$. A level for given m_F and R quantum numbers is then essentially $(2R+1)$-fold energetically degenerate, according to the manifold of the m_R substates.

5.4   Polarized samples

Figure 5.2 shows several measured REMPI spectra as a function of the probe laser frequency ν. The atoms of the cloud have initially been prepared either in state $m_f = -1$ (red data) or in state $m_f = +1$ (blue data). The measurements are carried out for various homogeneous magnetic fields in a range between 4.5 and 37.0 G. REMPI is carried out

---

[1] For a detailed description of the setup of the nested atom and ion traps see [17].

by switching on the probe laser for 500 ms. Afterwards, the magnetic field is turned off. We measure the remaining atom number 160 ms after the probe laser has been switched off, so that ions produced near the end of the REMPI period can still lead to atom losses. After normalization with the remaining atom number from an experiment where we work with a far off-resonant probe laser, we obtain the remaining atom fraction, as shown in Figure 5.2.

We first discuss the data set for $m_f = -1$ and the lowest magnetic field of 4.5 G. The strong resonance line at $\nu - \nu_0 \approx 0$ is a photoassociation (PA) signal, where two $f = 1, m_f = -1$ atoms which collide in an s-wave form a molecule in state $v' = 66$, $A^1\Sigma_u^+$ with $J' = 1$. The observed width of the PA line is larger than the natural linewidth of about 12 MHz (FWHM) of the excited level due to saturation effects caused by atom loss.
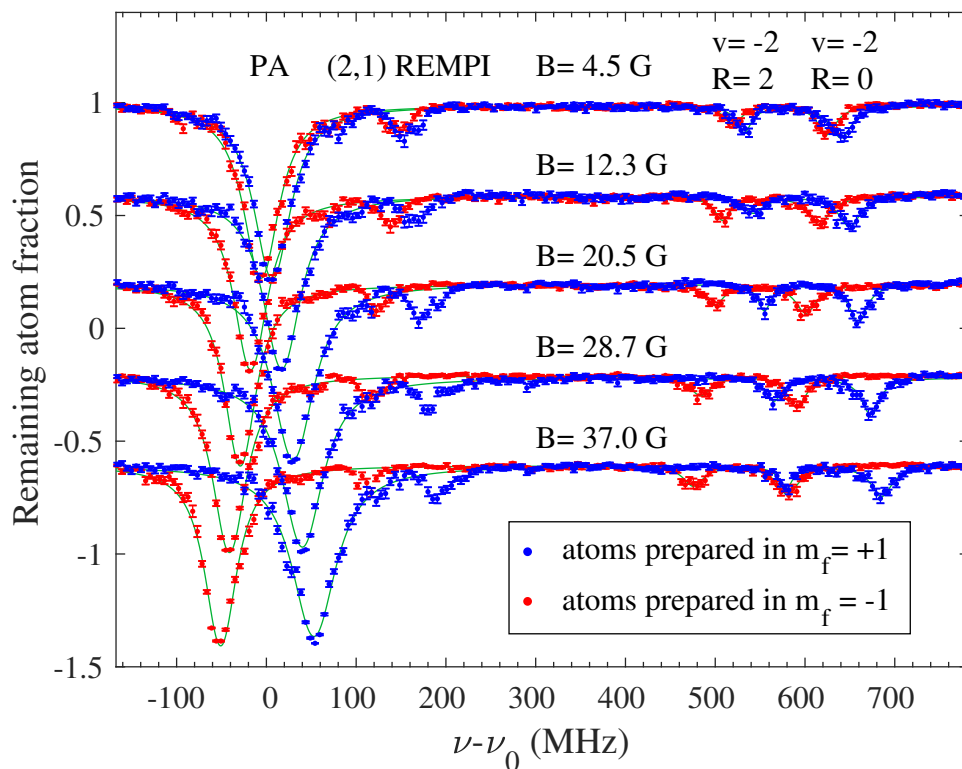
Figure 5.2: REMPI spectra for polarized samples. REMPI spectra for experiments where the atomic sample is initially prepared in the magnetic spin state $m_f = -1$ (red data) or $m_f = +1$ (blue data) for different magnetic fields B. Shown is the remaining atom fraction as a function of the probe laser frequency ν. $\nu_0 = 281,445.07(6)$ GHz. Nominally, the remaining atom fraction can range between 1 and 0, but in order to improve visibility data sets for different magnetic fields are offset relative to each other in vertical direction. The loss signals for $v = -2, R = 0$ and $v = -2, R = 2$ product molecules, the photoassociation line (PA), and (2,1) REMPI processes are labeled. The green lines are fits according to Eq. (5.1) to the resonances.

We now focus on the loss signals about $520\,\text{MHz}$ and $640\,\text{MHz}$ above the photoassociation line, which correspond to $v = -2, R = 2$ and $v = -2, R = 0$ product molecules, respectively. Here, v is the vibrational quantum number and R is the rotational quantum number. v is counted downwards starting from $v = -1$ for the most weakly bound vibrational state correlated to the atomic $f = 1, f = 1$ asymptote[2]. The $v = -2, R = 0, 2$ molecular products have been detected and identified in previous work of ours (see Ch. 4). Their F quantum number is $F = 2$. Figure 5.2 shows that their resonance lines shift towards lower probe laser frequencies when increasing the magnetic field B, in parallel to the photoassociation line. Furthermore, we note that the depths and the widths of the lines stay the same when the B-field is changed. This suggests that the molecules are produced in a particular m_F state, not a mix. We observe a very similar behavior when we switch to experiments with $f = 1, m_f = +1$ atoms [3] (blue data). Now, however, all lines shift in opposite direction as compared to the $f = 1, m_f = -1$ data. The observed linewidths are 30 ± 10 MHz (FWHM) which is a factor of 2 to 3 larger than the natural linewidth. The increased width can be explained as the result of several factors, such as the laser linewidth, a Doppler shift of the moving Rb_2 molecules, and saturation effects. We note that besides the already discussed lines in Figure 5.2, there are two additional lines (at around $v - v_0 = 90\,\text{MHz}$ and $140\,\text{MHz}$ for the data sets at $B = 4.5\,\text{G}$). These belong to so far unidentified molecular bound states which are ionized via (2,1) REMPI through a different intermediate state, see also Chapter 4.

We now carry out a more quantitative analysis of the Zeeman energy level shifts. Since the excited $v' = 66$, $A^1\Sigma_u^+$ level is essentially insensitive to applied magnetic fields, the observed line shifts in Figure 5.2 correspond directly to the Zeeman shifts of the atomic states or the molecular product states. In order to determine the center positions v_i of each observed resonance line i we fit the function

$$N(v)/N_0 = \exp\left(\sum_i \frac{-A_i}{(v - v_i)^2 + (\Gamma_i/2)^2}\right) \tag{5.1}$$

to the data of the remaining atom fraction, $N(v)/N_0$. Here, A_i is an amplitude, and Γ_i is the linewidth. The results are presented in Figure 5.3, together with additional REMPI data beyond the frequency range shown in Figure 5.2. The additional data correspond to

---

[2] Detailed information on the $X^1\Sigma_g^+ - a^3\Sigma_u^+$ level structure can be found, e.g., in Ch. 4 and [44].

[3] To prepare $m_f = +1$ atoms, we start with a cloud of $m_f = -1$ atoms at a small bias magnetic field of $B = 4.5\,\text{G}$ and suddenly reverse the magnetic field direction, which flips the quantization axis but the spins cannot follow [63]. The resulting $f = 1, m_f = +1$ population is 95% pure.

transitions from $v = -2, R = 2$ and $R = 4$ towards $J' = 3$ of $v' = 66, A^1\Sigma_u^{+}$[4]. Together with these, our study covers all possible [5] rotational product states $R = 0, 2, 4$ of the $v = -2$ state. Figure 5.3 shows that the $J' = 1$ and $J' = 3$ data sets for the v = -2, $R = 2$ state lie precisely on top of each other, as required by consistency. Next, we compare the measured energy positions of the product molecule levels to calculated Zeeman level positions (dashed lines).
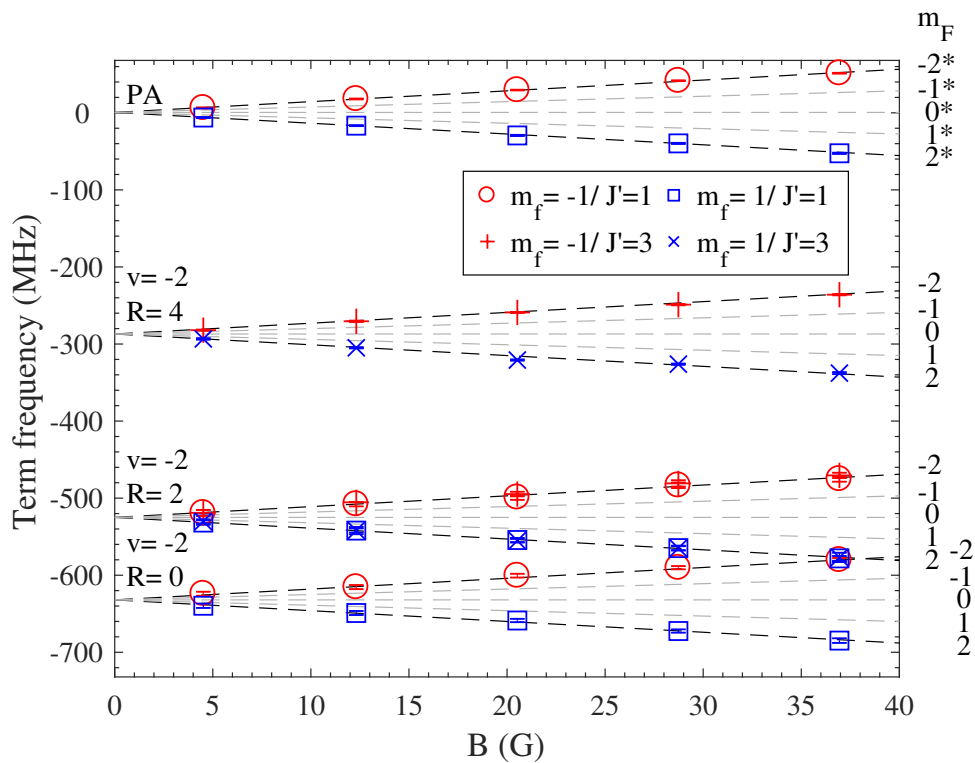
Figure 5.3: Zeeman shifts of the pure samples. Shown are the term frequencies (i.e. negative laser frequency positions relative to the threshold at $B = 0$) of the two-atom scattering states (PA) and the molecular levels $v = -2$, $R = 0, 2, 4$ as a function of the magnetic field B. The legend indicates for each plot symbol which spin polarization the atomic cloud has and which J'-level is addressed in the REMPI measurement. The error bars correspond to the 95% confidence intervals of the fits according to Eq. (5.1). The dashed lines are calculations. The asterisk (*) next to a m_F quantum number marks a two-atom scattering state.

Since the molecules are extremely weakly bound, their magnetic moment is essentially

---

[4] For a rotational quantum number R of the weakly-bound ground state Rb_2 molecule the selection rules for electric dipole transitions allow for $R \to J' = +1$ for $R = 0$, and $R \to J' = R \pm 1$, otherwise.

[5] According to the propensity rule from Chapter 4 dominantly weakly-bound product states with positive parity, i.e. even R, are produced in our experiment. Furthermore, for the v= -2 state, $R = 4$ is the last rotational bound state below the scattering asymptote.

equal to the sum of the magnetic moments of the free atoms a, b. In the limit of the linear Zeeman effect, the energy level positions are then given by $E_b + g_f \cdot \mu_B \cdot (m_{f,a} + m_{f,b}) \cdot B$, where E_b is the binding energy of the respective state at zero field, μ_B is Bohr's magneton, $g_f = -1/2$ is the g-factor, and $m_{f,a/b}$ is the magnetic quantum number of atom a/b, respectively. Figure 5.3 clearly shows that three-body recombination produces $m_F = +2$ molecules in an ensemble of $m_f = +1$ atoms and it produces $m_F = -2$ molecules in an ensemble of $m_f = -1$ atoms. Apparently, the total magnetic quantum number $m_F = m_{f,a} + m_{f,b}$ of the two atoms forming the molecule is conserved in three-body recombination. This goes well along with a propensity rule for the conservation of the F quantum number and the parity, observed in our previous work Chapter 4.

5.5 Mixed sample

Finally, we investigate molecular products in an atomic sample consisting of a mix of m_f states which has been produced by ramping the B-field through zero field. Figure 5.4 shows a REMPI spectrum for $B = 37 \, \text{G}$. As expected, the photoassociation signal around v_0 is now a multi-line structure involving all m_F components $-2, -1, 0, 1, 2$ resulting from all pair combinations of $m_f = -1, 0, 1$ atoms. The $v = -2, R = 0, 2$ molecular signal between 450 MHz and 700 MHz (inset is a zoom) is now a broad double dip as a result of the ten overlapping molecular signals corresponding to the different combinations of R and m_F quantum numbers. Since no further substructure is observable, a direct decomposition into molecular subcomponents is problematic. Therefore, we choose the following way for the analysis of the molecular signal. We first determine the three m_f-populations of the initial atom cloud and with these we predict the $v = -2, R, m_F$ populations of the molecules and the corresponding spectrum which can be compared to the measurements. From additional photoassociation loss measurements which are carried out without ion trap and a simple photoassociation model which assumes the same photoassociation efficiency for all $m_F = m_{f,a} + m_{f,b}$ atom pairs, we extract the following m_f distribution: 25%, 45%, 30% for $m_f = -1, 0, 1$, respectively. Using this, we predict the three-body recombination product molecule distribution to be 9%, 17%, 41%, 20%, 13% for $m_F = -2, -1, 0, 1, 2$, respectively. Here, we use that the m_F quantum number is conserved for three-body recombination and assume that the three-body recombination rate constant is identical for the different m_F channels. The corresponding calculated m_F signals are shown in the inset of Figure 5.4, using individual linewidths of 40 MHz.

The black line, which is the sum over all signals, agrees quite well with experimentally observed double-dip structure.
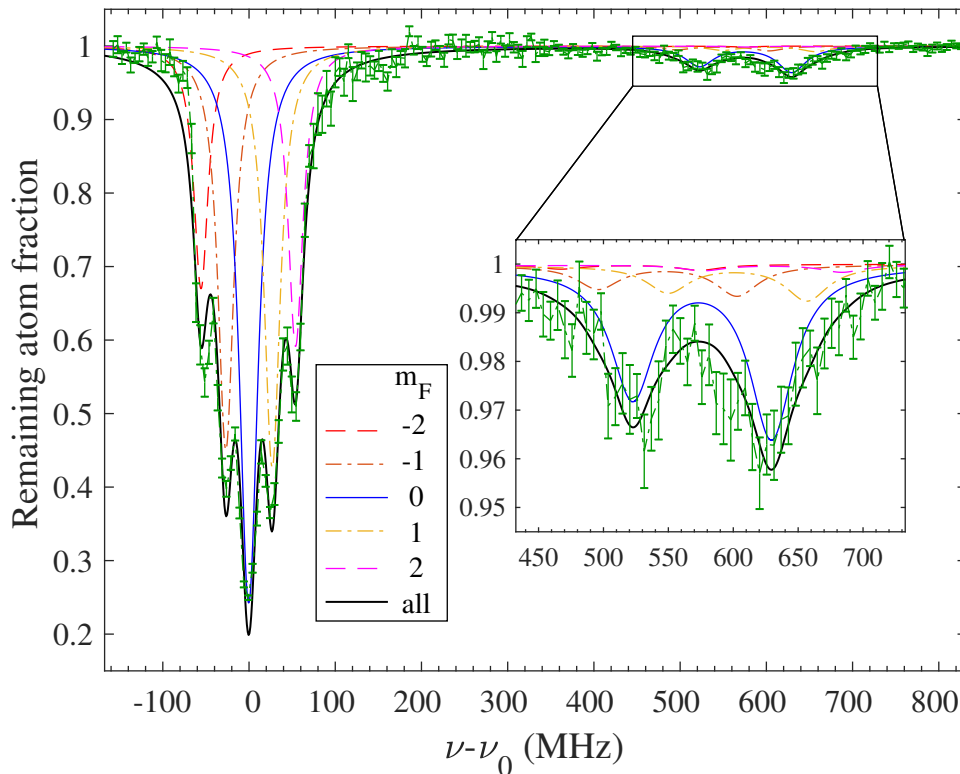
Figure 5.4: REMPI spectrum for mixed samples. REMPI spectrum for an initial cloud of atoms prepared in a mix of m_f quantum numbers at a magnetic field $B = 37$ G. The strong multi-line signal at $\nu - \nu_0 \approx 0$ corresponds to photoassociation. Using Eq. (5.1) it is decomposed into the different m_F components for atom pairs. The inset is a zoom into the $v = -2, R = 0$ and $v = -2, R = 2$ molecular signals. Here, the dashed and solid lines correspond to calculations for the individual molecular m_F populations which are formed in three-body recombination. The black solid line is the sum of these populations.

5.6 Conclusion

In conclusion, we have carried out state-to-state measurements for three-body recombination with neutral ^{87}Rb atoms in the regime of non-resonant two-particle interactions. We have demonstrated spectroscopic resolution of the m_F magnetic quantum states of the product molecules, in addition to the previously resolved vibrational, rotational, hyperfine degrees of freedom. Our studies suggest the propensity rule that the m_F quantum number is conserved when forming weakly-bound Rb$_2$ molecules via three-body recombination

of cold ^{87}Rb atoms.

For the future, we plan to probe more deeply bound molecular states in order to investigate whether this and the previously found propensity rules change, as indicated by our earlier work [12]. From such experiments, we can possibly gain information on how much the short range details of the interaction potentials influence the product distribution. Furthermore, it will be interesting to test whether the propensity rules found for ^{87}Rb break down for other atomic species. ^{87}Rb is special since its triplet and singlet scattering lengths are almost identical. Finally, we plan to further extend the detection method to also resolve the magnetic quantum numbers m_R of molecular mechanical rotation, as this would complete the experimental method for determining all internal quantum numbers of the molecule for the case that $\vec{R}$ and $\vec{F}$ are decoupled.

5.7   Introduction

The state-to-state experiments in Chapters 4 and 5 were using a REMPI detection scheme with a spin singlet intermediate level ($A\,^1\Sigma_u^+$ v$'=66$). Hence, pure triplet molecules could not be detected. Therefore, we now investigate the product molecules of the three-body recombination with an excited triplet potential as intermediate step. Due to selection rules, only product molecules with electron spin triplet character in the mixed $X\,^1\Sigma_g^+$-$a\,^3\Sigma_u^+$ electronic ground state complex can be excited to such an intermediate state. This allows us in principle to measure the triplet character of the three-body recombination product molecules of $f=1$, $m_f=-1$ atomic samples. In addition, we now are able to investigate $f=2$, $m_f=2$ atomic samples. If the magnetic quantum number of the scattering channel is conserved like for $f=1$ atomic samples (Ch. 5), there are no three-body recombination product molecules with singlet character, i.e. $F=4$, $m_F=4$ molecules are pure triplet molecules.

Starting from the mixed $X\,^1\Sigma_g^+$-$a\,^3\Sigma_u^+$ electronic ground state complex the product molecule is excited into the $c\,^3\Sigma_g^+$ potential and subsequently ionized. Our method is a two-color (1,2) REMPI (Resonance Enhanced Multi Photon Ionization), see Fig. 5.5. By using the $c\,^3\Sigma_g^+$ v$'=0$ intermediate state no energetically lower lying excited triplet states with gerade symmetry are available[6].

---

[6] The mixed $A\,^1\Sigma_u^+$-$b\,^3\Pi_u$ potential complex exists energetically below the used intermediate state, but due to selection rules the $b\,^3\Pi_u$ is not accessible from the mixed $X\,^1\Sigma_g^+$-$a\,^3\Sigma_u^+$ electronic ground state complex.
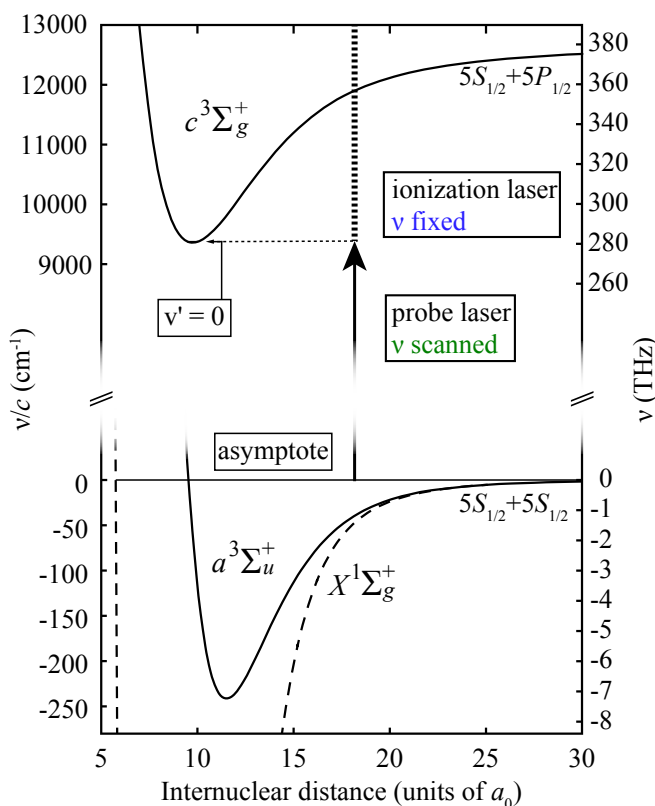
Figure 5.5: Scheme of the two-color (1,2) REMPI path for investigation of triplet molecules. Shown is the lower part of the relevant potential energy curves of Rb$_2$ together with the utilized lasers. The probe laser is used for the first resonant transition towards the $c\,^3\Sigma_g^+$ $v' = 0$ intermediate states. The probe laser frequency is scanned to generate a spectrum. From an intermediate state, the molecule is photoionized by the ionization laser i.e. the dipole trap laser in an off-resonant two-photon step.

Working with states of the $c\,^3\Sigma_g^+$ potential makes the interpretation of the measurements more difficult than when we worked with the $A\,^1\Sigma_u^+$ $v' = 66$ intermediate states as discussed in the Chapters 4 and 5, because the level structure of the $c\,^3\Sigma_g^+$ is much more complicated than for the $A\,^1\Sigma_u^+$ potential. The effective spin-spin interaction gives rise to a splitting of vibrational levels into 0_g^- and 1_g components and there is also substantial splitting due to the hyperfine interaction [43]. However, this also opens up new possibilities for determining the quantum numbers of molecular products after three-body recombination.

In the following sections, I present an analysis of preliminary data I took. However, in order to verify some of the results, additional measurements need to be carried out in future.

Extending our studies based on the present work, will enable us to obtain a conclusive understanding of the triplet molecule data.

First, I will explain the basic framework and the experimental parameters for the shown measurements (see Sec. 5.8). The first measurements presented, give an overview of the visible signals (see Sec. 5.9). After this, the magnetic substates of the product molecules are investigated (see Sec. 5.10). The chapter will be completed with a discussion of ion production rates (see Sec. 5.11).

5.8   General information

5.8.1   Notation

Before starting with the presentation and interpretation of the data, I want to recall the basic notation first. f is the quantum number of the total angular momentum of the atom $\vec{f} = \vec{i} + \vec{l} + \vec{s}$, $\vec{l}$ is the electronic total orbital angular momentum, $\vec{s}$ is the total electronic spin and $\vec{i}$ is the nuclear spin. m_f is the projection of $\vec{f}$ on the quantization axis (magnetic substate).

The molecular quantities are represented analogously by capital letters F, I, L, S, and m_F. For the molecular states additional quantum numbers are J, the quantum number of the total angular momentum $\vec{J} = \vec{R} + \vec{L} + \vec{S}$ with $\vec{R}$ being the rotational angular momentum. $\vec{F_{\text{tot}}} = \vec{J} + \vec{I} = \vec{R} + \vec{F}$ is the total angular momentum of the molecule including rotation.

The vibrational quantum number v in the $X\,^1\Sigma_g^+$-$a\,^3\Sigma_u^+$ potential is counted towards lower (more negative) numbers starting from the most-weakly bound state v=-1, which is the energetically closest one with respect to the $5s + 5s$ atomic asymptote. The quantum numbers of the $c\,^3\Sigma_g^+$ states carry a prime $'$. They are therefore F', I', J', F'_{tot}, ..., whereby v$'$ is counted upwards to more positive values starting from $v' = 0$ for the vibrational ground state.

Since the spectra presented in the following are dense, I introduce a new notation. Transitions of X-a states to certain intermediate states are typically given in the form of '(a number which identifies the intermediate state, v in the X-a potential, R in the X-a potential)'. Numbers that are zero are typically not given and multiple states are denoted with '[...]'.

For example: (1,-2,4), is the transition from the X-a state v=-2 $R = 4$ to an intermediate

state, which we identified previously as "line 1" in a photoassociation spectrum; (2,[-3,-4]), are the transitions from the *X-a* states v=-3 and v=-4 both with $R = 0$ to an intermediate state which we identified previously as "line 2" in a photoassociation spectrum.

5.8.2   Experimental parameters

We initially prepare an atom cloud in the hyperfine state $f = 1$ $m_f = -1$ (notation see Sec. 5.8.1) of about $4.5 \cdot 10^6$ atoms, with a peak atom density of $9 \times 10^{13}\,\text{cm}^{-3}$. In case of the hyperfine state $f = 2$, $m_f = 2$ we prepare atomic samples of about $3 \cdot 10^6$ atoms, with a peak atom density of $5 \times 10^{13}\,\text{cm}^{-3}$.

The measurements are typically performed at a magnetic field of 4.5 G. The three-body recombination coefficient is by a factor of two larger for $f = 2$, $m_f = 2$ atoms as compared to $f = 1$, $m_f = -1$ atoms [30]. For the used atom clouds this leads to about 40 % atom loss per second due to three-body recombination of an $f = 2$ atomic sample. The interaction time typically used is about 600 ms (1.1 s) for $f = 1$ ($f = 2$) atoms, respectively. Both interaction times are including 100 ms in which the probe laser is turned off, but ions are still located in the atom cloud. This is done for these measurements to have enough time to ramp the magnetic field back to 4.5 G for absorption imaging (also in case no different magnetic field was applied). We typically use ion detection scheme I with the given parameters. For ion detection scheme II the given atom cloud parameters are used for the production cloud. Both schemata are described in more detail in Section 4.2.5.

The following ionization laser frequencies are typically used for the state-to-state measurements. For $f = 1$ atoms the used ionization laser frequency is,

$$v_{ion:f=1} = 281\,649.723\,\text{GHz}.$$

For $f = 2$ atoms

$$v_{ion:f=2} = 281\,649.112\,\text{GHz}$$

is used. For these frequencies, the ionization efficiency is very sensitive on the MHz level of ionization laser frequency. In Section S5.13.1, I will talk about some problems for finding a good ionization laser frequency and present the experimental data to extract those ionization laser frequencies.

5.8.3 Theoretical transition frequencies

It is crucial for the evaluation of the measurements to know the precise frequency positions of the investigated transitions. The level structure of the $X\,^1\Sigma_g^+$- $a\,^3\Sigma_u^+$ complex and the corresponding binding energies E_b (at zero magnetic field) of the product molecules, are precisely known from measurements and coupled-channel calculations [42, 44, 64].

The initially prepared atomic sample has f and m_f. The used X-a states have $F = f + f$ with $m_F = m_{f_a} + m_{f_b}$ and a nuclear spin $I = 3$. As in Chapter 4 only X-a states of positive parity are discussed.

For small magnetic fields, the energy of the respective $5s + 5s$, $(f, m_f) + (f, m_f)$ atomic asymptote can be calculated using a linear Zeeman energy shift i.e. the respective state is shifted by a linear Zeeman splitting of the form

$$E_Z(B) = E_b + \mu_B \cdot g_f \cdot (m_{f_a} + m_{f_b}) \cdot B = E_b + \mu_B \cdot g_f \cdot m_F \cdot B.$$

$\mu_B = h \cdot 1.4\,\text{MHz/G}$ is the Bohr magneton, h is Planck's constant. The g_f-factor has a value of $g_f = -1/2$ ($g_f = 1/2$) for a ^{87}Rb ground state atom in the $f = 1$ ($f = 2$) hyperfine state, respectively (see Ch. 5).

The term frequencies of intermediate states are given relative to the respective $(f, m_f) + (f, m_f)$ asymptote of the ground state $5s + 5s$ dissociation threshold. Calculations of these term frequencies are carried out by using our simple model as presented in [43, 65]. These model calculations include the magnetic field dependence of the intermediate state. The calculations are utilized also to estimate the rotational composition of the intermediate states, as the rotation is not generally a good quantum number. The calculated photoassociation transitions have an offset. This offset is chosen to match the frequency of the first calculated photoassociation line with the first measured photoassociation signal for a magnetic field of 4.5 G. For $f = 1\ m_f = -1$ ($f = 2\ m_f = 2$) atomic samples the calculated photoassociation transition to the $I' = 3$, $\langle J' \rangle = 1.2$, $F'_{\text{tot}} = 2$ ($I' = 3$, $\langle J' \rangle = 1.3$, $F'_{\text{tot}} = 3$) state is set to be at 281071.265 GHz (281058.285 GHz), respectively (see also Sec. S5.13.2). From the intermediate state calculations extracted information is used to determine the possible transitions from the X-a states.

5.9 Analyzing the measured spectra for product molecule signals

In this section, we are investigating the optical transitions of the three-body recombination product molecules to the $c\,^3\Sigma_g^+$ potential. We are comparing the calculated transition frequencies with the measured spectra. This helps us to understand, which product molecule states are observable and are therefore populated by the three-body recombination. We consider the intermediate states of the $v' = 0$ vibrational state of the $c\,^3\Sigma_g^+$ potential. These states are identified in the Section S5.13.2. With the knowledge of these photoassociation frequencies, we are able to calculate the expected transition frequencies of the product molecules. All error bars in the given figures represent the standard deviations of the mean values.

5.9.1 Investigating product molecules of $f = 1$ atomic samples

The three-body recombination product molecules of the $f = 1$, $m_f = -1$ initial atomic quantum state have been probed in Chapter 4 via their singlet component (see Fig. 5.5). Here, we probe the triplet component of the product molecules by exciting them to the $v' = 0$ vibrational state of the $c\,^3\Sigma_g^+$ potential ((1,2) REMPI). Since most of the probed molecular levels have mixed singlet and triplet character, the spectra of the three-body recombination signals are expected to give similar results.

For the evaluation of transitions starting from X-a molecules a selected set of photoassociation data is used. Table 5.1 shows these data (see also Sec. S5.13.2). We present the measured frequencies together with the quantum numbers of the addressed intermediate states. For a simple denotation, we have labeled the given photoassociation transitions by counting them upwards in their order from low frequencies to higher frequencies.

Measurements with the 1_g manifold as intermediate level

Figure 5.6, shows the spectrum of the $c\,^3\Sigma_g^+$ $v' = 0$ 1_g excited states. The blue vertical lines indicate the photoassociation transitions of the Table 5.1. Knowing the term frequencies for molecular levels within the X-a state (see Sec. 5.8.3), we can calculate the

Table 5.1: Selected photoassociation lines. Shown are the transition frequencies ($\nu_{\text{offset}} = 281\,\text{THz}$) and quantum numbers of the excited state, as well as the identification number (Nr.), which is attributed to each excited level.

$\nu_{\text{meas}} - \nu_{\text{offset}}$ (GHz)	I'	$\langle J' \rangle$	F'_{tot}	Nr.
1_g				
71.265	3	1.2	2.0	(1)
71.968	3	1.3	3.0	(2)
73.350	3	2.0	1.0	(3)
73.916	3	2.0	2.0	(4)
74.826	1	1.9	2.0	(5)
75.013	1	2.1	3.0	(6)
0_g^-				
111.745	3	0.0	3.0	(1)
114.297	3	2.0	5.0	(2)
114.506	3	2.0	3.0	(3)
114.621	3	2.0	2.0	(4)
114.709	3	2.0	1.0	(5)

transition frequency from a X-a state to a given intermediate state. The 1_g triplet manifold has a mixed rotational character in the investigated range (see Sec. S5.13.2). Utilizing the simulations for the intermediate states an estimate of the relevant rotational contributions has been made. The predictions for the product molecule transitions are given by the red vertical lines.

The strong signals of three-body recombination product molecules i.e. the (1,-2,[2,0]) transitions, are overlapping[7] with the photoassociation peak PA (2) as seen around 71.9 GHz in Figure 5.6 (for notation, see Sec. 5.8.1). The same product molecule states measured via the PA (2) intermediate state i.e. (2,-2,[2,0]) at about 72.6 GHz show very strong signals and are clearly visible. We therefore assume that the ionization efficiency for the excited state addressed in PA (2) is good[8].

The (1,-2,4) transition and the (2,-2,4) transition could be the small bumps visible at 71.5 GHz and at 72.2 GHz, respectively. These transitions are in principle possible for

---

[7] Due to the denser level structure of the excited triplet state, the probability for an overlap of photoassociation signals and three-body recombination signals is increased, as compared to the singlet measurements.

[8] Already, the signal of PA (2) is indicating a large ion number, because the signal is much broader as the other photoassociation signals. For large ion production rates the peak heights are compressed and the bases of the signals are broadened. For more information about the strong non-linearity of ion detection scheme I see additional content in Sec. 4.2.5.

the two mixed J' intermediate states, but the excitation probability can be strongly suppressed because the rotational overlap can be small. So far the triplet measurements are in good agreement with the singlet measurements.
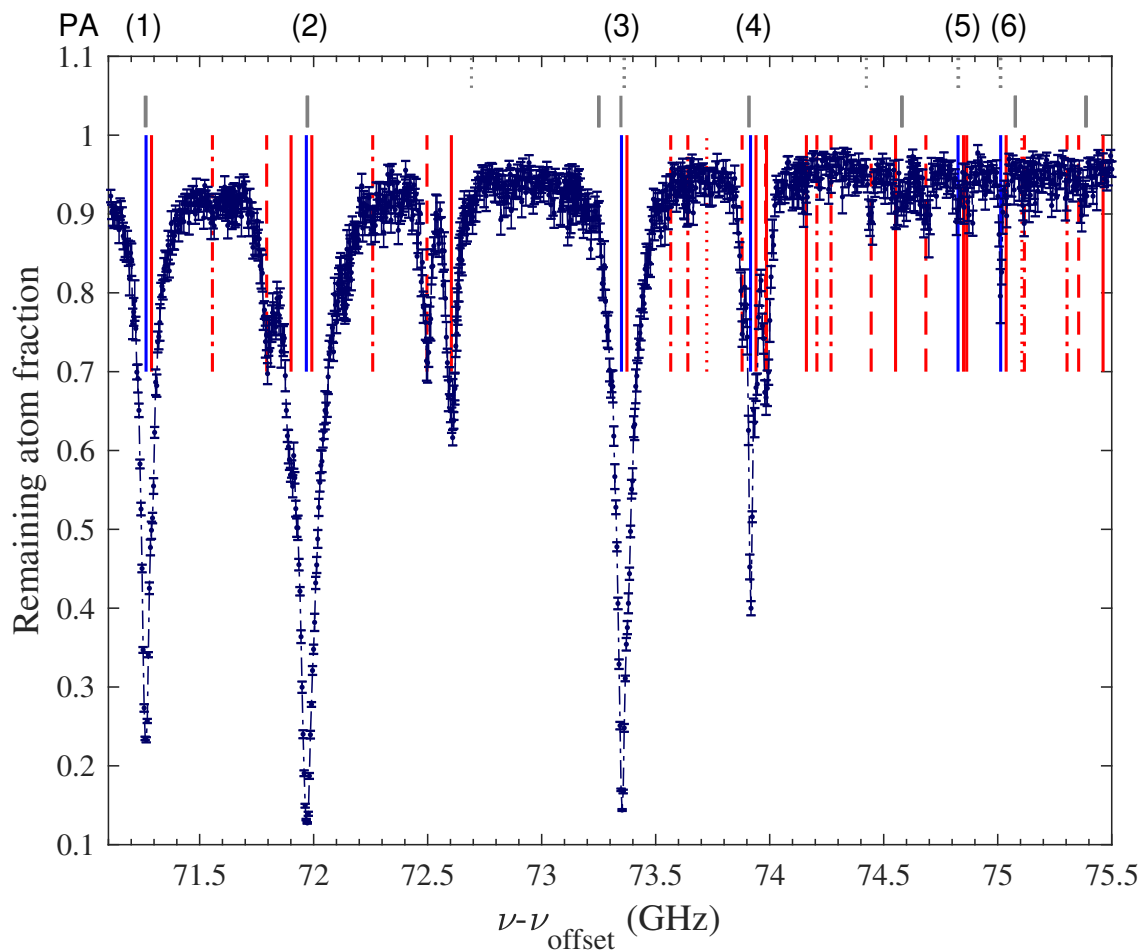
Figure 5.6: (1,2) REMPI spectrum for $f = 1, m_f = -1$ atoms using the $c^3\Sigma_g^+$ v$' = 0$ 1_g states as intermediate levels. The remaining atom fraction is plotted versus the probe laser frequency (with $\nu_{\text{offset}} = 281$ THz). At the top of the figure the calculated intermediate state frequency positions (see Sec. S5.13.2) are given as gray vertical lines ($I' = 3$ solid, $I' = 1$ dotted). The blue vertical lines indicate the positions of the selected photoassociation (PA) transitions given in Table 5.1 (the photoassociation line number is given at the top of the figure). The red vertical lines show the respective transitions involving X-a molecular states, the line style indicates the rotational state R of the initially formed molecule: solid $R = 0$, dashed $R = 2$, dash-dotted $R = 4$, and dotted $R = 6$. The vibrational state (v) is not indicated (for the vibrational and rotational ladder see Fig. 4.1B). The more densely packed region from PA (3) will be presented in more detail in Figure 5.7. Each data point represents the mean value of ten repetitions of the experiment and is measured with 3 mW probe laser power.

To be able to identify weak signals the resolution of the overview is not sufficient. Beginning from PA (3) Figure 5.7 shows a zoom into the overview. As the spectrum becomes more densely packed, the theoretically predicted X-a state positions of the three-body recombination product molecules are marked with their respective transition numbers. In this smaller area the weakest X-a state transitions ([3,4],-1) can be seen as small shoulders on the photoassociation signals (although the (3,-1) shoulder could also be coming from the $I' = 1$ photoassociation (gray dotted)).

The (3,-2,4) transition at about 73.65 GHz can be seen as a small bump. This is especially interesting, as we have already seen a small signal for the (1,-2,4) transition and for the (2,-2,4) transition. By being able to correlate the signals of product molecules in the same X-a states for various intermediate states it is possible to trust even very weak signals that could also be mistaken as noise, as it is unlikely to see matching noise at various positions. The (3,-2,[2,0]) transitions are well visible. Interestingly, it is still possible to observe the (4,-2,[2,0]) signals at about 74.45 GHz, of the weak PA (4). Besides the (4,-2) transition a small signal is visible (74.55 GHz). It could be the photoassociation transition (gray solid).

The next signal is the (2,-3,2) transition at about 74.7 GHz. This is the first signal of a v=-3 vibrational state of the three-body recombination product molecules we observe in this triplet measurement. The visibility of this signal further solidifies the assumption of a good ionization efficiency of the PA (2) intermediate state. Its rotational ground state transition (2,-3) cannot be seen clearly in the vicinity of other lines (74.9 GHz). The weak signals for these product molecule states are expected from the singlet measurements, where the v$= -3$, $R = 2$ state is also more highly populated as its rotational ground state (see Fig. 4.4). In this singlet measurement the product state v$= -3$, $R = 6$ is also populated, yet we do not see a good signal for the (2,-3,6) transition (73.7 GHz). This could be explained with a low excitation probability for the v$= -3$, $R = 6$ state into the low $\langle J' \rangle \approx 1.3$ intermediate state. Further measurements e.g. with a higher probe laser power are necessary to eventually show a better signal. Overall it can be stated that the observable product molecule states agree with the observed states in the singlet measurements (see Ch. 4).
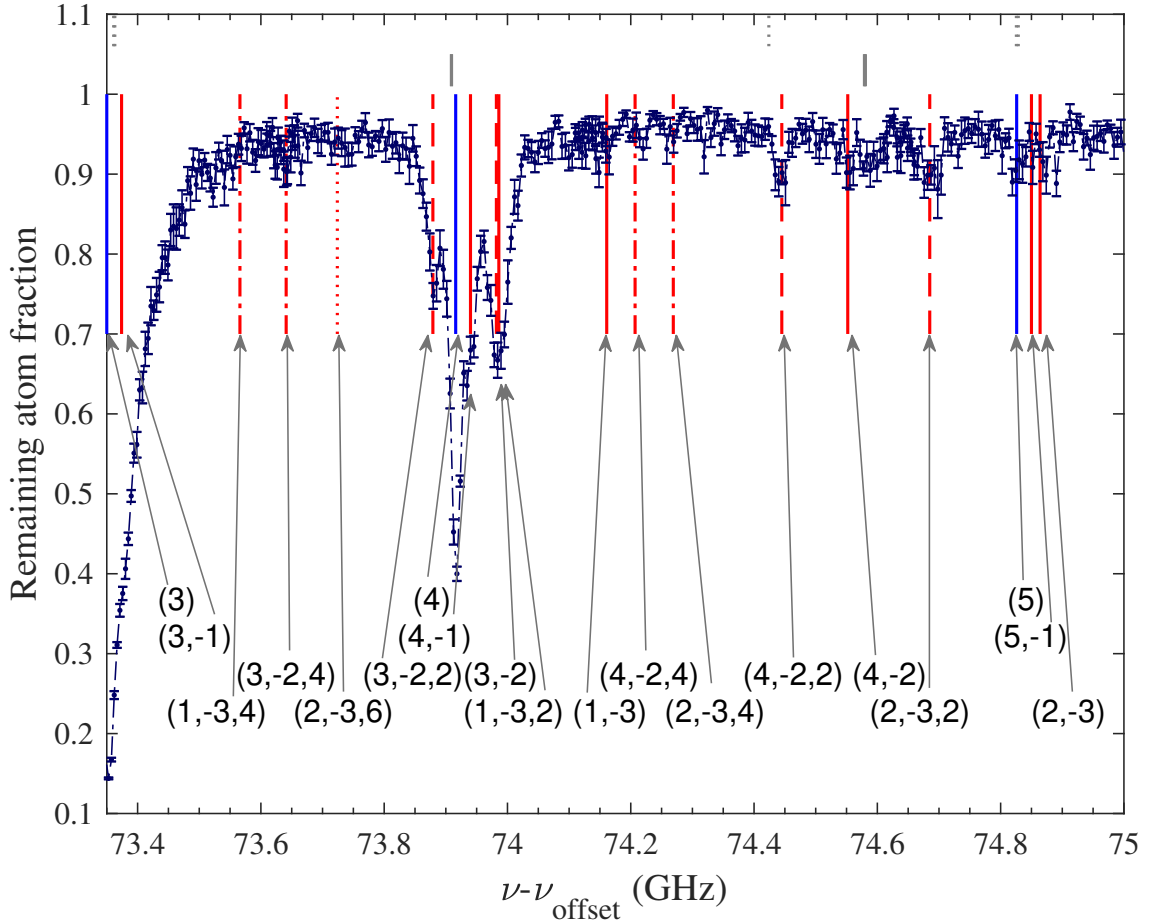
Figure 5.7: Zoom into the frequency region from about 73.3 **GHz to** 75 **GHz of Figure** 5.6.
The numbers (PA Nr., v, *R*) indicate the assigned transitions, where only non-zero quantum numbers are listed. The rows of the list are ordered by the vibrational states.

Measurements with the 0_g^- structure as intermediate level

After we have discussed the signals observed for the $c\,{}^3\Sigma_g^+\;v'=0\;1_g$ manifold as an intermediate level, we can continue with the $c\,{}^3\Sigma_g^+\;v'=0\;0_g^-$ manifold. This measurement is shown in Figure 5.8. The photoassociation number indices of the 0_g^- manifold start again from one. In Table 5.1, the used intermediate states can be found. In this manifold J' is a quite good quantum number [43]. The (1,-2,[2,0]) transitions at about 112.3 GHz show a good signal. The (1,-2,4) transition at about 112 GHz does not show a signal. Since, J' is a good quantum number it is expected that we cannot observe $R=4$ signals for the used $J'=0$ intermediate state.

The three photoassociation signals at about 114.5 GHz ([3,4,5]) have $J' = 2$. Since the structure is rather closely packed, the product molecules signals for the v$= -2$ rotational states are overlapping with each other. Therefore, it is difficult to estimate the product molecule signal strength.

In the measured range of the 0_g^- manifold (Fig. 5.8), we can observe a few unidentified signals, at about 113.25 GHz, 113.9 GHz, 115.5 GHz or 116 GHz. A possible source is discussed exemplarily for $f = 2$, $m_f = 2$ signals in the Sections S5.13.1 and S5.13.3.
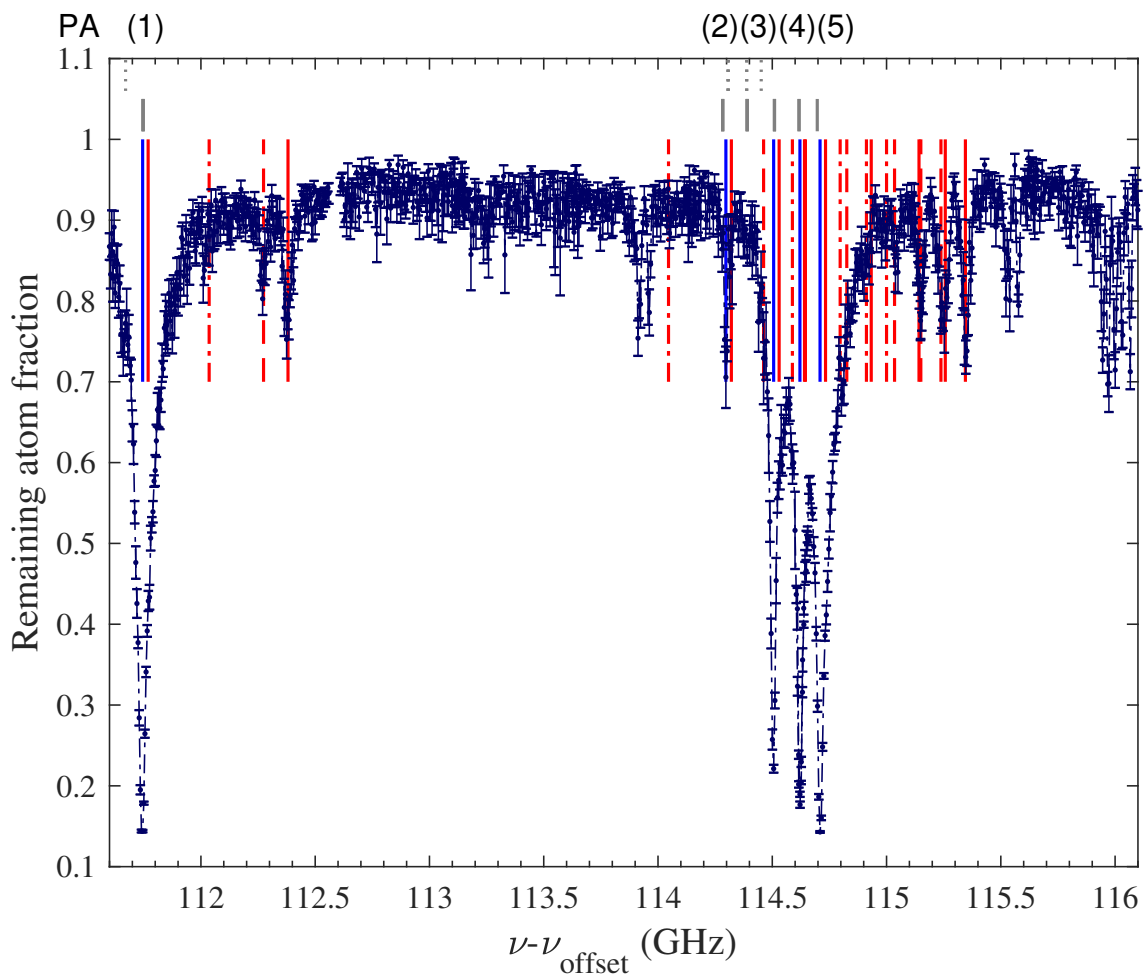
Figure 5.8: (1,2) REMPI spectrum for $f = 1$, $m_f = -1$ atoms using the $c^3\Sigma_g^+$ v$' = 0$ 0_g^- states as intermediate levels. The remaining atom fraction is plotted versus the probe laser frequency with the same notation as in Figure 5.6. The blue vertical lines indicate the position of the photoassociation transitions (PA) given in Table 5.1 (the photoassociation line number is given at the top of the figure). Each data point represents the mean value of ten repetitions of the experiment and the used probe laser power is 11 mW.

5.9.2 Investigating product molecules of $f = 2$ atomic samples

In this section, we are presenting state-to-state measurements via the $c\,^3\Sigma_g^+$ v$' = 0$ manifold ((1,2) REMPI, see Sec. 5.7). The spin stretched $f = 2$, $m_f = 2$ state of the used atomic samples, only allows for (two-body) collisions in a triplet channel. We are investigating if this will also change the population distribution of the three-body recombination product molecules compared to $f = 1$ atomic samples.

The measured selected intermediate state frequencies with the quantum numbers extracted from simulations (see Sec. S5.13.2) and the associated photoassociation number can be found in Table 5.2. These frequencies[9] are used for the calculations of the expected transition frequencies of the product molecules X-a states and their identification. The molecular binding energies of the $X\,^1\Sigma_g^+$-$a\,^3\Sigma_u^+$ ground state potential with $f = 2 + f = 2$ $5s + 5s$ asymptote are different[10] from the ones of the $f = 1 + f = 1$ $5s + 5s$ asymptote [64].

Measurements with the 1_g manifold as intermediate level

Figure 5.9 shows the measured $c\,^3\Sigma_g^+$ v$' = 0$ 1_g spectrum with the expected transitions marked as vertical lines. The data are measured for an interaction time of 1.1 s with ion detection scheme I. The used probe laser power is 23 mW.

In general the measurement looks more noisy than the $f = 1$ measurements. It has been taken with about twice the interaction time of the $f = 1$ measurement (see Sec. 5.8.2), background ions, although lower in number, have a stronger impact on the signal leading to a broader base line.

Starting from the first photoassociation line on the left PA (1) some observations can be made in the less busy part of the spectrum. The complete v$= -2$ rotational manifold is expected to be visible (from PA (1) to about 59 GHz). Good signals can be found for the (1,-2,[2,0]) transition at about 58.8 GHz (Fig. 5.9). Showing that these X-a states are populated by product molecules.

The next photoassociation line PA (2) is weaker as PA (1). Here again, the complete v$= -2$ rotational manifold is expected to be visible (around 60 GHz, the dotted line in between is the (1,-3,6) transition). A slightly smaller atom loss, the much narrower

---

[9] The rotational contributions of the rotationally mixed intermediate states have also been extracted from the simulations.

[10] The investigated X-a states with identical v and R but of different $f + f$ asymptotes are shifted by $<$ 10 MHz relative to the respective asymptotes.

linewidth, and the barely visible (2,-2,[2,0]) transitions at about 60.2 GHz, indicate a much weaker ion production rate.

Table 5.2: Selected photoassociation lines. Shown are the transition frequencies ($v_{offset} = 281$ THz) and quantum numbers of the excited state, as well as the identification number (Nr.), which is attributed to each excited level.

$v_{meas} - v_{offset}$ (GHz)	I'	$\langle J' \rangle$	F'_{tot}	Nr.
1_g				
58.285	3	1.3	3.0	(1)
59.584	3	1.6	4.0	(2)
60.897	3	2.0	3.0	(3)
61.403	3	2.3	5.0	(4)
61.689	3	2.0	4.0	(5)
63.370	3	3.0	3.0	(6)
63.726	3	2.9	4.0	(7)
63.955	3	3.0	5.0	(8)
66.575	3	3.9	3.0	(9)
66.928	3	3.9	4.0	(10)
67.220	3	3.9	5.0	(11)
0_g^-				
98.065	3	0.0	3.0	(1)
100.611	3	2.0	5.0	(2)
100.709	3	2.0	4.0	(3)
100.832	3	2.0	3.0	(4)

The $\langle J' \rangle \approx 2$ line triplet PA ([3,4,5]) at about 61.5 GHz is very strong again, but only the (5,-2,[2,0]) transitions of the line triplet are well visible. The other lines are overlapping with other transitions. For $R > 2$ product molecule X-a states no clear signals are visible in the so far discussed range.
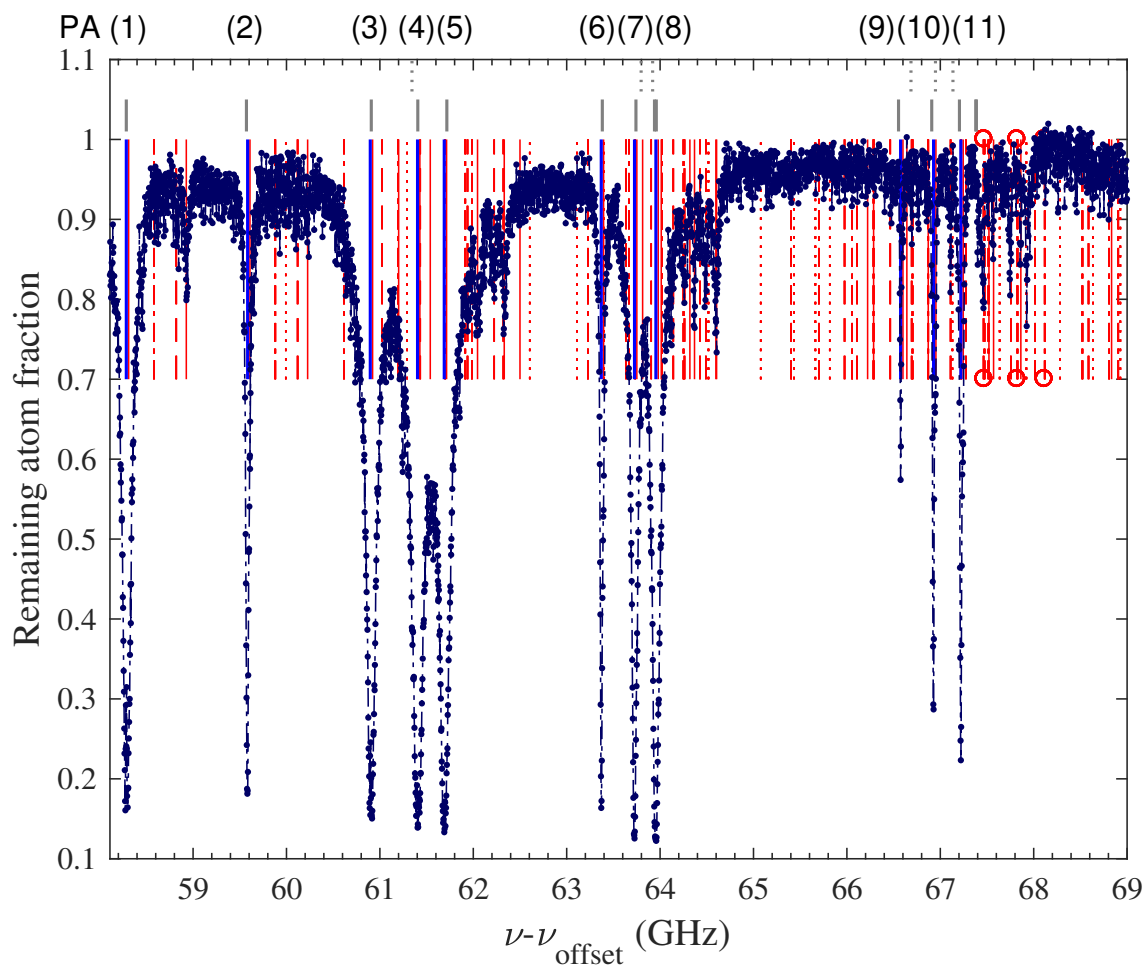
Figure 5.9: (1,2) REMPI spectrum for $f = 2$, $m_f = 2$ atoms using the $c^3\Sigma_g^+$ v' = 0 1_g states as intermediate levels. The remaining atom fraction is plotted versus the probe laser frequency with $\nu_{\text{offset}} = 281$ THz. At the top of the figure the calculated intermediate state frequency positions (see Sec. S5.13.2) are given as gray vertical lines ($I' = 3$ solid, $I' = 1$ dashed). The blue vertical lines indicate the positions of the selected photoassociation (PA) transitions given in Table 5.2 (the photoassociation line number is given at the top of the figure). The red vertical lines show the respective transitions from X-a molecules, the line style indicates the rotational state R of the initially formed molecule: solid $R = 0$, dashed $R = 2$ and, dash-dotted $R = 4$, dotted $R = 6$, and dash-dotted with a circle at the end $R = 8$. The vibrational state (v) is not indicated (for the vibrational and rotational ladder see Fig. 4.1B). Each data point represents the mean value of ten repetitions of the experiment. Error bars are not plotted for clarity, but are about ± 0.02 arb. unit. The following picture will show a zoom into a part of the displayed data (Fig. 5.10). More zoomed in figures can be found in Section S5.13.5.

Since the spectrum starts to become more densely packed, it will be zoomed in and exemplarily discussed in a smaller frequency range. The $\langle J' \rangle \approx 3$ line triplet PA ([6,7,8])

at about 63.5 GHz is shown in Figure 5.10. The figure already shows many theoretically predicted positions of more deeply bound vibrational (v=-3) and rotating states excited to the lower lying intermediate states PA ([1,...,5]). None of these transitions show a clear signal in the observed window.
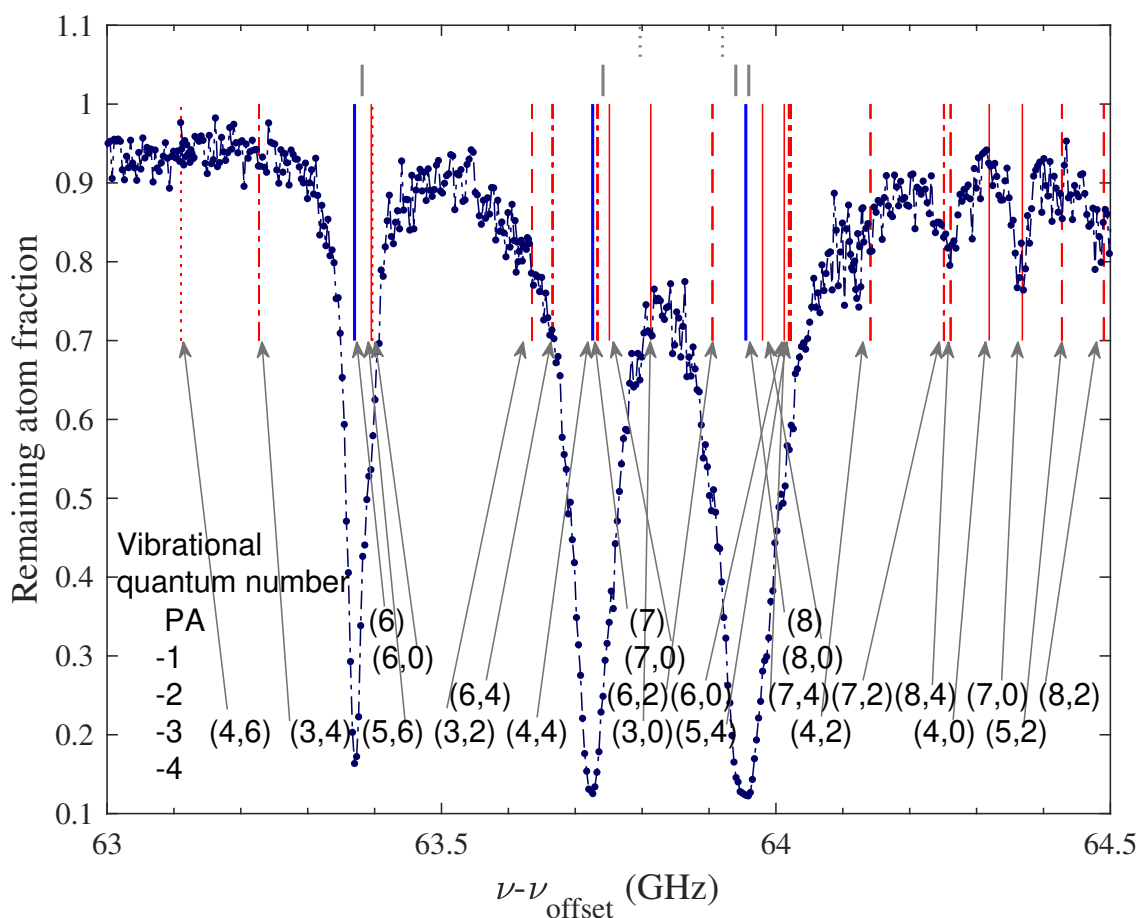
Figure 5.10: Zoom into the frequency region from about 63 GHz to 64.5 GHz **of Figure 5.9.** The arrows are labeled by (PA Nr., R). The arrows indicate the transitions marked with vertical lines. Due to the large number of states and limited space, the notation is changed here. The vibrational quantum number of the X-a state is indicated in the first column or if it is a photoassociation line the photoassociation number (PA).

The photoassociation PA (6) shows a nice shoulder (about 63.4 GHz). This shoulder is most likely the (6,-1) transition and therefore a signal of the most weakly bound state. Weak photoassociation signals are not broadened to a point where this signal is superim-

posed, similar to the effect explained in Sec. S5.13.4. The only definite product molecule signals observable are at frequencies where v$= -1, -2$ product molecule X-a states of the intermediate state triplet ([6,7,8]) are expected. The v$= -1$, $R = 0$ and v$= -2$, $R = 2, 0$ states of the by three-body recombination produced molecules are in general the only states that show a clear population (further discussion see Sec. S5.13.5). This is in contrast to the former measurements for the $f = 1$ $m_f = -1$ atomic samples, where also other three-body recombination product molecule X-a states have shown a clear population.
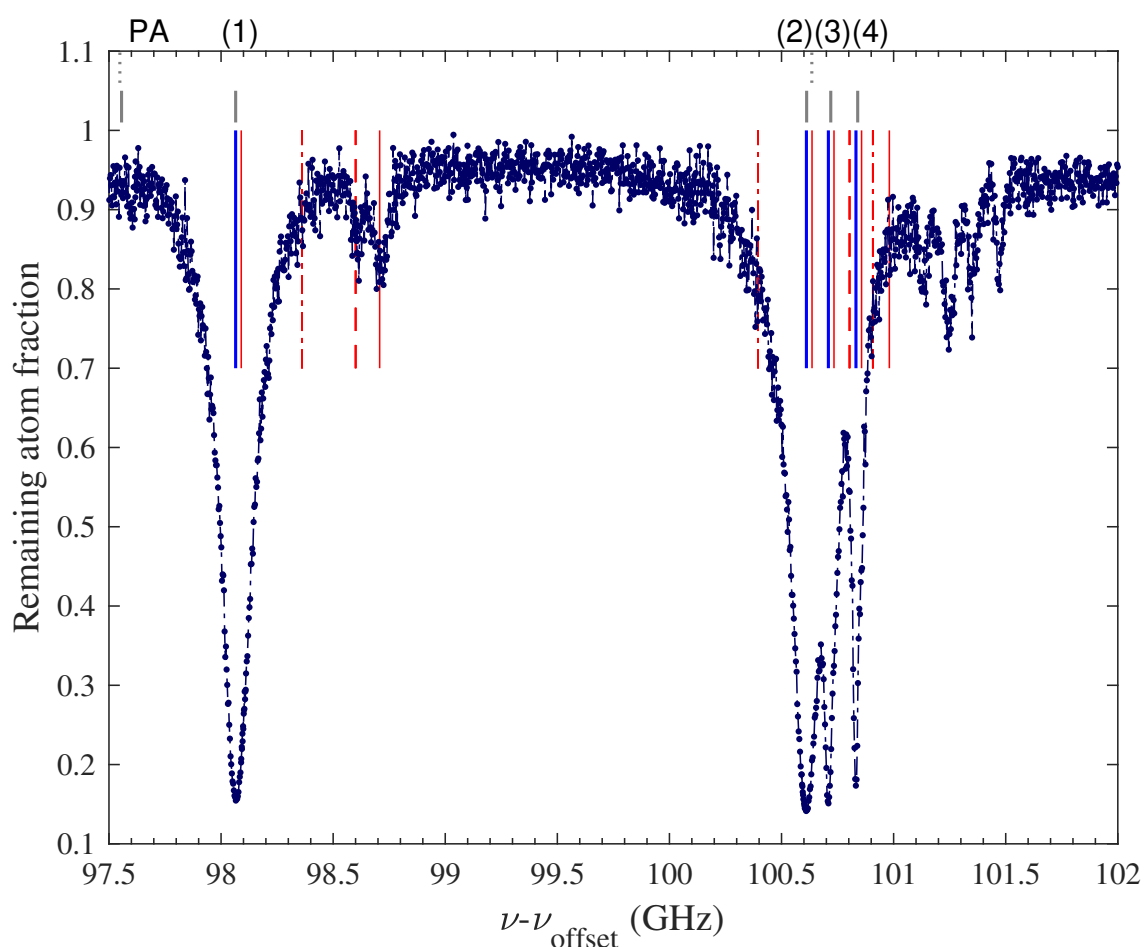
Figure 5.11: (1,2) REMPI spectrum for $f = 2$, $m_f = 2$ atoms using the $c\,^3\Sigma_g^+$ v$' = 0\ 0_g^-$ states as intermediate levels. The remaining atom fraction plotted versus the probe laser frequency, with the same notation as used in Figure 5.9. The blue vertical lines indicate the position of the photoassociation transitions (PA) given in Table 5.1 (the photoassociation line number is given at the top of the figure). Predictions for transitions of deeper bound X-a states to intermediate structures at lower frequencies are not displayed. Each data point represents the mean value of ten repetitions of the experiment. Error bars are not plotted for clarity, but are about ± 0.02 arb. unit.

Measurements with the 0_g^- manifold as intermediate level

The 0_g^- manifold measurement with theory lines is shown in Figure 5.11. The data are measured for an interaction time of $1.1\,\mathrm{s}$ with ion detection scheme I. The used probe laser power is $23\,\mathrm{mW}$.

This spectrum shows nice signals for the ([1,2,3,4],-2,[2,0]) transitions. Especially the (1,-2,[2,0]) transitions ($98.7\,\mathrm{GHz}$) are interesting. The (1,-2) transition shows a much broader signal than the (1,-2,2) transition. This could be possibly explained by a worse excitation probability of the $v = -2$, $R = 2$ state to the $J' = 0$ intermediate state PA (1), than the $v = -2$, $R = 0$ state. Such strongly varying excitation probabilities are problematic for determining the population distribution.

The $v = -1$ X-a state signal is in general not visible in this measurement since the probe laser power is too high and the signal is buried under the respective strong photoassociation signal. The spectrum will be discussed in more detail in Section 5.10.2 and Section 5.11.2. Some unidentified signals are observable, which are discussed in Section S5.13.3.

5.10 Magnetic field dependence of the spectra

In this section, we investigate three-body recombination product molecule spectra for different magnetic fields. This is done to resolve magnetic substate of the product molecules similar as in Chapter 5. All error bars in the given figures represent the standard deviations of the mean values.

5.10.1 Magnetic quantum number resolved measurements of $f = 1$ atomic samples

First, we will discuss REMPI spectra for a $f = 1$, $m_f = -1$ atomic sample. It was obtained using the intermediate states [2,3,4] within the $c^3\Sigma_g^+$ $v' = 0$ 0_g^- manifold (Tab. 5.1). For this intermediate state line triplet the Zeeman shift is rather small ($< 5\,\mathrm{MHz}$) for the magnetic fields applied here (see also [43]). For more information about the magnetic field calibration in our system see Section S5.13.6.
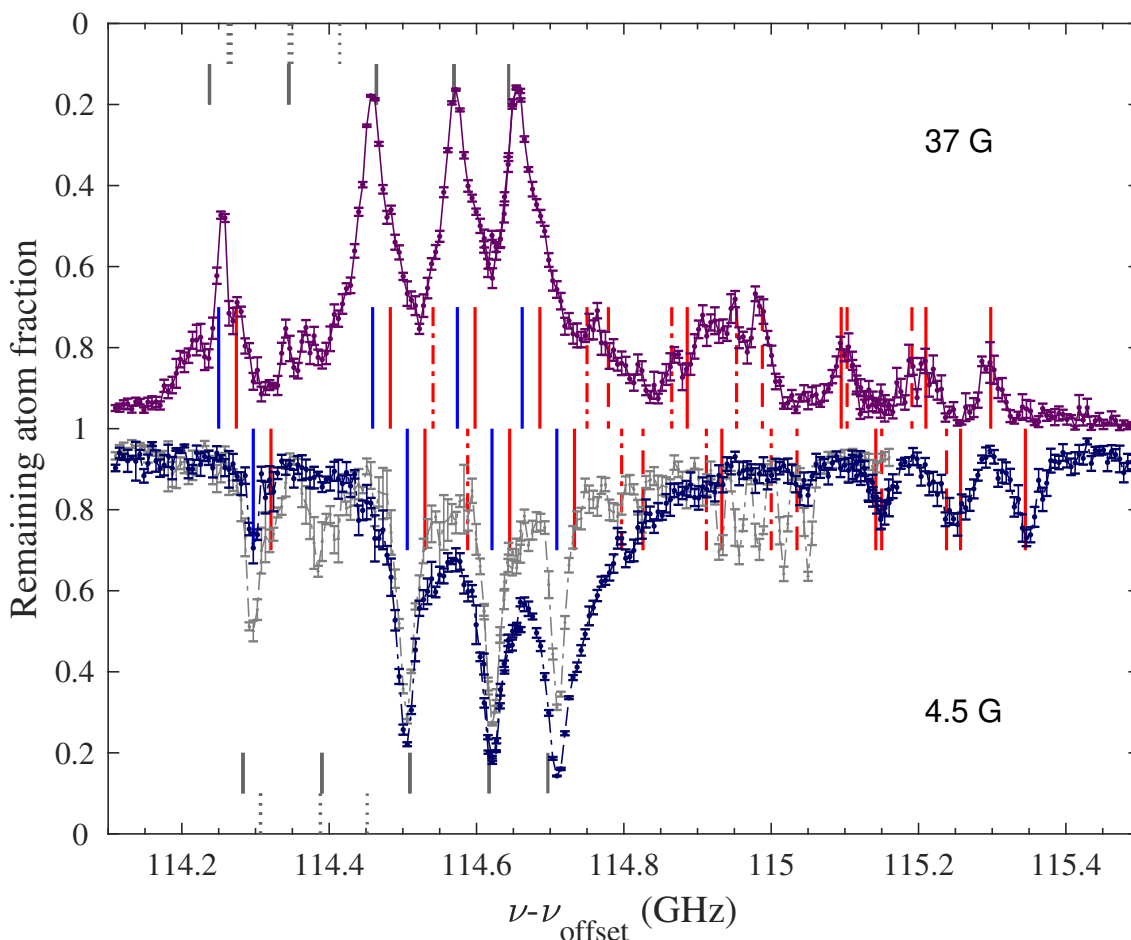
Figure 5.12: (1,2) REMPI spectra for two different magnetic fields of 4.5 G (lower part, blue and gray data) and 37 G (upper part, purple data) obtained using the intermediate states ([2,3,4]) of $c\,{}^3\Sigma_g^+$ **v′ = 0** 0_g^-**.** Shown is the remaining atom fraction of an atomic sample initially prepared in the $f = 1$, $m_f = -1$ state versus the probe laser frequency ($\nu_{\text{offset}} = 281$ THz). The used ionization laser frequency for the purple and the gray data is $\nu_{ion} = 281\,650.745$ GHz. The blue signal is measured with the standard ionization laser frequency of $\nu_{ion:f=1} = 281\,649.723$ GHz (see also Sec. 5.8.2). The blue vertical lines indicate the positions of the selected photoassociation (PA) transitions. The red vertical lines represent the predicted frequencies for transitions from X-a states, where the line style illustrates the rotational state R: solid $R = 0$, dashed $R = 2$, and dash-dotted $R = 4$. The blue and red vertical lines for the upper (37G) measurements are shifted by -47 MHz to account for the magnetic field induced shift. The gray lines at the bottom and top of the figure are simulated frequency positions for photoassociation transitions with $I = 3$ (solid) and $I = 1$ (dotted) for the respective magnetic field. The probe laser power was 11 mW. Each data point represents the mean value of ten repetitions of the experiment.

In Figure 5.12 three REMPI spectra for two different magnetic fields applied are shown. The blue data show the measurement results for the standard magnetic field of 4.5 G

used in our setup and an ionization laser frequency of $v_{ion:f=1} = 281\,649.723\,\text{GHz}$. This data is identical to the one presented in Figure 5.11. The purple data (see Fig. 5.12) are obtained for a magnetic field of 37 G using a different ionization laser frequency of $v_{ion} = 281\,650.745\,\text{GHz}$. The ionization laser frequency needed to be changed, as the ionization efficiency is strongly depending on the magnetic field for the here used parameters. This can be seen in the gray data set. It shows the data for the low magnetic field of 4.5 G, but for the ionization laser frequency of $v_{ion} = 281\,650.745\,\text{GHz}$. The signal strength of the photoassociations is decreased as compared to the blue data. For the ionization laser frequency of $v_{ion} = 281\,650.745\,\text{GHz}$ there are some unexpected peaks appearing in the spectrum e.g. at about 115 GHz (see Fig. 5.12). Nevertheless, the positions of the photoassociations lines PA ([2,3,4]) are not changed. This is important in order to compare the measurements for different magnetic fields obtained for the two different ionization laser frequencies (blue and purple data).

The blue and red vertical theory lines for 37 G are shifted by $-47\,\text{MHz}$ with respect to the theory lines at 4.5 G. As mentioned before the shift of the intermediate states is small. The gray vertical theory lines (simulations) agree very well with the blue vertical lines (selected PA transitions) (see Fig. 5.12). The magnetic field induced line shift is mainly given by the shift of the atomic $5s + 5s$ asymptote. Using a linear Zeeman shift for the asymptote results in an expected frequency shift with respect to 4.5 G of about $-46\,\text{MHz}$ for the $m_F = -2$, $F = 2$, $5s + 5s$ asymptote and the product molecules in the investigated v$= -1, -2$ X-a states (see Sec. 5.8.3). It is clearly visible that the signals of the photoassociations as well as the X-a state signals of molecules formed by three-body recombination follow this Zeeman shift. Therefore, we can state that the main proportion of product molecules is formed in $m_F = -2$, $F = 2$ states. This confirms the results of the singlet measurements, which reveal a conservation of the hyperfine and magnetic spin state in the three-body recombination (Ch. 5). For additional measurements connected to the $c\,^3\Sigma_g^+$ v$' = 0$ 1_g manifold see Section S5.13.7.

5.10.2 Magnetic quantum number resolved measurements of $f = 2$ atomic samples
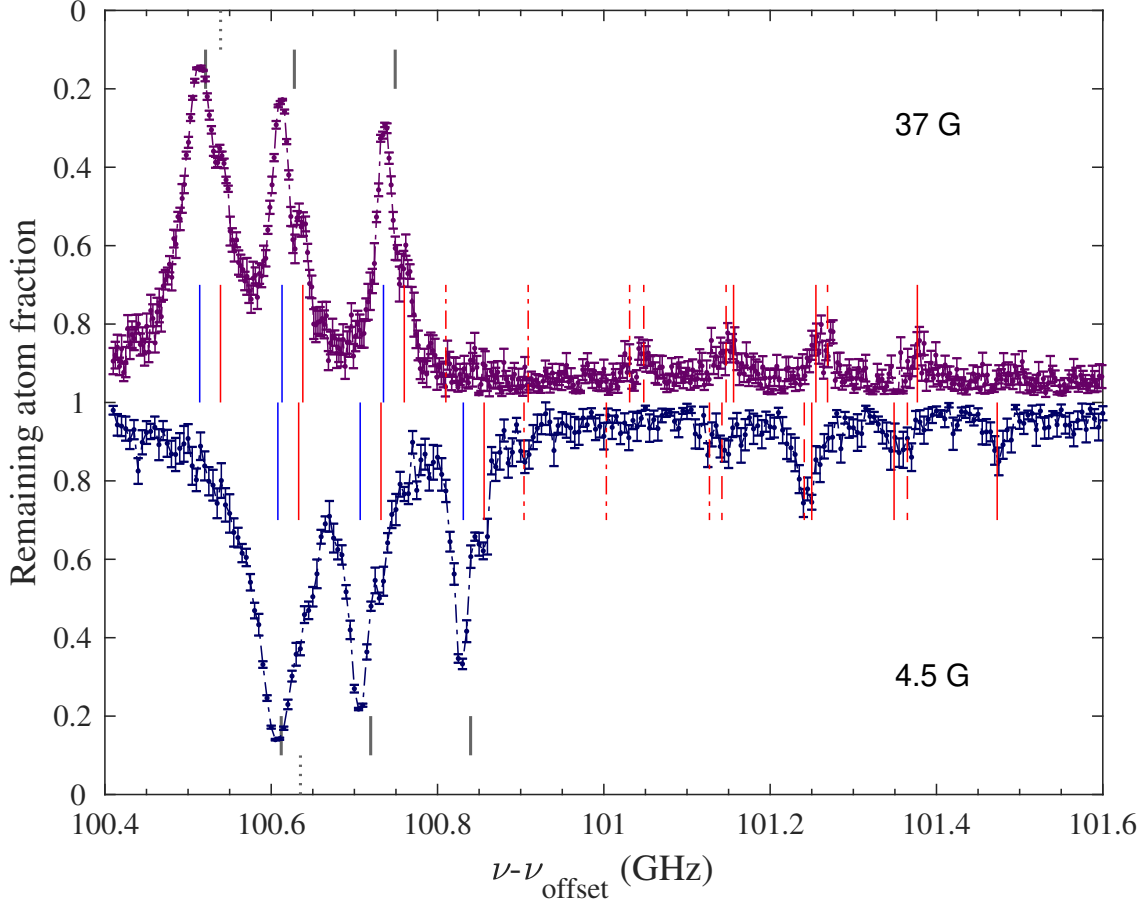
Figure 5.13: (1,2) REMPI spectra for two different magnetic fields of 4.5 G (lower part) and 37 G (upper part) obtained using the intermediate states ([2,3,4]) of $c^3\Sigma_g^+$ $v' = 0$ 0_g^-. Shown is the remaining atom fraction of an atomic sample initially prepared in the $f = 2$, $m_f = 2$ state versus the probe laser frequency ($\nu_{\text{offset}} = 281$ THz). The symbols lines and denotations are analogous to the ones of Figure 5.12. The standard ionization laser frequency of $\nu_{ion:f=2} = 281\,649.112$ GHz. was used for both measurements (see also 5.8.2). Blue and red vertical line positions of the 37 G measurement are shifted by -94 MHz with respect to the ones for 4.5 G. The used probe laser power is 3 mW. Each data point represents the mean value of ten repetitions of the experiment.

In this section we investigate REMPI spectra of $f = 2$, $m_f = 2$ atoms via the $c^3\Sigma_g^+$ $v' = 0$ 0_g^- manifold ([2,3,4]) intermediate states (see Tab. 5.2). These intermediate states have been chosen, since the Zeeman shift of the intermediate state is < 5 MHz. For an atomic sample of $f = 2$, $m_f = 2$ atoms the magnetic field induced shift of the relevant $5s + 5s$

asymtote is twice as large as for the $f = 1$, $m_f = -1$ atomic samples (see Sec. 5.8.3). Figure 5.13 shows the REMPI measurements for two different homogeneous magnetic fields carried out with $f = 2$ $m_f = 2$ atomic samples. Except for the applied homogeneous magnetic field, the used experimental parameters are given in Section 5.8.2. The blue and red vertical lines show the transition frequencies towards the given intermediate states for photoassociation (blue lines) and for photoexcitation of X-a three-body recombination product molecules (red lines). The notation is analogous to the one used in the $f = 1$ measurements (see Figure 5.12).

The 4.5 G measurement (blue) shows a nice agreement of the calculated frequencies with the measured signals. Also a nice agreement between the theory lines and the 37 G measurement can be seen, by shifting the theory lines of the 4.5 G measurement by -94 MHz. Using a linear Zeeman shift for the asymptote results with respect to 4.5 G in an expected frequency shift of about -91 MHz for the $m_F = -4$, $5s + 5s$ asymptote and the product molecules in the investigated v$= -1, -2$ X-a states (see Sec. 5.8.3). Therefore, the measurement indicates that for the spin stretched $f = 2$ atomic samples the magnetic substate and hyperfine state of the scattering channel is conserved for the main population, as already observed for $f = 1$ atomic samples.

5.11   Measurements of the ion production rates

In the former sections, I have shown signals that we have measured with our qualitative method. This method is well suited to derive general properties about the spectra. To get more information about the number of molecules formed via three-body recombination in the respective *X-a* states, it is necessary to count the number of ions resulting from ionization of these molecules (quantitative measurements). We count the number of ions with ion detection scheme II (see Sec. 4.2.5). All error bars in the given figures represent the standard deviations of the mean values.

5.11.1   Ion production rates of $f = 1$ atomic samples

In the following ion production rates for an initial sample of $f = 1$ $m_f = -1$ atoms are shown (notation see Sec. 5.8.1). To investigate the product molecules in the two v=-2, $R = 2, 0$ states we use the intermediate states $c\,^3\Sigma_g^+$ v$' = 0$ 0_g^- (1) and 1_g (2) (see Tab. 5.1). The presented results have to be considered as preliminary since additional measurements are necessary to gain full understanding.

With the ion production rate, the ionization efficiencies (see Sec. S5.13.8) and the absolute number of produced molecules, the branching ratio can be calculated. The branching ratio denotes the percentage of product molecules in the respective *X-a* state with respect to the absolute number of molecules produced by three-body recombination. The evaluation is performed analogously to Section 4.2, but the ionization efficiency η_1 is neglected. The ionization efficiency η_1 describes the probability of a three-body recombination product molecule to get excited into the intermediate state. To determine η_1, simulations (see Sec. 4.2.9) of the total excitation probability into the intermediate state are necessary. These simulations need saturation intensity measurements (see Sec. 4.2.8). These measurements need to be performed in future for all *X-a* states and intermediate states investigated.

In Figure 5.14, the signals of the product molecules in the two v=-2, $R = 2, 0$ states are shown. The calculated branching ratio is plotted versus the binding energy of the product molecules. The two different colors indicate different intermediate states that have been used. For these intermediate states different ionization laser frequencies are used in order

to achieve a good signal quality (see Sec. S5.13.8). The observed signals for the rotational states $R = 2, 0$ are of similar height, as already observed in the singlet measurement (see Chap. 4).
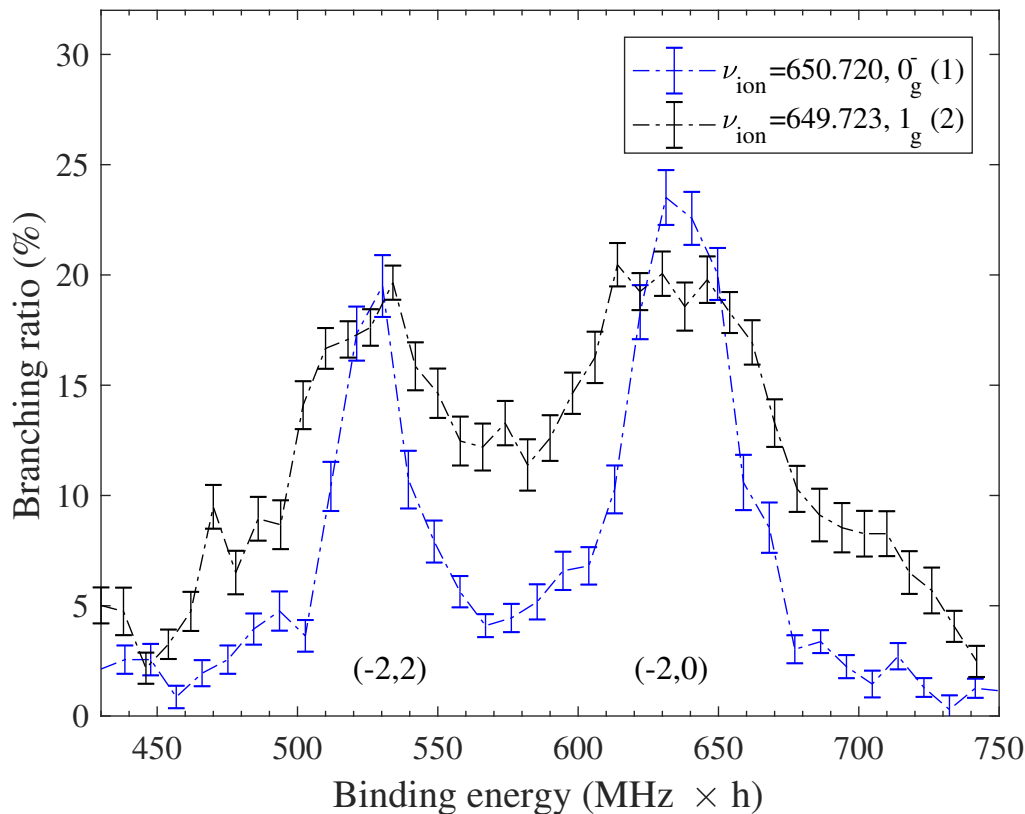
Figure 5.14: Estimated branching ratios, measured via the $c\,^3\Sigma_g^+$ $\mathrm{v}' = 0\ 0_g^-$ (1) and $c\,^3\Sigma_g^+$ $\mathrm{v}' = 0\ 1_g$ (2) intermediate states for two different ionization laser frequencies. Shown is the branching ratio versus the binding energy. The peak on the left is the v$= -2$, $R = 2$ X-a state signal and the peak on the right is the v$= -2$, $R = 0$ X-a state signal. The legend denotes the used ionization laser frequency $\nu_{\mathrm{ion}} = \nu_{\mathrm{ionlaser}} - \nu_{\mathrm{offset}}$ and the used intermediate state. A probe laser power of 18 mW and an interaction time of 150 ms was used. The atomic sample was prepared in the $f = 1$, $m_f = -1$ state and a single data point represents the average value of 51 (black scan), and 45 (blue scan) repetitions of the experiment, respectively. All error bars given in the figures represent the standard deviations of the mean values.

Comparing the branching ratio (on resonance for the two investigated states) to the singlet measurement (see Chap. 4), we find similar branching ratios of about 20%. This indicates that the observed population distribution measured via a singlet and a triplet intermediate state leads to the same results.

5.11.2 Ion production rates of $f = 2$ atomic samples
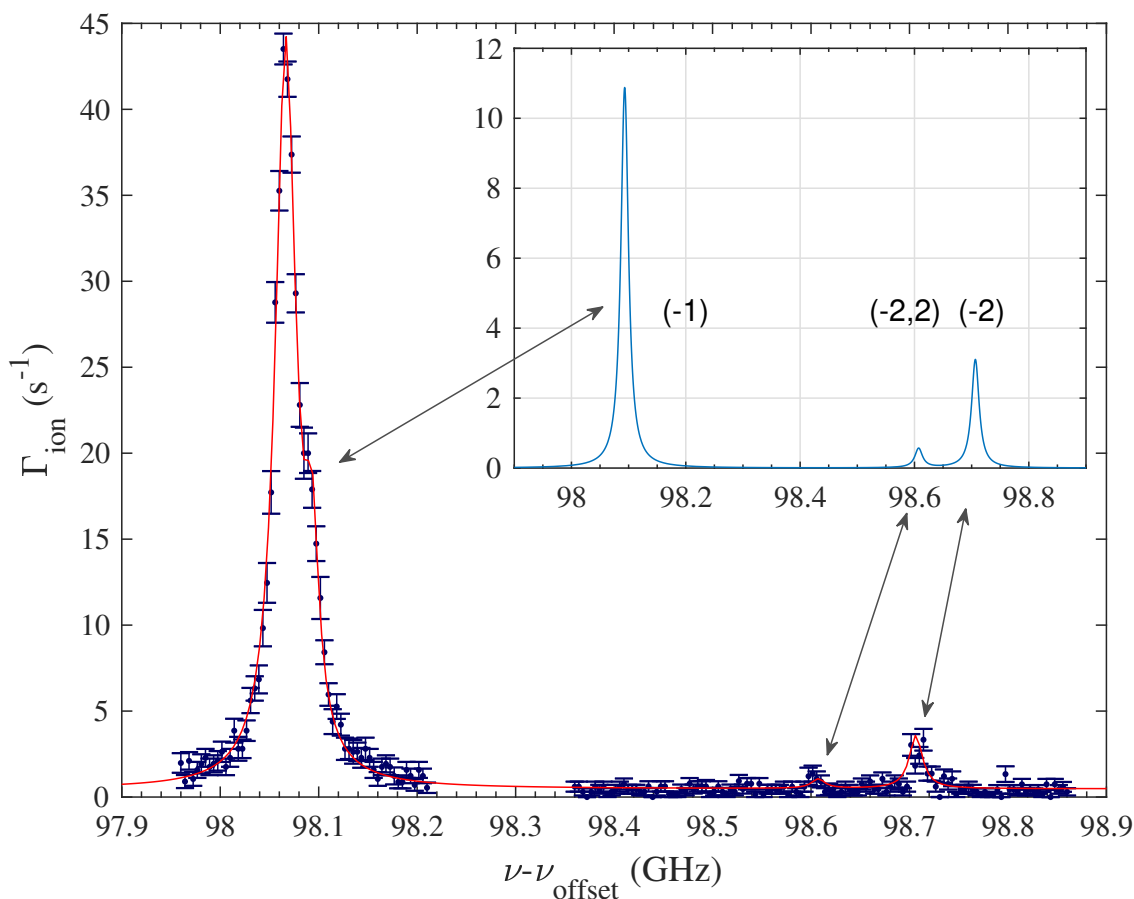
Figure 5.15: Measurement of ionization rates of product molecules using the $c\,^3\Sigma_g^+$ v$' = 0$ 0_g^- (1) intermediate state. The measurement was performed for atomic samples in the $f = 2$, $m_f = 2$ state. The ion production rate (Γ_{ion}) is plotted versus the probe laser frequency ($\nu_{\mathrm{offset}} = 281\,\mathrm{THz}$). The red curve is a fit of a sum of Lorentzian functions. The large resonance is the ion signal of the photoassociation. In the inset, the fit results for the X-a state molecules resulting from three-body recombination are displayed. The arrows indicate the frequency positions of the X-a state transitions in the measurement. Each data point in the measurement on the left (on the right) represents the mean value of 39 (47) repetitions of the experiment. The used probe laser power is 1.5 mW.

The results obtained for $f = 1$ atomic samples using a triplet intermediate state are similar to those obtained for the measurements using a singlet intermediate state, both qualitatively and quantitatively. The results obtained for $f = 2$ atomic samples with the qualita-

tive measurement method (see Sec. 5.9.2) indicate a different population distribution[11] as the results for $f = 1$ atomic samples (see Sec.5.9.1). Therefore, we might expect also to find a different behavior for the quantitative measurements as observed for $f = 1$ atomic samples.

The quantitative measurements for $f = 2\ m_f = 2$ atoms are carried out with ion detection scheme II (see Sec. 4.2.5). The used ionization laser frequency is the standard ionization laser frequency of $\nu_{ion:f=2} = 281\,649.112\,\text{GHz}$ (see Sec. 5.8.2) and the probe laser power is about 1.5 mW for all presented measurements. With the low probe laser power and for the X-a states to be probed, the first excitation step towards the intermediate state may not be saturated[12]. To get reliable values for the ion production rates with respect to specific transitions, measurements of the probe laser power dependence and simulations of the total excitation probability like in Section 4.2.9 need to be performed. As the signals are typically not saturated this will have a high influence on the ion production rates extracted. A rough approximation for the relative signal strengths will be provided further below. The advantage of a low probe laser power is that it is possible to measure both molecules formed by three-body recombination and molecules formed by photoassociation with the same set of parameters.

An overview REMPI spectrum for a $f = 2$, $m_f = 2$ atomic sample using the $c^3\Sigma_g^+$ v$' = 0$ 0_g^- manifold for the intermediate levels is shown in Figure 5.11 (p. 70). The frequency positions and quantum numbers of the corresponding intermediate states are given in Table 5.2 (p. 67) (see also Sec. 5.8.1 for the notation).

Photoionization via the 0_g^- $J' = 0$ intermediate state

The ion production rates for the photoassociation line (1) and the X-a state transitions (1,-1) and (1,-2,[2,0]) are shown in Figure 5.15. The interaction time is 150 ms. The measured ion production rate is given as Γ_{ion}. Fitting the spectrum with the sum of four Lorentzian functions (red curve) results in the X-a state resolved ion production rates as given in the inset. The corresponding values are given in Table 5.3. Figure 5.15 suggests that in the given frequency range the largest ion production rate is obtained for three-body

---

[11] For $f = 2$ atomic samples, only the v$= -1, -2\ R = 2, 0$ X-a states have shown signals of product molecules. For $f = 1$ atomic samples, product molecules have been found in the X-a states v$= -1, ..., -5$ with rotations up to $R = 6$.

[12] The term "not saturated" means that not all molecules in a given quantum state will get excited towards the intermediate state, see also Sec. 4.2.8.

Table 5.3: The measured ion production rates $\Gamma_{\text{ion}}(\text{PA}(n), v, R)$ for samples initially prepared in the $f = 2$, $m_f = 2$ state. The intermediate states associated with PA (n) are given in Table 5.2. The given values are preliminary and have to be verified with further measurements.

intermediate state	$v = -1$	$v = -2$	$v = -2\ R = 2$
PA (n)	(Hz)	(Hz)	(Hz)
	Γ_{ion}		
(1)	10.9	3.1	0.6
(2)	8	1.4	2.1
(3)	5.2	0.9	4.1
(4)	4.2	1	1.4

recombination product molecules in the most-weakly bound X-a state. Interestingly, for the $v = -2$, $R = 2$ state a very low ion production rate is measured as compared to the $v = -2$, $R = 0$ state. However, one has to be careful with a conclusive statement about this. It is possible that $R = 0$ and $R = 2$ states have different excitation cross sections for an intermediate state[13]. Nevertheless, it will be interesting to find out whether there is also a significant difference in the initial population of the $v = -2$, $R = 2,0$ states, because for the $f = 1$ measurements almost no such a difference was obtained both for the singlet (see Fig. 4.4) and for the triplet data (see Fig. 5.14).

Now, we want to compare the relative signal strength of molecular three-body recombination products in the $v = -1$ and $v = -2\ R = 0$ states. According to the simulations for the singlet measurements (see Sec. 4.2.9) a product molecule in the $v = -1$ state is by about a factor of two less likely to be excited towards an intermediate state than a product molecule in the $v = -2$ state (for 1.5 mW probe laser power). Assuming similar behavior for the $f = 2$ measurements, the relative population in the most-weakly bound X-a state would be about a factor of seven larger as in the $v = -2\ R = 0$ state. For the $f = 1$ atoms this factor was about 2.5 (see Fig. 4.4). Therefore, in terms of the population distribution it seems (the only clearly visible signals are the $v = -1$ and $v = -2\ R = 0,2$ transitions, see Sec. 5.9.2) that for $f = 2$ the population is shifted into the most-weakly bound state. It will be very interesting to check this with further experimental and theoretical investigations.

---

[13] For example this can be seen in Figure 5.11 (at about 98.6 GHz) the signal corresponding to the (1,-2) transition shows broadening which is not present for the (1,-2,2) transition. This effect is visible although the probe laser power was about 15 times larger (23 mW) as the power used here. This indicates a very different probe laser power dependence for the two transitions into the $J' = 0$ intermediate state.

Photoionization via the 0_g^- $J' = 2$ intermediate state triplet
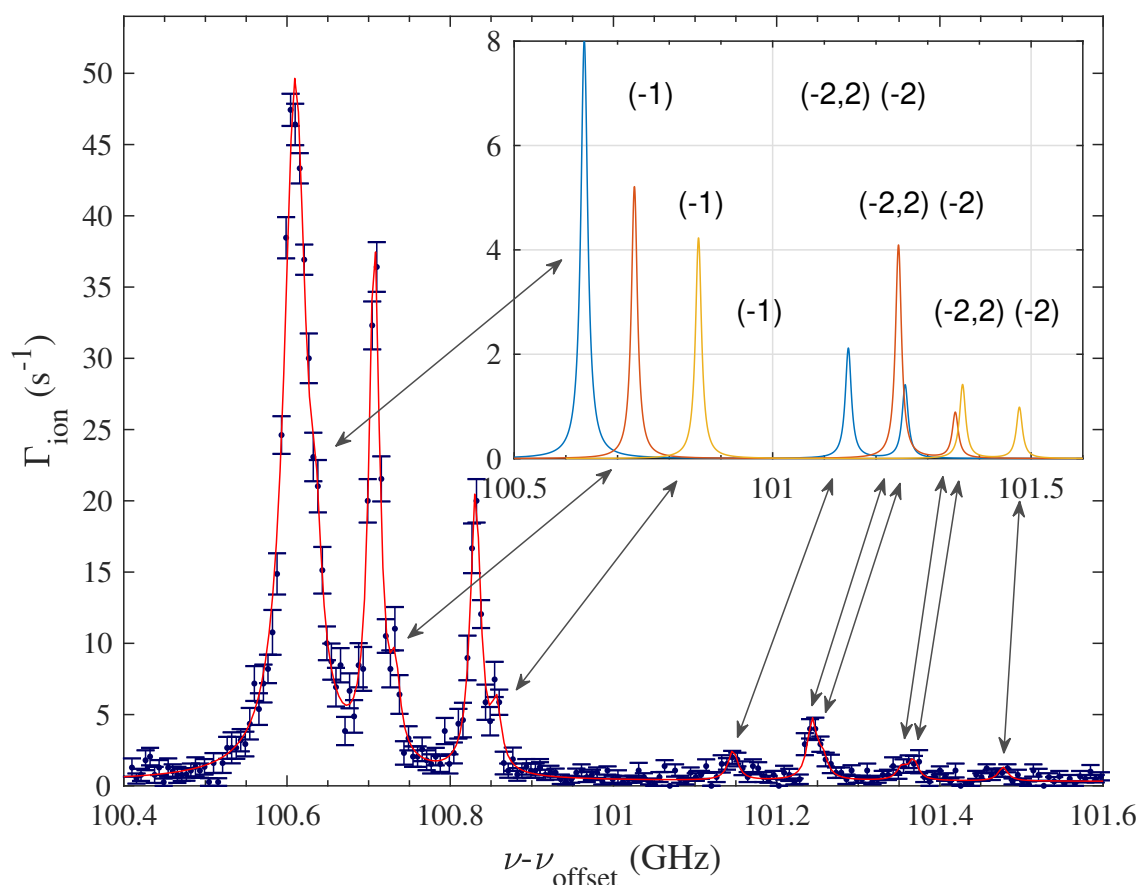
Figure 5.16: Measurement of ion production rates of product molecules using the $c\,^3\Sigma_g^+$ $v' = 0$ 0_g^- ([2,3,4]) intermediate state. The measurement is performed for atomic samples in the $f = 2$, $m_f = 2$ state. The measured ion production rate Γ_{ion} is plotted versus the probe laser frequency ($\nu_{offset} = 281\,THz$). The red curve is a fit of a sum of Lorentzian functions. The large resonances are the photoassociation signals. In the inset, the fit results for the X-a state molecules resulting from three-body recombination are displayed. The arrows assign the fitted peaks to the measured ones. Each data point in the measurement on the left (on the right) represents the mean value of 27 (14) repetitions of the experiment. The used probe laser power is 1.5 mW.

Next, a measurement for the $J' = 2$ intermediate states of the $c\,^3\Sigma_g^+$ $v' = 0$ 0_g^- manifold will be presented. Figure 5.16 shows the ion production rates associated with the PA ([2,3,4]) line-triplet (see Tab. 5.2). In this figure, the used measurement time is 150 ms

for frequencies below 101 GHz and 500 ms for frequencies above. The measured ion production rate is given as Γ_{ion}. The inset shows the fit result of the ion production rate for the respective X-a state transitions of the molecules formed by three-body recombination. The extracted rates are given in Table 5.3. The v= -1 signals are discussed in Section 5.11.5.

In the range of the v= -2 signals the measurement has low statistics, and in general these v= -2 signals are small and overlapping. Therefore, the fit results for the v= -2 X-a states have to be considered as tentative. Overall, the signals corresponding to the v= -2, $R = 2$ transitions are stronger than the v= -2, $R = 0$ transitions. In fact, for the intermediate states of $J' = 2$ character used here, the signal for the v= -2, $R = 2$ state is much larger as compared to Figure 5.15. From the comparison of Figures 5.15 and 5.16 it seems that transitions where J' is identical to R are connected to high signal strengths (due to a good excitation probability). However, to make a clear statement about the relative signal strength, further measurements with a higher probe laser power and more repetitions are necessary in order to get better signals. In the Section S5.13.9 preliminary ionization efficiencies for the states investigated in this section can be found.

5.11.3   Magnetic field dependence of three-body recombination in a $f = 2$ atomic sample

Here, I will discuss preliminary ion production rates of three-body recombination product molecules obtained at a homogeneous magnetic field of 37 G. As in the previous Section 5.11.2, we are using REMPI intermediate states of the $c\,^3\Sigma_g^+$ v$' = 0$ 0_g^- manifold.

Photoionization via the 0_g^- $J' = 0$ intermediate state at B=37 G

Figure 5.17 shows a quantitative measurement for the 0_g^- PA (1) and (1,-1) transitions (see Tab. 5.2). It was carried out for a homogeneous magnetic field of 37 G. The fit result for the (1,-1) transition is shown in the inset and the extracted ion production rate is given in Table 5.4. It was not possible to measure signals for the v=-2 transitions for the parameter set used here[14].

---

[14] We note that the observed v= -2 signal was already small in the measurements at low B-fields (Fig. 5.15). An interaction time longer than 150 ms (as used for Fig. 5.17) and especially a higher probe laser power could perhaps lead to a visible signal for these transitions.
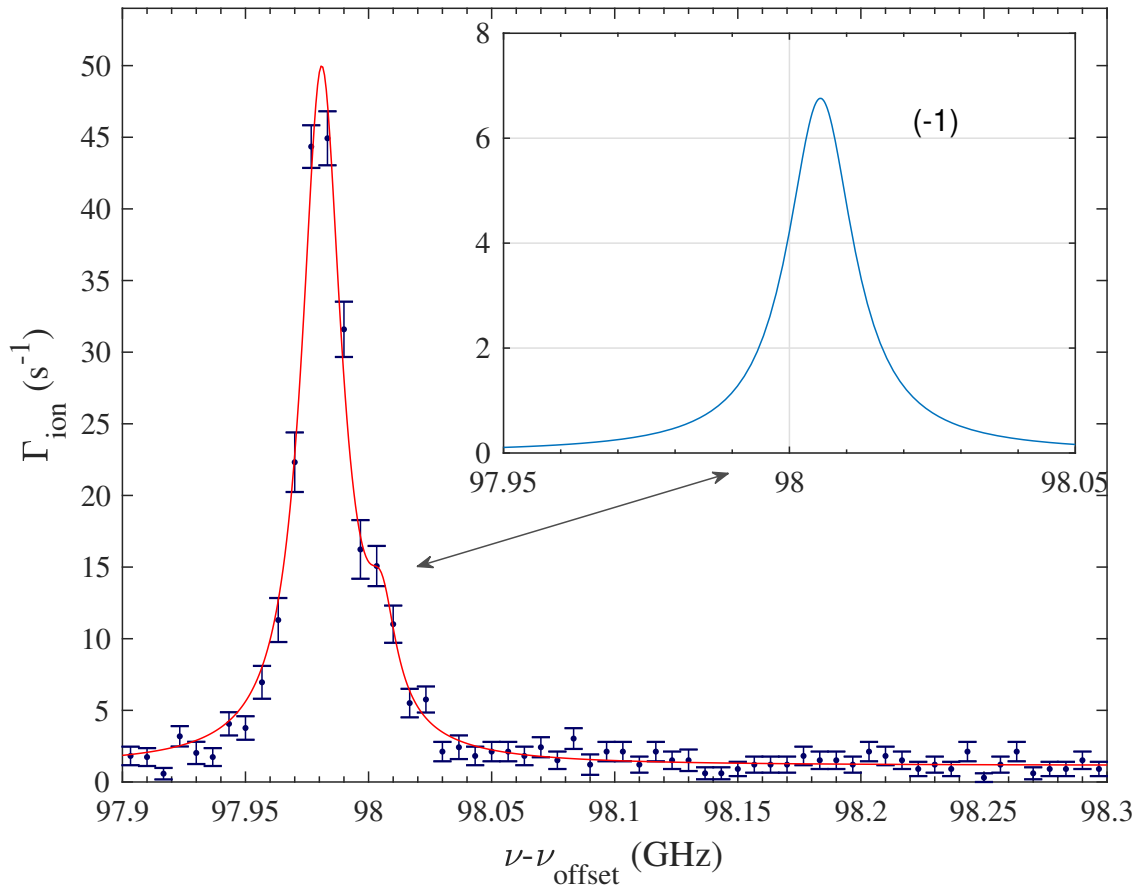
Figure 5.17: Ion production rate for the most-weakly bound X-a state measured via the $c^3\Sigma_g^+$ $v' = 0 \; 0_g^-$ (1) intermediate state. Shown is a spectrum of the photoassociation resonance PA (1) and the transition (1,-1) obtained at a magnetic field of 37 G for an atomic sample initially prepared in the $f = 2$, $m_f = 2$ state. The measured ion production rate Γ_{ion} is plotted versus the probe laser frequency ($\nu_{offset} = 281$ THz). The red curve is a fit of a sum of Lorentzian functions. In the inset, the fit result for the (1,-1) resonance is shown, where the arrow marks the position of the transition in the measurement. Here, the used ionization laser frequency is 281650.550 GHz, the interaction time is 150 ms and the probe laser power is 1.5 mW. Each data point represents the mean value of 22 repetitions of the experiment.

The measured ion production rate for the most-weakly bound X-a state is $\Gamma_{ion}(1, -1) \approx$ 7 Hz at the magnetic field of $B = 37$ G. This result is about 4 Hz smaller than the rate measured at $B = 4.5$ G given in Table 5.3. Two reasons could lead to the decrease of the measured ion production rate. One possibility is that the excitation probability of the X-a state into the intermediate state is different for the different magnetic fields applied.

The other possibility is that there is a change in the population distribution of the product molecules. The population could be in other $X\text{-}a$ states in particular different hyperfine and Zeeman states which cannot be resolved and show therefore no additional peaks as will be discussed later (see Sec. 5.11.5). The same reasons could also explain why no $X\text{-}a$ v$=-2$ signals are visible for the intermediate state PA (1).

Table 5.4: The measured $\Gamma_{\mathrm{ion}}(\mathrm{PA}(n),\mathrm{v},R)$ ion production rates for samples initially prepared in the $f=2$, $m_f=2$ state. The intermediate states associated with PA (n) are given in Table 5.2. The measurements are performed at a magnetic field of 37 G. The given values are preliminary and have to be verified with further measurements.

intermediate state	v$=-1$	v$=-2$	v$=-2$ $R=2$
PA (n)	(Hz)	(Hz)	(Hz)
		Γ_{ion}	
(1)	6.8		
(2)	5.8	0.2	0.3
(3)	5	0.5	0.8
(4)	1.9	0.4	0.5

Photoionization via the 0_g^- $J'=2$ intermediate state triplet at B=37 G

Next, we will present the signals connected to the $c\,^3\Sigma_g^+$ v'$=0$ 0_g^- $J'=2$ photoassociation line triplet (see Tab. 5.2). In Figure 5.18 the corresponding REMPI measurement around PA ([2,3,4]) is shown. An interaction time of 150 ms is used for the data on the left. To make the signals for the product molecules in the v$=-2$ $X\text{-}a$ states visible, we increased the interaction time to 1 s, see part of the data on the right. The v$=-2$ signals are observable now, but they are too weak to be really quantitative.

In the inset, the results from a fit of a sum of Lorentzian functions are shown. The extracted ion production rates are given in Table 5.4. They will be discussed in the Section 5.11.5 to derive a bigger picture.
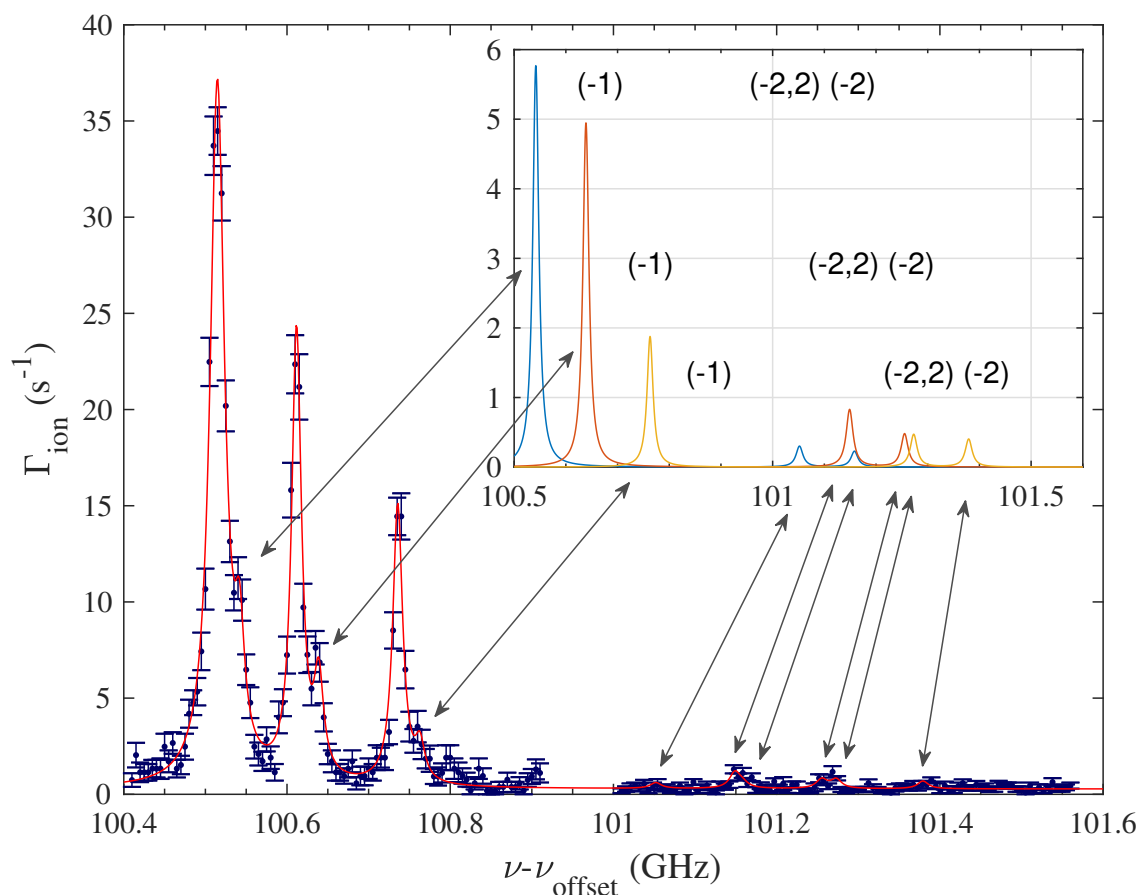
Figure 5.18: Ion production rates for *X-a* state product molecules photoionized via the $c^3\Sigma_g^+$ $v' = 0\ 0_g^-$ ([2,3,4]) intermediate states. The data are obtained at a magnetic field of $37\,\mathrm{G}$ for an atomic sample initially prepared in the $f = 2, m_f = 2$ state. The measured ion production rate Γ_{ion} is plotted versus the probe laser frequency ($\nu_{\mathrm{offset}} = 281\,\mathrm{THz}$). The red curve is a fit of a sum of Lorentzian functions. In the inset, the fit results are displayed. The arrows assign the fitted peaks to the measured ones. Each data point in the left half of the spectrum is measured with $150\,\mathrm{ms}$ interaction time and represents the mean value of 35 repetitions of the experiment. For the part of the spectrum on the right an interaction time of $1\,\mathrm{s}$ is used and here, each data point represents the mean value of 16 repetitions of the experiment. The used probe laser power is $1.5\,\mathrm{mW}$.

5.11.4   Rescaling of ion production rates for comparison

We have extracted ion production rates for various intermediate states and parameters. Every intermediate state and parameter set can have a different excitation probability in the first resonant REMPI step and can have a different ionization probability in the following ionization process. This leads to different observable ion production rates. The

rescaled ion production rate that is derived in the following can be used to compare product molecule signals from different intermediate states without knowing the excitation and ionization probabilities for the intermediate states. The rescaling can be used if no excitation step is saturated, since a saturation of an excitation step would distort the signal relations. This requirement is given for the data used later.

In a simple model, the ion production rate is given by

$$\Gamma_{\text{ion}}(\text{PA}(n), \text{v}, R) = \eta_1(\text{PA}(n), \text{v}, R) \cdot \eta_2(\text{PA}(n)) \cdot M(\text{v}, R).$$

η_1 is the probability to excite a molecule in the intermediate state, η_2 is the probability to ionize the molecule from the intermediate state, and M is the number of molecules that can be excited into the intermediate state (the actual variable of interest). The ion production rate during photoassociation is very similar with

$$\Gamma_{\text{PA}(n)} = \eta_1(\text{PA}(n)) \cdot \eta_2(\text{PA}(n)) \cdot A,$$

where $\eta_1(\text{PA}(n))$ is the probability to associate a molecule into the intermediate state, $\eta_2(\text{PA}(n))$ is the probability to ionize it, and A is the number of colliding atoms that could be photoassociated[15].

We define a factor $\alpha_{\text{PA}(n)}(\text{v}, R)$ as a factor describing the difference in the excitation probabilities of a photoassociation and a X-a state i.e. we can use $\alpha_{\text{PA}(n)}(\text{v}, R) \cdot \eta_1(\text{PA}(n), \text{v}, R) = \eta_1(\text{PA}(n))$. The relation between the ion production rate of a X-a state and the ion production rate of its intermediate state i.e. photoassociation is then given by

$$\frac{\Gamma_{\text{ion}}(\text{PA}(n), \text{v}, R)}{\Gamma_{\text{PA}(n)}} = \frac{M(\text{v}, R)}{\alpha_{\text{PA}(n)}(v, R) \cdot A}.$$

This can now be multiplied with the ion production rate of another photoassociation i.e the ion production rate of a reference photoassociation Γ_{Ref}. Assuming $\alpha_{\text{PA}(n)}(\text{v}, R) \approx \alpha_{\text{PA}(\text{ref})}(\text{v}, R)$[16], this leads to the rescaled ion production rate

$$\Gamma_{\text{ionre}}(\text{PA}(n), \text{v}, R) = \frac{\Gamma_{\text{Ref}} \cdot \Gamma_{\text{ion}}(\text{PA}(n), \text{v}, R)}{\Gamma_{\text{PA}(n)}} = \eta_1(\text{PA}(\text{Ref}), \text{v}, R) \cdot \eta_2(\text{PA}(\text{Ref})) \cdot M(\text{v}, R).$$

$$(5.2)$$

---

[15] For identical atom cloud parameters A is assumed to be constant.

[16] This is in general not true, but it gives a better approximation than comparing the not rescaled ion production rates.

The rescaled ion production rates for the *X-a* state product molecules investigated for $f = 2$, $m_f = 2$ atomic samples are given in Table 5.5. These values are used in the following Section 5.11.5 for the evaluation of the data via electric-dipole transition selection rules.

Besides the assumptions that are made in this approach another problem is the rather low number of repetitions for some data leading to possibly large uncertainties. The uncertainty of the given ion production rates should be smaller than $\pm$ 50% for the relative signal strength of different states. However, this value is based on experience and is not extracted from a full error calculation. More measurements are necessary to complete the data and extract fully reliable results.

Table 5.5: Rescaled ion production rates (using Eq. 5.2) for samples initially prepared in the $f = 2$, $m_f = 2$ state. The intermediate states associated with PA (n) are given in Table 5.2. As reference Γ_{Ref} we use the photoassociation transition PA (1) of the 4.5 G measurement (see Fig. 5.15). This results in the rescaled low field results Γ_{ionre} for the data shown in Table 5.3. For the data shown in Table 5.4 (37 G measurement) this results in the rescaled high field results $\Gamma_{\text{ionre}(2)}$. The given values are preliminary and have to be verified with further measurements.

intermediate state	v= −1	v= −2	v= −2 R = 2
PA (n)	(Hz)	(Hz)	(Hz)
Rescaled low field results: Γ_{ionre}			
(1)	10.9	3.1	0.6
(2)	7.1	1.3	1.9
(3)	6.1	1	4.8
(4)	9.2	2.1	3.1
Rescaled high field results: $\Gamma_{\text{ionre}(2)}$			
(1)	6		
(2)	6.8	0.3	0.4
(3)	9.1	0.9	1.5
(4)	5.5	1.2	1.4

5.11.5 Analyzing the $f = 2$ ion production rate measurements in terms of electric-dipole selection rules

Now, we discuss the derived preliminary ion production rates of the v$= -1$ X-a state for $f = 2$ $m_f = 2$ atomic samples in terms of electric-dipole transition selection rules. This analysis makes use of the possibilities that open up due to the different hyperfine components of the $c\,^3\Sigma_g^+$ 0_g^- intermediate states. They allow for a larger state selectivity of the (1,2) REMPI used for the state-to-state chemistry measurements. This can become important if the energetic separation of the investigated X-a states is too small to be resolved spectroscopically. We discuss the idea of this evaluation scheme as an example, since the preliminary data does not allow for a conclusive statement about the product molecule distribution.

From calculations it is known that the v$= -1$ X-a state has different hyperfine components [64, 42, 44]. The different hyperfine states for the v$= -1$ X-a state are located at frequency positions of $F_{tot} = 4 : -25\,$MHz, $F_{tot} = 2 : -30\,$MHz, and $F_{tot} = 0 : -32\,$MHz relative to the $f = 2 + f = 2$ $5s + 5s$ atomic asymptote (at $0\,$G). Due to the linewidth of the intermediate state of at least $14\,$MHz, these states cannot be resolved clearly in the measurement. However, we note that all our fits resulted in a resonance position of about $-25\,$MHz.

From the selection rules[17] $\Delta F_{tot} = 0, \pm 1$ and if $F_{tot} = 0$ then $\Delta F_{tot} = +1$ it follows that the $F_{tot} = 0$ X-a state cannot be excited to one of the intermediate states used here ($F'_{tot} \geqq 3$). A schematic of the experimental situation is shown in Figure 5.19a). The observed lines (purple line) are a composition of the signals arising from the $F_{tot} = 2$ X-a state (orange line) and the $F_{tot} = 4$ X-a state[18] (blue line). The fitting for data extraction (green dashed line) covers both possible hyperfine components of the v$= -1$ X-a state. In Figure 5.19b), the same situation is shown with the relevant quantum numbers, the measured and rescaled ion production rates Γ_{ionre} (see Sec. 5.11.4), and the estimated ion production rate Γ_{prod} in the v$= -1$ X-a state. Here the possible transitions are depicted with arrows. The signals of three-body recombination product molecules measured via the intermediate states PA (2) and PA (3) should show the same rescaled ion production rate coming only from $F_{tot} = 4$ product molecules. Indeed, they are very similar (see Fig. 5.19b)).

---

[17]This selection rules strictly hold, only for low magnetic fields [43].

[18]Note here, that the spectrum observable for this hyperfine component is identical to the observed photoassociation spectrum (see Fig. 5.11) of $f = 2$ atomic samples.

Figure 5.19: Schematic of the excitation pathways from different hyperfine components towards the $c\,^3\Sigma_g^+$ v$'$ = 0 0_g^- states. a) A schematic of the excitation spectra of the different F_{tot} components into the relevant $c\,^3\Sigma_g^+$ 0_g^- states leading to the observed signal (top line) which is fitted (top dashed line). Depending on the F_{tot}' of the intermediate state, electric-dipole selection rules only allow for $F_{\text{tot}} = 2$ transitions for certain intermediate states. b) The estimated ion production rate Γ_{prod} is given for each hyperfine level of the v$= -1$ X-a state. The arrows mark the transitions, which are allowed by electric-dipole transition selection rules. The intermediate states are given including the quantum numbers (see Tab. 5.2) and the rescaled ion production rate Γ_{ionre} of the 4.5 G measurement (see Sec. 5.11.4).

The two intermediate states PA (1) and PA (4) can contain also the $F_{tot} = 2$ product molecules (see Fig. 5.19a)). Indeed, they are again very similar and most importantly larger as the intermediate states which only contain signals of $F_{tot} = 4$ product molecules (see Fig. 5.19b)). A possible estimation of the ion production rates Γ_{prod} in the respective hyperfine components of the v= −1 state is given in the Figure 5.19b). The slight variations of rescaled ion production rates Γ_{ionre} could be explained by differences in the excitation probability of the product molecules that are not covered by the rescaling (see Sec. 5.11.4). The observation of $F_{tot} = 2$ product molecules would imply that spin flips can take place in the three-body recombination of $f = 2$ atoms.

Analogously, as a consistency check for these results we can use the ion production rates of the 37 G measurement (see Tab. 5.4). A schematic of the experimental situation is shown in Figure 5.20a). The Zeeman shift of the v= −1 $F_{tot} = 2$ X-a state (orange line) is only half the shift of the v= −1 $F_{tot} = 4$ X-a state (blue line) (for the respective positive stretched m_F state). Therefore, we can fit only the v= −1 $F_{tot} = 4$ X-a component (green dashed line) and hence should get about the same results for all used intermediate states (purple line). The relevant quantum numbers, the rescaled ion production rates $\Gamma_{ionre(2)}$ (see Sec. 5.11.4), and the estimated ion production rates Γ_{prod} in the v= −1 state are given in Figure 5.20b). For the measurements at 37 G, the data for the $F'_{tot} = 3$ intermediate states agree with the expected decrease of the signal strength. The rescaled ion production rates are by roughly 4 Hz smaller as the respective $B = 4.5$ G ion production rates, see also Figure 5.19b). In contrast to that the PA ([2,3]) intermediate states are only accessible from the $F_{tot} = 4$ component of the v= −1 X-a state and should stay constant for both magnetic fields. This is given for the signal measured via the $F'_{tot} = 5$ intermediate state, but not for the ion production rate measured via the $F'_{tot} = 4$ intermediate state. It therefore contradicts the made considerations. Another problem is that there is no $F_{tot} = 2$ product molecule signal observable as is expected (see Fig. 5.20a)). A possible explanation would be that a spin-flip in the three-body recombination could lead to a mixture of different m_F states that are washed out and therefore show no additional peak.

However, a conclusive statement cannot be made now due to the number of assumptions in this simplified evaluation and due to the preliminary character of the data. Further measurements and consistency checks have to be performed. Eventually this makes it possible to state that the scattering channels hyperfine state is not conserved for the molecules produced by a three-body recombination in ultracold $f = 2$, $m_f = 2$ spin stretched atomic samples. This result would be contrary to the results observed so far.
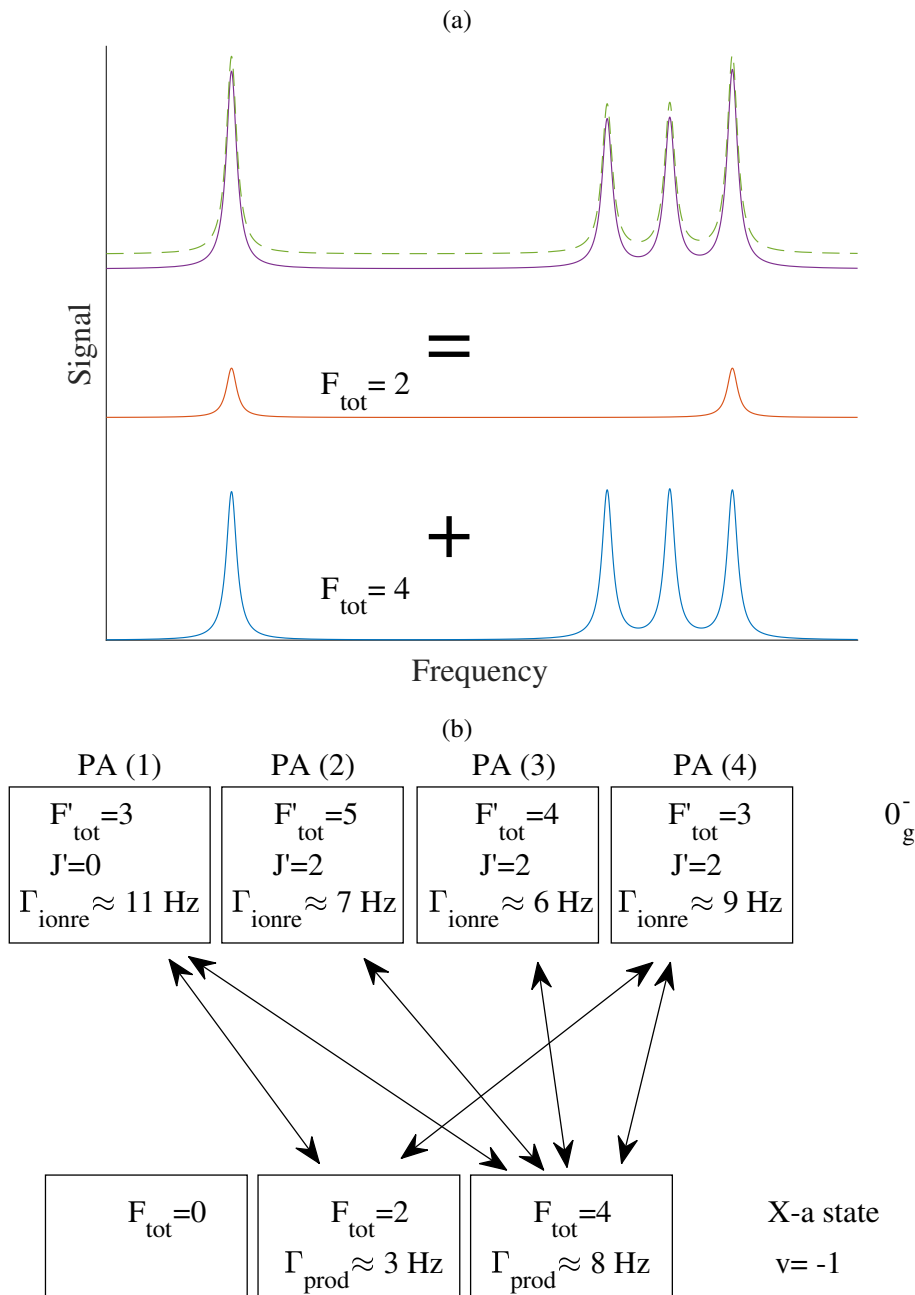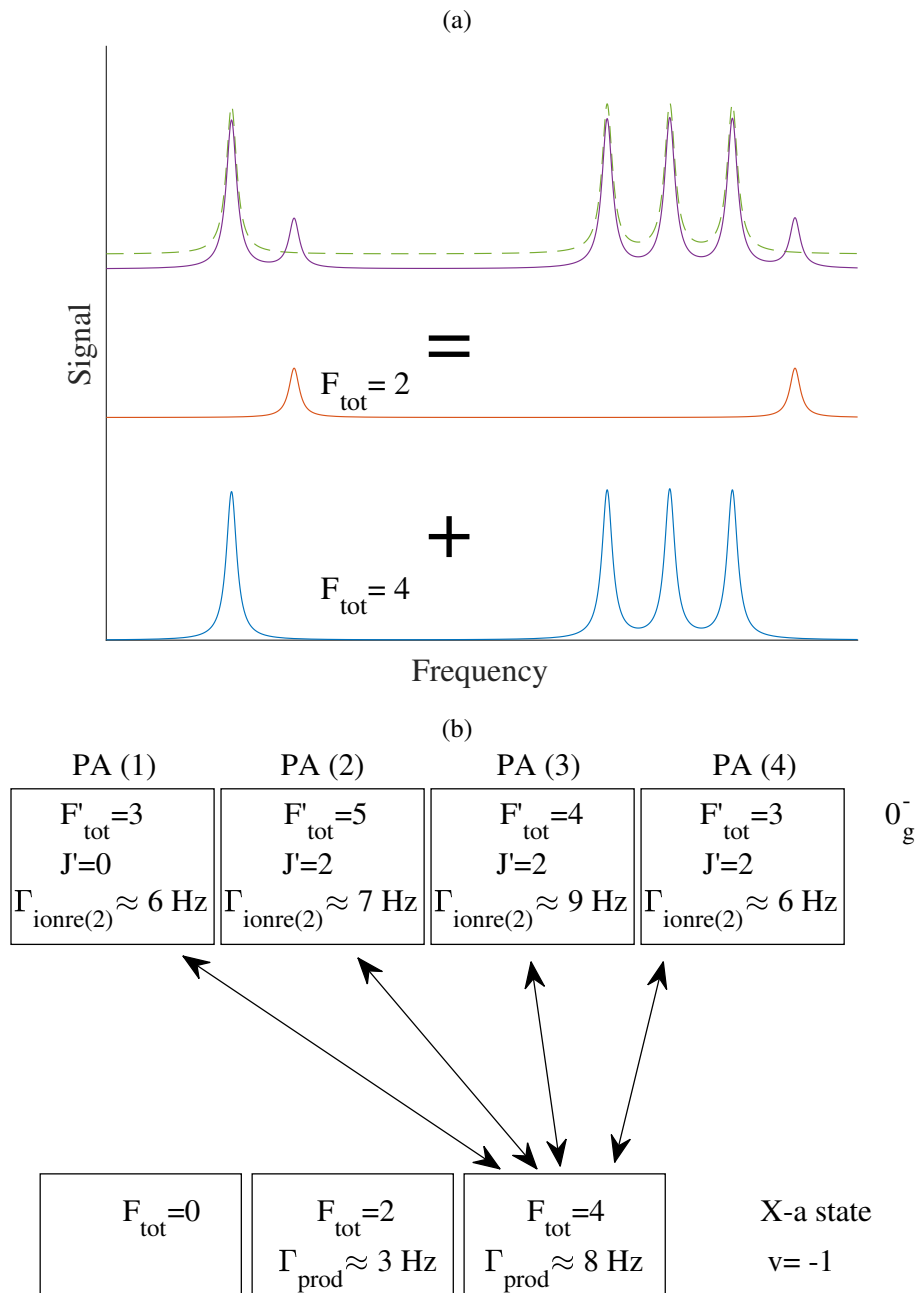
Figure 5.20: Schematic of the excitation pathways from different hyperfine components towards the $c\,{}^3\Sigma_g^+$ v$' = 0\ 0_g^-$ states. a) A schematic of the excitation spectra of the different F_{tot} levels into the relevant $c\,{}^3\Sigma_g^+\ 0_g^-$ states leading to the observed signal (top line) at 37 G, where only the $F_{tot} = 4$ component is fitted (dashed line). The applied magnetic field leads to a different Zeeman shift of the different F_{tot} components. b) The ion production rate Γ_{prod} is given for each hyperfine level of the v$= -1$ X-a state. The arrows mark the transitions, which are allowed by electric-dipole transition selection rules and have been fitted. The intermediate states are given including the quantum numbers (see Tab. 5.2) and the rescaled ion production rate Γ_{ionre} of the 4.5 G measurement (see Sec. 5.11.4).

5.12   Conclusion

We have studied three-body recombination where we photoionize the product molecules via the $v' = 0$ vibrational state of the $c\,^3\Sigma_g^+$ potential for $f = 1$, $m_f = -1$ and $f = 2$, $m_f = 2$ atomic samples. For the $f = 1$, $m_f = -1$ samples we find a relative broad population distribution in agreement with our previous measurement where we used a detection scheme via singlet intermediate states. The $f = 2$, $m_f = 2$ samples show a slightly different product molecule population distribution than observed for $f = 1$, $m_f = -1$ samples. The number of populated X-a states seems to be smaller and the population distribution in general seems to be shifted towards the most-weakly bound state.

A magnetic field has been applied to resolve the magnetic substates and the hyperfine states of the product molecules. A conservation of the hyperfine and magnetic substate of the two-body scattering channel was found for the three-body recombination product molecules for $f = 1$, $m_f = -1$ and $f = 2$, $m_f = 2$ atomic samples.

The quantitative measurements of $f = 1$, $m_f = -1$ atomic samples have shown similar results for a triplet intermediate state as obtained via a singlet intermediate state. The preliminary ion production rates for the $f = 2$, $m_f = 2$ atomic samples seem to indicate again a very strongly populated most-weakly bound X-a state. The evaluation of the quantitative measurements of $f = 2$, $m_f = 2$ atomic samples via dipole transition selection rules has shown that the conservation of the two-body scattering channel is not necessarily given for all the population and eventually spin flips are observable.

The performed measurements are a first step to understand the very complicated state-to-state chemistry measurements via $c\,^3\Sigma_g^+$ $v' = 0$ intermediate states. Further measurements are necessary to be able to give conclusive statements about some open questions.

5.13 Supplementary information

5.13.1 Optimizing the ionization laser frequency

Unwanted coupling of the ionization laser to molecular states
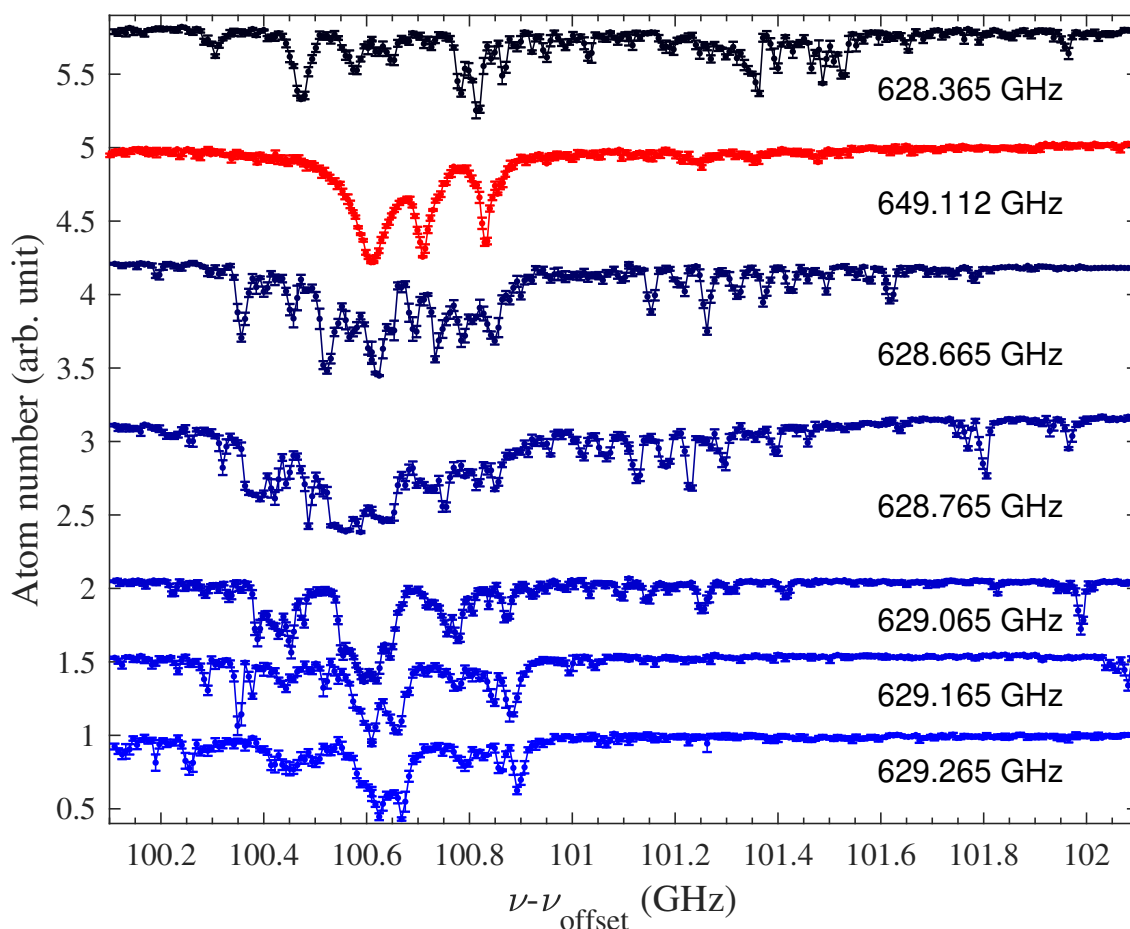
Figure 5.21: Deformation of the photoassociation signal of the intermediate level structure due to the ionization laser i.e. dipole trap laser. Shown is a part of the 0_g^-, $v' = 0$ spectrum of the $c\,^3\Sigma_g^+$ state when starting from $f = 2$, $m_f = 2$ atoms (see Tab. 5.2). We plot the atom number as a function of the probe laser frequency ν with $\nu_{\text{offset}} = 281\,\text{THz}$ for different ionization laser frequencies as given in the figure. The REMPI measurements (shades of blue) are offset vertically, proportional to their frequency difference to the $281\,629.265\,\text{GHz}$ measurement. In red the undisturbed structure at an ionization laser frequency of $281\,649.112\,\text{GHz}$ is displayed.

To detect the product molecules of three-body recombination via (1,2) REMPI it is essen-

Figure 5.22: REMPI schemes for the measurements shown in this section (analogous to Fig. 5.5). A shows one possibility of an unwanted coupling, where the ionization laser couples to *X-a* states (red arrow) producing a deformed line structure of the intermediate st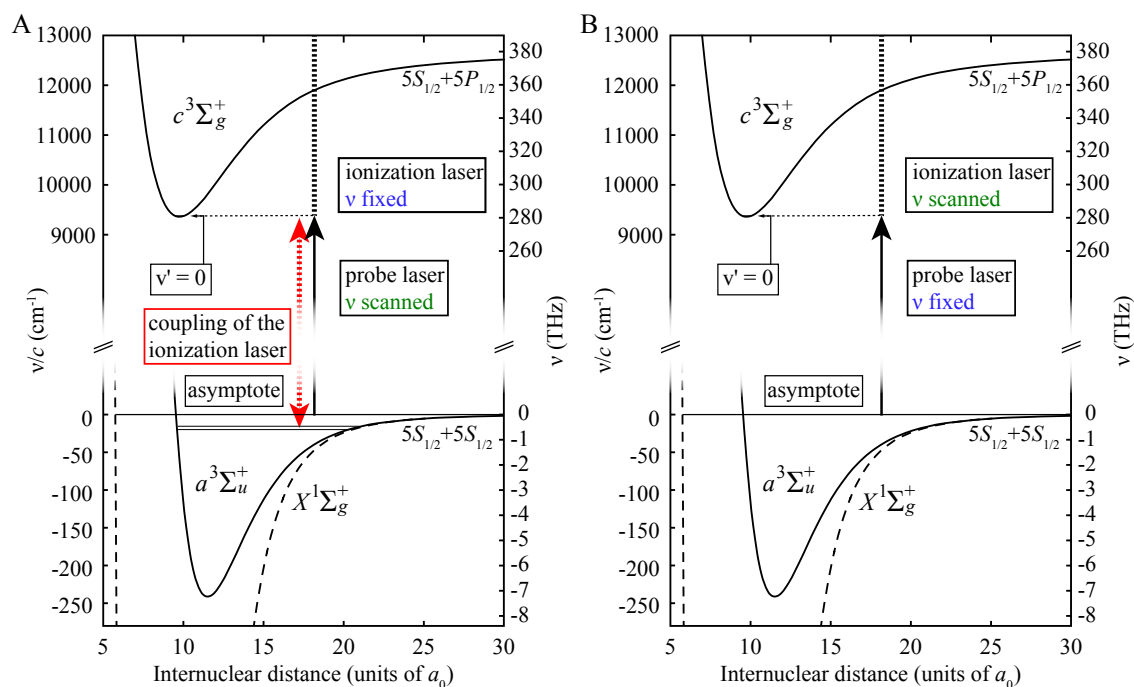ate (Fig. 5.21). **B** shows the excitation scheme used for the data shown in Figure 5.23, where the ionization laser frequency is scanned and the probe laser frequency fixed.

tial to find a good ionization path. The dipole trap laser (i.e. ionization laser) frequency must be chosen such that the intermediate level structure is not disturbed and a high ionization efficiency is achieved. The following measurements are used to describe the obstacles that have to be overcome for state-to-state chemistry measurements via a $c\,^3\Sigma_g^+$ 0_g^-, $v' = 0$ intermediate state.

First we tried to use ionization laser frequencies around 281.629 THz, similar to the one used for the detection of singlet states (see Sec. 4). By measuring REMPI spectra (see data in shades of blue Fig. 5.21), one clearly sees that at these laser frequencies additional lines occur. Small ionization laser frequency variations completely change the observable line structure, where the red curve shows the line structure of the $c\,^3\Sigma_g^+$, $v' = 0$, 0_g^- PA([2,3,4]) line triplet for reference (see Tab. 5.2). The deformation of the signals is due to a coupling of the intermediate states to other molecular states. Here the ionization laser couples the intermediate states probably to deeper bound *X-a* states, but higher excited states (e.g. (2,1) REMPI) would also be possible. Since the ionization laser frequency is

by about $530\,$GHz larger than the probe laser frequency, a coupling of the intermediate state to a X-a state with about the same binding energy is possible. This is schematically shown in Figure 5.22 A. In this figure, the coupling that is disturbing the intermediate state signal is shown with a red arrow. Below the $f = 2 + f = 2$, $5s + 5s$ asymptote of the X-a potentials the bound states v=-15[19] $R = 0,2$ with $F = 2$ are available in the range of $530.25 - 529.31\,$GHz [64]. A coupling to these states could be responsible for the distortion of the intermediate states. The next, more deeply bound states are to be found at about $600\,$GHz below the asymptote. Therefore, it is reasonable that an additional detuning of about $20\,$GHz of the ionization laser leads to signals that are not distorted (red reference curve).

However, this is only the first step to be able to ionize product molecules efficiently. The ionization laser frequency needs to be scanned in more detail, where the goal is to find a frequency with good ionization efficiency.

Scanning the ionization laser frequency

A fast method to indirectly measure the ionization efficiency is to photoassociate molecules (see Sec. 2.1.1) with a low intensity probe laser. The ionization laser ionizes a part of these molecules (see Fig. 5.22 B). The number of ions produced depends on the ionization laser frequency. Therefore, a spectrum can be measured by scanning the ionization laser frequency. The resulting atom loss induced by the ions is measured with ion detection scheme I. The low intensity of the probe laser is necessary to be in a range where the atom loss is still sensitive to changes in the number of produced ions i.e. not saturated (see additional content in Sec. 4.2.5). This method is also an indirect method to measure an excitation spectrum for the states that are addressed after the intermediate state. It is fast in order to find suitable ionization laser frequencies. Nevertheless, one has to be careful when using this method to find the optimal ionization frequency. The highest loss or even a lower loss can be the result of the former discussed couplings to X-a or highly excited states that shift or split lines.

---

[19]Here, the vibrational quantum number v is given relative to the $f = 1 + f = 1$, $5s + 5s$ asymptote.
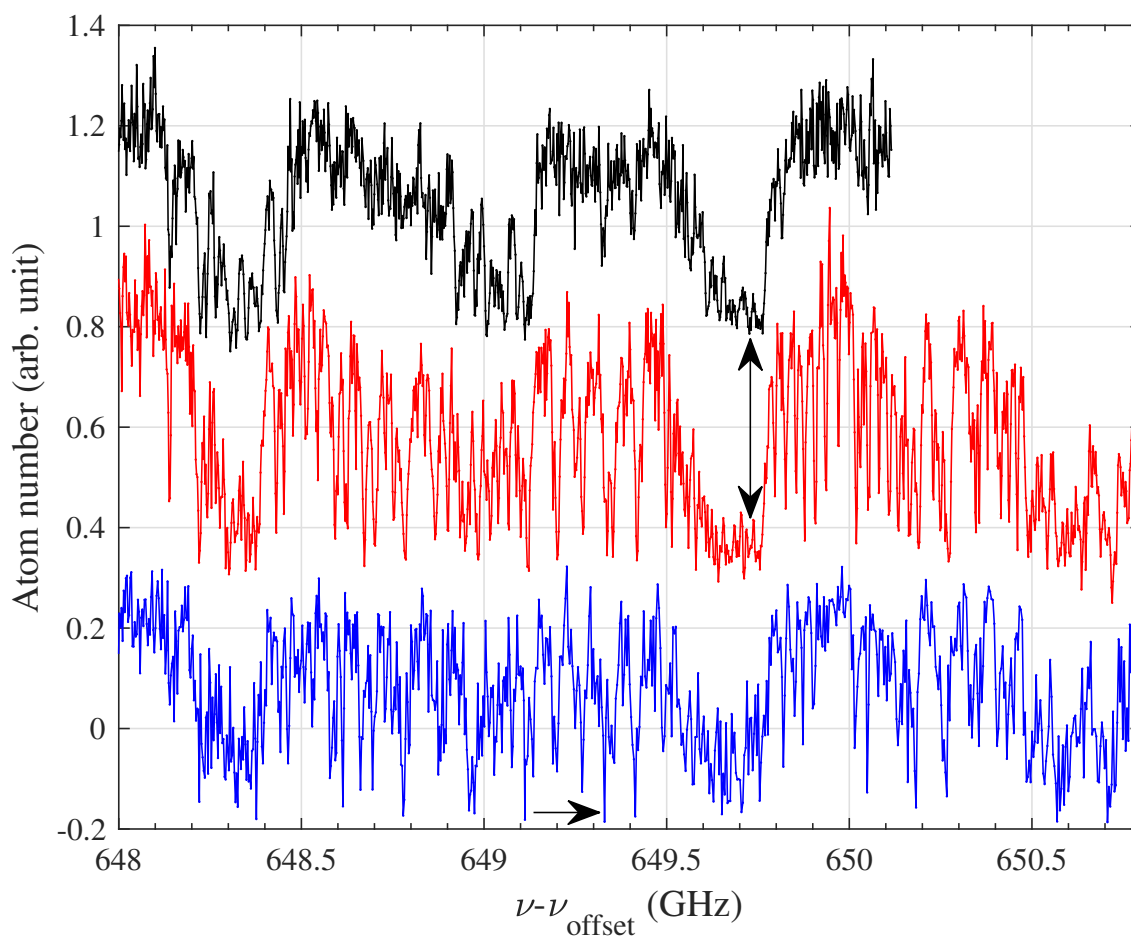
Figure 5.23: Indirectly measured ionization efficiency of the (1,2) REMPI ionization path using photoassociated molecules. The atom number is plotted versus the ionization laser frequency with $\nu_{\text{offset}} = 281\,\text{THz}$. Different data sets are vertically offset and the measurement scheme is explained in the text (Fig. 5.22 B). The black curve shows the data for the PA (1) intermediate state in the $c\,^3\Sigma_g^+$ $v' = 0$ 1_g manifold (see Tab. 5.1). The red curve shows the data for the PA (1) intermediate state in the $c\,^3\Sigma_g^+$ $v' = 0$ 0_g^- manifold. Both measured for $f = 1$ atomic samples. The blue curve displays the data for the PA (1) intermediate state in the $c\,^3\Sigma_g^+$ $v' = 0$ 0_g^- manifold measured for $f = 2$ atomic samples (see Tab. 5.2). The measurements have been performed with a probe laser power of $3\,\text{mW}$ and an interaction time of $500\,\text{ms}$. Each data point in the line represents the result of a single experimental run. The noise level in the measurements is about $0.1\,\text{arb. units}$. The for $f = 1$ ($f = 2$) atomic samples used standard ionization laser frequency is marked with an double arrow (arrow), respectively.

Figure 5.23 shows the remaining atom number as a function of the ionization laser frequency, as described before. The probe laser resonantly photoassosciates molecules where different colors indicate different intermediate states. Depending on the ionization

efficiency, the ionization laser produces a different number of ions leading to different atom loss. The black and red curves show the data for two probe laser frequencies for 1_g and 0_g^- states excited from $f = 1$ atoms. Most structures seem to be similar for both scans. Interestingly, we also observe a similar structure for the photoassociation of $f = 2$ atoms in the 0_g^- manifold (see Fig. 5.23 blue signal). Especially, the wider structures are at the same frequencies, whereas the narrower structures are slightly different.

From these spectra, we identified the ionization laser frequencies that give a good ionization efficiency. For $f = 1$ atoms the standard ionization laser frequency is,

$$v_{ion:f=1} = 281\,649.723\,\text{GHz}.$$

For $f = 2$ atoms

$$v_{ion:f=2} = 281\,649.112\,\text{GHz}$$

is used (see also Sec. 5.8.2). As can be seen in Figure 5.23 the used line for $f = 2$ atomic samples is much narrower as the structure used for $f = 1$ atomic samples and therefore the ionization efficiency is much more depending on the used intermediate state.

5.13.2 Identifying the photoassociation transitions

In this section, we are presenting measurements, which give an overview of the observed photoassociation structures (see Sec. 2.1.1). We will identify these transitions from the $5s + 5s$ asymptote to the intermediate states of the $c^3\Sigma_g^+$ $v' = 0$ manifold. With the knowledge of the term frequencies of the in the REMPI used intermediate states, we can calculate the frequencies for transitions to these levels when starting form molecular states within the X-a manifold.

Photoassociation spectra of $f = 1$ atomic samples

First, we are discussing atomic samples that are prepared in the hyperfine state $f = 1$, $m_f = -1$. For further information concerning the notation in the following, see Section 5.8.1, and for the typically used experimental parameters, see Section 5.8.2. Figure 5.24 shows the measured $c^3\Sigma_g^+$ $v' = 0$ 1_g manifold with the calculated[20] photoassociation transitions. Analogously, the Figure 5.25 shows the $c^3\Sigma_g^+$ $v' = 0$ 0_g^- manifold.

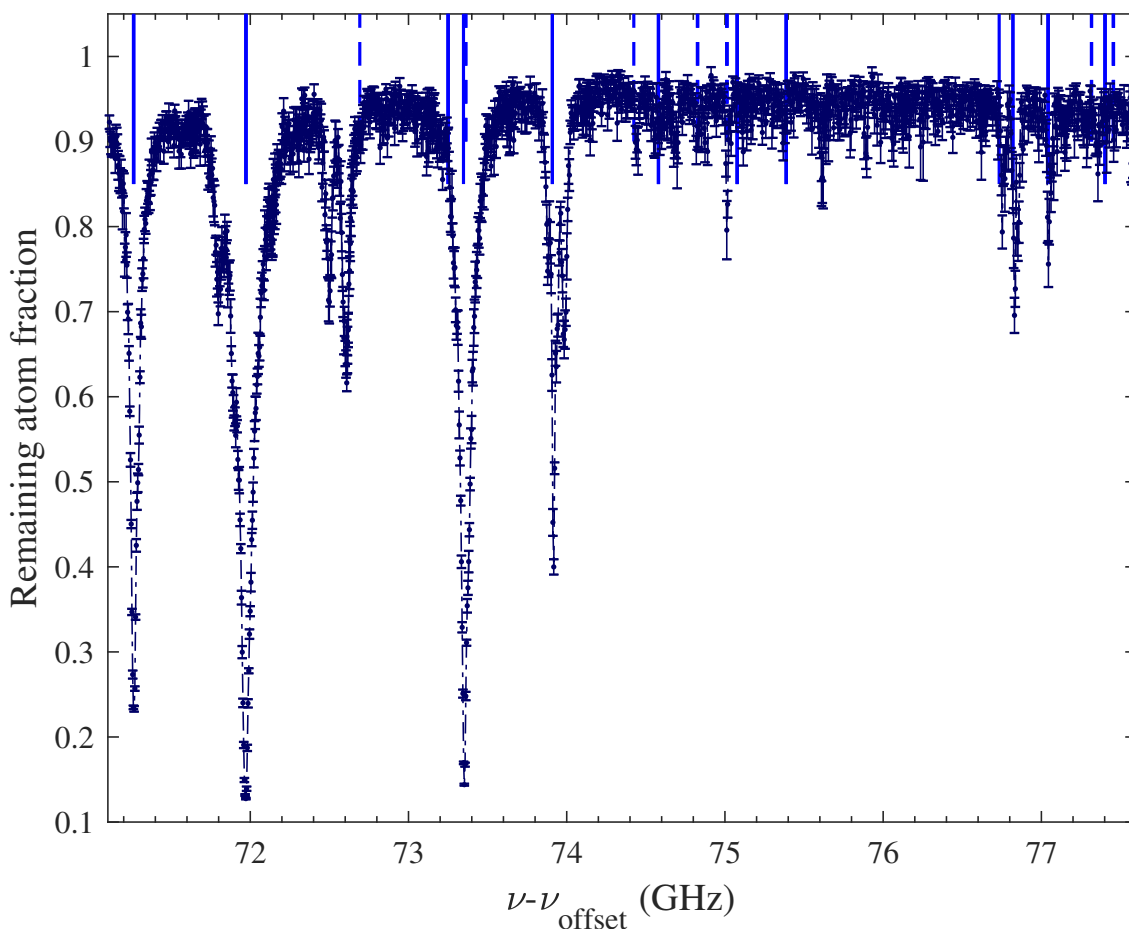[20]For more informations about the calculations see Sec. 5.8.3.

Figure 5.24: Comparison of the theoretically expected frequency positions of intermediate states (photoassociation) with the measurement. Shown is a measured (1,2) REMPI spectrum where we photoassociate molecules in the state $c\,^3\Sigma_g^+$ $v' = 0$ 1_g for an atomic sample of $f = 1$, $m_f = -1$ atoms ($\nu_{\text{offset}} = 281\,\text{THz}$). Blue vertical lines indicate the photoassociation model calculations (solid $I' = 3$, dashed $I' = 1$). The absolute offset of the model calculations is chosen to match the frequency of the first calculated photoassociation ($I' = 3$, $\langle J' \rangle = 1.2$, $F_{\text{tot}}' = 2$) with the first measured photoassociation signal. The data are measured for an interaction time of $600\,\text{ms}$ with ion detection scheme I. Also signals from three-body recombination product molecules are visible. Each data point represents the mean value of ten repetitions of the experiment and is measured with $3\,\text{mW}$ probe laser power. All error bars given in the figures represent the standard deviations of the mean values.

The frequencies of the measured and calculated photoassociation transitions for both the 1_g and 0_g^- component are given in Table 5.6. The corresponding quantum numbers of the intermediate states are a result of our calculations. We find good agreement for the model calculations and the measured transitions. Unidentified signals observable espe-

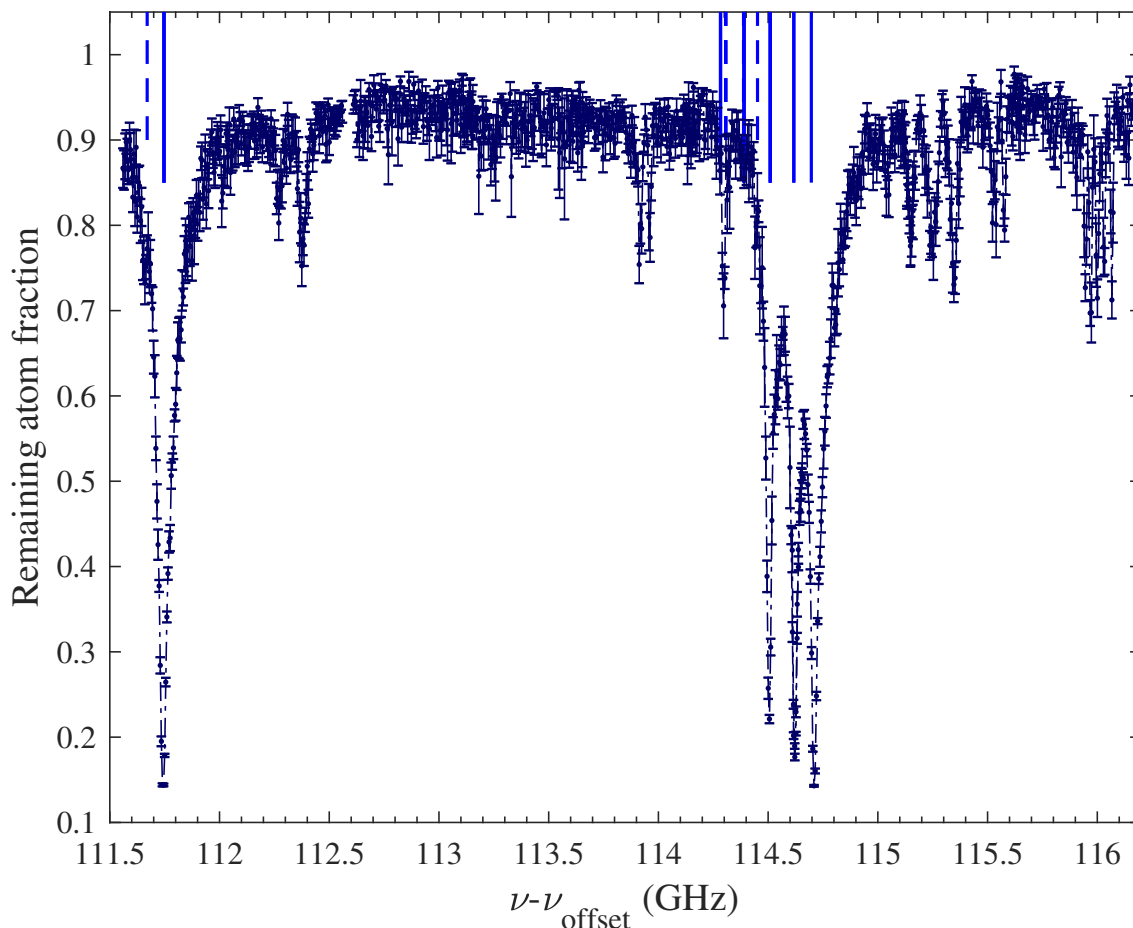cially around the 0_g^- manifold are discussed in Sec. S5.13.3.

Figure 5.25: Photoassociation spectrum of the theoretically expected frequency positions of intermediate states (photoassociation) with the (1,2) REMPI data. Shown is a measured spectrum where we photoassociate molecules in the state $c\,^3\Sigma_g^+\ v' = 0\ 0_g^-$ for an atomic sample of $f = 1, m_f = -1$ atoms ($\nu_{\text{offset}} = 281\,\text{THz}$). Blue vertical lines indicate the photoassociation model calculations (solid $I' = 3$, dashed $I' = 1$). The data are measured for an interaction time of $600\,\text{ms}$ with ion detection scheme I. Also signals from three-body recombination product molecules are visible. Each data point represents the mean value of ten repetitions of the experiment and the used probe laser power is $11\,\text{mW}$.

Since we use ion detection scheme I for these measurements, transitions of three-body re-combination product molecules are also visible in the shown spectra (e.g. $72.5\,\text{GHz}$ Fig. Both figures (Figs. 5.24 and 5.25) show that the strongest transitions are photoassocia-tion transitions towards low J' states (see Tab. 5.6). Since the asymptote for the initially prepared atoms has $J = 1$, the excitation probability is largest towards low J' states. Fur-

thermore, the ionization efficiency was optimized for such a transition (see Fig. 5.23). To get a better signal for higher J' states it could be beneficial to try to optimize the ionization efficiency for such a weak photoassociation signal (see Sec. S5.13.1). Note that especially for the low J' intermediate states of the 1_g manifold, J' is not a good quantum number. Since the hyperfine energy is comparable to the rotational energy for the low J' states of the 1_g manifold [43], the energy levels feature several rotational contributions. This complicates the evaluation of the product molecule spectra.

Table 5.6: Calculated (ν_{calc}) and measured (ν_{meas}) term frequencies for the $c\,^3\Sigma_g^+$ $v' = 0$ manifold, with $\nu_{\mathrm{offset}} = 281\,\mathrm{THz}$. The absolute offset of the model calculations is chosen to match the frequency of the first calculated photoassociation with the first measured photoassociation. $\Delta\nu = \nu_{\mathrm{calc}} - \nu_{\mathrm{meas}}$ is the frequency difference of the calculated and the measured line. If no measured frequency is given, $\Delta\nu$ is calculated with respect to the closest measured signal (of the next line above). Calculated intermediate states that are not in the measured range or have a high $\langle J' \rangle > 3.3$ are not shown. Measured signal strengths are indicated by s=strong (nearly all atoms are lost), n=normal (good signal), w=weak (barely visible), and ew=extremely weak (could also be noise) to give a rough impression of the signal quality. The initially prepared atoms are in the $f = 1, m_f = -1$ state. The nominal uncertainty of the wavemeter is 60 MHz. For the calculations, we have used the parameters that are given in [43]. Our measured results are in good agreement with those given in [43] within the nominal uncertainty of the wavemeter.

$\nu_{\mathrm{calc}} - \nu_{\mathrm{offset}}$ (GHz)	$\nu_{\mathrm{meas}} - \nu_{\mathrm{offset}}$ (GHz)	$\Delta\nu$ (MHz)	signal strength	I'	$\langle J' \rangle$	F'_{tot}
1_g						
71.265	71.265	ref.	s	3	1.2	2.0
71.973	71.968	5	s	3	1.3	3.0
72.692	72.697	-5	ew	1	1.1	1.0
73.250	73.265	-15	ew	3	1.6	4.0
73.348	73.350	-2	s	3	2.0	1.0
73.361		11		1	1.2	2.0
73.909	73.916	-7	n	3	2.0	2.0
74.424	74.440	-16	w	1	2.0	1.0
74.580	74.577	3	w	3	2.0	3.0
74.826	74.826	0	w	1	1.9	2.0
75.012	75.013	-1	n	1	2.1	3.0
75.077	75.116	-39	w	3	2.3	5.0
75.387	75.368	19	w	3	2.0	4.0
76.733	76.753	-20	n	3	3.0	1.0
76.820	76.830	-10	n	3	3.0	2.0
77.043	77.044	-1	n	3	3.0	3.0
77.316	77.357	-41	ew	1	3.0	2.0
77.401		44		3	2.9	4.0
77.455	77.456	-1	ew	1	3.0	3.0
77.580	77.578	2	ew	1	3.0	4.0
77.601		23		3	3.2	6.0
77.621		43		3	3.0	5.0
0_g^-						
111.670	111.660	10	w	1	0.0	1.0
111.747	111.745	2	s	3	0.0	3.0
114.283	114.297	-14	n	3	2.0	5.0
114.307	114.325	-18	ew	1	2.0	3.0
114.388	114.390	-2	ew	1	2.0	2.0
114.390		0		3	2.0	4.0
114.452	114.450	2	ew	1	2.0	1.0
114.510	114.506	4	s	3	2.0	3.0
114.617	114.621	-4	s	3	2.0	2.0
114.697	114.709	-12	s	3	2.0	1.0

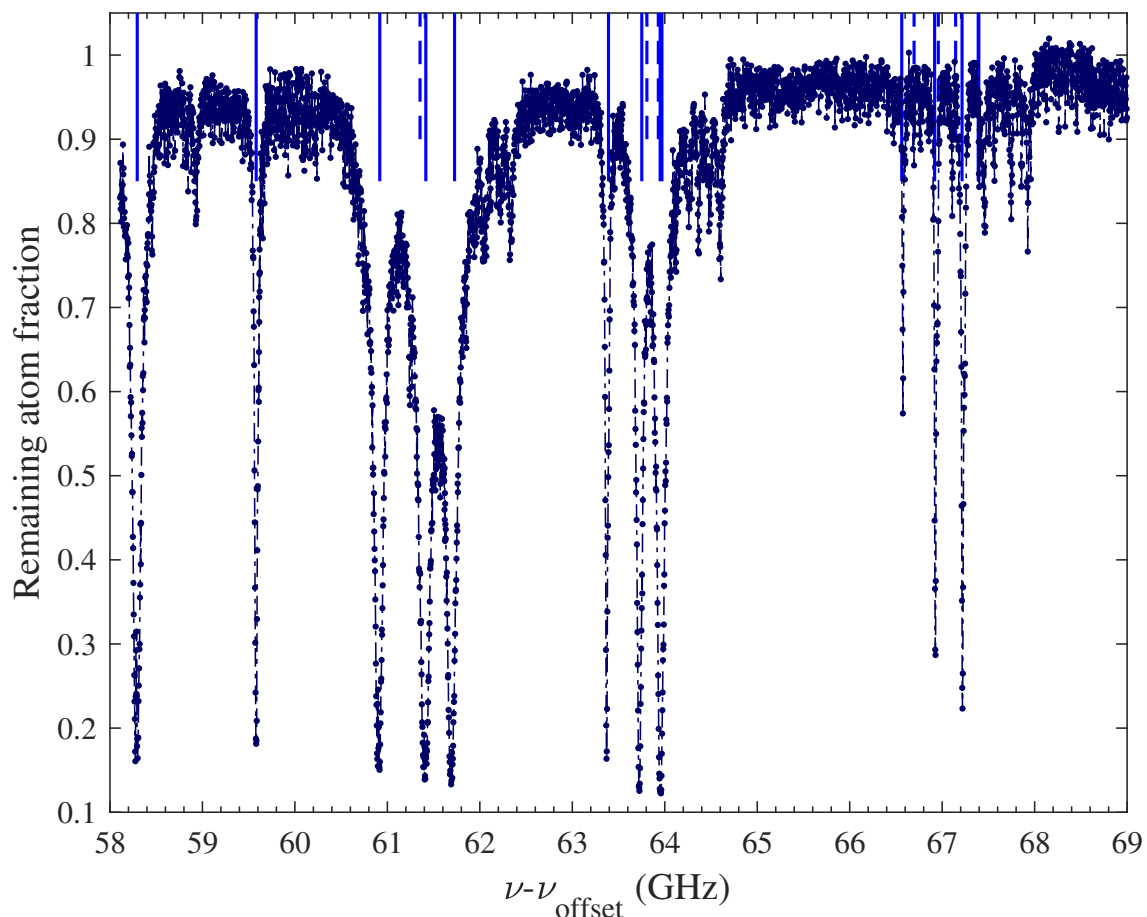**Photoassociation spectra of $f = 2$ atomic samples**

Figure 5.26: Photoassociation spectrum of the theoretically expected frequency positions of intermediate states (photoassociation) with the (1,2) REMPI data. Shown is a measured spectrum where we photoassociate molecules in the state $c^3\Sigma_g^+$ v$' = 0$ 1_g for an atomic sample of $f = 2$, $m_f = 2$ atoms ($\nu_{\text{offset}} = 281$ THz). Blue vertical lines indicate the photoassociation model calculations (solid $I' = 3$, dashed $I' = 1$). The absolute offset of the model calculations is chosen to match the frequency of the first calculated photoassociation line ($I' = 3$, $\langle J' \rangle = 1.3$, $F'_{\text{tot}} = 3$) with the first measured photoassociation signal. The data are measured for an interaction time of 1.1 s with ion detection scheme I. Also signals from three-body recombination product molecules are visible. Each data point represents the mean value of ten repetitions of the experiment.

The $f = 2 + f = 2$, $m_f = 2 + m_f = 2$ $5s + 5s$ asymptote is shifted by twice the ground state hyperfine shift of ^{87}Rb i.e. -13.67 GHz relative to the signals of the former Section S5.13.2. The measured distance for the two different atomic samples of the intermediate state with $I' = 3$, $\langle J' \rangle = 1.3$, $F'_{\text{tot}} = 3$ of the $c^3\Sigma_g^+$ v$' = 0$ 1_g manifold is about -13.68 GHz

and therefore only shows a slight deviation. The atomic samples of $f = 2$, $m_f = 2$ atoms have been measured with a probe laser power of $23\,\text{mW}$. For further information concerning the notation in the following, see Section 5.8.1, and for the typically used experimental parameters, see Section 5.8.2.
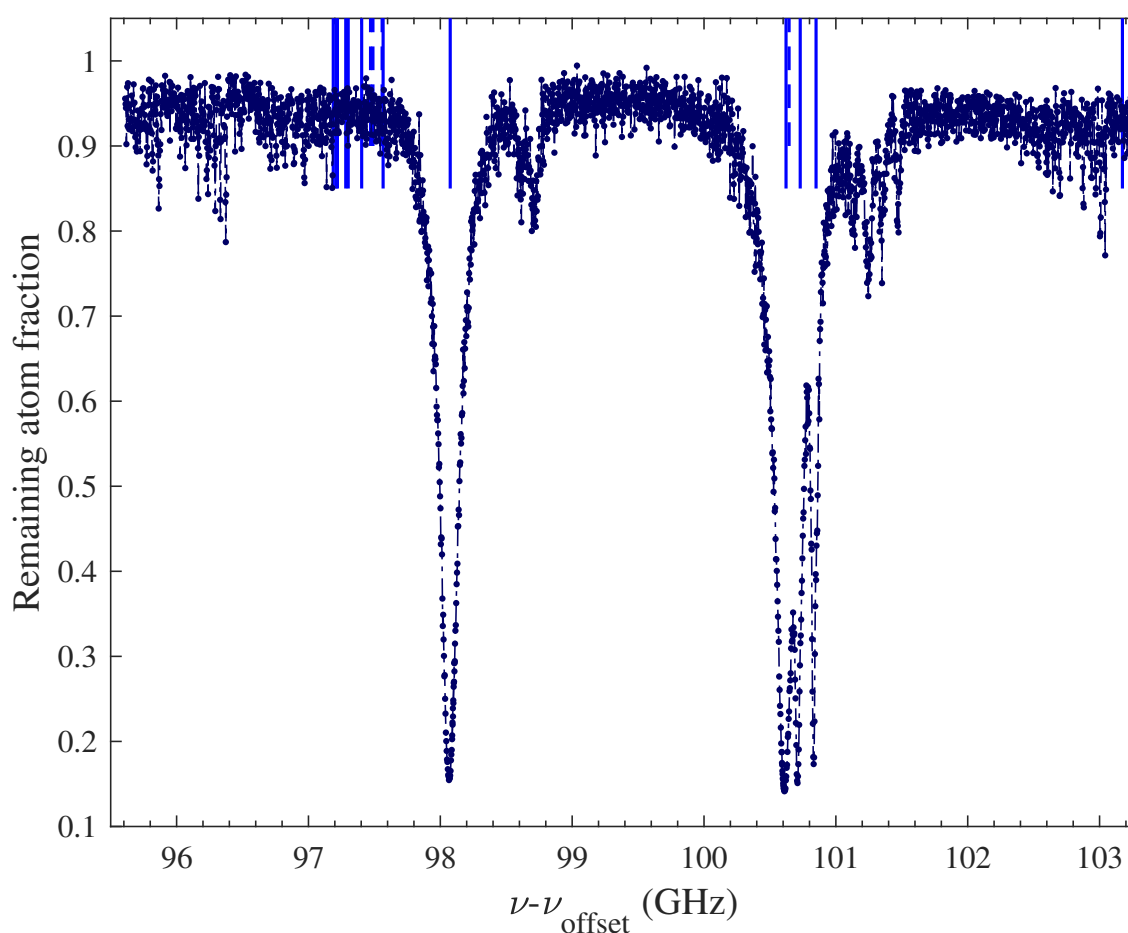
Figure 5.27: Photoassociation spectrum of the theoretically expected frequency positions of intermediate states (photoassociation) with the (1,2) REMPI data. Shown is a measured spectrum where we photoassociate molecules in the state $c\,^3\Sigma_g^+$ $v' = 0\,0_g^-$ for an atomic sample of $f = 2$, $m_f = 2$ atoms ($\nu_{\text{offset}} = 281\,\text{THz}$). Blue vertical lines indicate the photoassociation model calculations (solid $I' = 3$, dashed $I' = 1$). The data are measured for an interaction time of $1.1\,\text{s}$ with ion detection scheme I. Also signals from three-body recombination product molecules are visible. Each data point represents the mean value of ten repetitions of the experiment.

In Figure 5.26, the $c\,^3\Sigma_g^+$ $v' = 0\,1_g$ manifold and in Figure 5.27 the $c\,^3\Sigma_g^+$ $v' = 0\,0_g^-$ manifold measured with ion detection scheme I are shown. The blue vertical lines (solid

$I' = 3$, dashed $I' = 1$) indicate the positions of the calculated $c\,{}^3\Sigma_g^+$ $v' = 0$ manifold state positions (see Sec. 5.8.3) and are given in Table 5.7. The only exception is the bunch of blue vertical lines at the lower frequency side of the first measured 0_g^- photoassociation signal which are high $\langle J' \rangle > 6$ states of the 1_g manifold that are not given in the table. In general, it can be seen that the calculated intermediate state positions match very well. The higher probe laser power and long interaction time is beneficial for the signal strength of the measured photoassociation signals. Even high $\langle J' \rangle = 3.9$ states[21] can be detected with a strong signal, as a small number of ions leads to a strong atom loss. Unidentified signals observable especially around the 0_g^- manifold are discussed in the following Sec. S5.13.3.

---

[21] Note that J' is not a good quantum number for 1_g, but it is quite good for 0_g^- as mentioned in the section before and [43].

Table 5.7: Calculated (ν_{calc}) and measured (ν_{meas}) term frequencies for the $c\,^3\Sigma_g^+$ v$'=0$ manifold, with $\nu_{\text{offset}} = 281$ THz. The absolute offset of the model calculations is chosen to match the frequency of the first calculated photoassociation line ($I' = 3$, $\langle J'\rangle = 1.3$, $F'_{\text{tot}} = 3$) with the first measured photoassociation signal. $\Delta\nu = \nu_{\text{calc}} - \nu_{\text{meas}}$ is the frequency difference of the calculated and the measured line. If no measured frequency is given, $\Delta\nu$ is calculated with respect to the closest measured signal (of the next line above). Calculated intermediate states that are not in the measured range or have a high $\langle J'\rangle > 4.2$ are not shown. Measured signal strengths are indicated by s=strong (nearly all atoms are lost), n=normal (good signal), w=weak (barely visible), and ew=extremely weak (could also be noise) to give a rough impression of the signal quality. The initially prepared atoms are in the $f=2$, $m_f=2$ state. The nominal uncertainty of the wavemeter is 60 MHz. The used rotational constant for the model calculations is slightly changed compared to [43] ($B_{0f1} = 430$ MHz) and here given by $B_{0f2} = 432$ MHz. The rest of the simulation parameters are identical to the given reference.

$\nu_{\text{calc}} - \nu_{\text{offset}}$ (GHz)	$\nu_{\text{meas}} - \nu_{\text{offset}}$ (GHz)	$\Delta\nu$ (MHz)	signal strength	I'	$\langle J'\rangle$	F'_{tot}
1_g						
58.285	58.285	ref.	s	3	1.3	3.0
59.571	59.584	-13	s	3	1.6	4.0
60.908	60.897	11	s	3	2.0	3.0
61.344	61.241	103	w	1	2.1	3.0
61.406	61.403	3	s	3	2.3	5.0
61.717	61.689	28	s	3	2.0	4.0
63.381	63.37	11	s	3	3.0	3.0
63.741	63.726	15	s	3	2.9	4.0
63.797	63.796	1	ew	1	3.0	3.0
63.92	63.903	17	ew	1	3.0	4.0
63.940	63.955	-15	s	3	3.2	6.0
63.959		4		3	3.0	5.0
66.553	66.575	-21	n	3	3.9	3.0
66.686	66.695	-9	ew	1	4.0	3.0
66.908	66.928	-20	s	3	3.9	4.0
66.948		20		1	4.0	4.0
67.135	67.109	26	w	1	4.0	5.0
67.205	67.22	-15	s	3	3.9	5.0
67.38	67.397	-17	w	3	4.0	6.0
67.387		-10		3	4.1	7.0
0_g^-						
98.065	98.065	0	s	3	0.0	3.0
100.61	100.611	1	s	3	2.0	5.0
100.64		24		1	2.0	3.0
100.72	100.709	11	s	3	2.0	4.0
100.84	100.832	8	s	3	2.0	3.0

5.13.3   Unidentified signals in the measurements for $f = 2$ atomic samples
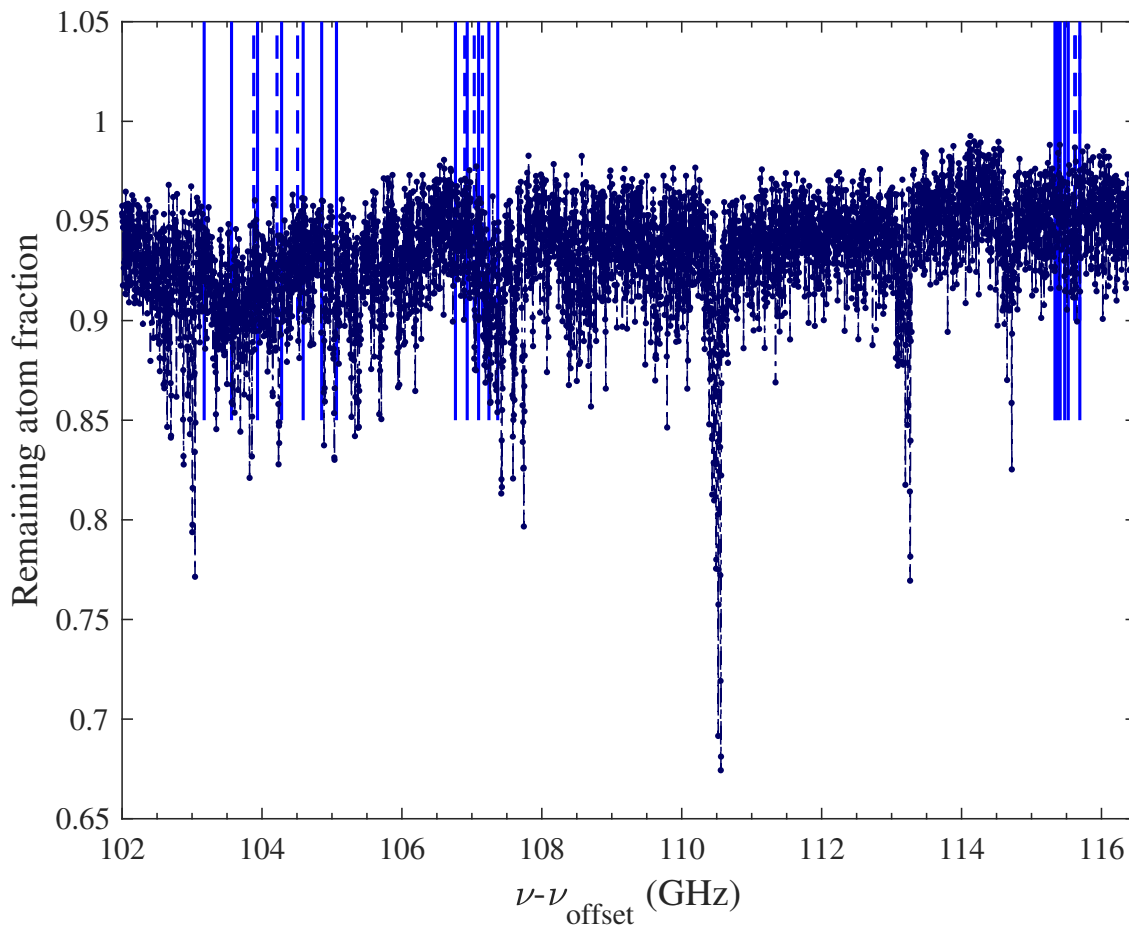

Figure 5.28: Unidentified signals measured for $f = 2$, $m_f = 2$ atoms at higher frequencies as the $c^3\Sigma_g^+$ $v' = 0$ 0_g^- manifold shown in Figure 5.27. The remaining atom fraction is plotted versus the probe laser frequency. Blue vertical lines indicate the photoassociation model calculations (solid $I' = 3$, dashed $I' = 1$), we cannot see evidence for them in the spectrum. The data are measured for an interaction time of $1.1\,\mathrm{s}$ with ion detection scheme I. Each data point represents the mean value of ten repetitions of the experiment. Error bars are not plotted for clarity, but are about ± 0.02 arb. unit.

Although the ionization laser frequency was optimized not to produce unwanted couplings, unidentified signals are occurring in some of the measurements. The unidentified signals of $f = 2$ atomic samples are shown exemplarily. In Figure 5.27, at about $96\,\mathrm{GHz}$ and $103\,\mathrm{GHz}$, many unidentified peaks with untypical line shapes are visible. A similar

type of resonances is also visible in the continuation of this figure (see Fig. 5.28). These signals are not matching with the theoretically expected positions of photoassociation transitions. They are also not matching with expected *X-a* state transitions, although the number of possible transitions was increased for the analysis (not shown).

Therefore, analog to Figure 5.21 it is likely that the ionization laser couples more deeply bound *X-a* states to the intermediate states in the vicinity (see Fig. 5.22A). Further investigations of the unidentified peaks are necessary to identify them.

5.13.4 Suppressed product molecule signals due to large ion numbers

At the used ionization laser frequencies, the ionization efficiency is generally larger than for the experiments where we photoionize via the spin singlet channel[22]. For large ion numbers it can become important to reduce the probe laser power (or interaction time) to be able to resolve the product molecule signals as can be seen in Figure 5.29. Here, the remaining atom fraction is plotted versus the probe laser frequency for two probe laser powers. The resulting atom loss induced by the ions is measured with ion detection scheme I. The black curve shows a measurement with a probe laser power of 3 mW. The product molecule transitions PA Nr. 2, v$= -2$, $R = 2,0$ (2,-2,[2,0]) around 72.55 GHz are clearly visible. The same transitions measured with a higher probe laser power of 50 mW (red curve) are barely visible. This has two reasons. First, at some probe laser power all possible product molecules can be excited. Further increasing the probe laser power then only increases the signal strength of the photoassociation signals. Using a probe laser power slightly above the maximum for the product molecule signal is therefore the optimum. This is also beneficial for the relative product molecule signal strength compared to other resonances e.g. lines from unwanted coupling mechanisms. Second, high ionization efficiency means that a low number of molecules in the intermediate state will lead to a sizeable number of ions. Due to the non-linearity of the atom loss using ion detection scheme I (see additional content in Sec. 4.2.5), the three-body recombination signals are drowned under the broadened (i.e background due to off-resonant excitation) photoassociation signal (red curve).

---

[22]More details about the ionization efficiency can be found later in the Sec. S5.13.8 and Sec. S5.13.9.
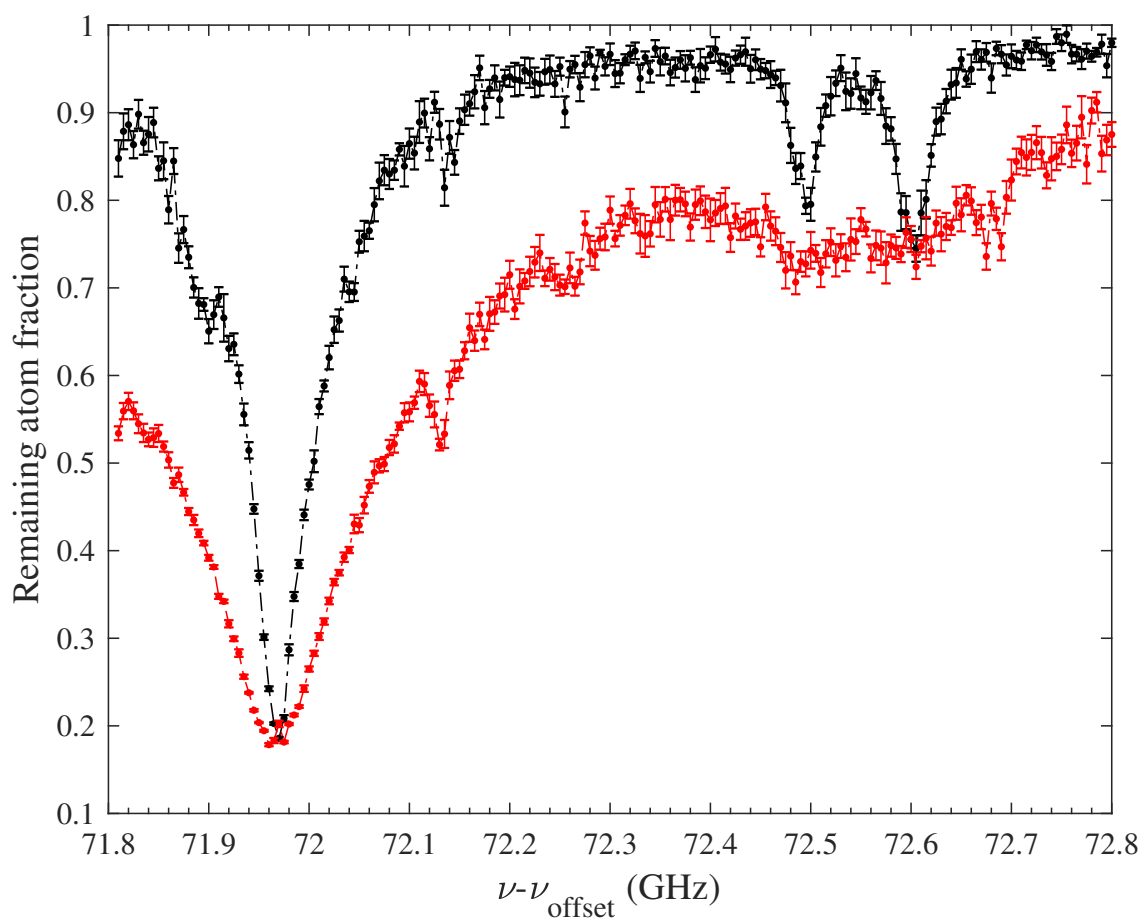
Figure 5.29: Product molecule and photoassociation REMPI signals for two probe laser powers. Shown is the remaining atom fraction plotted versus the probe laser frequency ($\nu_{offset} =$ 281 THz). The data display two-color (1,2) REMPI spectra for an $f = 1$, $m_f = -1$ atomic sample, utilizing the intermediate state $c\,^3\Sigma_g^+$ $v' = 0$ 1_g (2) (see Tab. 5.1). The strong atom loss feature on the left side is the photoassociation signal and the two signals around 72.55 GHz are the product molecule signals (2,-2,[2,0]). The black curve is measured with a probe laser power of 3 mW and the red curve with 50 mW.

5.13.5   Further analysis of the $f = 2$ atomic samples 1_g spectrum

In this section a further analysis of the data presented in Section 5.9.2 is shown. It is provided to justify the conclusions made. The bottom line is that we do not observe any clear product molecule signals except for the product molecules formed in v$= -1$ and the v$= -2$ $R = 0, 2$ states.
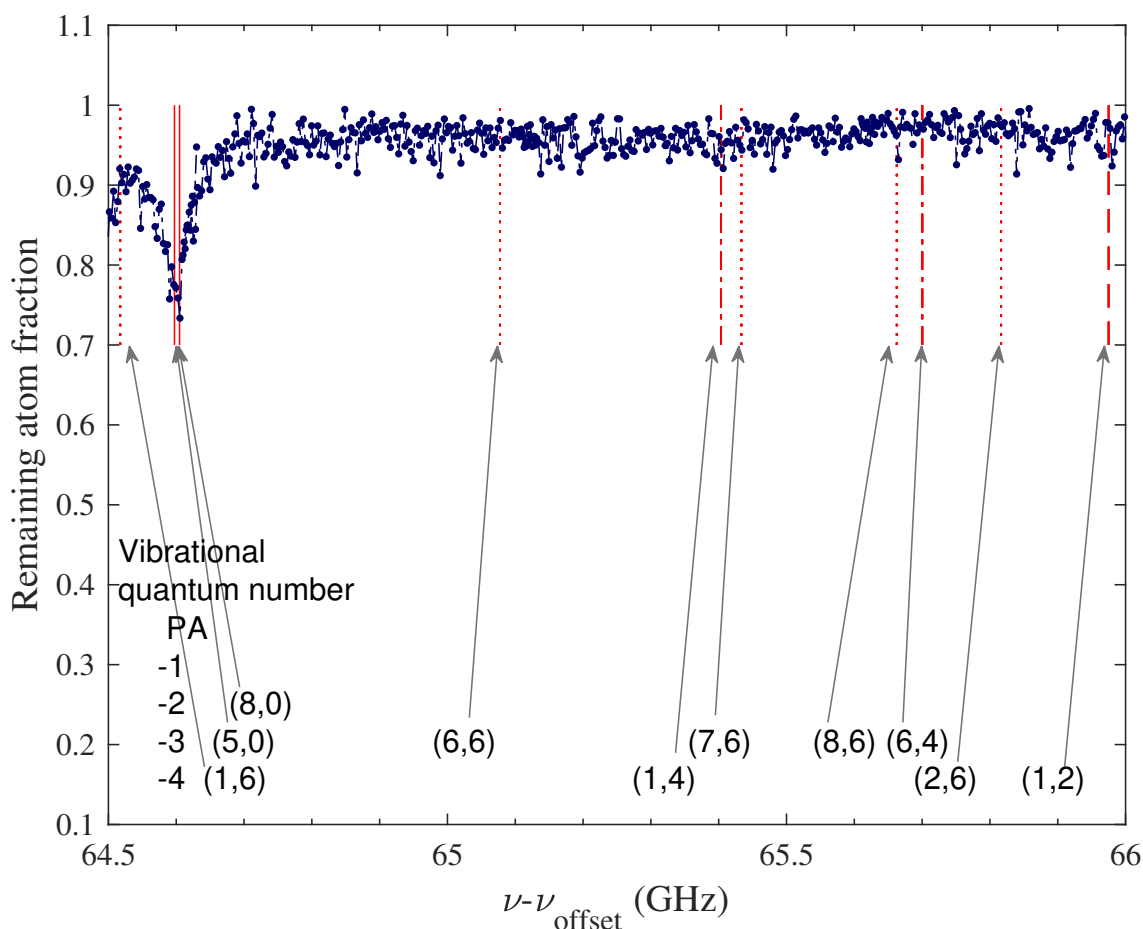
Figure 5.30:   Zoom into Figure 5.9. Shown is the frequency region from about 64.5 GHz to 66 GHz. At the top of the figure the calculated intermediate state frequency positions (see Sec. S5.13.2) are given as gray vertical lines ($I' = 3$ solid, $I' = 1$ dashed). The blue vertical lines indicate the positions of the selected photoassociation (PA) transitions given in Table 5.2. The red vertical lines show the respective transitions from X-a molecules, the line style indicates the rotational state R of the initially formed molecule: solid $R = 0$, dashed $R = 2$ and, dash-dotted $R = 4$, and dotted $R = 6$. The arrows indicate the transitions marked with vertical lines. The arrows are labeled by (PA Nr., R). Due to the large number of states, each horizontal row corresponds to a given vibrational bound state quantum number, which is indicated on the left hand side. Most of the expected transitions do not show a signal in this range.

In Figure 5.30 at about 64.6 GHz a signal is visible. The signals frequency is matching with the predicted positions of the (8,-2) i.e. PA Nr. 8, v$= -2$, $R = 0$ and the (5,-3) transitions (notation see 5.8.1). So far we could find many signals for v$= -2$ product molecules, but we could not observe any indications for v$= -3$ product molecules. Still, it is not fully possible to exclude a contribution of the more deeply bound signal of the strong interme-

diate state (5) to the signal of the (8,-2) transition. The small peak at 64.5 GHz is the tail of the (8,-2,2) transition seen at the right edge of Figure 5.10. All other predicted transition frequencies of v=−3 and v=−4 X-a states in the spectrum do not show a signal. The next part of the spectrum is shown in Figure 5.31 where the $\langle J' \rangle \approx 4$ triplet ([9,10,11]) is visible (see Tab. 5.2). Here it is remarkable that the respective product molecule transitions of the most-weakly bound X-a state ([9,10,11],-1) are very nicely visible for all three of them. The excitation probabilities for the photoassociation signals should be small because the two colliding atoms are starting with $J = 1$ maximally and the $J' = 2$ admixture of the $\langle J' \rangle = 3.9$ states should be comparatively small.

The (9,-2,2) transition at 67.1 GHz shows a good signal while its rotational ground state transition overlaps with the photoassociation PA (11). In the shown range, many small dips especially at positions of predicted transitions are visible e.g. at 66.7 GHz, 66.75 GHz, 66.85 GHz. These are difficult to interpret, as it could be more complex transitions involving more photons (see Sec. S5.13.3) or simply noise. For future work, it needs to be checked if these signals are product molecule signals or have another origin. The last nicely visible signal (at about 67.45 GHz) is most likely the (10,-2,2) transition. This signal exhibits an unusual line shape where the right side is very steep while the left side is much more extended. Eventually, we see a small signal for the expected photoassociations at that position that overlaps with the (10,-2,2) transition. Further measurements here also have to verify the origin of this signal. Anyway, still we cannot observe a clear signal of a more-deeply bound vibrational manifold as v= −2.

The last zoomed in part of the overview is Figure 5.32, where the (10,-2) transition can be observed (at about 67.6 GHz). The signal is much weaker than the (10,-2,2) transition in the former figure. A similar relation of the signal strengths between the two rotational components is also observable for the (11,-2,[2,0]) transitions at about 67.8 GHz.

The last observable signal in the spectrum of Figure 5.32 is very interesting. At a frequency of about 67.9 GHz a signal is visible at the position of the (5,-4,6) transition. It matches exactly the expected frequency and except for the rather broad base, the line shape is normal. The intermediate state used for this transition showed a strong loss feature for the photoassociation signal. To find out if the signal of this highly rotating state is real, we can correlate it to other signals. This is done exemplary in the following.

First, we note that the other states of the $\langle J' \rangle \approx 2$ line triplet do not show this X-a state ((3,-4,6) Fig. 5.31 and (4,-4,6) Fig. 5.32). This could be explained with a lower ionization rate as it can be estimated from the photoassociation signals in Figure 5.9. The next

step is to check if other v= $-3, -4$ *X-a* states can be detected via this intermediate state. No other clear signal is visible for the (5,[-3,-4],[...]) transitions, as many of them are overlapped with other lines.
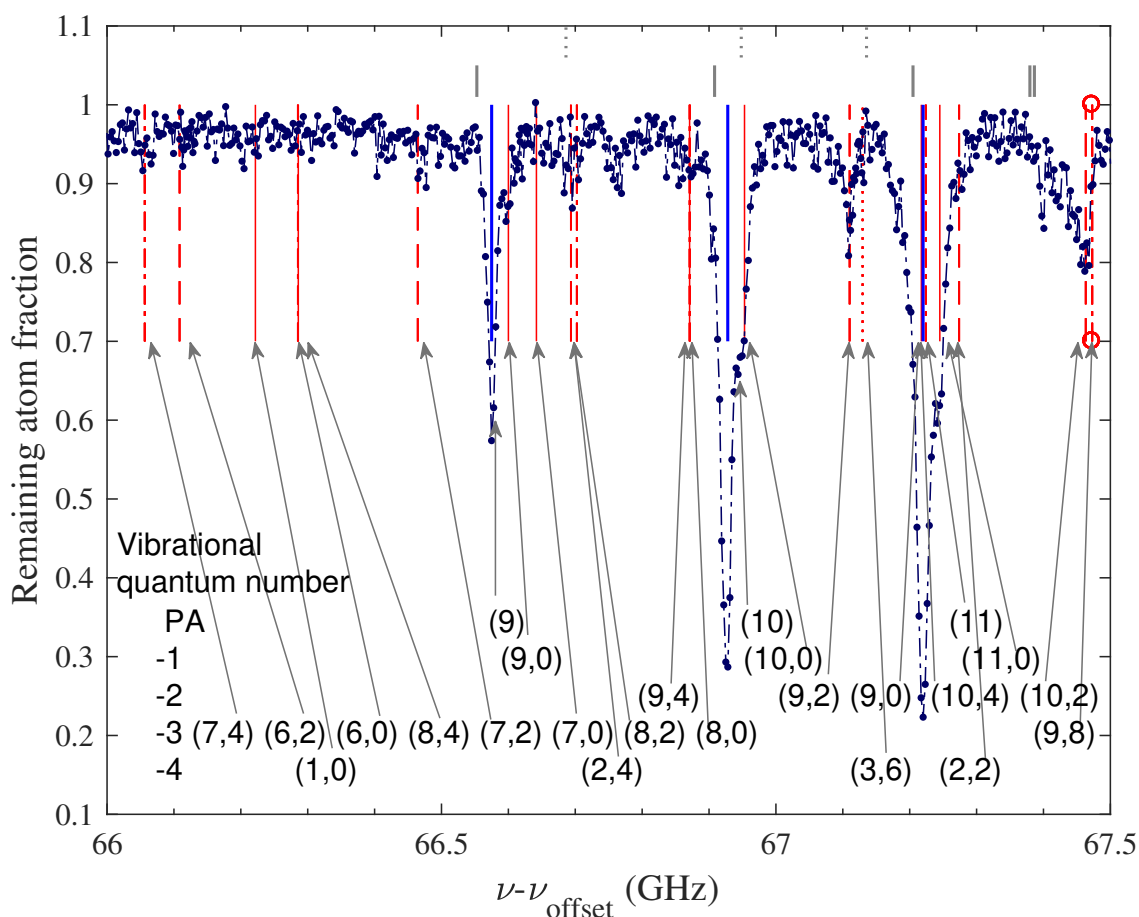

Figure 5.31: Zoom into Figure 5.9. Shown is the frequency region from about 66 GHz to 67.5 GHz. At the top of the figure the calculated intermediate state frequency positions (see Sec. S5.13.2) are given as gray vertical lines ($I' = 3$ solid, $I' = 1$ dashed). The blue vertical lines indicate the positions of the selected photoassociation (PA) transitions given in Table 5.2. The red vertical lines show the respective transitions from *X-a* molecules, the line style indicates the rotational state R of the initially formed molecule: solid $R = 0$, dashed $R = 2$ and, dash-dotted $R = 4$, dotted $R = 6$, and dash-dotted with a circle at the end $R = 8$. The arrows indicate the transitions marked with vertical lines. The arrows are labeled by (PA Nr., R). Due to the large number of states, each horizontal row corresponds to a given vibrational bound state quantum number, which is indicated on the left hand side.

Another possibility is that the signal's origin is the not drawn v$= -2$, $R = 2$ state of the theoretically expected intermediate states at 67.4 GHz in the former figure (gray line). If one assumes that low rotational states i.e. also the photoassociation are barely visible, but higher rotations are, it would be also expected to see its v$= -2$, $R = 4$ state[23]. However, at about 67.7 GHz where this transition is expected no signal is visible. Hence, it is not possible to make a final statement. Further measurements are necessary to verify the source of this signal. It would be a remarkable result for $f = 2$ atomic samples to verify such a large population in the v$= -4$, $R = 6$ X-a state.
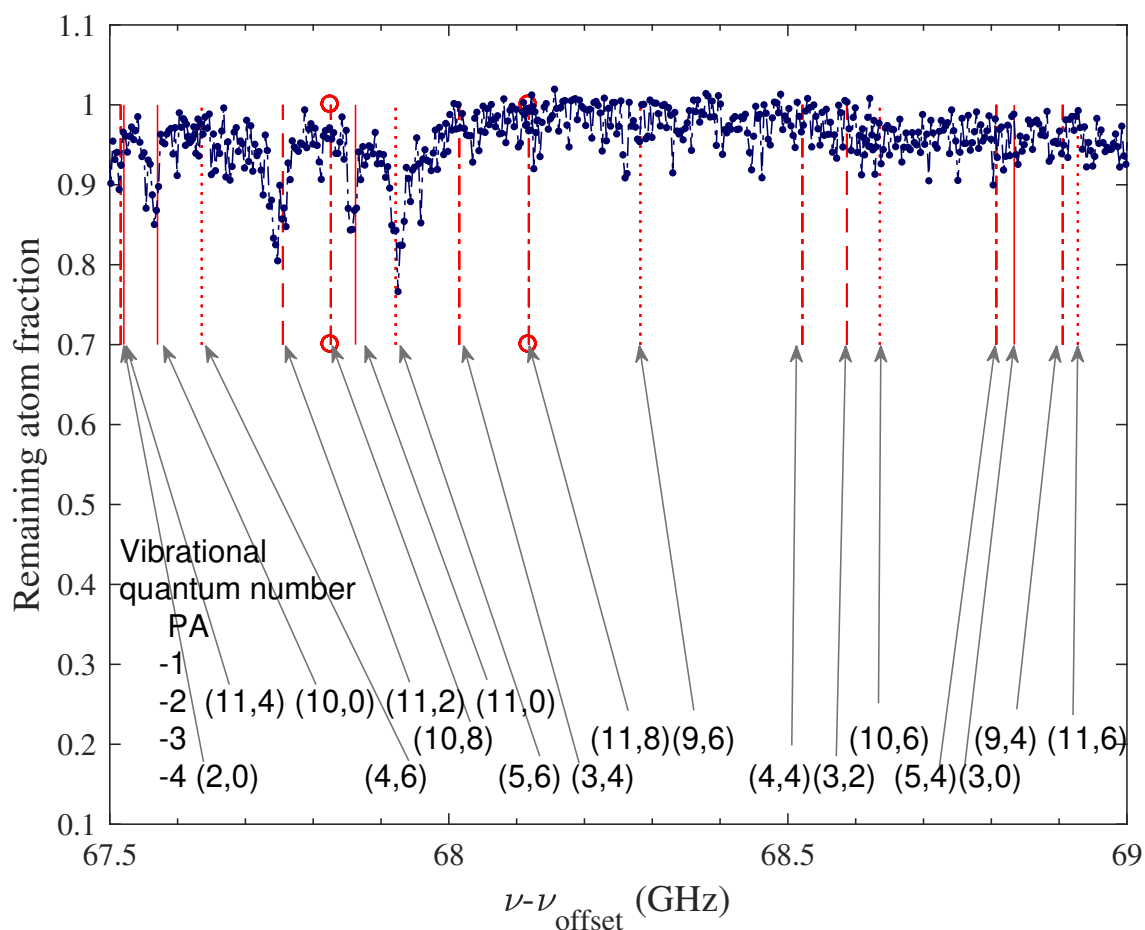
Figure 5.32: Zoom into Figure 5.9. Shown is the frequency region from about 67.5 GHz to 69 GHz. The notation for the vertical lines is the same as in the former figures. The arrows indicate the transitions marked with vertical lines. The arrows are labeled by (PA Nr., R). Due to the large number of states, each horizontal row corresponds to a given vibrational bound state quantum number, which is indicated on the left hand side.

---

[23] Assuming that there are product molecules in that state to be found.

In conclusion, we could not observe any clear signals for *X*-*a* states except for the v= −1 and v=−2, *R* = 2,0 product molecule states. Therefore, those are most likely the only considerably populated states for the three-body recombination in $f = 2$, $m_f = 2$ atomic samples.

5.13.6   Calibrating the magnetic field of the experimental setup
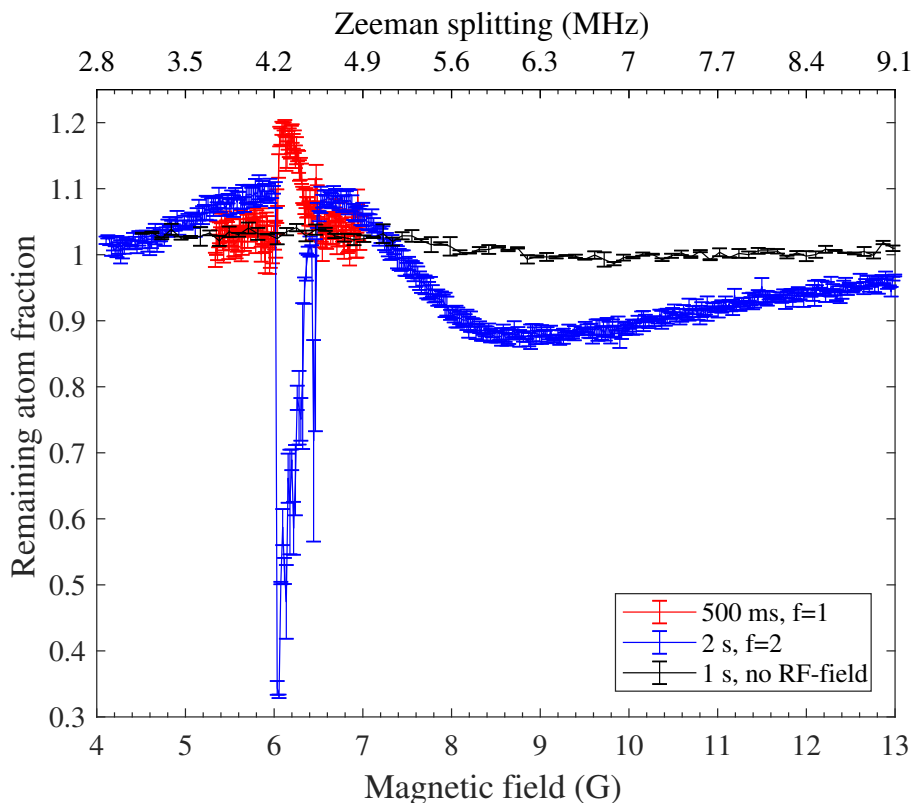
Figure 5.33: Zeeman tuned resonant RF transitions of Rb $f = 1,2$ atoms in the Paul trap RF-field. Shown is the measured remaining atom fraction after a holding time as given in the legend, plotted versus the magnetic field applied during that time. On top of the figure the relative Zeeman frequency shift for $\Delta m_f = 1$ corresponding to the applied magnetic field, is provided. The red and blue measurements are carried out with the Paul trap RF-fields being turned on and driven with a frequency of 4.214 MHz. The black measurements are obtained for the Paul trap being turned off completely and serve as a reference. All error bars given in the figures represent the standard deviations of the mean values.

Here we will discuss a phenomenon that occurs for our high-density atomic clouds in the Paul trap radio frequency electric field (RF-field). Figure 5.33 shows measurements of the remaining atom fraction as a function of the magnetic field for different parameter

settings. For these data, different atomic samples were prepared and the remaining number of atoms was measured after a certain holding time in the optical dipole trap, during which the respective magnetic field was applied. The red data shows results for $f = 1$, $m_f = -1$ atomic samples (notation, see Sec. 5.8.1) and the blue data shows results for $f = 2$, $m_f = 2$ atomic samples. For these measurements, the Paul trap was turned on, however, no ions were trapped, since the Paul trap was operated without confinement along the axial direction. It is clearly visible that at a magnetic field of about 6 G an increased atom number is visible for $f = 1$ atoms (red data) and a massive loss occurs for the $f = 2$ atoms (blue data). The black data represent a reference scan for $f = 2$ atoms where the Paul trap was completely turned off. It shows a stable atom number.

It turns out that the Zeeman frequency splitting of two m_f states ($\Delta m_f = 1$) is identical to the Paul trap RF drive frequency of 4.214 MHz, for the given field strength. Therefore, the most probable explanation for the massive change in atom number is that the Paul trap fields are coupling the Zeeman states in the initially spin-polarized atomic samples (see also [66]). The spin mixed samples show a different time evolution of the atom number than the spin-polarized samples. The tails of the resonances towards higher magnetic fields can be explained with the rather slow ramp speed of the magnetic field in our steel vacuum chamber.

It is not completely clear why for the $f = 1$, $m_f = -1$ atomic samples the atom number is increased on resonance, while for the $f = 2$, $m_f = 2$ samples it is strongly decreased. Indeed, the decay of the $f = 2$ sample is so fast, that it is difficult to measure the dynamics on the millisecond timescale e.g. by investigating Zeeman states of photoassociation signals. This has to be investigated in more detail in future. From the measurements we find the conversion factors (resulting magnetic field/voltage in control software) and (resulting magnetic field/current for the 'Feshbach coils') to be

$$41.05\,\text{G/V and } 2.053\,\text{G/A,}$$

respectively. The resulting magnetic fields are in very good agreement with observed Zeeman shifts of photoassociation signals. This can be seen in Chapter 5 and the measurements described Section 5.10.

5.13.7 Magnetic field dependence of $f = 1$ atomic samples measured via the 1_g manifold
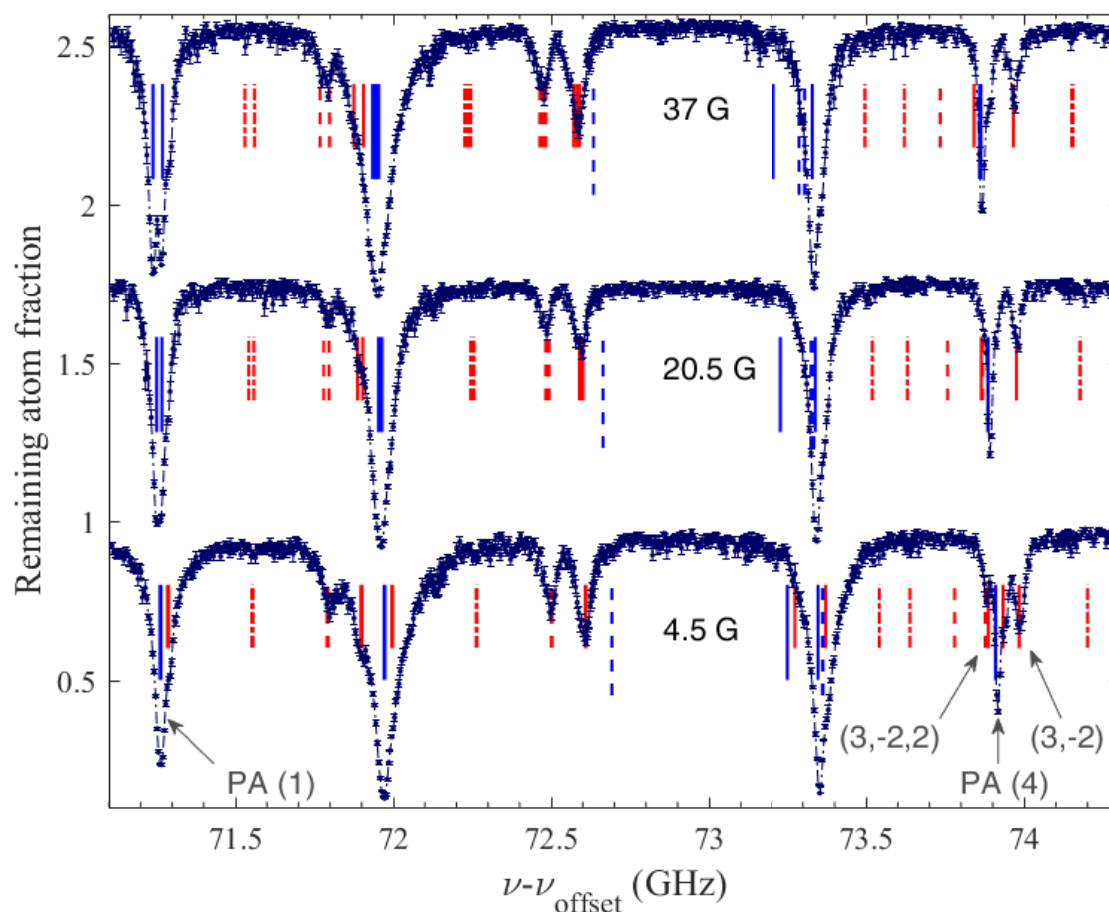

Figure 5.34: (1,2) REMPI spectra for different magnetic field strengths (as given in the plot) obtained using intermediate states of the $c\,^3\Sigma_g^+$ v' = 0 1_g manifold. Shown is the remaining atom fraction of an atomic sample initially prepared in the $f = 1$, $m_f = -1$ state versus the probe laser frequency ($\nu_{\text{offset}} = 281$ THz). The measurements are offset vertically proportional to the applied homogeneous magnetic field. The gray arrows indicate states, which are discussed in the text. The blue vertical lines are photoassociation transitions and are extracted from our simulation ($I' = 3$ solid, $I' = 1$ dashed). In the theoretical predictions, transitions towards different $m'_{F_{tot}}$ states ($m'_{F_{tot}} = -1, -2, -3$) are resolved, however no corresponding labeling is given in the plot for the sake of simplicity. In the measurement for a magnetic field of 4.5 G the calculated transitions (red vertical lines) from v= −1 and v= −2 X-a bound states are shown (presented in analogy to Fig. 5.12). For the other two measurements only the v= −2 transitions are shown (only into $I' = 3$ intermediate states) for the sake of simplicity. The used probe laser power is 3 mW. Each data point represents the mean value of ten repetitions of the experiment.

After we have seen the influence of the magnetic field on a REMPI spectrum for the $c\,^3\Sigma_g^+$ 0_g^- manifold (see Sec. 5.10.1), some measurements regarding the $c\,^3\Sigma_g^+\,1_g$ manifold will be shown. The 1_g intermediate states are interesting as they exhibit a larger Zeeman energy level shift than the investigated 0_g^- intermediate states. Thus, we do not only observe the Zeeman shift of the atomic $5s+5s$ asymptote, but also the Zeeman shifts for the intermediate states. Figure 5.34 shows the data for the $c\,^3\Sigma_g^+\,1_g$ manifold (see Tab. 5.1). The spectra are measured for three different magnetic fields of 4.5, 20.5, and 37 G.

Interesting behavior can be found in the given spectra. For example, the photoassociation resonance PA (1) at around 71.3 GHz clearly splits up into a doublet structure for high magnetic fields, which reflects the different Zeeman shifts of the $m'_{F_{tot}} = -1$ (dip on the left) and $m'_{F_{tot}} = -2$ (dip on the right) substates (37 G). For better visibility see also Figure 5.35, which shows a zoom into that region. In this figure we can also observe the most-weakly bound X-a state excited via the $m'_{F_{tot}} = -2$ sub level as a shoulder. The intermediate state's $m'_{F_{tot}}$ splitting is also found for the three-body recombination product molecule transition (1,-2,2) at around 71.8 GHz. For a slightly larger magnetic field as the applied 37 G it will be possible to fully separate the $m'_{F_{tot}}$ components. Note here that by utilizing intermediate states with different quantum numbers e.g. different $m'_{F_{tot}}$ sublevels, a higher selectivity for probing the three-body recombination product molecules can be achieved by exploiting dipole transition selection rules. This should be done for future measurements.

Interesting behavior is also visible for the photoassociation PA (4) signal at 73.9 GHz (marked with arrows in Figure 5.34). For higher magnetic fields the photoassociation PA (4) signal is shifting away from the (3,-2) transition and overlapping with the (3,-2,2) transition. This is interesting as different magnetic field shifts of intermediate states can be used to separate signals that are overlapping for specific magnetic fields, which helps to assign three-body recombination product states.

Figure 5.36 shows the continuation of Figure 5.34. For the expected photoassociation line[24] PA (X) at about 75.1 GHz no signal is visible (arrow in the figure). However, it seems that product molecules can be excited via the (X,-2,2) transition. There is a signal at around 75.6 GHz, which follows the expected magnetic field shift. For an invisible photoassociation line it is expected to also not observe the (X,-2,0) transition, since the $5s+5s$ asymptote and a $R=0$ X-a state have the same rotational character. Indeed, we

---

[24] Since this photoassociation line was not part of the evaluation we give it the photoassociation number 'X'.

cannot observe the (X,-2,0) transition, but with a similar argument we would expect to observe the (X,-2,4) transition. No signal is observable for this transition. Therefore no conclusive statement can be given and further measurements have to identify the origin of the observed line.

Anyway, by comparing magnetic field induced signal shifts to predicted line shifts, even highly rotating product molecules can be identified, although no related photoassociation signal with $R = 0$ is expected due to dipole transition selection rules.
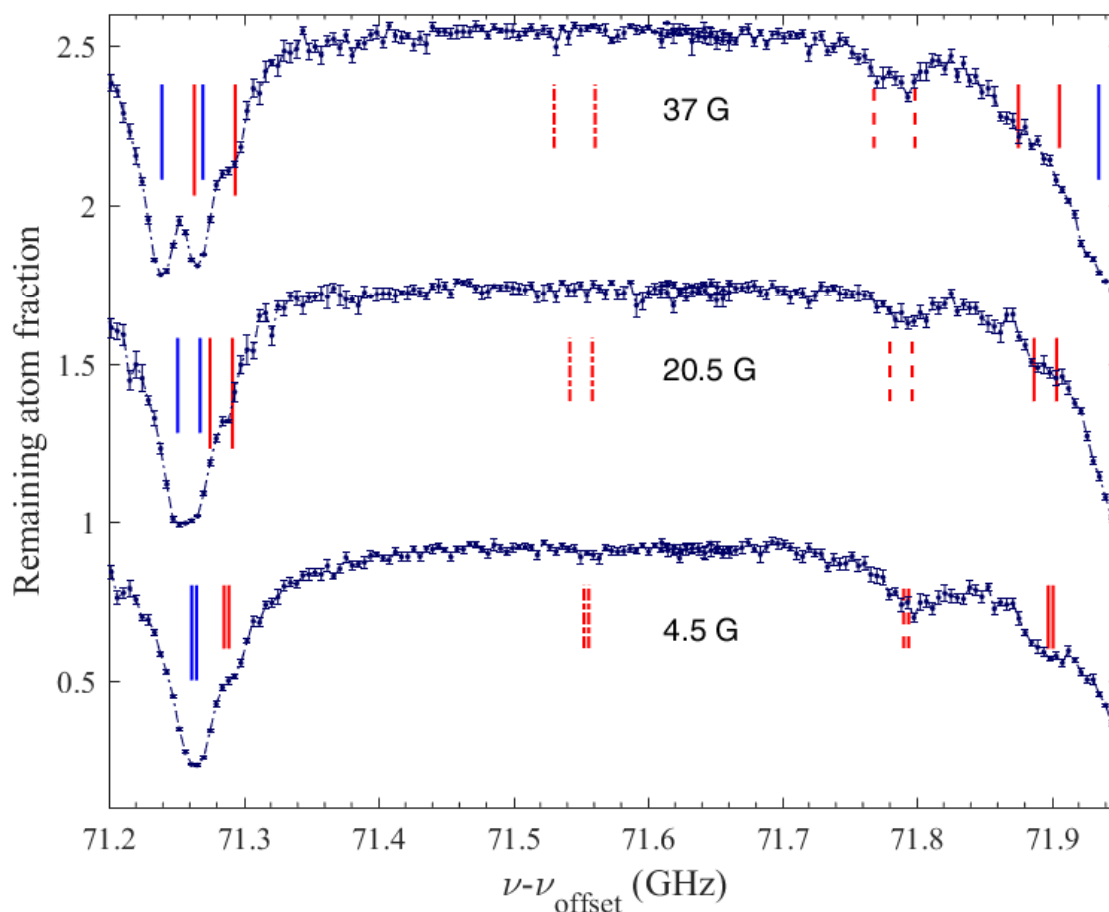

Figure 5.35: Zoom into the (1,2) REMPI spectra obtained using intermediate states of the $c\,^3\Sigma_g^+$ **v$'$ = 0 1$_g$ manifold.** Shown is the frequency range from 71.2 GHz to 71.95 GHz of Figure 5.34 with the same notation. Here the v= −1 state theory lines are given for all three magnetic fields.
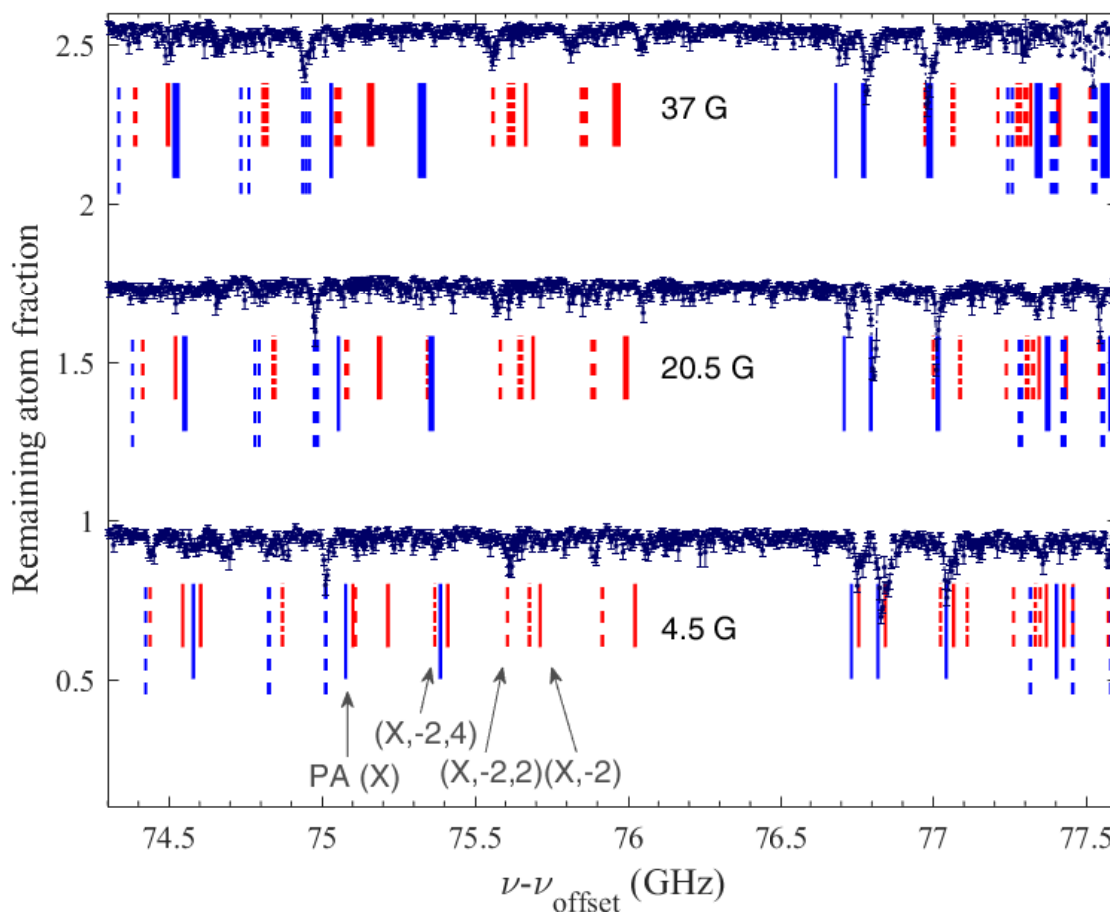
Figure 5.36: (1,2) REMPI spectra for different magnetic field strengths (as given in the plot) obtained using intermediate states of the $c^3\Sigma_g^+$ **v′ = 0** 1_g **manifold.** Continuation of Figure 5.34 with the same notation. Since the photoassociation line marked with the arrow PA (X) was not part of the initial evaluation we give it the photoassociation number 'X'. Using the standard notation we label the photoassociation and the v= −2 X-a states, respectively.

5.13.8   Consistency checks for the ionization efficiencies for $f = 1$ atomic samples

In the following the ionization efficiencies for the Section 5.11.1 are discussed. We use the v= −2, $R = 2,0$ molecule signals (notation see Sec. 5.8.1). For the investigation of

product molecules in these two states, we use different intermediate states and ionization laser frequencies for REMPI. The presented results have to be considered preliminary since additional measurements are necessary to gain full understanding.

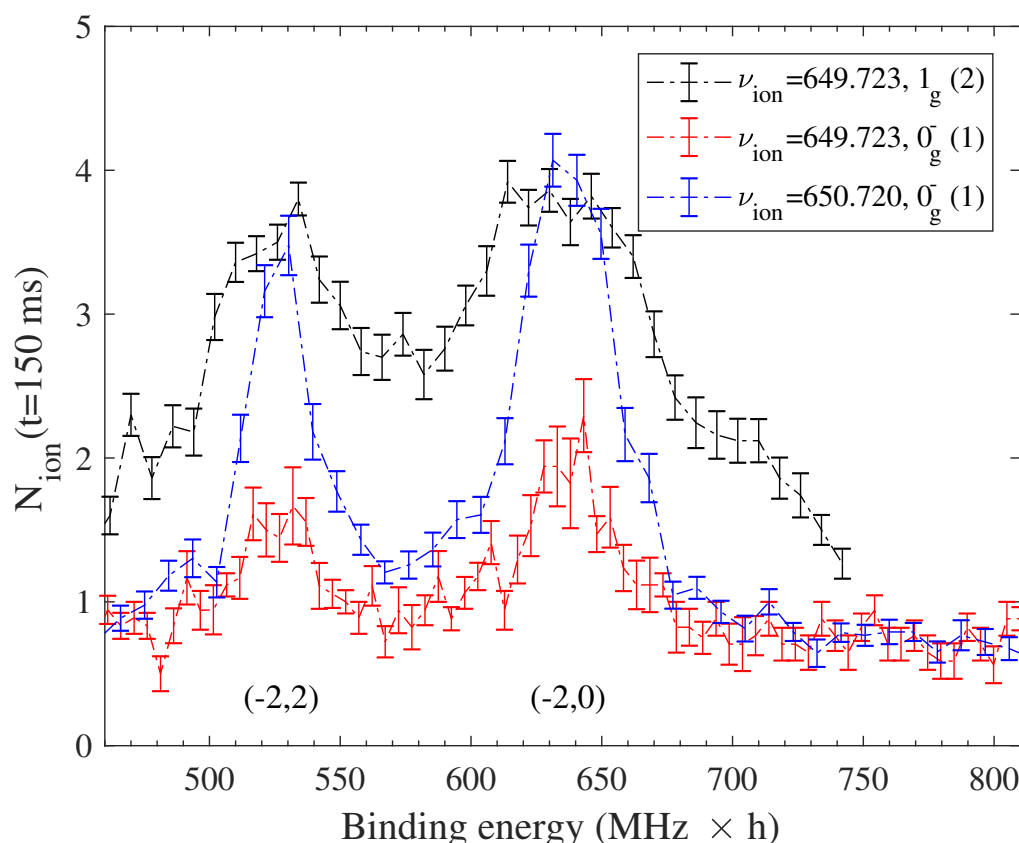**Figure 5.37: Number of produced ions for different intermediate states and ionization laser frequencies when starting from molecules in the states (-2,2) and (-2,0).** Shown is the measured number of ions N_{ion} in 150 ms versus the binding energy in the X-a potentials. The peak on the left is the v$= -2$, $R = 2$ X-a state signal and the peak on the right is the v$= -2$, $R = 0$ X-a state signal. The legend denotes the used ionization laser frequency $v_{ion} = v_{ionlaser} - v_{offset}$ and the used intermediate state. A probe laser power of 18 mW was used. The atomic sample was prepared in the $f = 1$, $m_f = -1$ state and a single data point represents the average value of 51 (black scan), 19 (red scan), and 45 (blue scan) repetitions of the experiment, respectively. All error bars given in the figures represent the standard deviations of the mean values.

We start the discussion with the bare measured data, i.e. no post-processing has been carried out. Figure 5.37 shows the three-body recombination product molecule signals of the v$= -2$, $R = 2, 0$ X-a states for different ionization laser frequencies and intermediate states (as given in the legend). The probe laser power and the ion collection time is the

same for all three curves. The black data shows an excitation to an intermediate state in the $c\,^3\Sigma_g^+\,1_g$ manifold for the standard ionization laser frequency for $f = 1$ atoms ($\nu_{ion:f=1} = 281\,649.723\,\text{GHz}$, see Sec. 5.8.2). The strong signals are broadened compared to the other signals shown. The red data is obtained for the same ionization laser frequency, but for a different intermediate state within the $c\,^3\Sigma_g^+\,0_g^-$ manifold. It is very weak. For the blue data, the ionization laser frequency is changed by about $1\,\text{GHz}$ compared to the red curve. The signals show the same height as for the black data, but a smaller linewidth. This shows two things, first a good ionization laser frequency is very much dependent on the exact intermediate state (different ionization laser frequencies) and second the probe laser power dependence for the two intermediate states seem to be different (broadening of the black data). This again shows what we have already suspected in Section 5.9.1. Hence, it is very difficult to make statements (as in Ch. 4) about the absolute populations of X-a states with product molecules resulting from three-body recombination, without further investigations of the intermediate states. In the following rough estimates of ionization efficiencies for some intermediate states are given and some consistency checks with the performed measurements are discussed.

With a method as described in Section 4.2.10 the ionization efficiency can be measured. From similar ionization efficiency measurements, the following preliminary ionization efficiencies could be derived:

$$\eta_2\{\nu_{ion} = 649.723, 0_g^-(1)\} \approx 9.3 \cdot 10^{-4},$$

$$\eta_2\{\nu_{ion} = 650.72, 0_g^-(1)\} \approx 1.4 \cdot 10^{-3},$$

and

$$\eta_2\{\nu_{ion} = 649.723, 1_g(2)\} \approx 1.4 \cdot 10^{-3}.$$

To test whether these ionization efficiencies are of the correct order of magnitude, we can use the data of Figure 5.37 and check the results for consistency. First, we use the 1_g (black) and the 0_g^- (blue) data of Figure 5.37. The 1_g signals show a line broadening as compared to the 0_g^- signals. Therefore, it can be assumed that all possible product molecules are exited towards the 1_g intermediate state. We find the same ionization efficiencies for both states ($\eta_2\{\nu_{ion} = 649.723, 1_g(2)\}$ and $\eta_2\{\nu_{ion} = 650.72, 0_g^-(1)\}$). Therefore, the 0_g^- signals cannot be larger as the 1_g signals. This is in agreement with the shown data.

Using the same figure (Fig. 5.37), we can use the signal height of the two different 0_g^- measurements to check the ionization efficiencies for the different ionization laser frequencies. For the $v_{ion} = 650.72, 0_g^-(1)$ measurement (blue) the signals are by a factor of two larger as compared to the $v_{ion} = 649.723, 0_g^-(1)$ measurement (red). Indeed, a similar factor is also given in the respective ionization efficiencies.

The estimated ionization efficiencies are larger than the efficiency extracted for the singlet measurements which was $\eta_2 = 6.6 \cdot 10^{-4}$ (Sec. 4.2.10). It can also be estimated if this is consistent by utilizing qualitative measurements. For this, we compare the 1_g (2,-2,[2,0]) signals shown at about 72.5 GHz in Figure 5.6 with the saturated signals for the same product molecule states of the singlet measurements at about 600 MHz in Figure 4.2. Clearly, the signals for the triplet measurement are larger[25]. Assuming a similar population for both intermediate states, this indicates a higher ionization efficiency for the REMPI via the triplet intermediate states.

5.13.9   Ionization efficiencies for the measured $f = 2$ atomic samples

From the heights of the photoassociation signals in Section 5.11.2 it clearly can be seen that every intermediate state leads to a different ion production rate. This can have two reasons. First, the excitation probability in the first step of the REMPI is different and second, the ionization efficiency from the intermediate states is different. From another set of measurements, the following rough ionization efficiencies can be extracted (similar to Sec. 4.2.10) for all four discussed intermediate states in the 0_g^- manifold:

$$\eta_2\{v_{ion} = 649.112, 0_g^-(1)\} \approx 2.6 \cdot 10^{-3},$$

$$\eta_2\{v_{ion} = 649.112, 0_g^-(2)\} \approx 3 \cdot 10^{-3},$$

$$\eta_2\{v_{ion} = 649.112, 0_g^-(3)\} \approx 5.4 \cdot 10^{-3},$$

and

$$\eta_2\{v_{ion} = 649.112, 0_g^-(4)\} \approx 5.5 \cdot 10^{-3}.$$

---

[25]The interaction time for the triplet measurements is 100 ms longer than for the singlet ones, but the atom loss difference is too large to be explained by the larger interaction time only.

With the estimated ionization efficiencies[26] we can deduce the behavior of the excitation probabilities. For this we can compare Figure 5.15 and Figure 5.16 together with the respective ionization efficiencies. This shows that the excitation probabilities towards the intermediate states connected to PA (1) and PA (2) are the best. This can be seen from the fact that the photoassociation signals are the largest ones although the ionization efficiencies are the smallest ones. The photoassociation signal PA (2) is slightly stronger than the photoassociation signal PA (1). Assuming the same excitation probability for both intermediate states, the difference in signal strength would be in line with the difference of the ionization efficiencies.

The ionization efficiencies seem to be about a factor of two larger for the intermediate states connected to PA (3) and PA (4). The respective photoassociation signals in Figure 5.16, still are rather weak. This indicates a comparatively low excitation probability from the atomic asymptote into these states.

---

[26] Note that these ionization efficiencies are at least about a factor of three better than the ones achieved for $f = 1$ atoms (see Sec. 5.13.8).

6 Stark spectroscopy of Rydberg atoms in an atom-ion hybrid trap

This chapter essentially corresponds to the publication:

Shinsuke Haze, Joschka Wolf, Markus Deiß, Limei Wang, Georg Raithel, and Johannes Hecker Denschlag, "Stark spectroscopy of Rydberg atoms in an atom-ion hybrid trap", *arXiv* **1901.11069** (2019).

Additional data to the original publication (marked with *) can be found in Section 6.7.2.

6.1   Abstract

We report on Rydberg spectroscopy of ultracold atoms in an atom-ion hybrid trap for probing the electric fields in a mixture of atoms and ions. We obtain spectra which exhibit excitation gaps corresponding to avoided level crossings in the Stark map. From these measurements we can conclude that the ground state atoms experience electrical fields of up to 250 V/cm. There is, however, a difficulty in interpreting the results, because some data indicate that the electrical fields are produced by the ions while other data indicate that they stem from the Paul trap. We discuss possible scenarios for explaining the measured data, provide first measurements to check these scenarios, and propose methods to finally solve this puzzle.

6.2   Introduction

In recent years, a new research field has come up where cold ions and ultracold neutral atoms are experimentally brought together to study their interactions in detail, for reviews see [67, 68, 69, 70]. In a number of experiments the interactions and reactions between cold atoms and ions have been investigated, e.g. [14, 71, 72, 73, 74, 75, 76, 77, 78, 79, 80, 81]. There is a considerable interest for tuning interactions, e.g. for controlling chemical reactions. By exciting atoms or ions to electronically excited states chemical reactions have been influenced, see e.g. [73, 82, 83, 84]. A particularly interesting way for inter-action tuning is coupling the atomic ground state to Rydberg states, making use of their extraordinary properties [16, 85, 86]. Recently, interactions between Rydberg atoms and ions have been observed [87, 88]. We report here on related experiments where we carry out Rydberg spectroscopy on a trapped ensemble of ultracold neutral Rb atoms and Rb$^+$ ions in the vicinity of the 27P-state. The idea of this experiment is to probe atoms as they collide with ions. As atom and ion approach each other the electrical field of the ion shifts the atomic Rydberg states into resonance with the spectroscopy laser light due to the Stark effect. As a consequence, Rydberg states can be excited which are subsequently detected. We observe excitation gaps in the Rydberg spectrum which correspond to avoided crossings of the Rb Stark map. These measurements show that the Rb atoms in the experiment experience electric field strengths of up to 250 V/cm. Concerning the origin of these fields, however, we obtain contradictory results. Several different measurements indicate that the electrical fields stem from trapped ions, but comparison of our measured Rydberg spectra with Stark map calculations seem to indicate that the electrical fields might originate from the Paul trap.

6.3   Experimental parameters

Our experiments are carried out in a hybrid setup of an optical dipole trap (ODT) and a linear Paul trap, allowing for simultaneous trapping of atoms and ions, see Figure 6.1(a). A detailed description of the apparatus can be found, e.g., in [17].

We start our experiments by initially preparing an ultracold gas of ^{87}Rb atoms in the crossed-beam ODT at 1064 nm. These atoms are spin-polarized in the hyperfine state

$(F = 1, m_F = -1)$ within the $5S_{1/2}$ electronic ground state. The sample has an atom number of about 3.4×10^6 and a temperature of 860 nK. We work with ODT trapping frequencies of $2\pi \times 24$ Hz in the axial direction and $2\pi \times 180$ Hz in the radial direction. The cloud has a Gaussian shape with a size of $\sigma_{x,y,z} = (60, 8, 8) \, \mu$m along the three directions of space and the peak atom density is 4.7×10^{13} cm^{-3}.
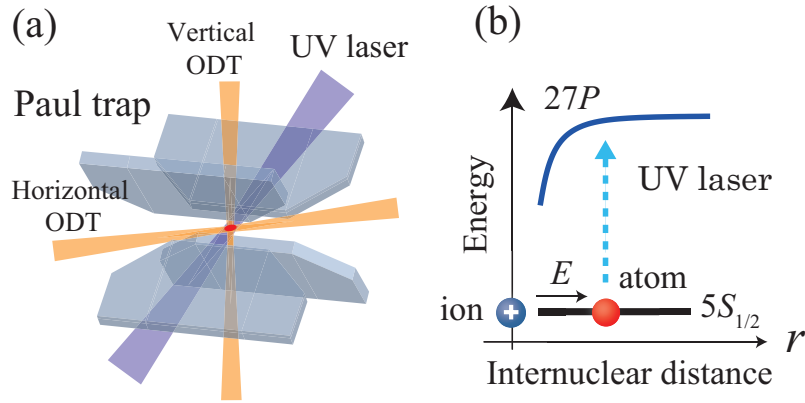

Figure 6.1: Scheme of the experimental setup and the physical system. (a) Rydberg spectroscopy setup in the hybrid atom-ion apparatus. Shown are the RF electrodes of the Paul trap, but not the endcap electrodes. The optical dipole trap laser beams are orange. The UV laser beam is purple. (b) Rydberg excitation of a $5S_{1/2}$ ground state atom towards the $27P$ state in the electrical field of an ion. The Stark effect shifts the $27P$ level into resonance at a particular distance.

The linear Paul trap is centered on the ODT. It is driven by a RF voltage at a frequency of $2\pi \times 4.2$ MHz. The resulting axial and radial trapping frequencies for a Rb$^+$ ion are $\omega_{a,r} = 2\pi \times (42, 207)$ kHz, respectively. Residual DC electric fields are well compensated as described in [46], i.e. excess micromotion is minimized.

For the Stark spectroscopy we address Rydberg states in the vicinity of the $27P$ level via single-photon excitation, starting from the Rb ground state. A frequency-doubled dye laser provides the corresponding ultraviolet (UV) light at a wavelength of about 298.5 nm (see also Sec. 2.2). The laser light is delivered to the vacuum chamber by a multi-mode optical fiber and therefore essentially unpolarized. The power of the UV laser beam is about 1 mW and its waist at the location of the atom cloud is typically 150 μm. For the measurements we use a light pulse of rectangular shape and 225 ms duration.

6.4 Experiments

Once an atom is excited to a Rydberg state it can be ionized e.g. via photoionization by the ODT laser. It is then subsequently trapped by the Paul trap. At the end of an experimental run we infer the approximate number of accumulated ions. However, we do have the capability to detect single ions with unit probability. The ion number is extracted from the measured atom loss from the cloud after an experimental run. The loss is mainly due to elastic collisions with ions in which atoms are kicked out of the shallow ODT, see [12, 46] and Chapter 4. We measure the atom loss via absorption imaging.

Stark spectroscopy probes the local electrical field of each Rb atom in the atomic cloud. This electrical field can either stem from an ion in the vicinity or from the ion trap. In Figure 6.1(b) we sketch the Stark shift of the Rydberg level $27P$ as a function of the distance between atom and ion, considering only the electrical field of a single ion. At a particular distance the UV laser can resonantly drive a transition to the Rydberg level.

Figure 6.2(a) shows the corresponding calculated Stark map. The $27P$ state is split into the fine structure components $27P_{1/2}$ and $27P_{3/2}$. Avoided crossings appear where the $27P$ levels cross the hydrogenic manifold 24Hy. The shown electric field ranges from 0 to $350\,\mathrm{Vcm}^{-1}$ corresponding to an atom-ion internuclear distance from ∞ to 203 nm. The Stark map for the field of a point charge is a distorted version of the standard Stark map for a homogeneous electrical field, see Figure 6.2(b). Due to the large size of the Rydberg wavefunction and the huge polarizability the electrical field gradients have a non-negligible contribution to the Stark level shift.

Figure 6.2(c) is the measured Rydberg spectrum. For this measurement the UV laser frequency was scanned with a stepsize of $100\,\mathrm{MHz}$. For every frequency setting a freshly prepared Rb cloud was exposed to the 225ms laser pulse and subsequently the remaining atom number was measured. The larger the loss, the larger the number of Rydberg atoms and ions that have been created. The ion production rate for a given laser frequency depends on several factors: the availability of resonant Rydberg levels, the transition matrix elements towards these levels, and the number of ground state atoms at the proper electric fields. According to the electric-dipole transition selection rules only the $27P$ state but not the high-l states can be addressed when starting from the $5S_{1/2}$ ground state. However, close to the avoided crossings P-state character is admixed to the respective high-l state branch. We clearly observe two loss peaks from the $27P_{1/2}$ and $27P_{3/2}$ Rydberg reso-
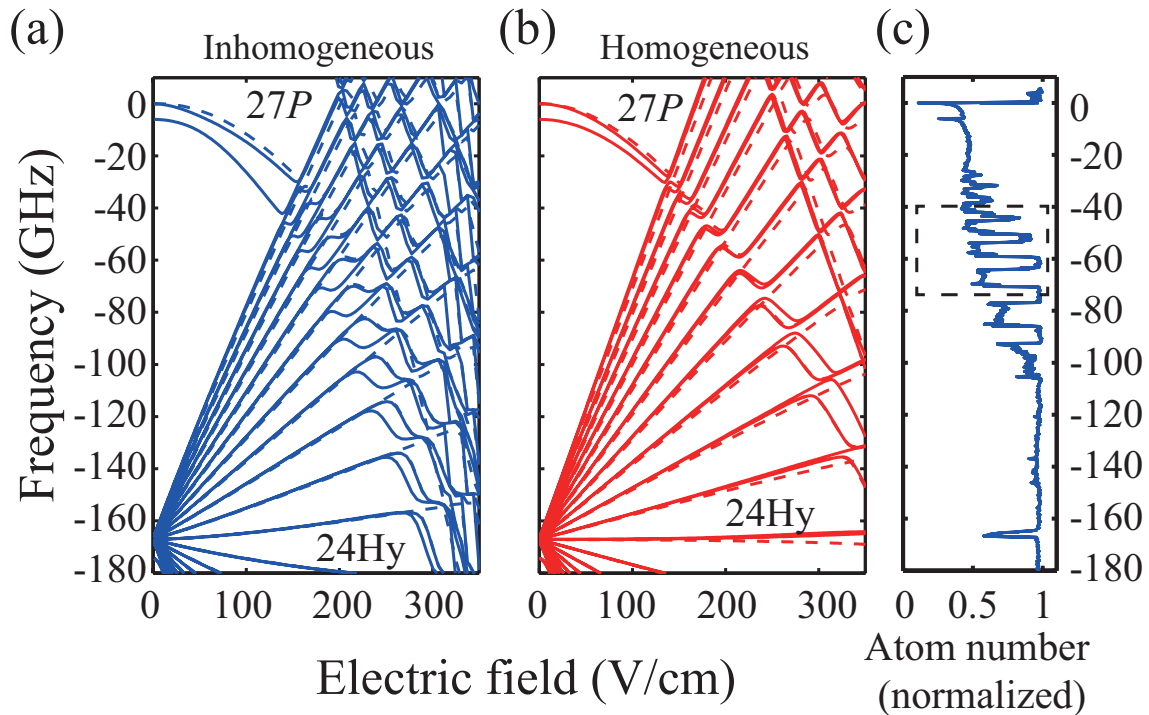
Figure 6.2: **(a) and (b) Stark maps in the vicinity of the** $27P$ **state of** ^{87}**Rb.** The zero-field position of the $27P_{3/2}$ level serves as frequency reference. It corresponds to an offset laser frequency of $1,004.48423$ THz. (a) Stark map for the inhomogeneous field of a point charge. (b) Stark map for a homogeneous field. Solid (dashed) lines indicate $|m_j| = 1/2$ ($|m_j| = 3/2$) states. Avoided level crossings occur between the $27P$ levels and high-l states of the hydrogenic manifold (24Hy). (c) Measured Rydberg excitation spectrum. Each data point represents an average of 3 to 4 repetitions of the experiment. The black dashed box corresponds to the zoom in Figure 6.3.

nances at zero field. For increasing UV laser frequencies the loss signal quickly vanishes because of lack of P-states. For decreasing UV laser frequencies the loss signal decreases gradually. Although the two P-levels are still present, for resonant excitation increasing electrical fields are required and a decreasing number of atoms experience these stronger electrical fields.

At the relative frequency of about -30 GHz, a strongly modulated, almost step like behavior of the measured signal occurs which coincides with the avoided crossings of the P-levels with the hydrogenic manifold. The modulation stops at a relative frequency of about -100 GHz which corresponds to an electrical field strength of around 250 V/cm. Within the small atom cloud such a large field can only stem from ions. From the known parameters of our ion trap we calculate that the maximal electrical trap fields at the $1/e^2$-rim of the cloud are about 30 V/cm.

6.5   Homogeneous versus inhomogeneous
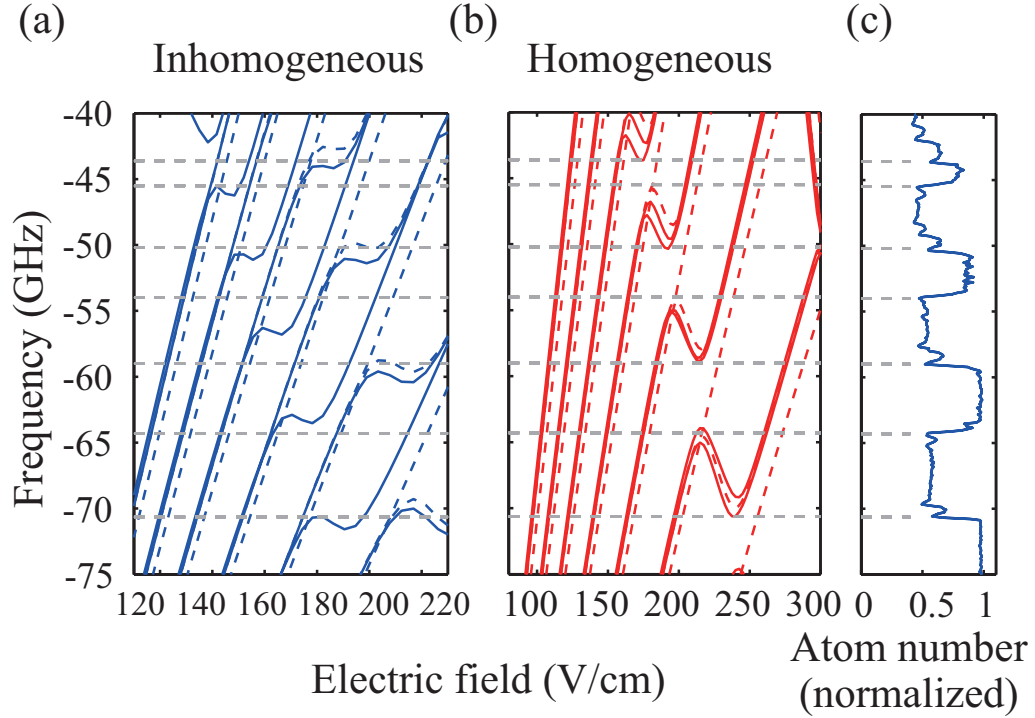

Figure 6.3:   Zooms into the plots of Figure 6.2, as indicated by the dashed box in Figure 6.2(c). The dashed horizontal lines are guides to the eye.

It turns out, however, that this conclusion is somewhat in conflict with further analysis of our spectroscopic data. Figure 6.3 is a zoom into the plots of Figure 6.2, corresponding to the dashed box in Figure 6.2(c). When comparing the measured data with the calculated Stark maps it becomes clear that the Stark spectrum for homogeneous fields matches the data much better than the Stark spectrum for the fields of a point charge. For example, there is a very good correspondence of the measured excitation gaps to the calculated energy gaps at the avoided crossings for the Stark spectrum (b). Close inspection shows that this is not the case for the Stark spectrum (a).

A simple possible explanation for the observations could be that the excitation of Rydberg atoms generally takes place at a distance of about 700 μm from the trap center where the electrical fields of the Paul trap reach 250 V/cm. Here, possibly a non-trapped background gas of Rb atoms could provide enough ion signal. In order to test this hypothesis, we displaced the focus of the UV laser so that the laser did not overlap anymore with the cold atom cloud. The laser is then still able to excite Rydberg states at a distance of

700 μm from the trap center but not anymore within the atomic cloud. In our experiments, however, we observe that the Rydberg signal vanishes. This shows, contrary to the assumption, that most Rydberg excitations occur within the atomic cloud. In a second
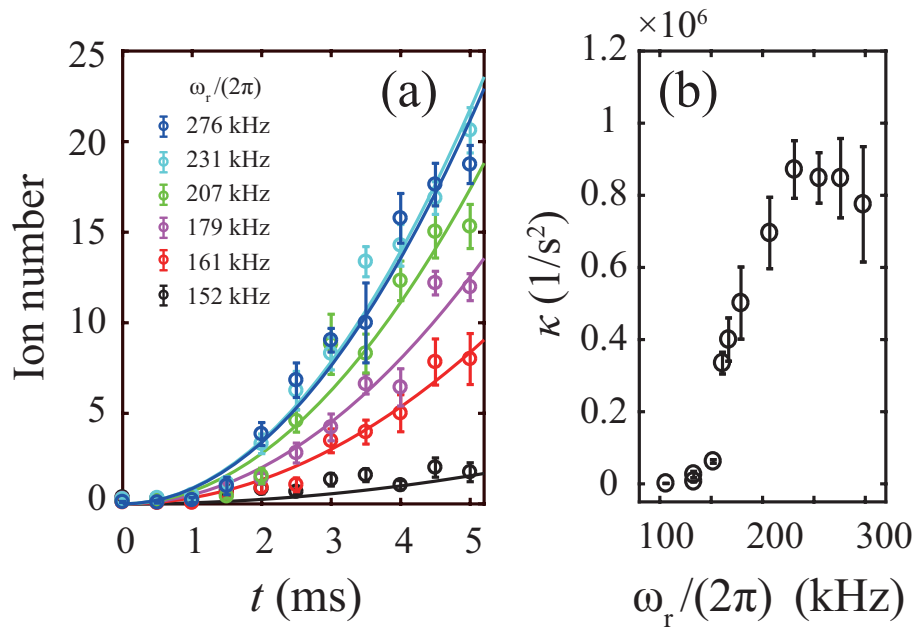

Figure 6.4: The time and trap frequency dependence of the ion production. (a) Non-linear increase of the number of trapped ions with time. Different colors indicate different radial trapping frequencies ω_r of the ion trap as given by the legend. The error bars correspond to the statistical uncertainties in the underlying atom number measurements. The solid lines are fits of a quadratic function κt^2 to the data. (b) Fit parameter κ as a function of ω_r. The error bars represent the uncertainties as determined by the fits.

set of experiments, in order to shed more light on the process of Rydberg excitation, we studied the dynamics of the ion production. For this, we measured how the number of trapped ions increases as a function of exposure time t to the UV laser. Figure 6.4(a) shows the results obtained for a fixed laser frequency corresponding to -69 GHz and for different radial trapping frequencies of the Paul trap. We find a nonlinear increase of the ion number which indicates that the presence of an ion facilitates the production of a second one. Therefore, this again supports the notion of a Rydberg atom being excited in the electrical field of an ion. Empirically we find that the data sets are described well with the quadratic fit function κt^2 (see solid lines), where κ is the fit parameter.

We find that κ generally increases with the trapping frequency, see also Figure 6.4(b). This can be explained as follows. By increasing the radial trapping frequency of the Paul

trap we increase the ion density within the atom cloud. Again, this goes along with the notion that the ion assists the Rydberg excitation. At radial trapping frequencies larger than $\omega_r \approx 2\pi \times 230\,\text{kHz}$ the parameter κ saturates. Possibly there is a reduced compressibility of the ionic cloud due to the Coulomb repulsion.

6.6   conclusion

In conclusion, we have carried out Rydberg spectroscopy of a mixed atom-ion ensemble within a combined trap. By comparing our measured spectra to calculated Stark maps we can infer that large electrical fields of about 250 V/cm are present. However, we have obtained apparently contradictory results for the source of these fields. Several measurements indicate that these fields should originate from ions, however, the structure of the measured spectrum rather points towards ion trap fields. To solve this question further investigation is needed. One possibility is to use a digital ion trap that exhibits periods of zero electrical field for the measurements [89, 90, 91]. The spectroscopy is then performed in a pulsed way at these periods. This ensures that only electrical fields of ions are available for Stark shifts. Another possibility is to study the non-linearity coefficient κ as a function of laser frequency in order to check whether its behavior follows the Stark spectrum of a point charge.

6.7 Supplementary information

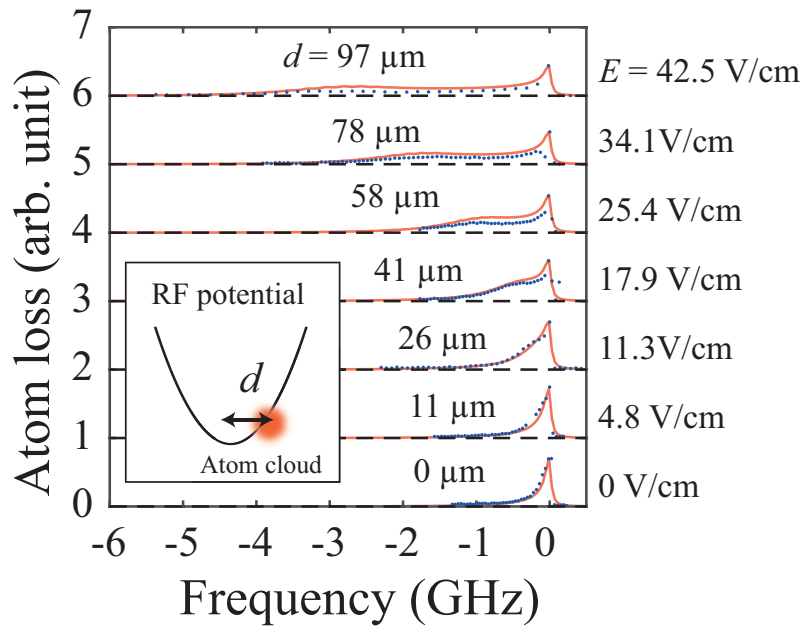### 6.7.1 Effect of the Paul trap RF electrical field

Figure 6.5: Rydberg spectroscopy in the electrical fields of a Paul trap in the absence of ions.   Shown is the measured atom loss as a function of the frequency of the UV laser light in the vicinity of the $27P_{3/2}$ resonance line. Spectra are taken for various distances d between the atom cloud center and the Paul trap center (see inset and legend). The electrical field strength on the right hand side is the RF-field amplitude of the Paul trap at distance d. For better visibility the spectra are shifted with respect to each other in vertical direction. The red solid lines are the results of numerical calculations.

In order to test and verify our general understanding of Rydberg excitation of atoms in the electric fields of a Paul trap we have carried out the following Rydberg spectroscopy measurement. We operate the linear Paul trap with the end cap electrodes turned off such that there is no axial confinement, and ions quickly escape from the trap. Thus, we can exclude any atom-ion interactions in the Rydberg spectroscopy. The electric field distribution of the trap is approximately the same as for the trap with the end caps turned on. We perform Rydberg spectroscopy in the vicinity of the $27P_{3/2}$ resonance line. Here, only atoms are lost that have been excited to the Rydberg state. Figure 6.5 shows the

observed spectra (blue dots). Each spectrum corresponds to a controlled displacement of the ODT together with the atom cloud from the Paul trap center by a distance d, as sketched by the inset in Figure 6.5. Thus, the corresponding atomic clouds experience different electric field amplitudes in their center as indicated on the right hand side of the figure. The oscillating and inhomogeneous electrical fields of the Paul trap lead to a broadening and distortion of the $27P_{3/2}$ resonance line. For the maximum value of $d = 97\,\mu$m presented here, the resonance line spans a frequency interval of about 4 GHz. The red solid lines are the results of numerical simulations taking into account the temporal and spatial distribution of the electric fields, the spatial distribution of the atoms and the quadratic dependence of the Stark shift on the electrical field. We find good agreement between the measurements and the calculations. This gives us confidence that we have a good general understanding of our experimental conditions.

6.7.2   Additional content*

In this section I present additional content regarding the Figures 6.2 and 6.3. The Figure 6.6 shows the data for frequencies down to about -360 GHz. The first part of the data b) (dark blue) is obtained for an interaction time of 75 ms and the second part of the data b) (blue) is obtained for an interaction time of 225 ms. It can be seen from the comparison with the Figure 6.2 that the $27P$ resonance lines (around zero E-field) in Figure 6.6 are much stronger pronounced compared to the remaining signals of the spectrum (dark blue). The reason for this is the much shorter interaction time and therefore lower ion numbers. The large ion numbers lead to a strong saturation of the atom loss of the $27P$ signals (around zero E-field) in the Figure 6.2. This shows the strong non-linear scaling resulting from ion detection scheme I as explained in Section 4.2.5.

The second part of the data (blue) in Figure 6.6 b) is measured with the same interaction time as used for Figure 6.2. The extended frequency range reveals additional atom loss signals. It can be seen in the Stark map Figure 6.6 a) that the additional strong atom loss signals of b) can be assigned to the $27S$ and the $25D$ state, respectively. It is not directly obvious why we can observe these transitions, as the transitions to the pure S and D states are dipole forbidden. A possible explanation is that these states have a P-state admixture. In order to test this explanation, we need to calculate whether the P-State admixtures are large enough.
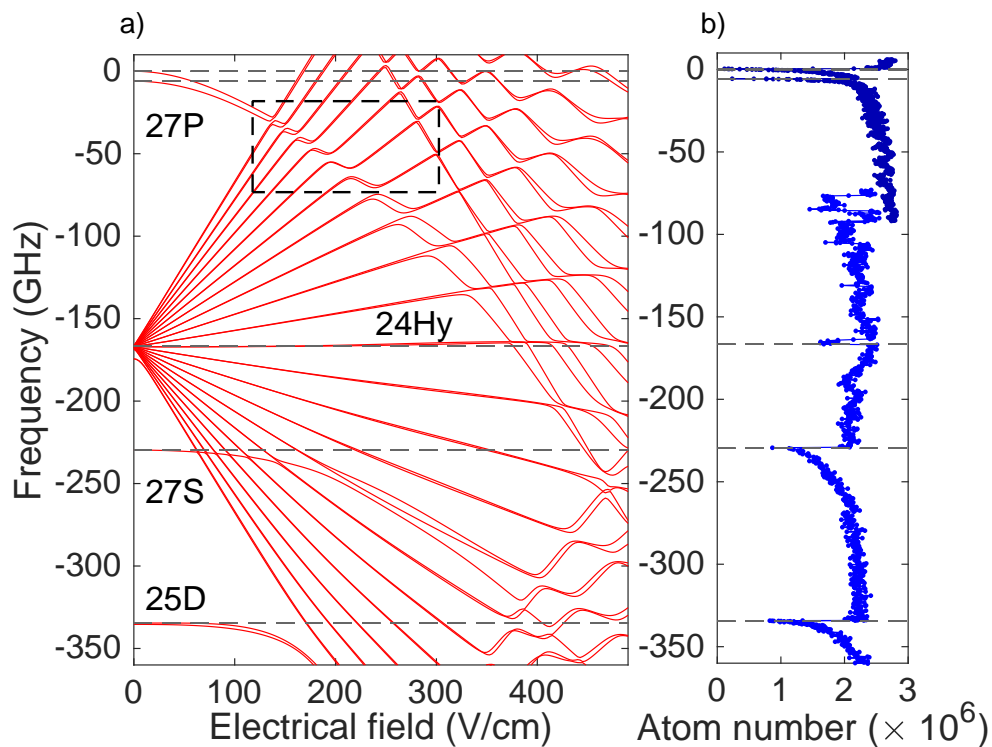
Figure 6.6: Calculated Stark map for a homogeneous electrical field (a) and measured Rydberg excitation spectrum (b). Shown in a) is the calculated level spectrum around the 27P levels versus a homogeneous electric field. The calculations have been performed by Georg Raithel from the University of Michigan. The frequency is referenced to the $5S_{1/2}$ to $27P_{3/2}$ transition at zero field. Only the $m_j = 1/2$ compononent is shown here. The fan of lines below the $27P_{3/2}$ and $27P_{1/2}$ levels are the 24 hydrogenic (Hy) high-l levels that produce many avoided crossings with the 27P states. The dashed lines mark the positions of significant signals in the measurement. The black box shows the area of a zoom in which is given in Figure 6.7. The blue data in the plot b) show the measured atom number as function of the frequency. The data in the range from 0 GHz to -100 GHz (dark blue) are measured for an interaction time of 75 ms, while the data in the range from about -70 GHz to -360 GHz (blue) are measured for an interaction time of 225 ms. Each data point represents the result of a single experimental run. The data points are plotted as polygonal chain.
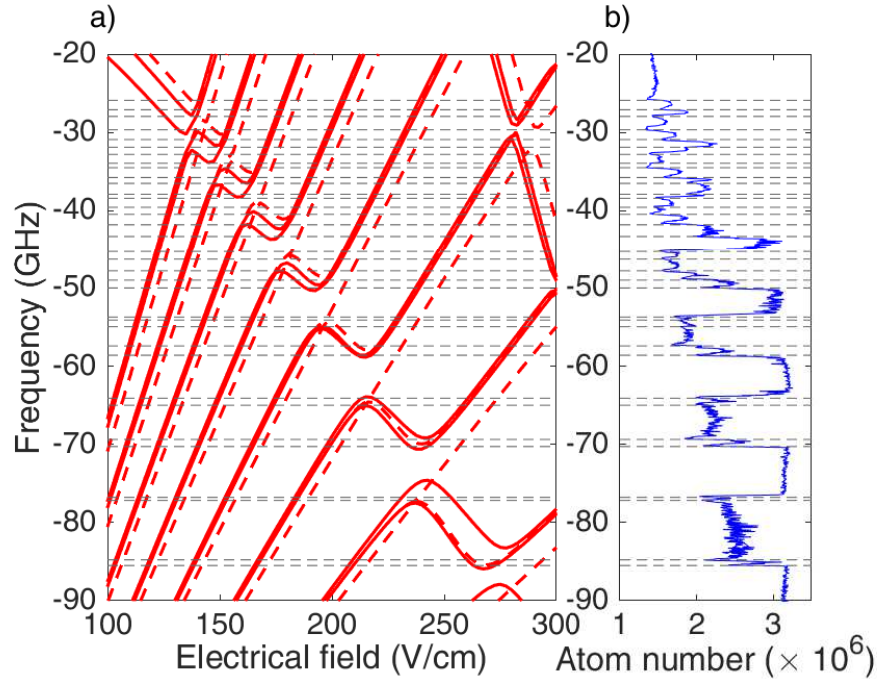
Figure 6.7: Shown zoom into the Stark map a) and the corresponding measurement b) of Figure 6.6. This figure includes different m_j states, where $m_j = 1/2$ is given by solid lines and $m_j = 3/2$ is given by dashed lines. The grey dashed horizontal lines mark signal positions from the measurement. The interaction time for the measurement is 225 ms. Each data point represents the result of a single experimental run. The data points are plotted as polygonal chain.

A zoom into the region indicated by the black box in Figure 6.6 is shown in Figure 6.7. As compared to Figure 6.3 a larger frequency range is shown here and more resonances (i.e. also smaller features) are marked (grey horizontal lines). The shown Stark map calculations a) are carried out for a homogeneous electrical field and the results for different m_j states are presented, where m_j is the projection of the total angular momentum $\vec{j}$ on the electric field axis. We clearly resolve the different m_j lines as can be seen from the grey horizontal lines which in general show good agreement between theory and experiment. Still some expected resonance positions do not show a signal (e.g. the avoided crossing around -76 GHz). Further investigations are necessary to explain the reason for this.

7 Observation of spin-orbit dependent electron scattering using long-range Rydberg molecules

This chapter is a preliminary revised version of the publication:

Markus Deiß, Shinsuke Haze, Joschka Wolf, Limei Wang, Florian Meinert, Christian Fey, Frederic Hummel, Peter Schmelcher and Johannes Hecker Denschlag,
"Observation of spin-structure of ultralong-range Rydberg molecules",
arXiv **1901.08792** (2019).

Additional data to the original publication (marked with *) can be found in Section 7.8.10.

7.1   Abstract

We present experimental evidence for spin-orbit interaction in electron-neutral scattering using ultralong-range Rydberg molecules. The molecular setup serves as a micro laboratory to perform precise scattering experiments in the low-energy regime of a few meV. Here, the spin-orbit interaction is given by the coupling between the total electronic spin of a loosely bound Rydberg electron and the valence electron of a ground state atom, and the orbital angular momentum of the Rydberg electron with respect to the ground state atom. Our measurements are carried out with a cold gas of ^{87}Rb atoms in the regime of resonant p-wave interaction, which, due to its attractive character, leads to the formation of Rb$_2$ molecules. As a further consequence, the spin substructures of vibrational

135

states feature large level splittings that can clearly be resolved in our data. Since the characteristic multiplet spin substructures of different vibrational ladders are explored, an unambiguous assignment of all spin states is possible. Our work paves the way for understanding and exploiting spin dynamics in ultralong-range Rydberg molecules, and provides valuable information for the description of related, complex few-body systems with numerous interacting spins, angular momenta, and motional degrees of freedom.

7.2   Introduction

Since their prediction almost twenty years ago [92] and boosted by their first observation [93], ultralong-range Rydberg molecules have become a research area of major interest (for a review, see, e.g. [94, 95, 96]). However, still, the spin substructure of these molecules is hardly understood which prevents corresponding applications. In particular, one of the main unresolved questions in these systems concerns the coupling between the total electronic spin and the relative orbital angular momentum between the Rydberg electron and the ground state atom. This special type of spin-orbit interaction has been predicted almost twenty years ago [97], and currently gains increased interest in theoretical works employing refined models [98, 99]. From the experimental side, some preliminary indication of such a kind of spin-orbit interaction has been found recently [100], however no clear evidence has been demonstrated so far. It has escaped observation although a variety of spectroscopic studies with impressive resolution were carried out, investigating molecules correlated with S, P, or D Rydberg atomic states (e.g. [93, 101, 102, 103, 104, 105, 106, 107, 108, 109, 110, 111, 112, 113, 114]), while starting with different atomic species (Rb, Cs, Sr).

In our setup, we work in a so far unexplored parameter regime where resonant p-wave interactions increase the level splittings of the spin substructures of vibrational states. Specifically, we investigate ultralong-range $^{87}Rb_2$ Rydberg molecules consisting of a $5S_{1/2}$ ground state atom and a $16P_{3/2}$ Rydberg atom. The molecular bound states are located in the second outermost well of the Born-Oppenheimer potential energy curve (PEC). That specific well is significantly influenced by the p-wave shape resonance. Our experiments are carried out using photoassociation spectroscopy for an ultracold cloud of ground state atoms spin-polarized either in one of the hyperfine states $F = 1$ or $F = 2$. Rydberg molecules, produced via photoassociation, are detected in an ion trap after ion-

ization. We observe several vibrational ladders, each belonging to a different spin state. These spin states can be distinguished since characteristic single, double, and triple line multiplet substructures of respective vibrational levels are resolved. The measured fine structure spectra are complete since all expected transition lines are assigned to resonances in the data. This assignment is possible due to comparison with model calculations on the basis of a pseudopotential Hamiltonian and including spin-spin and spin-orbit interactions [99]. The agreement between experiment and theory is very good in view of the complexity of the potential structure to be described here. As we will show, the relatively large splittings in the observed spin substructures originate almost entirely from the given special type of spin-orbit interaction.

This article is structured as follows. In Section 7.3 we introduce the relevant molecular potential energy curves in order to establish a basis for the following discussion. Subsequently, in Section 7.4 the obtained spectroscopic data are presented. Section 7.5 is devoted to a description of our theoretical model and the explicit study of the effect of different types of spin-spin and spin-orbit coupling mechanisms on the multiplet line splittings. Finally, in Section 7.6, we give a comparison of our experimental and theoretical results for the vibrational ladders.

7.3   Molecular system and potential energy curves

The basic setup of the molecular system is sketched in Figure 7.1. A ground state atom is located at position $\vec{R}$ relative to the ionic core of a Rydberg atom. The Rydberg electron at position $\vec{r}$ has spin $\vec{s}_1$ and features an orbital angular momentum $\vec{l}$ relative to the ionic core. Furthermore, the total angular momentum of the Rydberg electron is $\vec{j} = \vec{l} + \vec{s}_1$ with the corresponding magnetic quantum number m_j.

The ground state atom possesses an electronic spin $\vec{s}_2$ and a nuclear spin $\vec{I}$, which together form the angular momentum $\vec{F} = \vec{I} + \vec{s}_2$ with corresponding magnetic quantum number m_F. This coupling describes hyperfine interaction, which, in the presence of spin-dependent scattering channels, effectively mixes the collective electronic singlet and triplet states of the valence electrons [102, 108, 111, 113, 114, 115].

In the reference frame of the ground state atom the Rydberg electron is located at position $\vec{X} = \vec{r} - \vec{R}$. It has the orbital angular momentum $\vec{L}$, which can couple to the total electronic spin $\vec{S} = \vec{s}_1 + \vec{s}_2$. In addition, $\vec{L}$ and $\vec{S}$ can be combined to form $\vec{J} = \vec{L} + \vec{S}$ with

corresponding magnetic quantum number M_J. The given $\vec{L} \cdot \vec{S}$ type of spin-orbit interaction is observed in the present work. We make use of the fact that it can lead to significant modifications of molecular potential energy curves, especially when the kinetic energy of the Rydberg electron is close to the p-wave shape resonance. This is the regime that we investigate in our experiments.
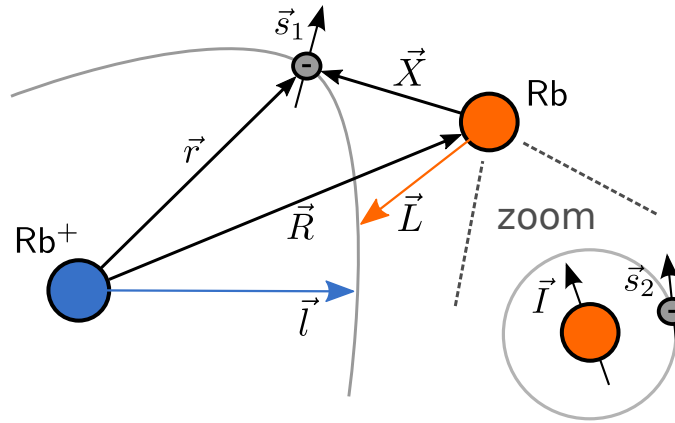

Figure 7.1: Composition of the molecular system (see text).

Solving the electronic problem in Born-Oppenheimer approximation, one obtains the adiabatic PECs which serve as input for the nuclear, vibrational Schrödinger equation. Figure 7.2 shows the PECs around the second outermost wells located at an internuclear distance of about $260\,a_0$, where a_0 represents the Bohr radius. These results are obtained from our model calculations as described in Section 7.5.1 including s- and p-wave interactions. For comparison, in Section 7.8.2 of the Appendix also a discussion is provided for the case when p-wave interaction is neglected, in order to give a simplistic picture of the molecule (see also Fig. 7.9). Indeed, at distances $R < 300\,a_0$, p-wave interactions strongly influence the shapes of the PECs. This is a consequence of a p-wave shape resonance of the interaction between the P orbital Rydberg electron and the ground state atom. The resonance occurs when the collision energy between these two partners is approximately[1] $E_r^{\text{avg}} = 26.6\,\text{meV}$ as experimentally derived recently [116]. Here, the resonant p-wave interaction gives rise to so-called butterfly PECs [117, 118], which originate from the hydrogenic $n = 14$ manifold and cross through the other Rydberg levels (n is the prin-

---

[1] E_r^{avg} represents an average value which follows the rule $E_r^{\text{avg}} = \left[\sum_{J=0}^{2} (2J+1)E_r^J \right] / \left[\sum_{J=0}^{2} (2J+1) \right]$. Here, E_r^J are the characteristic energies where the p-wave shape resonance occurs for the three individual channels $J = (0, 1, 2)$ (see also the discussion in Section 7.5.2)

ciple quantum number). After the butterfly PECs have crossed the P orbital PECs at a distance of $R \approx 230\,a_0$ they steeply go down to energies as low as about $-300\,\text{GHz} \times h$ before they bend over due to level repulsion with the lower $n = 13$ hydrogenic manifold [see Fig. 7.2(a)]. There, the butterfly PECs exhibit potential wells which support several vibrational states. Such butterfly bound molecular states have been observed for the first time quite recently [110].
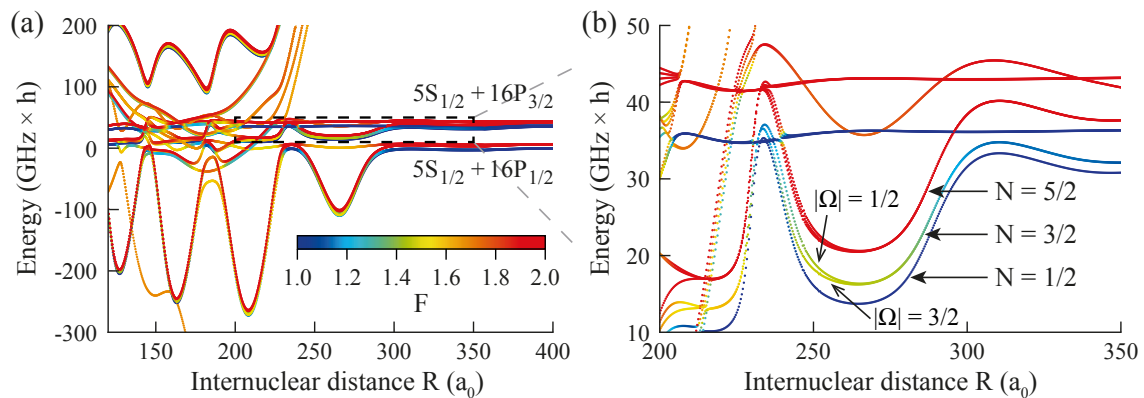

Figure 7.2: The molecular PECs and a zoom of the area of interest. (a) The molecular PECs correlated to the $5S_{1/2} + 16P_j$ atomic asymptotes for $j \in \{1/2, 3/2\}$ and different hyperfine states $F \in \{1, 2\}$ of the $5S_{1/2}$ atom. The color code represents the expectation value of the quantum number F. (b) Zoom into the dashed rectangle in (a) indicating the region of interest for the present work. N and Ω are quantum numbers which label the PECs. The $N = 5/2$, $3/2$, $1/2$ branches are composed by a triplet, doublet, and singlet substructure of $|\Omega|$ states, respectively. For convenience, in Section 7.8.1 of the Appendix also a representation of the PECs in terms of the total electronic spin character is given.

In our work, however, we focus on a different region which is shown in Figure 7.2(b). These potential wells are located very close to the internuclear distance where the p-wave shape resonance cuts through, and are characterized by admixture of the butterfly states. Thus, the perturbation due to the resonant p-wave interaction is particularly strong in that part of the potential manifold. This perturbation gives rise to sizeable mixing of hyperfine states (F mixing) and significant splittings of different spin states.

For labeling classes of PECs the quantum number N associated with the angular momentum $\vec{N} = \vec{s}_1 + \vec{s}_2 + \vec{I}$ is used. States with dominant $F = 2$ ($F = 1$) content are characterized by $N = 5/2$ ($N = 1/2$), respectively, and states with pronounced F mixing have $N = 3/2$ [see Fig. 7.2(b)]. N provides the correct multiplicity, however, strictly speaking, N is not a good quantum number. Instead, the projection of the total angular momentum of the

(non-rotating) molecular system on the internuclear axis, $\Omega = m_l + m_1 + m_2 + m_I$, represents a good quantum number, and it is appropriate to further discriminate the PECs. Here, m_l, m_1, m_2, m_I are the magnetic quantum numbers of l, s_1, s_2, I, respectively. Due to the axial symmetry of the system, there is energetic degeneracy with respect to $\pm\Omega$. The $N = 5/2$ manifold consists of three components which have the quantum numbers $|\Omega| = \{1/2, 3/2, 5/2\}$, the $N = 3/2$ curve splits up into two components with $|\Omega| = \{1/2, 3/2\}$, while for $N = 1/2$ there is only a single curve featuring $|\Omega| = 1/2$. As an example, we have marked the $|\Omega| = 1/2$ and $|3/2|$ states in Figure 7.2(b). However, the energetic separation of the different $|\Omega|$ PECs is more clearly visible in Figure 7.6. Please note that Ω is not the projection quantum number of N. In our experiments, which we will describe in the following, we observe clear signatures of the $|\Omega|$ spin state splittings. Since these splittings are susceptible to $\vec{L} \cdot \vec{S}$ coupling, they provide a means for observing the special type of spin-orbit interaction we are looking for.
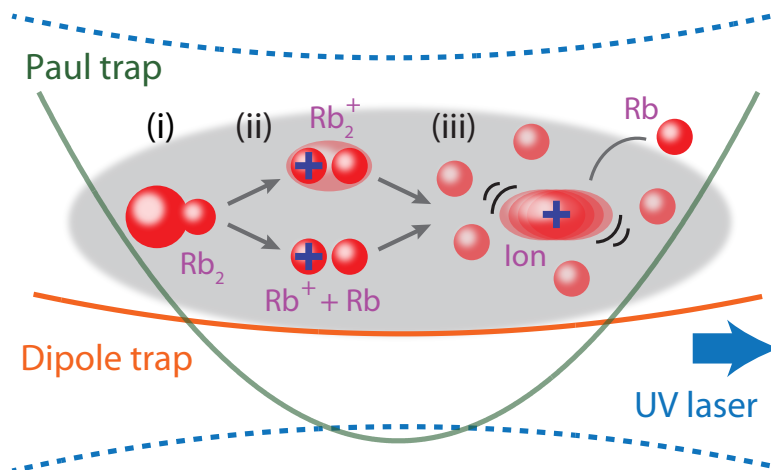
7.4   Experiments

Figure 7.3: Illustration of the experimental setup and scheme. The orange solid line indicates the dipole trap potential for the ultracold neutral atoms while the green solid line represents the Paul trap potential for ions. (i) Inside the atom cloud (indicated by the gray colored area) Rb_2 Rydberg molecules are produced by means of the UV photoassociation laser (blue dashed line and blue arrow). (ii) The molecules can decay into ions, where processes leading to Rb^+ and Rb_2^+ are possible, in general (see, e.g., [119, 120]). A resulting ion is captured by the Paul trap. (iii) The micromotion-driven ion elastically collides with Rb atoms leading to atom loss from the dipole trap.

The experiments are carried out in a hybrid atom-ion setup [17] consisting of a crossed optical dipole trap for an ultracold cloud of ^{87}Rb ground state atoms and a linear Paul trap for detecting Rydberg molecules after ionization. The dipole trap is operated at a wavelength of 1065 nm and has a potential depth of about $20\,\mu\text{K} \times k_\text{B}$. The atomic sample is either prepared in the hyperfine state $F = 1, m_F = -1$ or in the state $F = 2, m_F = +2$. It has a temperature of $\approx 1\,\mu\text{K}$, and typically consists of about 4×10^6 atoms. The cloud is Gaussian-shaped with a size of $\sigma_{x,y,z} \approx (70, 10, 10)\,\mu\text{m}$ along the three directions of space. The general procedure of our experiment is illustrated in Figure 7.3. In step (i) Rb$_2$ Rydberg molecules are created by photoassociation using a narrow-linewidth laser with a wavelength of about 302 nm (for technical details on the photoassociation laser setup, see Section 7.8.3 of the Appendix). Some of these molecules decay into ions (ii) which are subsequently trapped in the linear Paul trap with its potential depth of about 1 eV. The Paul trap is centered on the optical dipole trap so that the trapped ions are immersed in the atom cloud. We detect the ions (iii) by measuring the losses they inflict on the atom cloud, as demonstrated in Chapter 4 and [46]. In brief, the losses are due to micromotion-driven elastic collisions between atoms and ions, which expel atoms out of the shallow dipole trap (see also Sec. 4.2.5). Even a single ion can lead to a significant signal. In general, the number of remaining atoms decreases with increasing number of ions. By measuring the atom loss as a function of the frequency of the photoassociation laser light we obtain a spectrum of the molecular Rydberg states. In Figure 7.4 two measured Rydberg photoassociation spectra in the vicinity of the atomic $16P$ Rydberg state are presented. We note that not all of the experimentally observed lines are resolved in these two spectra. The normalized atom loss $L = 1 - \tilde{N}/\tilde{N}_0$ is shown as a function of the frequency of the photoassociation laser light. $\tilde{N}$ is the remaining number of atoms after an experimental run and $\tilde{N}_0$ is the remaining number of atoms when the photoassociation laser was turned off. The atom numbers are measured via absorption imaging. For the measurements of Figure 7.4 the frequency of the photoassociation laser was scanned in steps of 20 MHz, and each data point represents a single run of the experiment. Scan (a) (blue data points) shows data for atoms prepared in the hyperfine state $F = 1, m_F = -1$, while scan (b) (red data points) was obtained for atoms prepared in $F = 2, m_F = +2$. For $F = 1$ samples, the laser frequency ν is given in terms of $\Delta \nu = \nu - \nu_0$, whereas for $F = 2$ samples it is given in terms of $\Delta \tilde{\nu} = \nu - \nu_0 + 2 \times \nu_\text{hfs}$. Here, $\nu_0 = 991.55264\,\text{THz}$ is the resonance frequency for the $16P_{1/2}$ atomic Rydberg line when starting with $F = 1, m_F = -1$ atoms, and $\nu_\text{hfs} = 6.835\,\text{GHz}$ is the hyperfine splitting of the electronic ground state of ^{87}Rb

[121, 122]. The frequency offset difference of $2 \times \nu_{hfs}$ helps to directly compare positions of molecular resonance lines in the $F = 1$ and $F = 2$ data. Besides the photoassociation signals the spectra also include the $16P_{3/2}$ and $16P_{1/2}$ atomic Rydberg lines which are marked with arrows. A discussion of the atomic lines is given in Section 7.8.4 of the Appendix. In the following, we focus on the frequency range of $10\,\text{GHz} < \Delta\nu < 40\,\text{GHz}$, which corresponds to the potential curves shown in Figure 7.2(b).
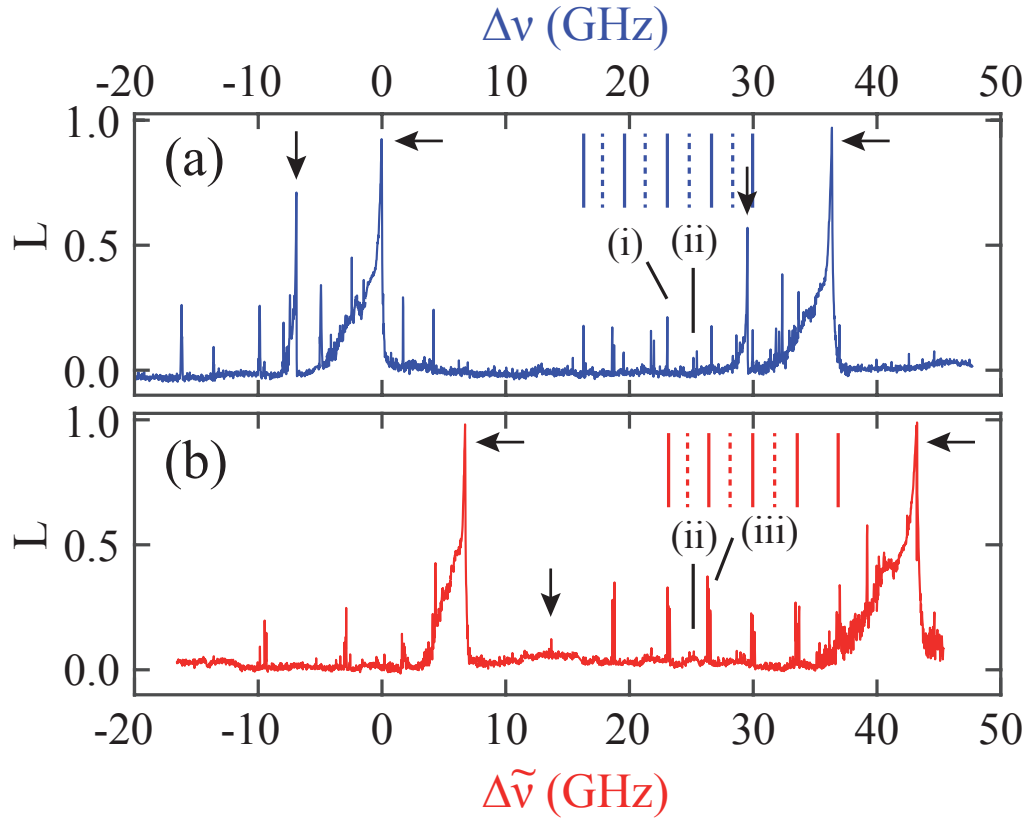

Figure 7.4: Spectra measured for atomic samples initially prepared in the hyperfine state $F = 1$ (a) and $F = 2$ (b), respectively. Shown is the atom loss L as a function of the frequency ν of the UV spectroscopy laser light. The frequency ν is provided in terms of $\Delta\nu = \nu - \nu_0$ (a) and $\Delta\tilde{\nu} = \nu - \nu_0 + 2 \times \nu_{hfs}$ (b), where $\nu_0 = 991.55264\,\text{THz}$ and $\nu_{hfs} = 6.835\,\text{GHz}$. For the two spectra, the frequency offsets are chosen to be different by $2 \times \nu_{hfs}$ in order to vertically line up identical molecular lines. The data of (a) are obtained for a pulse duration of $125\,\text{ms}$ of the spectroscopy light while for (b) $200\,\text{ms}$ are used (the light intensities, micromotion energies and ion-atom cloud interaction times are about the same for both scans). Here, the horizontal and vertical black arrows mark resonances assigned to atomic transitions. The black solid lines and corresponding denotations (i), (ii), and (iii) indicate multiplet line structures that are investigated in more detail in Figure 7.5. The vertical red dashed (red solid) lines illustrate the frequency positions of observed weak (strong) three line structures for $F = 2$ (see text). In analogy, the vertical dashed and solid blue lines illustrate single line structures for $F = 1$.

In contrast to the atomic signals, the molecular signals have rather symmetric line shapes with typical linewidths (FWHM) on the order of several tens of MHz. As an example, we show a high resolution scan of a typical molecular line in Figure 7.5(i) (blue data) which approximately has the shape of a Gaussian. This particular line is identical to the one labeled with (i) in Figure 7.4(a). A discussion of the line shapes and line widths is given in Section 7.8.5 of the Appendix, where also electric dipole moments of the molecular states are provided. Without ion trap no photoassociation loss signal is visible in the data of Figure 7.5(i) (see flat magenta curve). We note, that the loss-signal strengths in Figure 7.4 have a strongly non-linear dependence on the number of trapped ions. While the largest loss signals correspond to hundreds of ions the smallest loss peaks are the result of only a few ions.
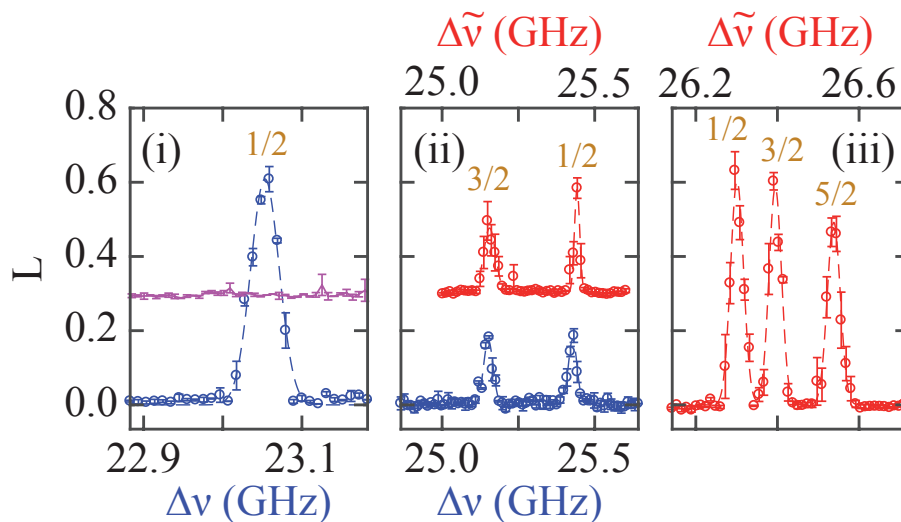

Figure 7.5: Multiplet resonance structures observed for atomic samples initially prepared in the hyperfine state $F = 1$ (blue data points) and $F = 2$ (red data points), respectively. The individual lines are labeled with the $|\Omega|$ quantum number of the corresponding assigned molecular state (see also Fig. 7.6). In the left panel for the magenta data points the Paul trap was off during the spectroscopy pulse. Here, the pulse duration of the spectroscopy light was 200 ms for the $F = 1$ data and 300 ms for the $F = 2$ data. For better visibility the magenta data points and also the red data points in the center panel are shifted in vertical direction by 0.3. The error bars represent the statistical uncertainty. Dashed blue and red lines are the results of Gaussian fits.

A data analysis shows that the measured photoassociation spectra in the range $10\,\text{GHz} < \Delta\nu < 40\,\text{GHz}$ consist of three different vibrational ladders, each with a different multiplet substructure of the vibrational levels. The frequency spacings between the vibrational levels of a given ladder are approximately equidistant and typically between 1.4 to 1.8 GHz.

The three vibrational manifolds clearly correspond to the PECs characterized by $N = 1/2$, $3/2$, and $5/2$, respectively, as shown in Figure 7.2(b). Actually, we find that one of the ladders can only be observed when starting with an ensemble of $F = 2$ atoms. The vertical red solid and dashed lines in Figure 7.4(b) indicate measured frequency positions of corresponding vibrational levels. Such a selective behavior is expected for the $N = 5/2$ state according to dipole transition selection rules. Indeed, the substructure of the vibrational levels of this particular manifold is given by line triplets. This supports the assignment to the $N = 5/2$ state due to its predicted splitting into the components $|\Omega| = \{1/2, 3/2, 5/2\}$. Figure 7.5(iii) shows such a triplet of lines. The scan represents a high resolution measurement of the structure (iii) in Figure 7.4(b). We observe that the line triplets generally follow a systematic behavior. The separation between adjacent resonances is typically on the order of about 100 MHz. Furthermore, the splitting between the first and second line is only about $2/3$ of the splitting between the second and the third line. In addition, the signal strength of the third resonance is generally smaller as compared to the other two resonances which are of similar strength (see also Fig. 7.10 in the Appendix). The second one of the three ladders consists of a succession of line doublets. These levels can be observed both for $F = 2$ as well as $F = 1$ samples. Clearly, this ladder corresponds to the $N = 3/2$ state in Figure 7.2(b) which is of mixed F character, and splits up into the components $|\Omega| = \{1/2, 3/2\}$. An example for such a line doublet is shown in Figure 7.5(ii) where measurements for $F = 1$ and $F = 2$ atomic samples are presented. This doublet is found in Figs. 7.4(a) and (b) at locations (ii). The strengths of line doublet signals are generally lower for $F = 2$ as compared to $F = 1$ (except for the structure at $\Delta \nu \sim 18.7$ GHz). In fact, some of the line doublets could only be detected for $F = 1$. Typically, the line splitting within a line doublet is a few hundred MHz. Finally, the third ladder corresponds to the $N = 1/2$ PEC in Figure 7.2(b) which has $|\Omega| = 1/2$. It can only be addressed from $F = 1$ atomic samples. This vibrational manifold consists of a sequence of single line structures as illustrated in Figure 7.4(a) by the vertical blue solid and dashed lines [see also Fig. 7.5(i)].

Finally, we note that quite generally for each of the ladders the signal strength strongly alternates between adjacent vibrational levels. In the spectra of Figure 7.4 this is indicated by the vertical solid and dashed lines. Although not visible in Figure 7.4, in experiments with higher signal-to-noise ratio we observe also the much weaker resonances at the positions of the dashed vertical lines. How to improve the signal-to-noise ratio is discussed in more detail in Section 7.8.6 of the Appendix (corresponding measurements are shown in

Figure 7.10). An overview of all measured resonance lines and splittings is given in Table 7.3 of the Appendix.

7.5 Calculations

7.5.1 Model for PEC calculations

We calculate molecular PECs by using the electronic Hamiltonian

$$H = H_{\text{Ryd}} + H_g + V. \tag{7.1}$$

H_{Ryd} describes the interaction of the Rydberg electron in the potential of the ionic Rb^+ core, and has eigenstates $\phi_{nljm_j}(\vec{r})$ with energies E_{nlj}. The energies E_{nlj} are taken from spectroscopic measurements [123, 124] and are utilized as input to analytically determine the long-range behavior (larger than several Bohr radii a_0) of $\phi_{nljm_j}(\vec{r})$ in terms of appropriately phase shifted Coulomb wave functions. Knowledge on the wave functions for smaller distances is not necessary for our purpose. $H_g = A\vec{I} \cdot \vec{s}_2$ represents the Hamiltonian of hyperfine interaction in the ground state atom with eigenstates $|Fm_F\rangle$, where $A = 3.417\,\text{GHz} \times h/\hbar^2$ [122]. The term V describes the interaction between the Rydberg electron and the ground state atom which is largely determined by the orbital angular momentum $\vec{L}$ of the Rydberg electron in the reference frame of the ground state atom. For $L = 0$ there is s-wave interaction, while p-wave interaction is given for $L = 1$. We employ a generalized Fermi pseudopotential [99, 125]

$$V = \sum_\beta \frac{(2L+1)^2}{2} a(L,S,J,k) \frac{\delta(X)}{X^{2(L+1)}} |\beta\rangle \langle\beta| \tag{7.2}$$

(using atomic units). Here, $X = |\vec{r} - \vec{R}|$ is the absolute distance between the Rydberg electron and the ground state atom (see Fig. 7.1), and β is a multi-index that defines projectors onto the different scattering channels $|\beta\rangle = |LSJM_J\rangle$. The interaction strength in each channel depends on the scattering lengths/volumes $a(L,S,J,k) = -k^{-(2L+1)} \tan\delta(L,S,J,k)$, where $\delta(L,S,J,k)$ are phase shifts of an electron with wave number k that scatters off a ^{87}Rb ground state atom. As basis for our simulations we employ phase shift data from [116]. The wave number is calculated via the semiclassical relation $k = \sqrt{2/R - 1/n_{\text{eff}}^2}$.

scattering channel			model	mapping
s-wave (L = 0)	S = 0	J = 0	λ_1	$a(0,0,0,k) \mapsto \lambda_1 a(0,0,0,k) + (1-\lambda_1)a(0,1,1,k)$
	S = 1	J = 1		$a(0,1,1,k) \mapsto a(0,1,1,k)$
p-wave (L = 1)	S = 0	J = 1	λ_2	$a(1,0,1,k) \mapsto \lambda_2 a(1,0,1,k) + (1-\lambda_2)a(1,1,J_{\mathrm{avg}},k)$
	S = 1	J = 0	λ_3	$a(1,1,0,k) \mapsto \lambda_3 a(1,1,0,k) + (1-\lambda_3)a(1,1,J_{\mathrm{avg}},k)$
		J = 1		$a(1,1,1,k) \mapsto \lambda_3 a(1,1,1,k) + (1-\lambda_3)a(1,1,J_{\mathrm{avg}},k)$
		J = 2		$a(1,1,2,k) \mapsto \lambda_3 a(1,1,2,k) + (1-\lambda_3)a(1,1,J_{\mathrm{avg}},k)$

Table 7.1: Overview of the scattering lengths/volumes $a(L,S,J,k)$ that are modified via control parameters λ_1, λ_2, and λ_3 in order to study the splitting mechanisms in Figure 7.6.

To compute the PECs in the vicinity of the $16P_{1/2}$ state (which represents the closest asymptotic state) we use the effective principle quantum number $n_{\mathrm{eff}} = 13.3447$. Please note that neither $\vec{F}$ nor $\vec{j}$ are conserved quantities, since V neither commutes with H_{Ryd} nor with H_{g}.

In general, for our calculations the Hilbert space is restricted to a subset of Rydberg states in the spectral region of interest, as described in Appendix 7.8.7. The PECs obtained by taking into account both *s*-wave and *p*-wave interactions in Eq. (7.1) are shown in Figure 7.2. For comparison, in Section 7.8.2 of the Appendix, also the potential energy curves are discussed for the case when *p*-wave interaction is ignored, i.e. $a(L = 1, S, J, k) = 0$ (see Fig. 7.9). The cusps in the outer wells of the PECs, e.g. around $R = 360\,a_0$ in Figure 7.9 and Figure 7.2, occur due to the non-analytic behavior of k close to the classical turning point, where k becomes zero.

7.5.2 Comparison of spin-spin and spin-orbit interactions

In the following, we investigate in detail the reasons for the splitting of the PECs with a given N quantum number into the various Ω components. It will turn out that the spin-orbit interaction between the total electronic spin $\vec{S}$ and the orbital angular momentum of the Rydberg electron $\vec{L}$ with respect to the ground state atom (i.e. $\vec{L} \cdot \vec{S}$ coupling) is by far the dominating mechanism. For our investigation, we introduce three control parameters λ_1, λ_2, and λ_3 that govern the strengths of the different scattering channels. The mapping is summarized in Table 7.1. We analyze the impact of the individual control parameters on the PECs for an internuclear distance of $265\,a_0$, which corresponds to about the loca-

tions of the minima of the potential wells in Figure 7.2(b). This choice is motivated by the positions of the barycenters of the vibrational wave functions. The results are shown in Figure 7.6.

When $\lambda_1 = \lambda_2 = \lambda_3 = 0$, the electron-atom interaction V is insensitive to the total electronic spin $\vec{S}$ and the interaction can be simplified to[2] [92, 118]

$$V = 2\pi a_s(k)\delta(\vec{R} - \vec{r}) + 6\pi a_p(k)\overleftarrow{\nabla}_{\vec{r}} \cdot \delta(\vec{R} - \vec{r})\overrightarrow{\nabla}_{\vec{r}} \tag{7.3}$$

with $a_s(k) = a(0, 1, 1, k)$, $a_p(k) = a(1, 1, J_{\mathrm{avg}}, k)$, and $\vec{R} = R\hat{e}_z$. The phase shift for J_{avg} corresponds to the situation, in which the $\vec{L} \cdot \vec{S}$ coupling is neglected. For the resonance energy E_r^{avg} associated with this phase shift we use the value $E_r^{\mathrm{avg}} = 26.6\,\mathrm{meV}$ taken from [116]. Figure 7.6 shows that for this case there is no splitting of the PECs both for the $F = 1$ and the $F = 2$ branch. We now let $\lambda_1 > 0$, while keeping $\lambda_2 = \lambda_3 = 0$. The parameter λ_1 introduces a singlet s-wave interaction channel with a scattering length that is discriminable from the triplet s-wave scattering length. As a consequence, typically, a splitting of each of the $F = 1, 2$ branches occurs, i.e. a separation of states with mixed F character from those with pure $F = 1, 2$ character is obtained. This is explained in more detail in Section 7.8.8 of the Appendix. The given energy separations change as a function of the internuclear distance (see Fig. 7.9). For the specific choice of $265\,a_0$, however, the curves visible in Figure 7.6 are dominated by p-wave interactions. Hence, the parameter λ_1 does not have any significant effect. In particular, there is also no splitting of $|\Omega|$ components within the individual F branches. We note that in general the parameter λ_1 does not generate $|\Omega|$ state splittings, i.e. also for other internuclear distances.

The next regime is $\lambda_1 = 1$, $\lambda_2 > 0$, and $\lambda_3 = 0$. The parameter λ_2 introduces a difference between the singlet and triplet channels for p-wave scattering corresponding to a spin-spin interaction in the p-wave channel. As can be seen from Figure 7.6, λ_2 has a strong effect on the F branches. PECs of mixed F character split off from states of pure $F = 1, 2$ character and separate by several GHz from each other for $\lambda_2 = 1$. In addition, the parameter λ_2 lifts the energetic degeneracy of the $|\Omega|$ components for the individual F branches (see also Sec. 7.8.8 of the Appendix). However, the introduced splittings of the $|\Omega|$ states are below $1\,\mathrm{MHz}$ for this specific internuclear separation, and therefore very small.

---

[2] The operator $\overleftarrow{\nabla}_{\vec{r}} \cdot \delta(\vec{R} - \vec{r})\overrightarrow{\nabla}_{\vec{r}}$ is a shorthand for $\sum_{i,j}|\psi_i\rangle\langle\psi_j| \int d^3r \delta(\vec{R} - \vec{r})\left(\overrightarrow{\nabla}_{\vec{r}}\psi_i^*(\vec{r})\right) \cdot \left(\overrightarrow{\nabla}_{\vec{r}}\psi_j(\vec{r})\right)$, where the $\{|\psi_i\rangle\}$ form an orthonormal basis of the Hilbert space and $\psi_i(\vec{r}) \equiv \langle\vec{r}|\psi_i\rangle$.
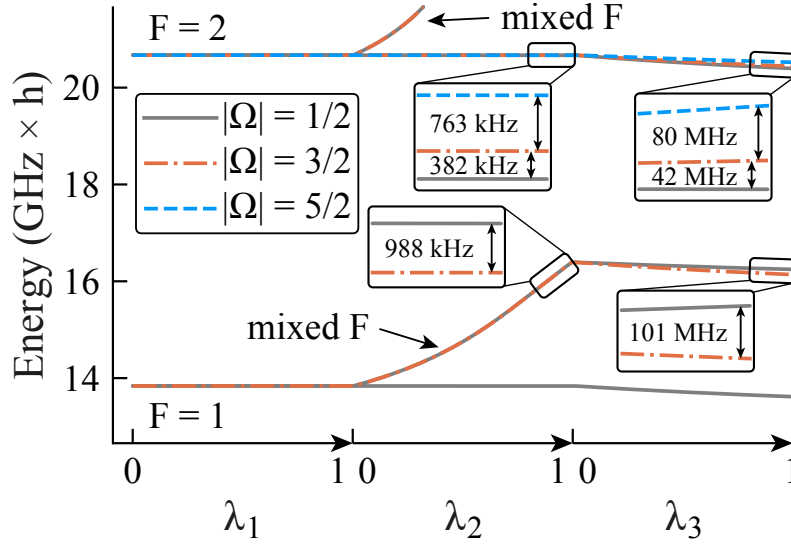
Figure 7.6: Values of the molecular PECs in the vicinity of the $16P_{1/2}$ **state at an internuclear distance** $R = 265\,a_0$ **as a function of the interaction control parameters** $\lambda_{1,2,3}$ **(see also Table 7.1).** On the left, where $\lambda_1 = \lambda_2 = \lambda_3 = 0$, interaction is identical for singlet and triplet states. *s*-wave and *p*-wave interactions are, however, not identical. When going to the right λ_1, λ_2, and λ_3 are subsequently turned on. Parameter λ_1 changes the singlet *s*-wave interaction, which does not have a significant impact on the PECs. In contrast, parameter λ_2 modifies the singlet *p*-wave scattering and introduces a splitting of the lines in two respects. First, branches of mixed *F* character separate from branches of pure *F* character. Second, the $|\Omega|$ components within these branches slightly split off from each other. Parameter λ_3 introduces a $\vec{L} \cdot \vec{S}$ type of interaction. This enhances the $|\Omega|$ splittings by about two orders of magnitude.

Finally, for the regime $\lambda_1 = \lambda_2 = 1, \lambda_3 > 0$ the full interaction introduced in Eq. (7.2) is realized by including the *J* dependency of the *p*-wave triplet scattering. The physical origin of the *J* dependency is $\vec{L} \cdot \vec{S}$ spin-orbit coupling. Each *J* channel ($J = \{0, 1, 2\}$) is associated with a characteristic energy E_r^J where the *p*-wave shape resonance occurs. For our scattering phase shifts these values are $E_r^{J=(0,1,2)} = (24.4, 25.5, 27.7)\,\text{meV}$, respectively [116]. We note that the energies E_r^J follow the Landé interval rule. Thus, electronic triplet states of different *J* experience different interaction strength for any given internuclear separation. Figure 7.6 shows that this leads to additional, strikingly large splittings of the $|\Omega|$ components, on the order of tens of MHz for the $F = 2$ branch up to about 100 MHz for the lower mixed *F* branch. It is by about two orders of magnitude larger than the splitting due to *p*-wave λ_2 spin-spin interaction. Therefore, we conclude that the shapes of the observed multiplet substructures are almost entirely determined by the $\vec{L} \cdot \vec{S}$ type of spin-orbit interaction. In absolute terms, calculated and measured splittings of $|\Omega|$ states deviate only by a factor of two to three (cf. Tab. 7.3 of the Appendix), which

represents a reasonable agreement in view of the complexity of the system to be modeled here.

We note, that in general, the $|\Omega|$ splittings depend on the internuclear distance R due to the energy dependence of the scattering lengths/volumes $a(L, S, J, k)$ as well as the spatial variation of the Rydberg electron wave function. This can be seen, e.g., when considering the PECs in Figure 7.2(b). Here, the $F = 1$ and $F = 2$ branches correspond to the $N = 1/2$ and $N = 5/2$ curves, respectively, while the mixed F branches are represented by the $N = 3/2$ curves. For example, when considering the $N = 3/2$ doublet, within the potential wells, for smaller values of R the $|\Omega| = 1/2$ and $|\Omega| = 3/2$ states are further energetically separated from each other than for higher values of R. Such a behavior can be explained by the enhancement of the multiplet line splittings due to resonant p-wave interactions which become more pronounced when approaching the p-wave shape resonance. Indeed, it is this mechanism that enables us to measure the given spin substructures at all. In order to check for consistency we have varied the internuclear separation around the value of $R = 265\, a_0$ used for Figure 7.6. A corresponding analysis reveals that the ratios of $|\Omega|$ splittings introduced by parameters λ_2 and λ_3 are robust, i.e. over the whole potential wells of Figure 7.2(b) $\vec{L} \cdot \vec{S}$ coupling still remains the dominant interaction that energetically separates the $|\Omega|$ components. Only when going to the left of the barriers very close to the p-wave shape resonance (e.g. at an internuclear distance of about $220\, a_0$) the relative impact of the parameter λ_2 is significantly increased.

At last, we consider the triplet substructures associated with $|\Omega| = \{1/2, 3/2, 5/2\}$ corresponding to $N = 5/2$. Both, in our measurements and calculations (see Table 7.3 of the Appendix) we find that the ratio of the energy separations between the $|\Omega| = 1/2$ and $3/2$ components, and the $|\Omega| = 3/2$ and $5/2$ components is about $2 : 3$ on average for the vibrational states. When simply applying the Landé interval rule for a $\vec{L} \cdot \vec{S}$ type spin-orbit interaction assuming Russell-Saunders coupling, ratios of $1 : 2$ would be expected for a triplet of pure $J = (0, 1, 2)$ states. However, J is not a good quantum number for the molecular system considered here. Indeed, the different $|\Omega|$ channels feature different J admixtures, which, in addition, vary as a function of internuclear distance R. Thus, the Landé interval rule cannot be applied to describe the given $|\Omega|$ splittings. Nevertheless, we want to point out that in future, it will be interesting to investigate other molecular manifolds of purer J characters, since deviations from the Landé interval rule can direct to the significance of relativistic effects [126].

In this section the generalized pseudopotential of Eq. (7.2) was used in order to investi-

gate different types of spin-spin and spin-orbit interactions. For convenience, however,
we show in Section 7.8.9 of the Appendix how conventional representations of spin-spin
and spin-orbit interactions can be derived from the pseudopotential approach, in general.

7.6   Comparison of results for vibrational ladders

For each of the states characterized by the quantum numbers N and $|\Omega|$ we have measured
the full vibrational progression over a large part of the potential wells. All measured and
calculated term energies are given in Table 7.3 of the Appendix. For convenient discus-
sion the data for the six different vibrational ladders are visualized in Figure 7.7. Here, the
same PECs are shown as in Figure 7.2(b), however these together with the predicted term
energies are shifted by 1.94 GHz to higher energies. Then, the calculated and measured
positions for the lowest vibrational level of $N = 1/2$ coincide at the experimental value
of 16.30 GHz $\times h$ [see Fig. 7.7(a)]. Such a shift is well within the uncertainty of absolute
energy determinations in the perturbative electronic structure calculations, which is on the
order of a few GHz [99, 127]. The assignment of the experimental resonance position of
16.30 GHz $\times h$ to the vibrational ground states is reasonable since it represents the lowest
observed singlet structure and it features a strong signal strength. Basically, the observed
alternation of the signal strength between adjacent vibrational states (see Table 7.3 of the
Appendix) can be explained as a consequence of the change of an approximate g/u sym-
metry of the vibrational molecular wave function from one vibrational state to another.
The excitation rate to a molecular state is proportional to the Franck-Condon factor (see,
e.g., [109]). Indeed, for molecular wave functions with g symmetry the Franck-Condon
factors should in general be significantly higher as compared to molecular wave functions
with u symmetry. The vibrational ground state of a potential well features g symmetry
and thus should entail a strong signal strength.

As can be seen from Figure 7.7 the measured vibrational spacings are in very good agree-
ment with the predicted values for each of the six vibrational ladders characterized by the
quantum numbers N and $|\Omega|$. This means that the shapes and the depths of the potential
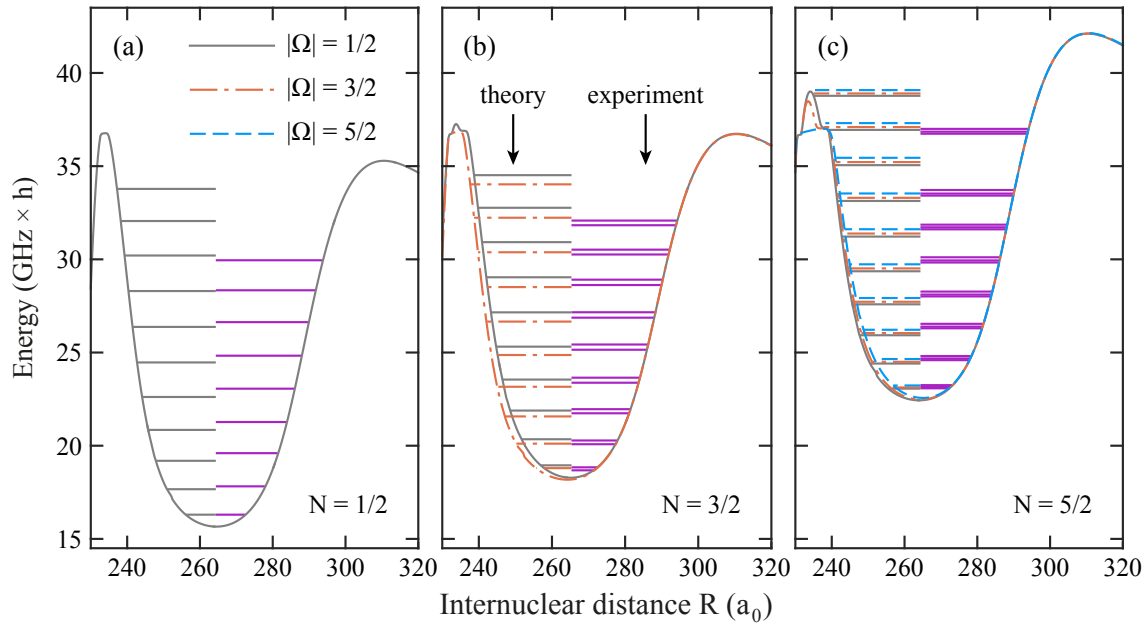wells are very well described by our model calculations.

Figure 7.7: Comparison of measured molecular term energies (purple horizontal lines) and calculated molecular term energies for $N = 1/2$ **(a),** $N = 3/2$ **(b), and** $N = 5/2$ **(c).** The results of the calculations for the different $|\Omega|$ states are indicated by the line color and line style as given in the legend. Here, the PECs and the predicted term energies are shifted by 1.94 GHz to higher energies for better comparison to the experimental data. Numerical values for the energy positions of vibrational states corresponding to the six different ladders characterized by the quantum numbers N and $|\Omega|$ can be found in Table 7.3 of the Appendix.

7.7 Conclusions and Outlook

In conclusion, using ultralong-range Rydberg molecules, we observed spin-orbit dependent electron-neutral scattering. Here, the coupling between the total electronic spin and the relative orbital angular momentum of the scattering electron with respect to the ground state atom gives rise to various interaction channels, which were resolved in the experiment. This observation became possible, since we explored a parameter regime where resonant p-wave interactions induced by a p-wave shape resonance increase the relevant energy splittings. In our measurements, various vibrational ladders, each with a characteristic substructure of level singlets, doublets, and triplets were revealed. By carrying out model calculations we were able to explain these line multiplicities, and to unambiguously assign all expected spin states to the corresponding experimental resonances.

In future work, it will be interesting to tune the resonant p-wave interactions by studying

ultralong-range Rydberg molecular states with different principal quantum numbers close to $n = 16$. In this regime of low n the shapes of the PECs of the p-wave molecular states vary strongly, since the crossings with the butterfly states occur at different internuclear distances for different n. For example, from our calculations we expect that for $n = 14$ Rb_2 molecules the p-wave shape resonance cuts through the second outermost potential wells which gives rise to avoided crossings and strong distortions of the potential wells. The molecular level structure will thus be determined by an interplay of adiabatic (e.g. quantum reflections of the wave functions [112, 115]) and diabatic dynamics.

For this reason, Rb_2 molecules in the regime of low principal quantum numbers can serve as an ideal testbed to study the strengths of various spin-spin and spin-orbit coupling mechanisms. Such studies could be complemented, e.g., by working with Cs_2 dimers. For instance, for Cs_2 ultralong-range Rydberg molecules the effect of the $\vec{L} \cdot \vec{S}$ spin-orbit coupling is predicted to be typically larger than for Rb_2 due to the much larger splittings in the energetic positions of the p-wave shape resonances associated with the individual channels $J = (0, 1, 2)$ [126, 128].

Our work paves the way for in-depth investigations of spin states of ultralong-range Rydberg molecules. Hence, we expect it to spark increased efforts to establish a consistent theoretical treatment of spin dynamics in such molecular systems. An extended set of data will help to assess current limitations in the model descriptions. For example, it will be valuable to gain information about the possible breakdown of the Born-Oppenheimer approximation due to avoided crossings of the PECs (as recently investigated with macrodimers [129]). This question directs to the necessity of full vibronic structure investigations [130] that take into account non-adiabatic couplings between PECs. In addition, it might turn out that the effective pseudopotential approach is not adequate to fully describe all relevant interactions. Generally, this approach suffers from limited accuracy due to convergence issues [99, 127]. Improvements may be achieved, e.g., by R-matrix methods [131]. To resolve these problems, an extended experimental and theoretical investigation is necessary.

Finally, we want to point out that the research on many-body and mean-field effects in polyatomic systems [132, 133, 134, 135, 136] can benefit from the gained information about spin-coupling mechanisms.

Note added. In parallel work to ours the group of T. Pfau in Stuttgart studied $\vec{L} \cdot \vec{S}$ coupling using Rb_2 S state molecules in the context of negative-ion resonances [116].

7.8   Appendix

7.8.1   Electronic spin character of the potential energy curves

In Figure 7.8 the same PECs as in Figure 7.2 of the main text are presented, however, with a different color coding. Here, the expectation value of the quantum number S of the total electronic spin is shown. Interestingly, the curves differ quite substantially in their spin character despite the fact that the hyperfine character is nearly constant for a given set of curves that belong to the same N. This leads in turn to rather different electronic dipole moments of the corresponding electronic states (cf. Sec. 7.8.5 of the Appendix).
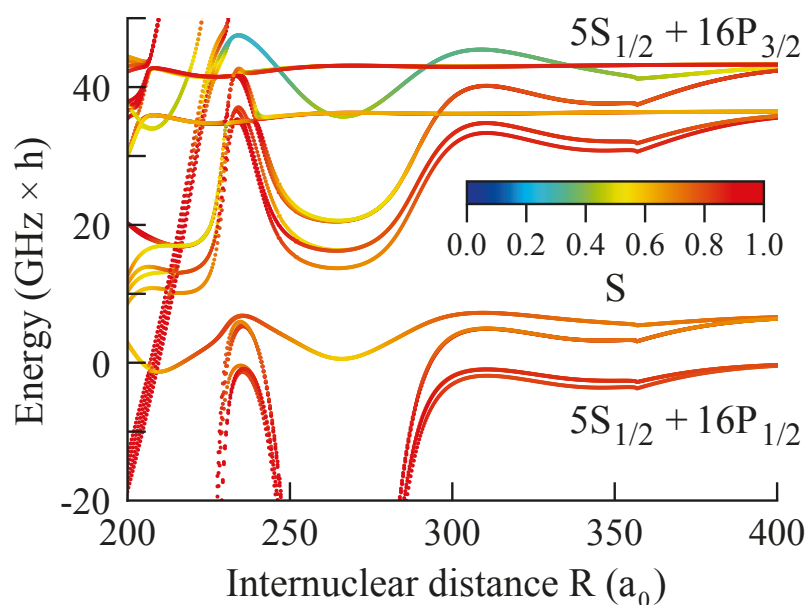
Figure 7.8: The molecular PECs correlated to the $5S_{1/2} + 16P_j$ **atomic asymptotes for** $j \in \{1/2, 3/2\}$ **and different hyperfine states** $F \in \{1, 2\}$ **of the** $5S_{1/2}$ **atom.** Here, the color code represents the expectation value of the quantum number S of the total electronic spin.

7.8.2   Simplistic description of the molecule and pure *s*-wave approach

The Rydberg electron features a large, spatially extended wave function with many nodes. For illustration, the inset of Figure 7.9 shows the electronic $16P$ orbital of the Rydberg atom, which overlaps with the ground state atom at distance R. The ground state atom and the Rydberg electron interact locally, which can entail molecular binding. When the

ground state atom is bound far away from the Rydberg ionic core, a so-called ultralong-
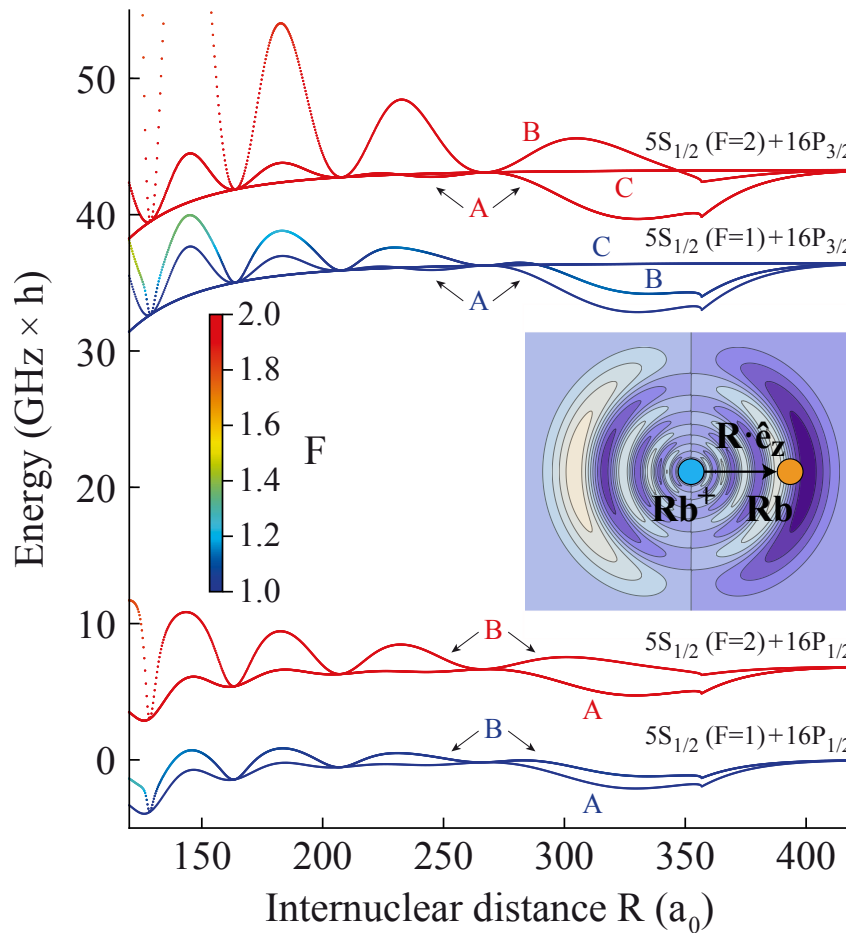range molecule is formed.

**Figure 7.9: The molecular Born-Oppenheimer potentials when *s*-wave interactions between
electron and ground state atom are taken into account but *p*-wave interactions are neglected.**
The colors of the curves indicate the expectation value of the F quantum number of the ground
state atom. From each atomic asymptote two oscillatory potentials emerge. They have $|m_j| = 1/2$
and feature the nodes of the electronic wave function. The deeper PECs (marked with A) are
associated with pure triplet scattering and the shallower PECs (marked with B) are associated
with mixed singlet/triplet scattering. The PECs labeled with C have $|m_j| > 1/2$ and do not show
an oscillatory behavior. In the inset a sketch of an ultralong-range Rydberg molecule is shown. It
consists of a Rb^+ ionic core, an electronic Rydberg $16P$ state orbital, and a ground state Rb atom
which is located at position $\vec{R} = R\hat{e}_z$ relative to the ionic core. The $16P$ electronic orbital is given
in a contour plot representation.

To a first approximation the interaction between the ground state atom and the Ryd-
berg electron can be modeled by a short-range, *s*-wave Fermi-type pseudopotential. In

Figure 7.9 the Born-Oppenheimer PECs are shown, when p-wave interaction is neglected in Eq. (7.1). The oscillatory behavior of the PECs reflects the radial wave function of the Rydberg electron. In the potential wells of the PECs vibrational bound states of ultralong-range Rydberg molecules exist. For large separations, $R \gtrsim 400\,a_0$, the PECs go over into the atomic asymptotes corresponding to the Rydberg levels $16P_{1/2}$ and $16P_{3/2}$, and the hyperfine states $F = 1$ and $F = 2$ of the ground state atom. At shorter distances hyperfine states are getting mixed.

7.8.3   Photoassociation setup

The photoassociation laser operates at wavelengths of around 302 nm. The laser light is generated by a frequency-doubled cw dye laser (see also Sec. 2.2) with a narrow short-time linewidth of a few hundred kilohertz. The laser is frequency-stabilized to a wavelength meter (High Finesse WS7) which is repeatedly calibrated to an atomic ^{87}Rb reference signal at a wavelength of 780 nm in intervals of hours. We achieve a shot-to-shot frequency stability of below ± 10 MHz for the 302 nm light.

A multi mode optical fiber is used to transfer the UV light to the experimental table. At the location of the atoms the spectroscopy beam has a waist ($1/e^2$ radius) of about 1.5 mm and the power is typically in the range of 4 to 10 mW. The light pulse has a rectangular shape and the atoms are exposed to the laser radiation for a duration on the order of 0.1 to 1 s.

7.8.4   Atomic lines

The strong resonance lines marked with horizontal black arrows in the spectra (a) and (b) of Figure 7.4 correspond to the atomic transitions towards $16P_{1/2}$ and $16P_{3/2}$. Here, the atom loss of the atomic cloud is close to 100%. The $16P_{1/2}$ line is located at $\Delta \nu = 0$ in (a) and at $\Delta \tilde{\nu} \approx \nu_{\text{hfs}} = 6.835$ GHz in (b) which corresponds to the ground state hyperfine splitting. For the excited Rydberg P state the hyperfine splitting can be neglected. The asymmetric tail on the red side of each atomic resonance line arises from the Stark effect due to the electric fields of both the Paul trap and the trapped ions (see also Chapter 6 and [87, 88]). The strong resonance lines marked with vertical black arrows in the spectra (a) and (b) of Figure 7.4 also correspond to transitions towards the atomic $16P_{1/2}$ and

$16P_{3/2}$ states. These lines are shifted by about $\pm\nu_{\text{hfs}}$ relative to the atomic resonance lines
marked with horizontal black arrows. Apparently, each of the prepared $F = 1$ ($F = 2$)
samples is not 100% pure but contains a fraction of atoms in the other spin state $F = 2$
($F = 1$), respectively. Although these admixed fractions are possibly on the percent level
or less they still can give rise to large signals due to the non-linear behavior of the atomic
loss, as discussed in the main text.

7.8.5   Lineshapes and linewidths of molecular signals

The natural lifetimes of the molecular states considered here should be on the order of the
one of the atomic $16P_{3/2}$ Rydberg state, which is predicted to be about $4\,\mu$s [137]. Corre-
spondingly, the expected linewidth of molecular signals is below $1\,$MHz. The measured
linewidths of several tens of MHz exceed this value by more than one order of magni-
tude. Since the observed molecular states are located rather deep in the potential wells of
Figure 7.2(b) their lifetime is not limited due to inward tunneling and subsequent decay
as the tunneling rates are negligibly small. We note that there are tiny avoided level cross-
ings in the PECs (barely visible in Fig. 7.2). For example, we have looked into avoided
crossings at an internuclear distance around $252\,a_0$. Our analysis shows that the widths of
these avoided crossings are too small to give rise to significant probability fluxes leaking
out of the wells. Furthermore, such a leaking would entail a dynamic to larger internu-
clear distances preventing short-range decay.

Another parameter that can influence lineshapes and linewidths is the electric field. In
our experimental scheme an ion trap is used and therefore dc and ac electric fields are
present. We now estimate energy level shifts due to the Stark effect via the relation
$E_{\text{sh}} = -|\vec{d}|\cdot|\vec{\mathscr{E}}|\cdot\cos(\theta)$, where θ represents the angle between the vector of the dipole
moment $\vec{d}$ and the vector of the electric field $\vec{\mathscr{E}}$.

To this end, we have calculated the electric dipole moments for the molecular states char-
acterized by N and $|\Omega|$. For each of these states the calculation has been carried out for
the internuclear separation corresponding to the minimum of the respective potential well.
The obtained results for the electric dipole moments d are given in Table 7.2 in units of
ea_0, where e is the elementary charge. The sign of d is determined by the different con-
tributions of each element of the gradient of the wave function. The magnitude of d is
substantially different for the various states considered. In general, the absolute values of
the electric dipole moments are small for states with dominant singlet character and large

Table 7.2: Calculated electric dipole moments for molecules in states characterized by N and $|\Omega|$. The results are obtained for internuclear distances corresponding to the minima of the respective potential wells.

N	$|\Omega|$	d (ea_0)
1/2	1/2	24.5
3/2	1/2	4.25
3/2	3/2	12.7
5/2	1/2	-107
5/2	3/2	-46.2
5/2	5/2	0.15

for states with dominant triplet character (cf. Fig. 7.8).

The amplitudes of the different electric field components of the ion trap are ideally zero at its center and increase with increasing distance from the center. At a distance of $2\,\mu m$ the dc field amplitude is $\sim 2 \times 10^{-3}\,V\,cm^{-1}$ and the ac field amplitude is $\sim 1\,V\,cm^{-1}$. Using the state $N = 5/2$, $|\Omega| = 1/2$, which features the largest absolute value for the electric dipole moment, and assuming that $\theta = 0$, we estimate an upper threshold for the level energy shift of about $0.3\,MHz \times h$ and $140\,MHz \times h$ for the dc and ac electric field components, respectively. Therefore, the energy level shifts due to static electric fields can safely be neglected, but the ac field might lead to sizeable broadening of the molecular lines, since, to first approximation in the molecule formation the angle θ is randomly sampled. In contrast, a corresponding estimation for the state $N = 5/2$, $|\Omega| = 5/2$ yields a maximum contribution of $0.2\,MHz \times h$ due to the ac field.

Nevertheless, in our measurements we find that the linewidths are very similar for all measured resonances. Such a behavior is not expected as the electric dipole moments for the different molecular states show a strong variation (see Table 7.2). Correspondingly, the linewidths seem not to be dominated by the impact of the Stark effect. We can explain this by the fact that the photoassociation rate scales linearly with atomic density. Consequently, the formation of molecules preferentially takes place right in the center of the atom cloud, i.e. at the center of the ion trap. There, however, the electric field and the field variation are generally small. The given explanation is in agreement with the observation of rather symmetric lineshapes of molecular resonances.

The measured large widths of several tens of MHz of the molecular lines might be explained by a combination of the uncertainty of the UV photoassociation laser of about

$\pm 10\,\text{MHz}$, and limitations in the lifetime due to the subsequent ionization or inelastic collisions of Rydberg molecules with Rb atoms.

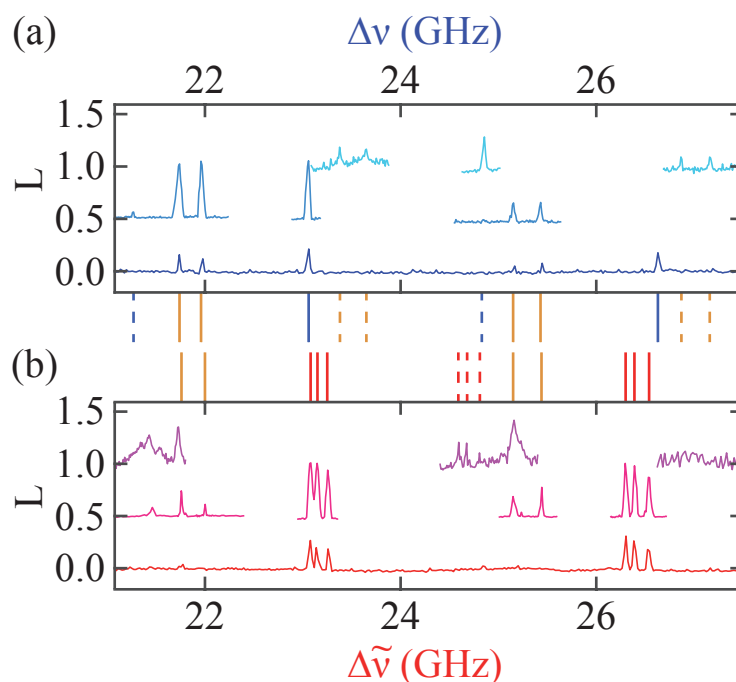### 7.8.6 Mining of experimental data

Figure 7.10: Measured series of line multiplets for atomic samples initially prepared in the hyperfine state $F = 1$ (a) and $F = 2$ (b). The blue and red data curves are the same as in Figure 7.4. All other spectra are obtained for individually optimized experimental parameters to locally increase the signal-to-noise ratio. For better visibility light blue and magenta data (cyan and purple data) are shifted in vertical direction by 0.5 (1.0). Blue, orange, and red vertical lines on the bottom of plot (a) [on the top of plot (b)] indicate the frequency positions of measured resonances belonging to line singlets, line doublets, and line triplets, respectively. The alternating signal strength behavior for each multiplet series is illustrated by the line style, where solid (dashed) lines represent strong (weak) signals.

In general, we have various parameters available to tune signal strengths for the detection of ultralong-range Rydberg molecules. These are the intensity and pulse duration of the spectroscopy light, but also the ionic micromotion energy and the interaction time between trapped ions and neutral atoms. Figure 7.10 shows how signals change when we vary these parameters, as indicated by different line colors and scan ranges. The dark blue data in (a) and the red data in (b) are zooms into Figure 7.4(a) and (b), respectively. Ad-

ditional resonance lines which are not visible in these two spectra, can be revealed after individual parameter optimization. The blue, orange, and red vertical lines represent the center frequency positions of the measured resonances of line singlets, line doublets, and line triplets. Solid and dashed vertical lines mark strong and weak signals, respectively. They alternate between adjacent vibrational states for each of the three observed ladders. Within the given frequency range we observe almost the complete series of expected resonances for each multiplet structure. Only the weak line doublets for $F = 2$ are missing in Figure 7.10(b) (see purple data scan at around $\Delta\tilde{\nu} = 27\,\mathrm{GHz}$).

7.8.7 Restricting the Hilbert space for numerical calculations

The Hamiltonian H is constructed in a finite basis set that includes the 15S, 16S, 17S, 14P, 15P, 16P, 13D, 14D, 15D states, and the hydrogenic states with higher orbital angular momenta $l \geq 3$ with principle quantum numbers $n = 12$, $n = 13$, and $n = 14$. All these states are considered with all possible total angular momenta j, while the projections m_j are truncated to include $|m_j| \leq 3/2$. According to the choice of the molecular axis lying on the z axis, states with $|m_j| > 3/2$ do not interact with the ground state atom. Additionally, the nuclear and electronic spins of the ground state atom are taken into account completely ($m_I = \{\pm 1/2, \pm 3/2\}$ and $m_2 = \pm 1/2$). Note, that placing the perturber onto the z axis significantly reduces the basis set. Since the scattering interaction V vastly exceeds the Zeeman energy for any magnetic fields occurring due to the experimental setup, the atomic orbitals align along the internuclear axis. This is different, however, when the interaction with an external field is comparable or larger than the scattering interaction [103]. An alternative approach to derive the PECs that circumvents a finite basis set are Green's function methods employed for example in [97, 117]. However, these approaches do not incorporate spin interactions that are crucial for the interpretation of our results. Nevertheless, we used the Green's function approach and a reduced spin model which neglects fine and hyperfine structure to find the optimal basis size. The corresponding basis was then employed for the full model calculations.

7.8.8   Discussion of splitting mechanisms

The separation of states with mixed F character from those with pure $F = 1, 2$ character as a function of the internuclear distance R can directly be seen, e.g., in the PECs of Figure 7.9 for $R \lesssim 370\, a_0$. Each asymptote breaks up into two oscillatory PECs, marked with A and B. There is an additional, non-oscillatory PEC, marked with C, for each $P_{3/2}$ asymptote. These C PECs correspond to Rydberg states with $m_j = \pm 3/2$ which do not undergo s-wave interaction, because the ground state atom on the z axis is located at the node of the $|m_l| = 1$ electronic orbital. The remaining interaction of the C PECs in Figure 7.9 is then solely through the attractive $1/R^4$ polarization potential due to the Rb$^+$ ionic core.

In the literature [102, 108, 113, 115] each pair of oscillatory PECs is subclassified into a 'deeper' curve (A) and a 'shallower' curve (B). The deeper curves correspond in Figure 7.6 to the lines which are flat as a function of λ_1. They are flat because they are insensitive to the singlet s-wave interaction. However, the deeper curves are not pure triplet states due to Rydberg fine structure. We explain how this is possible with the following example. We consider the electronic state of a Rydberg atom in a P state with total orbital angular momentum $j = 1/2$ and projection $m_j = 1/2$ and a ground state atom in a polarized nuclear spin state $F = 2$ and $m_F = 2$,

$$\begin{pmatrix} \psi_{m_l=0,\uparrow}(\vec{r}) \\ \psi_{m_l=1,\downarrow}(\vec{r}) \end{pmatrix} \otimes |F = 2, m_F = 2\rangle \, . \tag{7.4}$$

To first order perturbation theory (with respect to weak s- and p-wave interaction) this state must be an eigenstate of the Hamiltonian, as it is the only possible realization of an $\Omega = 5/2$ state in the Hilbert subspace considered here. The spin-up component has $m_l = 0$ and the spin-down component has $m_l = 1$. Together with the spin-stretched ground state atom, the spin-up component forms a pure spin triplet. Therefore, this component does not interact in the s-wave singlet channel. The spin-down component is a mixed singlet/triplet state. However, it still does not interact in the s-wave singlet channel because $m_l = 1$ and hence the ground state atom is located at the node of the electronic wave function. Thus, despite the fact that the state of Eq. (7.4) has a singlet component, it is insensitive to s-wave singlet interaction.

The state of Eq. (7.4) is just one example for the many degenerate eigenstates associated

with the deep PECs. The degeneracy of the deep and shallow PECs can be obtained with the help of the spin operator $\vec{N}^2$, where $\vec{N} = \vec{S} + \vec{I} = \vec{s}_1 + \vec{F}$. $\vec{N}^2$ does not commute with H_{Ryd} due to the Rydberg fine structure, however, it is still useful for labeling the scattering channels, as we show in the following. The basis states of a given F branch all have a similar form as the state of Eq. (7.4). Within the vector space spanned by these basis states, we want to determine the dimension of the subspace that is susceptible to singlet s-wave interaction. Since the $|m_l| = 1$ component of a basis state does not contribute to s-wave interaction, we only consider its $m_l = 0$ component, of which the spin can be up or down. Thus, the problem can be reduced to determining the dimension of the formed $S = 1$ subspace when coupling an electronic spin $\vec{s}_1$ to the angular momentum F manifold where $\vec{F} = \vec{I} + \vec{s}_2$. For this, we divide up the resulting new manifold into subspaces with good quantum number N. Since $\vec{N}^2$ commutes with both $\vec{S}^2$ and $\vec{F}^2$, this will help us sorting out the spin structure. We note, however, that $\vec{S}^2$ and $\vec{F}^2$ do not commute. For $F = 2$, N can be $N = 5/2$ or $N = 3/2$. Since the $N = 5/2$ subspace must have $S = 1$ it belongs to branch A. With the help of Wigner $6j$ coefficients one can show that the $N = 3/2$ subspace, however, contains states with singlet and triplet character and therefore belongs to branch B. Similarly, for $F = 1$, we have the subspaces $N = 3/2$ and $N = 1/2$. $N = 1/2$ goes along with $S = 1$ and thus belongs to branch A, whereas $N = 3/2$ includes both S characters and belongs to branch B. As the difference in the singlet and triplet s-wave interactions becomes larger, the two $N = 3/2$ manifolds of the $F = 1$ and $F = 2$ branches start mixing. The degree of F mixing depends on the relative strength of the differential singlet/triplet s-wave interaction and the hyperfine interaction H_{g}. The F mixing due to the presence of a singlet s-wave scattering channel is essential for the spin flip effect observed in [111]. N reproduces the multiplicities for the PECs, which are visible in Figure 7.2(b) and Figure 7.6. For the $F = 2$ asymptote, the deep curve corresponds to $N = 5/2$ and has six degenerate states of pure $F = 2$ character. For the $F = 1$ asymptote, the deep curve corresponds to $N = 1/2$ and has two degenerate states of pure $F = 1$ character. The shallow curves of both, the $F = 1$ and the $F = 2$ asymptote correspond to $N = 3/2$ and have four degenerate states of mixed $F = 1$ and $F = 2$ character each. While this regime of interactions is sufficient to describe the PECs at the outer potential wells (in this case for $R > 300\,a_0$), additional p-wave related interactions become important for smaller internuclear separations, which are already relevant in the parameter regime of λ_2.

The difference between the singlet and triplet channels introduced via parameter λ_2 af-

fects in particular the spinor components with $m_l = \pm 1$, which only probe the p-wave interaction but not the s-wave interaction. Although the state with $\Omega = 5/2$ of Eq. (7.4) is of pure triplet character in its $m_l = 0$ component, it is of mixed singlet/triplet character in its $m_l = 1$ component, as discussed before. As a consequence, it will experience a first order level shift. States with a different $|\Omega|$ have different mixing ratios and will exhibit different shifts. Therefore, the spin-selective p-wave interaction generally leads to a splitting of $|\Omega|$ states. This splitting, however, arises only due to the Rydberg fine structure and is, hence, not visible in S state ultralong-range Rydberg molecules recently studied [138], since they do not exhibit such a kind of fine structure related to λ_2.

7.8.9 Alternative representation of spin-spin and spin-orbit interaction

The pseudopotential that models the interaction between the Rydberg electron and the ground state atom is given in Eq. (7.2) of the main text. Our aim is now to rewrite the given interaction potential in terms of operators such as $\vec{s}_1 \cdot \vec{s}_2$ and $\vec{L}_{\text{tot}} \cdot \vec{S}$, respectively. First, we consider the example of pure s-wave scattering, i.e. $L = 0$. In this case one obtains $J = S$ and $M_J = M_S$ and therefore Eq. (7.2) reads

$$V_{L=0} = \frac{\delta(X)}{2X^2} \sum_{S=0}^{1} \sum_{M_S=-S}^{S} a(0,S,S,k)|0,S,S,M_S\rangle\langle 0,S,S,M_S|. \tag{7.5}$$

We compare this expression now to the ansatz

$$V_{L=0} = \left[c_1 \hat{1} + c_2 \vec{s}_1 \cdot \vec{s}_2\right] \frac{\delta(X)}{2X^2}|L=0\rangle\langle L=0|. \tag{7.6}$$

For this Eq. (7.6) is represented as a 4×4 matrix in the basis $|S, M_S\rangle$. From the comparison of Eq. (7.6) and Eq. (7.5) we find that both expressions are identical if $c_1 = [a(0,0,0,k) + 3a(0,1,1,k)]/4$ and $c_2 = a(0,1,1,k) - a(0,0,0,k)$. As expected, there is no spin-spin coupling, i.e. $c_2 = 0$, when the s-wave singlet and triplet scattering lengths/volumes $a(0,0,0,k)$ and $a(0,1,1,k)$ are equal. Furthermore, c_1 corresponds to the averaged s-wave scattering length/volume.

Now, as we have seen that the basic mapping works, in principle, we turn to a treatment of spin-orbit coupling. Since spin-orbit interaction only takes place in the p-wave triplet

channel we consider only the subspace with $L = 1$ and $S = 1$. In this subspace the inter-action potential reduces to

$$V_{L=S=1} = \frac{9\delta(X)}{2X^4} \sum_{J=0}^{2} \sum_{M_J=-J}^{J} a(1,1,J,k)|1,1,J,M_J\rangle\langle 1,1,J,M_J|. \tag{7.7}$$

Again we make an ansatz

$$V_{L=S=1} = \left[c_3\hat{1} + c_4\vec{L}\cdot\vec{S} \right] \frac{9\delta(X)}{2X^4} |L=1,S=1\rangle\langle L=1,S=1|. \tag{7.8}$$

From the comparison of Eq. (7.8) and Eq. (7.7) follows

$$a(1,1,0,k) = c_3 - 2c_4,$$
$$a(1,1,1,k) = c_3 - c_4,$$
$$a(1,1,2,k) = c_3 + c_4. \tag{7.9}$$

This means that the coefficients c_3 and c_4 are over-determined. Therefore, the representa-tions of $V_{L=S=1}$ given in Eq. (7.7) and Eq. (7.8) are only identical if the scattering volumes satisfy certain conditions, such as, e.g.,

$$\frac{a(1,1,0,k) - a(1,1,1,k)}{a(1,1,1,k) - a(1,1,2,k)} = \frac{1}{2}. \tag{7.10}$$

We have checked whether the scattering lengths/volumes fulfill Eq. (7.10). It turns out that for wave numbers k far away from the p-wave shape resonance the given relation holds. However, when approaching the p-wave shape resonance the ratio deviates increasingly from $1/2$ until it diverges at the resonance energy. Thus, the given ansatz of Eq. (7.8) is not sufficient to describe spin-orbit interaction in the near-resonant regime. As a next step, we take into account the second-order correction in the expansion, i.e. the interaction potential is expressed by

$$V_{L=S=1} = \left[c_3\hat{1} + c_4\vec{L}\cdot\vec{S} + c_5(\vec{L}\cdot\vec{S})^2 \right] \times \frac{9\delta(X)}{2X^4} |L=1,S=1\rangle\langle L=1,S=1|. \tag{7.11}$$

Now, the comparison of Eq. (7.11) and Eq. (7.7) yields

$$
c_3 = \frac{-a(1,1,0,k) + 3a(1,1,1,k) + a(1,1,2,k)}{3},
$$
$$
c_4 = \frac{-a(1,1,1,k) + a(1,1,2,k)}{2},
$$
$$
c_5 = \frac{2a(1,1,0,k) - 3a(1,1,1,k) + a(1,1,2,k)}{6}.
$$
(7.12)

The result implies that the $\vec{L} \cdot \vec{S}$ coupling vanishes, i.e. $c_2 = c_3 = 0$, only if all scattering volumes are equal, which agrees with our expectation. In general, such second order interaction between states comes about in an indirect way via other states which are of mixed character and mediate the coupling. In particular, close to the p-wave shape resonance such mixing can occur which supports our finding. It will be interesting to investigate this second order spin-orbit interaction in more detail in future, and to identify the involved molecular states.

Table 7.3: Measured and calculated molecular energy level positions. The subscripts e and t denote experimental and theoretical results, respectively. $\Delta\nu_e$ and $\Delta\tilde{\nu}_e$ are measured resonance frequencies, while $\Delta\nu_t$ corresponds to computed term frequencies (referenced to the calculated $5S_{1/2} + 16P_{1/2}$ dissociation threshold). The subscript s indicates splittings between Ω states within individual multiplet structures and the subscript v is used to mark vibrational splittings for a given Ω quantum number. Signal strengths of measured and calculated resonance lines are classified in weak (w) or strong (s). Not-observed lines are labeled with n.o. Values of $\Delta\nu_e$ indicated by ($*$) characterize experimental signals which might come from different molecular states than considered here. These signals are not taken into account for Figure 7.7. The resonance at $\Delta\tilde{\nu}_e = 31.86\,\text{GHz}$ marked with ($**$) is rather broad and expected to consist of a $N = 5/2$ and a $3/2$ molecular line which cannot be resolved. We just give this frequency for the corresponding lines of the double as well as the triple line pattern.

experiment ($F = 1$)				experiment ($F = 2$)				theory				
$\Delta\nu_e$	$\delta\nu_{s,e}$	$\delta\nu_{v,e}$	signal strength	$\Delta\tilde{\nu}_e$	$\delta\tilde{\nu}_{s,e}$	$\delta\tilde{\nu}_{v,e}$	signal strength	$\lvert\Omega\rvert$	$\Delta\nu_t$	$\delta\nu_{s,t}$	$\delta\nu_{v,t}$	signal strength
(GHz)	(GHz)	(GHz)		(GHz)	(GHz)	(GHz)			(GHz)	(GHz)	(GHz)	
vibrational ladder of single lines ($N = 1/2$, pure triplet)												
16.30			s					0.5	14.36			s
17.82		1.52	w					0.5	15.73		1.37	w
19.60		1.78	s					0.5	17.25		1.52	s
21.27		1.67	w					0.5	18.91		1.66	w
23.06		1.79	s					0.5	20.67		1.76	s
24.83		1.77	w					0.5	22.53		1.86	w
26.63		1.80	s					0.5	24.43		1.90	s
28.34		1.71	w					0.5	26.36		1.93	w
29.95		1.61	s					0.5	28.27		1.91	s
31.38*		1.43	w					0.5	30.11		1.84	w
32.34*		0.96	s					0.5	31.84		1.73	s
double line pattern ($N = 3/2$, mixed singlet/triplet)												
18.68			s	18.64			s	1.5	16.86			s
18.84	0.16		s	18.80	0.16		s	0.5	17.01	0.15		s
20.08		1.40	w	20.12		1.48	w	1.5	18.17		1.31	w
20.28	0.20	1.44	w	20.32	0.20	1.52	w	0.5	18.41	0.24	1.40	w
21.74		1.66	s	21.76		1.64	s	1.5	19.63		1.46	s
21.96	0.22	1.68	s	22.00	0.24	1.68	s	0.5	19.95	0.32	1.54	s
23.38		1.64	w	n.o.				1.5	21.22		1.59	w
23.65	0.27	1.69	w	n.o.				0.5	21.61	0.39	1.66	w

Table 7.3: Continuation

experiment ($F = 1$)				experiment ($F = 2$)				theory					
$\Delta\nu_e$	$\delta\nu_{s,e}$	$\delta\nu_{v,e}$	signal strength	$\Delta\tilde{\nu}_e$	$\delta\tilde{\nu}_{s,e}$	$\delta\tilde{\nu}_{v,e}$	signal strength	$|\Omega|$	$\Delta\nu_t$	$\delta\nu_{s,t}$	$\delta\nu_{v,t}$	signal strength	
(GHz)	(GHz)	(GHz)		(GHz)	(GHz)	(GHz)			(GHz)	(GHz)	(GHz)		
25.15		1.77	s	25.15			s	1.5	22.93		1.71	s	
25.43	0.28	1.78	s	25.44	0.29		s	0.5	23.37	0.44	1.76	s	
26.87		1.72	w	n.o.				1.5	24.72		1.79	w	
27.16	0.29	1.73	w	n.o.				0.5	25.21	0.49	1.84	w	
28.62		1.75	s	28.65			s	1.5	26.57		1.85	s	
28.91	0.29	1.75	s	28.93	0.28		s	0.5	27.10	0.53	1.89	s	
30.26		1.64	w	n.o.				1.5	28.44		1.87	w	
30.52	0.26	1.61	w	n.o.				0.5	28.98	0.54	1.88	w	
31.83		1.57	s	31.86**			s	1.5	30.29		1.85	s	
32.08	0.25	1.56	s	32.10	0.24		s	0.5	30.83	0.54	1.85	s	
								1.5	32.08		1.79	w	
								0.5	32.58	0.50	1.75	w	

triple line pattern ($N = 5/2$, pure triplet)

				21.36*			w						
				21.43*	0.07		w						
				21.54*	0.11		w						
				23.08		1.72	s	0.5	21.12			s	
				23.15	0.07	1.72	s	1.5	21.18	0.06		s	
				23.25	0.10	1.71	s	2.5	21.29	0.11		s	
				24.59		1.51	w	0.5	22.47		1.35	w	
				24.68	0.09	1.53	w	1.5	22.56	0.09	1.38	w	
				24.81	0.13	1.56	w	2.5	22.71	0.15	1.42	w	
				26.30		1.71	s	0.5	23.99		1.52	s	
				26.39	0.09	1.71	s	1.5	24.10	0.11	1.54	s	
				26.54	0.15	1.73	s	2.5	24.28	0.18	1.57	s	
				28.01		1.71	w	0.5	25.65		1.66	w	
				28.11	0.10	1.72	w	1.5	25.78	0.13	1.68	w	
				28.27	0.16	1.73	w	2.5	25.98	0.20	1.70	w	
				29.83		1.82	s	0.5	27.42		1.77	s	
				29.94	0.11	1.83	s	1.5	27.57	0.15	1.79	s	
				30.11	0.17	1.84	s	2.5	27.79	0.22	1.81	s	
				31.61		1.78	w	0.5	29.28		1.86	w	

Table 7.3: Continuation

experiment ($F = 1$)				experiment ($F = 2$)				theory				
$\Delta\nu_e$	$\delta\nu_{s,e}$	$\delta\nu_{v,e}$	signal strength	$\Delta\tilde{\nu}_e$	$\delta\tilde{\nu}_{s,e}$	$\delta\tilde{\nu}_{v,e}$	signal strength	$|\Omega|$	$\Delta\nu_t$	$\delta\nu_{s,t}$	$\delta\nu_{v,t}$	signal strength
(GHz)	(GHz)	(GHz)		(GHz)	(GHz)	(GHz)			(GHz)	(GHz)	(GHz)	
				31.72	0.11	1.78	w	1.5	29.44	0.16	1.87	w
				31.86**	0.14	1.75	w	2.5	29.67	0.23	1.88	w
				33.42		1.81	s	0.5	31.19		1.91	s
				33.53	0.11	1.81	s	1.5	31.36	0.17	1.92	s
				33.72	0.19	1.86	s	2.5	31.59	0.23	1.92	s
				n.o.				0.5	33.11		1.92	w
				n.o.				1.5	33.28	0.17	1.92	w
				n.o.				2.5	33.51	0.23	1.92	w
				36.74			s	0.5	35.00		1.89	s
				36.85	0.11		s	1.5	35.16	0.16	1.88	s
				37.00	0.15		s	2.5	35.37	0.21	1.86	s
								0.5	36.83		1.83	w
								1.5	36.96	0.13	1.80	w
								2.5	37.14	0.18	1.77	w

7.8.10 Additional content*

A larger frequency range as compared to Figure 7.10 is shown in Figure 7.11. The plot nicely reveals the different vibrational ladders in the measurement and also the alternating line strengths from one vibrational state to another are visible. This can be seen for example for the line triplets, where the signals at about 21 GHz are weak, the signals at about 23 GHz are strong and so on (Fig. 7.11 b)). As described before, this can be explained by the gerade (g) or ungerade (u) symmetry of the wave functions of the excited states. The overlap with the ground state wave function is in general bigger for gerade wave functions leading to a higher excitation probability.
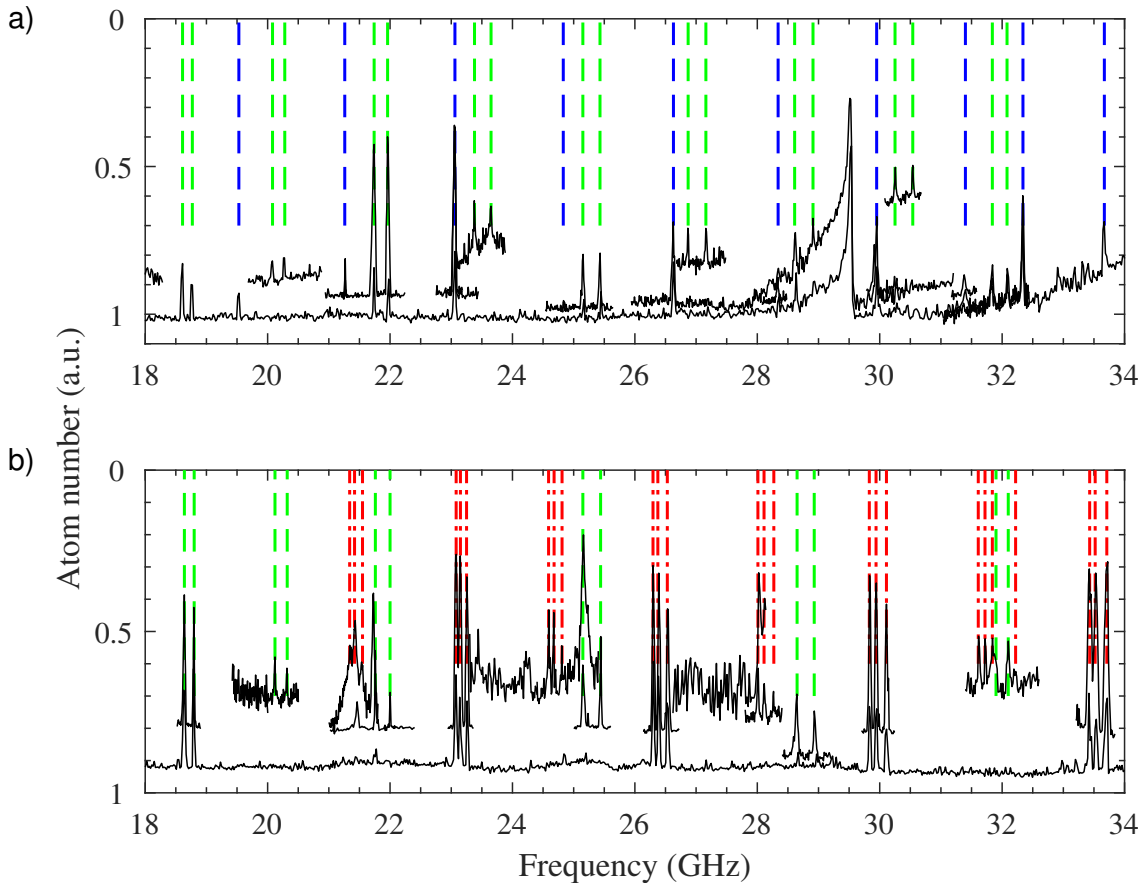
Figure 7.11: Larger frequency range of the data presented in Figure 7.10. The data for atoms initially prepared in the hyperfine state f=1 [f=2] are shown in a) [b)], respectively. The atom number scale is inverted to show peaks corresponding to increased atom loss. The vertical offsets of different data sets are runs with different measurement parameters. A higher base line atom number is related to longer interaction times such that also weaker resonance signals can be detected. The vertical lines indicate the measured vibrational states displayed in Figure 7.7. The blue and red vertical lines show the measured states in the $N = 1/2$ and the $N = 5/2$ potential, respectively. The green vertical lines indicate the states in the $N = 3/2$ potential visible for both initial hyperfine states. The not marked line in the $f = 1$ measurement is a mixed hyperfine state pure atomic transition.

8 Outlook

Several experiments have been discussed in this thesis. The results suggest many more future experiments on the topics. In this outlook, I will give an overview of a few of the most promising projects for ultracold state-to-state chemistry that can be investigated with the BaRbIE-system.

- In the current work, we have investigated the three-body recombination product molecules formed in weakly bound X-a states (binding energies of up to $h \times 17\,\text{GHz}$). In Chapter 4 we have shown that we have measured the population distribution for about 90% of the product molecules. All of them have been formed in X-a states with total positive parity. Furthermore, did we find a decline of the population of increasing deeply bound vibrational levels that is roughly proportional to the inverse of the square root of the binding energy. Therefore, it is not expected to find considerable population in vibrational states, which are deeper bound as the $v = -5$ vibrational state (about $h \times 17\,\text{GHz}$ binding energy).

  In the preceding work of Härter et al. [12] more-deeply bound product molecules have been investigated. They found product molecules in these more-deeply bound states (binding energies of up to $h \times 750\,\text{GHz}$). Contrary to our current work, they also found a population of product molecules in X-a states with total negative parity. These ambiguities need to be investigated in more detail. Therefore, we plan to extent the investigated range of molecular states populated by the product molecules to more-deeply bound X-a states.

  Increasing the sensitivity of the currently used two-color REMPI scheme can enable us to detect small populations of product molecules in more-deeply bound X-a states. For a refined two-color REMPI, it is planned to replace the laser used for the atomic dipole trap and the ionization of the molecules by two different lasers.

A laser at 1550 nm will be used for the atomic dipole trap. This long wavelength will strongly reduce possible transitions from X-a states to an intermediate state and therefore will reduce unwanted couplings and background ionization.

The ionization will be performed more controlled with the additional ionization laser. We plan to use a one photon transition to ionize the electronically excited molecules after the first state selective transition. This reduces the complexity of the former two photon ionization scheme. For this purpose, we have bought a frequency doubled OPO (Optical-Parametric-Oscillator). We will use it with a wavelength of roughly 488 nm. The wavelength is chosen such that the background ionization and unwanted couplings are suppressed.

The refined two-color REMPI will have several advantages. The reduced background ionization rate allows for extended possible interaction times. The one photon step into the continuum will work for a broader range of intermediate states. This will reduce the complexity of finding a good ionization efficiency. Furthermore, an ionization laser which is not used for dipole trapping paves the way for more advanced measurement schemes. For example, it can be used to operate the ionization laser in a pulsed fashion to extract the lifetime of excited molecules in the atom cloud.

- In the future, it will be very interesting to perform state-to-state chemistry measurements for atoms with different scattering properties. So far we have performed our state-to-state chemistry measurements only for the atomic isotope ^{87}Rb. For this isotope, the singlet and the triplet scattering lengths are positive and very similar.

  The only other stable isotope of rubidium is ^{85}Rb. This isotope has very interesting scattering properties. It has an about 24 times larger singlet scattering length than ^{87}Rb. Furthermore, the triplet scattering length is negative and is 4 times larger than for ^{87}Rb [139].

  The different scattering lengths of the two isotopes lead to different three-body recombination rate coefficients. ^{85}Rb has an a thousand times larger three-body recombination rate coefficient than ^{87}Rb [30]. Therefore, it is likely that ^{85}Rb might have a different product distribution after three-body recombination. It would be interesting to verify this.

  Another interesting point is that ^{85}Rb exhibits a strong Feshbach resonance at a comparatively low magnetic field of about 160 G [140]. So far we have been in-

vestigating the population distribution of the product molecules for non-resonant interactions. By utilizing the Feshbach resonance of ^{85}Rb it will be possible to investigate the population distribution of the product molecules in the range of non-resonant to resonant interactions.

- We have used our experimental methods mainly to investigate product molecules after a three-body recombination. The experimental methods could also be used in future, to investigate collision-induced relaxation of molecules.

  For this, the molecules can be initially prepared in well-defined quantum states e.g. by a stimulated Raman adiabatic passage (STIRAP) of Feshbach molecules. Subsequently, these molecules can undergo collisions with atoms or with themselves. This can lead to a relaxation of the molecules into different vibrational states. The population distribution of these states can be investigated by probing the product states with our measurement scheme.

Bibliography

[1] W. Heitler, and F. London, *Wechselwirkung neutraler Atome und homöopolare Bindung nach der Quantenmechanik.* Zeitschrift für Physik **46**, 455 (1927).

[2] B. S. Park, *Computational Imperatives in Quantum Chemistry.* Edited by Christian Joas, Christoph Lehner, and Jürgen Renn, in HQ-1: Conference on the History of Quantum Physics (MPI-Preprint 350), , Berlin: Max Planck Institute, 299-322, (2008).

[3] X. Yang, *State-to-State Dynamics of Elementary Bimolecular Reactions.* Annu. Rev. Phys. Chem. **58**, 433 (2007).

[4] S. Y. T. van de Meerakker, H. L. Bethlem, N. Vanhaecke, and G. Meijer, *Manipulation and Control of Molecular Beams.* Chem. Rev. **112**, 4828 (2012).

[5] J. Jankunas, and A. Osterwalder, *Cold and Controlled Molecular Beams: Production and Applications.* Annu. Rev. Phys. Chem. **66**, 241 (2015).

[6] Y. Wang, J. P. D'Incao, and B. D. Esry, *Cold three-body collisions in hydrogen-hydrogen-alkali-metal atomic systems.* Phys. Rev. A **83**, 032703 (2011).

[7] J. Wang, J. P. D'Incao, and C. H. Greene, *Numerical study of three-body recombination for systems with many bound states.* Phys. Rev. A **84**, 052721 (2011).

[8] J. F. E. Croft, C. Makrides, M. Li, A. Petrov, B. K. Kendrick, N. Balakrishnan, and S. Kotochigova, *Universality and chaoticity in ultracold K+KRb chemical reactions.* Nat. Commun. **8**, 15897 (2017).

[9] J. Rui, H. Yang, L. Liu, D.-C. Zhang, Y.-X. Liu, J. Nan, Y.-A. Chen, B. Zhao, and J.-W. Pan, *Controlled state-to-state atom-exchange reaction in an ultracold atom-dimer mixture.* Nat. Phys. **13**, 699 (2017).

[10] T. Weber, J. Herbig, M. Mark, H.-C. Nägerl, and R. Grimm, *Three-Body Recombination at Large Scattering Lengths in an Ultracold Atomic Gas*. Phys. Rev. Lett. **91**, 123201 (2003).

[11] S. Jochim, M. Bartenstein, A. Altmeyer, G. Hendl, C. Chin, J. Hecker Denschlag, and R. Grimm, *Pure Gas of Optically Trapped Molecules Created from Fermionic Atoms*. Phys. Rev. Lett. **91**, 240402 (2003).

[12] A. Härter, A. Krükow, M. Deiß, B. Drews, E. Tiemann, and J. Hecker Denschlag, *Population distribution of product states following three-body recombination in an ultracold atomic gas*. Nat. Phys. **9**, 512 (2013).

[13] A. Härter, A. Krükow, A. Brunner, W. Schnitzler, S. Schmid, and J. Hecker Denschlag, *Single Ion as a Three-Body Reaction Center in an Ultracold Atomic Gas*. Phys. Rev. Lett. **109**, 123201 (2012).

[14] A. Krükow, A. Mohammadi, A. Härter, J. Hecker Denschlag, J. Pérez-Ríos, and C. H. Greene, *Energy scaling of cold atom-atom-ion three-body recombination*. Phys. Rev. Lett. **116**, 193201 (2016).

[15] A. Krükow, A. Mohammadi, A. Härter, and J. Hecker Denschlag, *Reactive two-body and three-body collisions of* Ba^+ *in an ultracold Rb gas*. Phys. Rev. Lett. **94**, 030701(R) (2016).

[16] L. Wang, M. Deiß, G. Raithel, and J. Hecker Denschlag, *Controlling cold atom-ion collisions using a Rydberg state*. arXiv **1901.08781** (2019)

[17] S. Schmid, A. Härter, A. Frisch, S. Hoinka, and J. Hecker Denschlag, *An apparatus for immersing trapped ions into an ultracold gas of neutral atoms*. Rev. Sci. Instrum. **83**, 053108 (2012).

[18] S. Schmid, *Dynamics of a cold trapped ion in a Bose-Einstein condensate*, Ph.D. thesis, Universität Ulm (2011).

[19] A. Härter, *Two-Body and Three-Body Dynamics in Atom-Ion Experiments*, Ph.D. thesis, Universität Ulm (2013).

[20] A. Krükow, *Three-Body Reaction Dynamics in cold Atom-Ion Experiments*, Ph.D. thesis, Universität Ulm (2016).

[21] K. M. Jones, E. Tiesinga, P. D. Lett, and P. S. Julienne, *Ultracold photoassociation spectroscopy: Long-range molecules and atomic scattering*. Rev. Mod. Phys. **78**, 483 (2006).

[22] R. Löw, H. Weimer, J. Nipper, J. B. Balewski, B. Butscher, H. P. Büchler, and T. Pfau, *An experimental and theoretical guide to strongly interacting Rydberg gases*. J. Phys. B: At. Mol. Opt. Phys. **45**, 113001 (2012).

[23] Y. Colombe, D. H. Slichter, A. C. Wilson, D. Leibfried, and D. J. Wineland, *Single-mode optical fiber for high-power, low-loss UV transmission*. Opt. Express **22**, 19783 (2014)

[24] A. J. Moerdijk, H. M. J. M. Boesten, and B. J. Verhaar, *Decay of trapped ultracold alkali atoms by recombination*. Phys. Rev. A **53**, 916 (1996).

[25] P. O. Fedichev, M. W. Reynolds, and G. V. Shlyapnikov, *Three-body recombination of ultracold atoms to a weakly bound s level*. Phys. Rev. Lett. **77**, 2921 (1996).

[26] J. Söding, D. Guéry-Odelin, P. Desbiolles, F. Chevy, H. Inamori, and J. Dalibard, *Three-body decay of a rubidium Bose-Einstein condensate*. Appl. Phys. B **69**, 257 (1999).

[27] C. Chin, R. Grimm, P. Julienne, and E. Tiesinga, *Feshbach resonances in ultracold gases*. Rev. Mod. Phys. **82**, 1225-1286 (2010).

[28] E. A. Burt, R. W. Ghrist, C. J. Myatt, M. J. Holland, E. A. Cornell, and C. E. Wieman, *Coherence, Correlations, and Collisions: What One Learns about Bose-Einstein Condensates from Their Decay*. Phys. Rev. Lett. **79**, 337 (1997).

[29] G. Quéméner, and P. S. Julienne, *Ultracold Molecules under Control!* Chem. Rev. **112**, 4949 (2012).

[30] B. D. Esry, C. H. Greene, and J. P. Burke, *Recombination of Three Atoms in the Ultracold Limit*. Phys. Rev. Lett. **83**, 1751 (1999).

[31] J. P. D'Incao, and B. D. Esry, *Scattering Length Scaling Laws for Ultracold Three-Body Collisions*. Phys. Rev. Lett. **94**, 213201 (2005).

[32] D. S. Petrov, *Three-Boson Problem near a Narrow Feshbach Resonance*. Phys. Rev. Lett. **93**, 143201 (2004).

[33] J. Pérez-Ríos, S. Ragole, J. Wang, and C. H. Greene, *Comparison of classical and quantal calculations of helium three-body recombination*. J. Chem. Phys. **140**, 044307 (2014).

[34] Y. Wang, and P. S. Julienne, *Universal van der Waals physics for three cold atoms near Feshbach resonances*. Nat. Phys. **10**, 768 (2014).

[35] E. Braaten, and H.-W. Hammer, *Universality in few-body systems with large scattering length*. Phys. Rep. **428**, 259-390 (2006).

[36] T. Kraemer, M. Mark, P. Waldburger, J. G. Danzl, C. Chin, B. Engeser, A.D. Lange, K. Pilch, A. Jaakkola, H.-C. Nägerl, and R. Grimm, *Evidence for Efimov quantum states in an ultracold gas of caesium atoms*. Nature **440**, 315 (2006).

[37] Z. Shotan, O. Machtey, S. Kokkelmans, and L. Khaykovich, *Three-Body Recombination at Vanishing Scattering Lengths in an Ultracold Bose Gas*. Phys. Rev. Lett. **113**, 053202 (2014).

[38] M. L. González-Martínez, O. Dulieu, P. Larrégaray, and L. Bonnet, *Statistical product distributions for ultracold reactions in external fields*. Phys. Rev. A **90**, 052716 (2014).

[39] D. Nesbitt, *Toward State-to-State Dynamics in Ultracold Collisions: Lessons from High-Resolution Spectroscopy of Weakly Bound Molecular Complexes*. Chem. Rev. **112**, 5062 (2012).

[40] A. N. Drozdova, A. V. Stolyarov, M. Tamanis, R. Ferber, P. Crozet, and A. J. Ross, *Fourier transform spectroscopy and extended deperturbation treatment of the spin-orbit-coupled $A^1\Sigma_u^+$ and $b^3\Pi_u$ states of the Rb_2 molecule*. Phys. Rev. A **88**, 022504 (2013).

[41] M. Deiß, B. Drews, J. Hecker Denschlag, and E. Tiemann, *Mixing of 0^+ and 0^- observed in the hyperfine and Zeeman structure of ultracold Rb_2 molecules*. New J. Phys. **17,** 083032 (2015).

[42] J. Wolf, M. Deiß, A. Krükow, E. Tiemann, B. P. Ruzic, Y. Wang, J. P. D'Incao, P. S. Julienne, and J. Hecker Denschlag, *State-to-state chemistry for three-body recombination in an ultracold rubidium gas*. Science **358**, 921 (2017).

[43] B. Drews, M. Deiß, J. Wolf, E. Tiemann, and J. Hecker Denschlag, *Level structure of deeply bound levels of the $c^3\Sigma_g^+$ state of $^{87}Rb_2$*. Phys. Rev. A **95**, 062507 (2017).

[44] C. Strauss, T. Takekoshi, F. Lang, K. Winkler, R. Grimm, J. Hecker Denschlag, and E. Tiemann, *Hyperfine, rotational, and vibrational structure of the $a^3\Sigma_u^+$ state of $^{87}Rb_2$*. Phys. Rev. A **82**, 052514 (2010).

[45] Y. Guan, X. Han, J. Yang, Z. Zhou, X. Dai, E. H. Ahmed, A. M. Lyyra, S. Magnier, V. S. Ivanov, A. S. Skublov, and V. B. Sovkov, *Updated potential energy function of the Rb_2 $a^3\Sigma_u^+$ state in the attractive and repulsive regions determined from its joint analysis with the $2^3\Pi_{0g}$ state*. J. Chem. Phys. **139**, 144303 (2013).

[46] A. Härter, A. Krükow, A. Brunner, and J. Hecker Denschlag, *Minimization of ion micromotion using ultracold atomic probes*. Appl. Phys. Lett. **102**, 221115 (2013).

[47] T. Mukaiyama, J. R. Abo-Shaeer, K. Xu, J. K. Chin, and W. Ketterle, *Dissociation and Decay of Ultracold Sodium Molecules*. Phys. Rev. Lett. **92**, 180402 (2004).

[48] P. Staanum, S. D. Kraft, J. Lange, R. Wester, and M. Weidemüller, *Experimental Investigation of Ultracold Atom-Molecule Collisions*. Phys. Rev. Lett. **96**, 023201 (2006).

[49] N. Zahzam, T. Vogt, M. Mudrich, D. Comparat, and P. Pillet, *Atom-Molecule Collisions in an Optically Trapped Gas*. Phys. Rev. Lett. **96**, 023202 (2006).

[50] G. Quéméner, P. Honvault, J.-M. Launay, P. Soldán, D. E. Potter, and J. M. Hutson, *Ultracold quantum dynamics: Spin-polarised $K + K_2$ collisions with three identical bosons or fermions*. Phys. Rev. A **71**, 032722 (2005).

[51] N. P. Mehta, S. T. Rittenhouse, J. P. D'Incao, J. von Stecher, and C. H. Greene, *General Theoretical Description of N-Body Recombination*. Phys. Rev. Lett. **103**, 153201 (2009).

[52] J. Wang, J. P. D'Incao, Y. Wang, and C. H. Greene, *Universal three-body recombination via resonant d-wave interactions*. Phys. Rev. A **86**, 062511 (2012).

[53] B. M. Axilrod, and E. Teller, *Interaction of the van der Waals type between three atoms*. J. Chem. Phys. **11**, 299 (1943).

[54] J. L. Bohn, A. M. Rey, and J. Ye, *Cold molecules: Progress in quantum engineering of chemistry and quantum matter*. Science **357**, 1002 (2017).

[55] N. Balakrishnan, *Perspective: Ultracold molecules and the dawn of cold controlled chemistry* . J. Chem. Phys. **145**, 150901 (2016).

[56] R. V. Krems, *Cold controlled chemistry*. Phys. Chem. Chem. Phys. **10**, 4079 (2008)

[57] L. D. Carr, D. DeMille, R. V. Krems, and J. Ye, *Cold and ultracold molecules: science, technology and applications*. New J. Phys. **11**, 055049 (2009).

[58] J. Doyle, B. Friedrich, R. V. Krems, and F. Masnou-Seeuws, *Editorial: Quo vadis, cold molecules?*. Eur. Phys. J. D **31**, 149 (2004).

[59] S. Knoop, F. Ferlaino, M. Berninger, M. Mark, H.-C. Nägerl, R. Grimm, J. P. D'Incao, and B. D. Esry, *Magnetically Controlled Exchange Process in an Ultracold Atom-Dimer Mixture*. Phys. Rev. Lett. **104**, 053201 (2010).

[60] D. K. Hoffmann, T. Paintner, W. Limmer, D. S. Petrov, and J. Hecker Denschlag, *Reaction kinetics of ultracold molecule-molecule collisions*. Nat. Commun. **9** 5244 (2018).

[61] F. Ferlaino, A. Zenesini, M. Berninger, B. Huang, H.-C. Nägerl, and R. Grimm, *Efimov Resonances in Ultracold Quantum Gases*. Few-Body Syst **51**, 113 (2011).

[62] M. McDonald, I. Majewska, C.-H. Lee, S. S. Kondov, B. H. McGuyer, R. Moszynski, and T. Zelevinsky, *Control of Ultracold Photodissociation with Magnetic Fields*. Phys. Rev. Lett. **120**, 033201 (2018).

[63] T. Volz, S. Dürr, S. Ernst, A. Marte, and G. Rempe, *Characterization of elastic scattering near a Feshbach resonance in ^{87}Rb*. Phys. Rev. A **68**, 010702(R) (2003).

[64] E. Tiemann, *private communication* (2017).

[65] J. Hecker Denschlag, *A toy model for a diatomic molecule*. Phys. Scr. **91**, 083012 (2016).

[66] K. Shibata, A. Torii, H. Shibayama, Y. Eto, H. Saito, and T. Hirano, *Interaction modulation in a long-lived Bose-Einstein condensate by rf coupling*. Phys. Rev. A **99**, 013622 (2019).

[67] A. Härter, and J. Hecker Denschlag, *Cold atom-ion experiments in hybrid traps*. Contemp. Phys. **55**, 33 (2014).

[68] S. Willitsch, *Ion-atom hybrid systems*. Proc. Int. Sch. Phys. Enrico Fermi **189**, 255 (2015).

[69] M. Tomza, K. Jachymski, R. Gerritsma, A. Negretti, T. Calarco, Z. Idziaszek, and P. S. Julienne, *Cold hybrid ion-atom systems*. Rev. Mod. Phys. **91**, 035001 (2019).

[70] C. Sias and M. Köhl, *Hybrid Quantum Systems of Atoms and Ions*. Quantum gas experiments - exploring many-body states, Imperial College Press, London (2014).

[71] A. T. Grier, M. Cetina, F. Oručević, and V. Vuletić, *Observation of Cold Collisions between Trapped Ions and Trapped Atoms*. Phys. Rev. Lett. **102**, 223201 (2009).

[72] W. G. Rellergert, S. T. Sullivan, S. Kotochigova, A. Petrov, K. Chen, S. J. Schowalter, and E. R. Hudson, *Measurement of a Large Chemical Reaction Rate between Ultracold Closed-Shell ^{40}Ca Atoms and Open-Shell $^{174}Yb^+$ Ions Held in a Hybrid Atom-Ion Trap*. Phys. Rev. Lett. **107**, 243201 (2011).

[73] L. Ratschbacher, C. Zipkes, C. Sias, and M. Köhl, *Controlling chemical reactions of a single particle*. Nat. Phys. **8**, 649 (2012).

[74] F. H. J. Hall and S. Willitsch, *Millikelvin Reactive Collisions between Sympathetically Cooled Molecular Ions and Laser-Cooled Atoms in an Ion-Atom Hybrid Trap*. Phys. Rev. Lett. **109**, 233202 (2012).

[75] I. Sivarajah, D. S. Goodman, J. E. Wells, F. A. Narducci, and W. W. Smith, *Evidence of sympathetic cooling of Na^+ ions by a Na magneto-optical trap in a hybrid trap*. Phys. Rev. A **86**, 063419 (2012).

[76] K. Ravi, S. Lee, A. Sharma, G. Werth and S. Rangwala, *Cooling and stabilization by collisions in a mixed ion-atom system*. Nat. commun. **3**, 1126 (2012).

[77] T. Sikorsky, Z. Meir, R. Ben-shlomi, N. Akerman, and R. Ozeri, *Spin-controlled atom-ion chemistry*. Nat. Commun. **9**, 920 (2018).

[78] J. Deiglmayr, A. Göritz, T. Best, M. Weidemüller, and R. Wester, *Reactive collisions of trapped anions with ultracold atoms*. Phys. Rev. A **86**, 043438 (2012).

[79] D. Hauser, S. Lee, F. Carelli, S. Spieler, O. Lakhmanskaya, E. S. Endres, S.l S. Kumar, F. Gianturco, and R. Wester, *Rotational state-changing cold collisions of hydroxyl ions with helium.* Nat. Phys. **11**, 467 (2015).

[80] J. Joger, H. Fürst, N. V. Ewald, T. Feldker, M. Tomza, and R. Gerritsma, *Observation of collisions between cold Li atoms and Yb$^+$ ions.* Phys. Rev. A **96**, 030703(R) (2017).

[81] S. Haze, R. Saito, M. Fujinaga, and T. Mukaiyama, *Charge-exchange collisions between ultracold fermionic lithium atoms and calcium ions.* Phys. Rev. A **91**, 032709 (2015).

[82] F. H. J. Hall, M. Aymar, N. Bouloufa-Maafa, O. Dulieu, and S. Willitsch, *Light-Assisted Ion-Neutral Reactive Processes in the Cold Regime: Radiative Molecule Formation versus Charge Exchange.* Phys. Rev. Lett. **107**, 243202 (2011).

[83] M. Mills, P. Puri, M. Li, S. J. Schowalter, A. Dunning, C. Schneider, S. Kotochigova, E. R. Hudson, *Engineering excited-state interactions at ultracold temperatures.* Phys. Rev. Lett. **122**, 233401 (2019).

[84] M. Li, M. Mills, P. Puri, A. Petrov, E. R. Hudson, and S. Kotochigova, *Excitation-assisted nonadiabatic charge-transfer reaction in a mixed atom-ion system.* Phys. Rev. A **99**, 062706 (2019).

[85] T. Secker, R. Gerritsma, A. W. Glaetzle, and A. Negretti, *Trapped Ions in Rydberg-Dressed Atomic Gases.* Phys. Rev. A **94**, 013420 (2016).

[86] T. Secker, N. V. Ewald, J. Joger, H. Fürst, T. Feldker, and R. Gerritsma, *Controlled long-range interactions between Rydberg atoms and ions.* Phys. Rev. Lett. **118**, 263201 (2017).

[87] F. Engel, T. Dieterle, T. Schmid, C. Tomschitz, C. Veit, N. Zuber, R. Löw, T. Pfau, and F. Meinert, *Observation of Rydberg Blockade Induced by a Single Ion.* Phys. Rev. Lett. **121**, 193401 (2018).

[88] N. V. Ewald, T. Feldker, H. Hirzler, H. Fürst, and R. Gerritsma, *Observation of Interactions between Trapped Ions and Ultracold Rydberg Atoms.* Phys. Rev. Lett. **122**, 253401 (2019)

[89] L. Ding, M. Sudakov, and S. Kumashiro, *A simulation study of the digital ion trap mass spectrometer*. Int. J. Mass Spectrom. **221**, 117 (2002).

[90] S. Bandelow, G. Marx, and L. Schweikhard, *The stability diagram of the digital ion trap*. Int. J. Mass Spectrom. **336**, 47 (2013).

[91] N. Deb, L. L. Pollum, A. D. Smith, M. Keller, C. J. Rennick, B. R. Heazlewood, and T. P. Softley, *Coulomb crystal mass spectrometry in a digital ion trap*. Phys. Rev. A **91**, 033408 (2015).

[92] C. H. Greene, A. S. Dickinson, and H. R. Sadeghpour, *Creation of Polar and Non-polar Ultra-Long-Range Rydberg Molecules*. Phys. Rev. Lett. **85**, 2458 (2000).

[93] V. Bendkowsky, B. Butscher, J. Nipper, J. P. Shaffer, R. Löw, and T. Pfau, *Observation of ultralong-range Rydberg molecules*. Nature **458**, 1005 (2009)

[94] J. P Shaffer, S. T Rittenhouse, and H. R Sadeghpour, *Ultracold Rydberg molecules*. Nat. Commun. **9**, 1965 (2018).

[95] C. Fey, F. Hummel, and P. Schmelcher, *Ultralong-range Rydberg molecules*. arXiv **1907.13416** (2019).

[96] M. T. Eiles, *Trilobites, butterflies, and other exotic specimens of long-range Rydberg molecules*. J. Phys. B: At. Mol. Opt. Phys. **52**, 113001 (2019).

[97] A. A. Khuskivadze, M. I. Chibisov, and I. I. Fabrikant, *Adiabatic energy levels and electric dipole moments of Rydberg states of Rb_2 and Cs_2 dimers*. Phys. Rev. A **66**, 042709 (2002).

[98] S. Markson, S. T. Rittenhouse, R. Schmidt, J. P. Shaffer, and H. R. Sadeghpour, *Theory of Ultralong-Range Rydberg Molecule Formation Incorporating Spin-Dependent Relativistic Effects: Cs(6s)-Cs(np) as Case Study*. Chem. Phys. Chem. **17**, 3683 (2016).

[99] M. T. Eiles, and C. H. Greene, *Hamiltonian for the inclusion of spin effects in long-range Rydberg molecules*. Phys. Rev. A **95**, 042515 (2017).

[100] O. Thomas, C. Lippe, T. Eichert, and H. Ott, *Experimental realization of a Rydberg optical Feshbach resonance in a quantum many-body system*. Nat. Commun. **9**, 2238 (2018).

[101] M. A. Bellos, R. Carollo, J. Banerjee, E. E. Eyler, P. L. Gould, and W. C. Stwalley, *Excitation of Weakly Bound Molecules to Trilobitelike Rydberg States*. Phys. Rev. Lett. **111**, 053001 (2013).

[102] D. A. Anderson, S. A. Miller, and G. Raithel, *Photoassociation of Long-Range nD Rydberg Molecules*. Phys. Rev. Lett. **112**, 163201 (2014).

[103] A. T. Krupp, A. Gaj, J. B. Balewski, P. Ilzhöfer, S. Hofferberth, R. Löw, T. Pfau, M. Kurz, and P. Schmelcher, *Alignment of D-State Rydberg Molecules*. Phys. Rev. Lett. **112**, 143008 (2014).

[104] K. S. Kleinbach, F. Meinert, F. Engel, W. J. Kwon, R. Löw, T. Pfau, and G. Raithel, *Photoassociation of Trilobite Rydberg Molecules via Resonant Spin-Orbit Coupling*. Phys. Rev. Lett. **118**, 223001 (2017).

[105] W. Li, T. Pohl, J. M. Rost, S. T. Rittenhouse, H. R. Sadeghpour, J. Nipper, B. Butscher, J. B. Balewski, V. Bendkowsky, R. Löw, and T. Pfau, *A Homonuclear Molecule with a Permanent Electric Dipole Moment*. Science **334**, 1110 (2011).

[106] J. Tallant, S. T. Rittenhouse, D. Booth, H. R. Sadeghpour, and J. P. Shaffer, *Observation of Blueshifted Ultralong-Range Cs_2 Rydberg Molecules*. Phys. Rev. Lett. **109**, 173202 (2012).

[107] D. Booth, S. T. Rittenhouse, J. Yang, H. R. Sadeghpour, and J. P. Shaffer, *Production of trilobite Rydberg molecule dimers with kilo-Debye permanent electric dipole moments*. Science **348**, 99 (2015).

[108] H. Saßmannshausen, F. Merkt, and J. Deiglmayr, *Experimental Characterization of Singlet Scattering Channels in Long-Range Rydberg Molecules*. Phys. Rev. Lett. **114**, 133201 (2015).

[109] B. J. DeSalvo, J. A. Aman, F. B. Dunning, T. C. Killian, H. R. Sadeghpour, S. Yoshida, and J. Burgdörfer, *Ultra-long-range Rydberg molecules in a divalent atomic system*. Phys. Rev. A **92**, 031403(R) (2015).

[110] T. Niederprüm, O. Thomas, T. Eichert, C. Lippe, J. Pérez-Ríos, C. H. Greene, and H. Ott, *Observation of pendular butterfly Rydberg molecules*. Nat. Commun. **7**, 12820 (2016)

[111] T. Niederprüm, O. Thomas, T. Eichert, and H. Ott, *Rydberg Molecule-Induced Remote Spin Flips*. Phys. Rev. Lett. **117**, 123002 (2016).

[112] V. Bendkowsky, B. Butscher, J. Nipper, J. P. Balewski, J. P. Shaffer, R. Löw, T. Pfau, W. Li, J. Stanojevic, T. Pohl, and J. M. Rost, *Rydberg Trimers and Excited Dimers Bound by Internal Quantum Reflection*. Phys. Rev. Lett. **105**, 163201 (2010).

[113] F. Böttcher, A. Gaj, K. M. Westphal, M. Schlagmüller, K. S. Kleinbach, R. Löw, T. Cubel Liebisch, T. Pfau, and S. Hofferberth, *Observation of mixed singlet-triplet Rb_2 Rydberg molecules*. Phys. Rev. A **93**, 032512 (2016).

[114] J. L. MacLennan, Y.-J. Chen, and G. Raithel, *Deeply bound ($24D_J + 5S_{1/2}$) ^{87}Rb and ^{85}Rb molecules for eight spin couplings*. Phys. Rev. A **99**, 033407 (2019).

[115] D. A. Anderson, S. A. Miller, and G. Raithel, *Angular-momentum couplings in long-range Rb_2 Rydberg molecules*. Phys. Rev. A **90**, 062518 (2014).

[116] F. Engel, T. Dieterle, F. Hummel, C. Fey, P. Schmelcher, R. Löw, T. Pfau, and F. Meinert, *Precision Spectroscopy of Negative-Ion Resonances in Ultralong-Range Rydberg Molecules*. Phys. Rev. Lett. **123**, 073003 (2019).

[117] M. I. Chibisov, A. A. Khuskivadze, and I. I. Fabrikant, *Energies and dipole moments of long-range molecular Rydberg states*. J. Phys. B: At. Mol. Opt. Phys. **35**, L193 (2002).

[118] E. L. Hamilton, C. H. Greene, and H. R. Sadeghpour, *Shape-resonance-induced long-range molecular Rydberg states*. J. Phys. B: At. Mol. Opt. Phys. **35**, L199 (2002).

[119] T. Niederprüm, O. Thomas, T. Manthey, T. M. Weber, and H. Ott, *Giant Cross Section for Molecular Ion Formation in Ultracold Rydberg Gases*. Phys. Rev. Lett. **115**, 013003 (2015).

[120] M. Schlagmüller, T. C. Liebisch, F. Engel, K. S. Kleinbach, F. Böttcher, U. Hermann, K. M. Westphal, A. Gaj, R. Löw, S. Hofferberth, T. Pfau, J. Pérez-Ríos, and C. H. Greene, *Ultracold Chemical Reactions of a Single Rydberg Atom in a Dense Gas*. Phys. Rev. X **6**, 031020 (2016).

[121] S. Bize, Y. Sortais, M. S. Santos, C. Mandache, A. Clairon, and C. Salomon, *High-accuracy measurement of the ^{87}Rb ground-state hyperfine splitting in an atomic fountain*. Europhys. Lett. **45**, 558 (1999).

[122] E. Arimondo, M. Inguscio, and P. Violino, *Experimental determinations of the hyperfine structure in the alkali atoms*. Rev. Mod. Phys. **49**, 31 (1977).

[123] W. Li, I. Mourachko, M. W. Noel, and T. F. Gallagher, *Millimeter-wave spectroscopy of cold Rb Rydberg atoms in a magneto-optical trap: Quantum defects of the ns, np, and nd series*. Phys. Rev. A, **67**, 052502 (2003).

[124] J. Han, Y. Jamil, D. V. L. Norum, P. J. Tanner, and T. F. Gallagher, *Rb nf quantum defects from millimeter-wave spectroscopy of cold ^{85}Rb Rydberg atoms*. Phys. Rev. A, **74**, 054502 (2006).

[125] F. Hummel, C. Fey, and P. Schmelcher, *Spin-interaction effects for ultralong-range Rydberg molecules in a magnetic field*. Phys. Rev. A, **97**, 043422 (2017).

[126] C. Bahrim and U. Thumm, *Low-lying $^3P^o$ and $^3S^e$ states of Rb^-, Cs^-*. Phys. Rev. A **61**, 022722 (2000).

[127] C. Fey, M. Kurz, P. Schmelcher, S. T. Rittenhouse, and H. R. Sadeghpour, *A comparative analysis of binding in ultralong-range Rydberg molecules*. New J. Phys. **17**, 055010 (2015).

[128] U. Thumm and D. W. Norcross, *Evidence for very narrow shape resonances in low-energy electron-Cs scattering*. Phys. Rev. Lett. **67**, 3495 (1991).

[129] S. Hollerith, J. Zeiher, J. Rui, A. Rubio-Abadal, V. Walther, T. Pohl, D. M. Stamper-Kurn, I. Bloch, and C. Gross, *Quantum gas microscopy of Rydberg macrodimers*. Science **364**, 664 (2019).

[130] H. Köppel, W. Domcke, and L. S. Cederbaum, *Multimode Molecular Dynamics Beyond the Born-Oppenheimer Approximation*. Adv. Chem. Phys. **57**, 59 (1984).

[131] M. Tarana and R. Čurík, *Adiabatic potential-energy curves of long-range Rydberg molecules: Two-electron R-matrix approach*. Phys. Rev. A **93**, 012515 (2016).

[132] C. Fey, M. Kurz, and P. Schmelcher, *Stretching and bending dynamics in triatomic ultralong-range Rydberg molecules*. Phys. Rev. A **94**, 012516 (2016).

[133] M. Schlagmüller, T. Cubel Liebisch, H. Nguyen, G. Lochead, F. Engel, F. Böttcher, K. M. Westphal, K. S. Kleinbach, R. Löw, S. Hofferberth, T. Pfau, J. Pérez-Ríos, and C. H. Greene, *Probing an Electron Scattering Resonance using Rydberg Molecules within a Dense and Ultracold Gas*. Phys. Rev. Lett. **116**, 053001 (2016).

[134] M. T. Eiles, J. Pérez-Ríos, F. Robicheaux, and C. H. Greene, *Ultracold molecular Rydberg physics in a high density environment*. J. Phys. B: At. Mol. Opt. Phys. **49**, 114005 (2016).

[135] R. Schmidt, H. R. Sadeghpour, and E. Demler, *Mesoscopic Rydberg Impurity in an Atomic Quantum Gas*. Phys. Rev. Lett. **116**, 105302 (2016).

[136] Y. Ashida, T. Shi, R. Schmidt, H. R. Sadeghpour, J. I. Cirac, and E. Demler, *Quantum Rydberg Central Spin Model*. arXiv **1905.08523** (2019).

[137] C. E. Theodosiou, *Lifetimes of alkali-metal–atom Rydberg states*. Phys. Rev. A **30**, 2881 (1984).

Theoretical prediction of splitting induced by LS coupling

[138] F. Hummel, C. Fey, and P. Schmelcher, *Alignment of s-state Rydberg molecules in magnetic fields*. Phys. Rev. A., **99**, 023401 (2019).

[139] J. P. Burke, and J. L. Bohn, *Ultracold scattering properties of the short-lived Rb isotopes*. Phys. Rev. A **59**, 1303 (1999).

[140] C. L. Blackley, C. R. Le Sueur, J. M. Hutson, D. J. McCarron, M. P. Köppinger, H.-W. Cho, D. L. Jenkin, and S. L. Cornish, *Feshbach resonances in ultracold ^{85}Rb*. Phys. Rev. A **87**, 033611 (2013).

Erklärung

Ich versichere hiermit, dass ich die Arbeit selbständig angefertigt habe und keine anderen als die angegebenen Quellen und Hilfsmittel benutzt sowie die wörtlich oder inhaltlich übernommenen Stellen als solche kenntlich gemacht habe.

Ulm, den 16.09.2019

....

Joschka Wolf

Erklärung über individuellen Beitrag zur Dissertation

Teile dieser Dissertation sind in Ko-Autorenschaft mit anderen Wissenschaftlern entstanden. Dies bezieht sich auf die Kapitel 4, 5 und 6, die deckungsgleich mit den an entsprechender Stelle aufgeführten wissenschaftlichen Publikationen sind, sowie auf Kapitel 7 welches eine überarbeitete vorläufige Version der aufgeführten Publikation ist.

- Kapitel 4 und 5: Ich war bei der Ausarbeitung der Messmethoden, der Aufnahme der gezeigten Messdaten, der Datenanalyse und dem Schreiben der Publikationen in hauptverantwortlichem Maße beteiligt.

- Kapitel 6: Ich war bei der Ausarbeitung der Messmethoden, der Aufnahme der Messdaten und der Datenanalyse in wesentlichem Maße beteiligt. Ich habe beim Schreiben der Publikation assistiert.

- Kapitel 7: Ich war bei der Ausarbeitung der Messmethoden, der Aufnahme der Messdaten und der Datenanalyse in wesentlichem Maße beteiligt.

Ulm, den 16.09.2019   Joschka Wolf   ....

                                              Unterschrift

Bestätigung der Richtigkeit der Angaben durch den Betreuer der Dissertation:

Ulm, den 16.09.2019   Johannes Hecker Denschlag   ....

                                              Unterschrift

Danksagung